# Coherent transfer of electron spins in tunnel-coupled quantum dots

Hanno Flentje

▶ **To cite this version:**

Hanno Flentje. Coherent transfer of electron spins in tunnel-coupled quantum dots. Quantum Physics [quant-ph]. Université Grenoble Alpes, 2016. English. NNT : 2016GREAY039 . tel-01526450

**HAL Id: tel-01526450**
**https://theses.hal.science/tel-01526450**

Submitted on 23 May 2017

**HAL** is a multi-disciplinary open access archive for the deposit and dissemination of scientific research documents, whether they are published or not. The documents may come from teaching and research institutions in France or abroad, or from public or private research centers.

L'archive ouverte pluridisciplinaire **HAL**, est destinée au dépôt et à la diffusion de documents scientifiques de niveau recherche, publiés ou non, émanant des établissements d'enseignement et de recherche français ou étrangers, des laboratoires publics ou privés.

Communauté
UNIVERSITÉ Grenoble Alpes

## THÈSE

Pour obtenir le grade de

**DOCTEUR DE la Communauté UNIVERSITÉ GRENOBLE ALPES**

Spécialité : **Nanophysique**

Arrêté ministériel : 07 aôut 2006

Présentée par

**Hanno Flentje**

Thèse dirigée par **Tristan Meunier**

préparée au sein **Institut Néel**
et de **L'École Doctorale de Physique de Grenoble**

# Coherent transfer of electron spins in tunnel-coupled quantum dots

Thèse soutenue publiquement le **Septembre 26, 2016**,
devant le jury composé de :

**Professeur, David Ferrand**
Professeur, Université Grenoble Alpes, Grenoble, Président
**Professeur, Ferdinand Kuemmeth**
Associate Professor, Niels-Bohr Insitute, Copenhagen (Danemark), Rapporteur
**Docteur, Takis Kontos**
Directeur de recherche, Laboratoire Pierre Aigrain (LPA), Paris, Rapporteur
**Professeur, Wolfgang Wernsdorfer**
Professor, Institute of Technology (KIT), Karlsruhe (Allemagne), Examinateur
**Docteur, Tristan Meunier**
Chercheur à L'Institut Néel, Directeur de thèse

## Abstract

Recent technological advances hint at the future possibility to use electron spins as carriers and storage of information. Due to their quantum nature, individually controlled electron spins can not only be used to store classical information, but could also find implementation as quantum bits in a quantum computer. In this envisioned device, the superposition of different spin states could be used to perform novel calculation procedures more efficiently than their classical counterparts.

A promising implementation of a controllable single electron spin system is an electron trapped in a lateral quantum dot. This nanoscale solid state device allows to isolate and coherently manipulate the spin of individual electrons with electrostatic potentials. In this thesis we study electrons in quantum dot structures using a manipulation technique which we call the "isolated regime". In this regime the manipulation of individual electron charges in several connected quantum dots is shown to be simplified. This allows to implement a novel spin manipulation scheme to induce coherent exchange of a quantum of spin between two electrons via a variation of the tunnel-coupling between adjacent quantum dots. This manipulation scheme is observed to lead to a reduced sensibility to charge noise at a "sweet spot" and thereby allows to obtain high quality spin oscillations.

The improved charge control in the isolated regime is then used to achieve circular coupling in a triple quantum dot device with high tunnel-rates. This allows to directly probe the coherence of a superposition of two electron spins which are displaced on a closed loop in the three quantum dots. Our measurements demonstrate coherent electron transport over distances of up to 5 µm. During the transfer the coherence time is found to be significantly increased. We identify the underlying mechanism for the enhancement with a motional narrowing of the nuclear field gradients originating from the crystal environment. The limiting decoherence source is found to be single electron spin-flips induced by a real space motion of the electrons. Our results on the coherent transport of electrons can be used to asses the scaling possibilities of spin qubit implementations on two-dimensional lattices.

# Contents

# Introduction

One of the most significant scientific discoveries of the last century has been the quantum nature of the composing building blocks of our environment. The implications of this new theoretical construction on our understanding of physical processes are severe and often against our native intuition. It follows that the surrounding world is at its core no longer deterministic, but the expectation value of a great number of coin flips. Moreover, the emerging laws governing these coin flips are highly non-intuitive. The most notable example is the possibility of the coin being heads and tails at the same time. This paradox is only lifted when an "observer" is asked to measure the outcome of the experiment. Then the coin will give a clear answer, be it heads or tails. Philosophical questions aside, this finding broke several established paradigms and resulted in the development of the theory known as quantum mechanics. The often surprising implications of this quantum theory have been most rigorously researched in the last hundred years and the performed experiments seem so far to prove every theoretical prediction.[1–7] The theory has for example allowed to accurately describe light and its interaction with matter[8,9] as well as to unravel the structure of the atoms.[10] At the same time it is able to predict the behaviour of macroscopic solid-state systems paving the way for our recent technological advance.[11–14] Lately even the predicted entanglement of two particles, which Einstein called a "spooky" interaction at distance, has been observed in several laboratories all over the world.[15,16] Very recently three experiments that increased the distance of this spooky interaction were performed, which closed the remaining loopholes in the interpretation of previous measurements.[17–19] This proof of the non-locality of the phenomenon again showed the predictive power of quantum mechanics.

The remarkable agreement of this unintuitive theory with the measured reality has made quantum mechanics a theory credible enough, that researchers all around the world are nowadays shifting from its investigation to its application. A significant scientific effort is hereby invested into the investigation of model two-level quantum systems also called "qubits".[20,21] In analogy to the classical bit used in a computer, the qubit is a system whose

state can be in the states 1 and 0. However, being a quantum system, it is also possible for the qubit to be in a coherent superposition of 1 and 0. This makes them interesting candidates for solving complex computational problems in a "quantum computer", due to the effect of computational operations affecting all states in a given superposition.[22–24] At the same time they are expected to solve fundamental physics problems when linked to form a well controlled model system also called a "quantum simulator".[25]

For both of these applications, the control over the model system has to meet several conditions.[20,21] For its use in a quantum computer, the qubit has to be initialized to a well known initial state. A well defined set of unitary operations on single qubits as well as operations involving several qubits are necessary to implement useful computations. During the operation time, the coherent superposition states produced by the unitary operations have to be preserved. That means that the operation time has to be much shorter than the decoherence time of the quantum state. The decoherence stems from the qubits exposure to its surrounding environment, making it necessary to isolate the quantum system as much as possible from its surroundings. Finally the quantum state has to be read out with a high fidelity to recover useful knowledge. Similarly, for the construction of a quantum simulator, high requirements on the qubit coherence, control possibilities as well as inter qubit coupling variation have to be fulfilled. To make the results of the simulation useful, the number of inter-connected qubits has also to be large, while their addressability and coherence have to stay conserved.

Currently various well controlled quantum systems are tested for their viability regarding the implementation of scalable model quantum systems.[26–29] Electrons in lateral quantum dots hereby emerge as a versatile candidate due to the natural two-level system created by the electron spin.[21] The quantum dot is an artificial box that confines the electron in a semiconductor crystal on nanometer scales and allows to influence its properties. The great advances made in semiconductor technology allow to obtain high quality crystals to limit the effect of the environment on the electron and promise a scaling route for the implementation of large qubit systems.

The spin of the electron in a quantum dot can nowadays be routinely initialized, controlled and read-out in small systems.[30–33] However, the crystal environment leads to a strong environmental effect on the coherent dynamics and the scaling-up of the structures has appeared to be non-trivial.[34–36] To cope with these problems, several approaches are taken. First of all, researchers try intricate manipulation and control schemes to limit the influence of the environment.[37,38] At the same time, several approaches try to influence the nature of the crystal by changing its composition and purity. Recently, quantum dots in isotopically purified silicon crystals have shown promising results regarding their coherence

time and are expected to allow reaching new levels of quantum control in semiconductor qubits.[39,40]

In this thesis, we investigated lateral quantum dots created with a conventional approach using high mobility two-dimensional electron gases in AlGaAs/GaAs heterostructures. In these crystals, we can create arbitrary potential landscapes and we can confine single electrons at will using only electrical control. Our focus will hereby lie on the developement of novel spin manipulation schemes as well as the investigation of the fundamental limitations of larger quantum systems in solid state devices. While the number of quantum dots in an investigated sample is easily increased, controlling the additional degrees of freedom and coupling the electron spins in a useful way remains a challenge. Additionally, the transport process when electrons are meant to be exchanged between the quantum dots is currently a heavily researched topic involving several different approaches. In this thesis, quantum dot systems with up to three coupled quantum dots will be investigated. A novel manipulation scheme developed in our laboratory will be shown to allow coherent operations on the spin of isolated electrons. Finally, our results on coherent transport of electron spins in a quantum dot array will be presented.

Following this introduction, the thesis is structured in the following way:

- In the first chapter the necessary general concepts for the manipulation of quantum dots will be introduced. A focus will hereby lie on the spin dynamics of the isolated electrons and their coupling to the environment of the semiconductor crystal
- In the second chapter, information on the sample fabrication, the necessary cold temperature technology and the complex experiment control scheme will be presented. This allows us to identify the technological constrictions limiting the control over quantum systems with current technology.
- In the third chapter, our recently developed tool of isolated charge manipulation in quantum dots will be introduced and applied to three different multi-dot devices. The demonstrated control over the charge of isolated electrons will be critical for the investigation of coherent spin manipulations.
- In the fourth chapter, we will focus on the spin of the isolated electrons in our devices. The spin measurement techniques will be introduced in detail and applied to a novel spin manipulation scheme. It will be shown that this scheme leads to a relaxed condition on the spin decoherence processes by allowing to perform more computational operations on a single qubit within a given coherence time. Then the spin dynamics of larger quantum dot systems will be investigated. The spin of a two electron pair is shown to be a powerful probe for the characterisation of quantum

dot coupling strengths. Finally, this tool will allow to perform an investigation of the coherence of electron transport in a multi-dot structure. The results of this work will be analysed using the available control parameters and allow an insight into the internal dynamics of the electron transport process.

- In the last chapter, we will discuss the implications of the obtained results on the viability of electron spins as qubits and show the perspectives of this work as well as avenues for future experiments.

# CHAPTER 1

## General concepts and state-of-the-art

### 1.1 Introduction

Starting with the first observation of the quantisation of conductance in a 1 dimensional constriction by van Wees et al.[41], the electrostatically patterned two-dimensional electron gas created in a AlGaAs/GaAs heterostructure has become a model system for mesoscopic physics and was used to fabricate some of the first artificial atoms.[42–44] The physics of these so called quantum dots, which are strongly coupled to a reservoir following Fermi statistics is particularly rich and has received much theoretical and experimental attention.[45–49] One of the more remarkable achievements is the observation and explanation of the Kondo effect using such a quantum dot.[50–53] While they have also been used as single electron sources or phase shifters in the developing field of quantum electron optics,[54–57] our work focuses on the isolation of the electrons trapped inside those structures. Nowadays not only the control over the charge of the quantum dot but also the spin of the trapped electrons has become standard in many laboratories across the world. As there is already an excellent array of reviews on the subject,[58–61] I will in this chapter focus only on the theoretical concepts necessary for the subsequent descriptions of the experiments as well as the simulations performed during this thesis.

### 1.2 Lateral quantum dots

One of the classic problems in quantum physics is a particle confined in a box, also called a quantum dot (QD). It turns out that when the box becomes small enough, the particle will no longer behave like a classical ping-pong ball, but its properties will be that of a wave described by the Schrödinger equation. If we assume that the electron is trapped inside a box with infinitely high potential walls on each side, then one can very easily show

that the energy of the particle becomes quantised and depends on the size of the box:

$$E = \frac{h^2 k_n^2}{2m_e} \; ; \qquad k_n = \frac{n\pi}{L} \tag{1.1}$$

where $h$ is Planck's constant, $n$ the wavenumber, $m_e$ the particles mass and $L$ the size of the Box. It turns out that even for an electron confined in a very small box of $L = 20$ nm, the energy of the ground state is only 1 meV, which is negligible at room temperature ($\approx$ 23 meV). To observe the quantum effects due to the confinement not only would it be necessary to reduce the temperature of the sample, but also to fabricate such very small structures to increase the energy of the states.

Nowadays the continued effort by the scientific community as well as the semiconductor integrated circuit industry has made the design of such nanostructures possible. Several techniques are available and used for the fabrication of quantum dots and include self assembled (or bottom-up) and top-down approaches. While self-assembled structures can be made very small and with very low defect density, their sizes and positions are usually randomly distributed and they are still lacking in reproducibility and scalability.

Therefore it is interesting to follow a top-down approach where all the design parameters are imposed by lithographic definition. While it limits the structure size to the resolution of the lithography technique, it offers maximum control over the size and the position of the created structures. As mentioned earlier we can benefit from the great effort to produce high quality two-dimensional electron gases in a GaAs/AlGaAs heterostructure.

To fabricate these structures one has to use Molecular Beam Epitaxy (MBE), a crystal growth technique which allows almost atomic vertical sharpness on interfaces between different crystals and produces very low defect densities below $1 \times 10^{14}\,\mathrm{cm}^{-3}$.[62] In this technique one begins with a monocrystalline GaAs substrate and then adds different atomic species in an ultra high vacuum chamber by evaporation of different high purity sources. This results in a very controllable vertical stack of materials and allows a sharp interface between $\mathrm{Al}_x\mathrm{Ga}_{1-x}\mathrm{As}$ and GaAs with typically x$\approx$ 0.33. As the lattice parameter of the crystals shows very small variation with the composition x,[63] this interface is almost strain free and of a high quality.

Due to the different energy bandgaps of the two materials and with clever engineering, one can induce a very small region around the interface where electrons can be strongly confined by the discontinuity of the crystal energies. By adjusting the doping concentration and profile, a high mobility two dimensional electron gas (2DEG) with engineered electron densities can be created. A typical growth profile can be seen in Fig. 1.1. The corresponding conduction band profile shown on the right side experiences a sharp kink at the interface

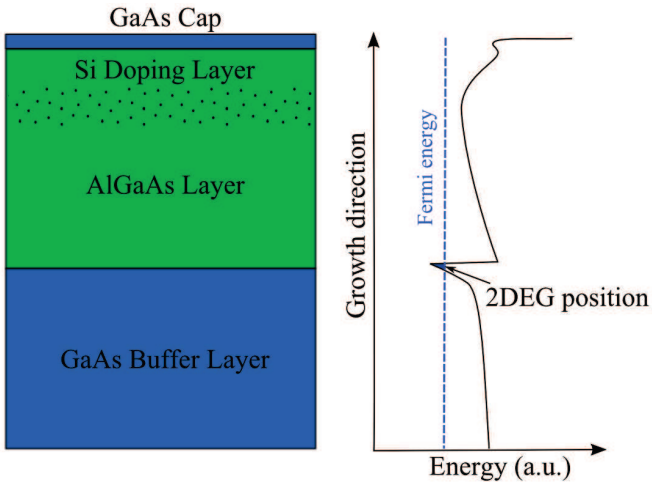


**Figure 1.1:** Simplified schematic of the heterostructure used for the fabrication of the lateral quantum dots. On the left the material stack commonly used is shown with the interface usually 90 nm below the surface. The right side shows a corresponding energy diagram of the conduction band. The 2DEG is located at the interface of the two materials where the conduction band lies below the Fermi energy

of the two materials and goes below the Fermi energy. In this strongly confined region the 2DEG is formed. The extent of the 2DEG in the growth direction has been shown to be of the order of 10-20 nm[64] and is generally negligible compared to confining structures in the lateral direction. As the purity of the crystal and the sharpness of the interface achieved in some laboratories can be very high, the electrons confined in the 2DEG can attain very high mobilities of up to $35 \times 10^6\,\mathrm{cm}^2/\mathrm{Vs}$[65] at low temperatures as revealed by magnetoconductance measurements. This corresponds to a mean free path of over 100 µm before an electron in the 2DEG loses energy due to a scattering process. The quantum dot will be localized on a much smaller scale and will therefore have a high chance to be free of impurities that alter its properties. The attainable low electron densities of the order of $1 \times 10^{11}\,\mathrm{cm}^{-2}$ result in a large Fermi wavelength of $\lambda_F \approx 50$ nm and a large screening length that is on the order of the 2DEG thickness.[66] This allows to form lateral constrictions for quantum dots by applying negative voltages on metallic gates deposited on the crystal. The 2DEG located around 90-100 nm below the surface of the crystal will in response be locally depleted and arbitrary structures can be formed as schematically shown in Fig 1.2. This approach not only minimizes contamination of the effective area with etching techniques but also creates a variable and smooth potential landscape.

The Schottky contacts formed by the metallic gates on the semiconductor prevent current flow at low temperatures and the interaction of the gates with the quantum dot can be seen

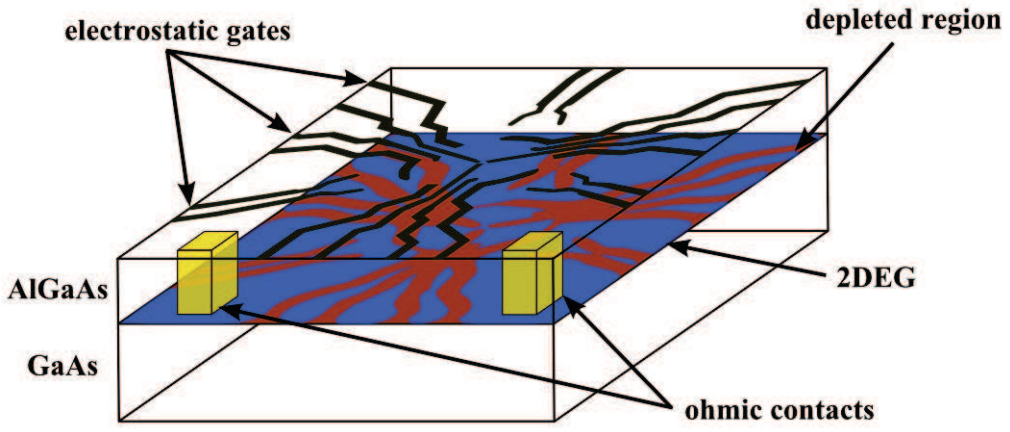


**Figure 1.2:** Schematic view of the quantum dot area of our devices. The electrostatic gates (black) are deposited on the surface. By applying negative voltages, the two dimensional electron gas (blue) can be locally depleted (red). Transport measurements are possible through ohmic contacts (yellow) which are thermally annealed to fabricate a metallic contact to the 2DEG.

as purely capacitive. Ohmic contacts to the 2DEG can be made by defining contact pads of Au-Ge on top of the structure and alloying the semiconductor in an elevated temperature annealing step. These contacts can have low resistances of $R_c \approx 2 \times 10^{-4}\ \Omega\,\mathrm{cm}^2$[67] and allow transport measurement through the structure.

Using state-of-the-art lithography methods, the size of the structures defined by the metallic gates can be of the same order of magnitude as the large Fermi wavelength, which allows to observe quantum effects. Additionally, the size of the structures is several orders of magnitude smaller than the inelastic scattering length ($\approx 100$ µm) making any electron trajectory ballistic. At low temperatures, the variable voltages allow to change the electrostatic energies with resolutions much larger than the typical energy scales of the defined quantum dots. The properties of the quantum dots can therefore be controlled electrically with high precision.

In the following we will focus on the properties of the artificial atoms created in this approach and the control of the charge and spin degrees of freedom of common QD systems. This description will begin with a single QD and later be extended to multiple coupled QDs.

## 1.3 Charge states in quantum dots

While we ultimately want to use the spin degree of freedom of the trapped electrons in our experiments, this property is very weakly coupled to the (controllable) environment. The charge degree of freedom however is very strongly coupled to the Fermi gas as well as the electrostatic gates. We can use this to implement a spin measurement by transferring information from spin to charge. Nonetheless, this information transfer requires excellent control over the electron charge as we will see later. In this section we will therefore focus on the precise dynamics of the charge of an electron in a quantum dot. As shown above, once the artificial atom's size becomes small enough, quantum effects will dominate the energy dispersion of the electron with the energy scaling with $1/L^2$. At the same time there is a charging energy implied by the selfcapacitance of the electron trapped on a small disk scaling with $1/L$.[68] This result follows directly from the formula for the energy stored on a capacitor $U = \frac{Q^2}{2C}$ where the capacitance of the thin disk is given by $C = 8\varepsilon_0 r$. For the size of our quantum dot this energy usually dominates the quantum confinement energy, which allows us to model our system with a simple electrostatic model of capacitively coupled charge islands. While a more complex treatment[69] is necessary to understand all the features seen in experiments, it turns out that the simple model allows us to get a qualitative understanding and even make quantitative predictions of the behaviour of our system.

### 1.3.1 Describing a quantum dot with the constant interaction model

In the constant interaction model, we assume that the electrons in the quantum dots behave classically in the sense that their interactions with the electrons in the environment can be parametrized with a capacitance $C$.[61] This capacitance is the sum of the different contributions of the gates and the Fermi sea $C_{sum} = C_R + C_G + C_L$ as depicted in Fig. 1.3. It is also assumed that the single particle energy spacings are independent of interactions with these electrons and the charge in the dot is quantized. We can then follow van der Wiel et al.[60] to calculate the energy spectrum and response of our system. In a system of nodes connected by capacitors, the charge on a node is linearly related to the potential of the node with the relation

$$\vec{Q} = \boldsymbol{C}\,\vec{V}. \tag{1.2}$$

Here $\vec{Q}$ is the sum of the charges on the capacitors for the different nodes, $\boldsymbol{C}$ is the capacitance matrix and $\vec{V}$ the respective potential on the nodes. For our simple case, we can find this relation by considering the sum of the charges stored on each capacitor

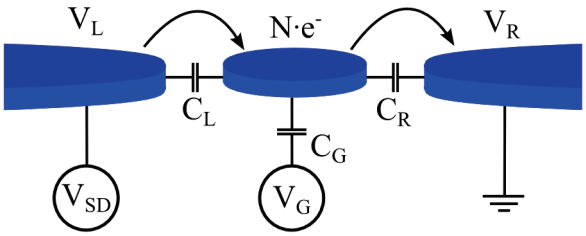


**Figure 1.3:** Schematic of a simple representation of the constant interaction model with one quantum dot. The quantum dot in the middle is coupled to the two reservoirs on each side via two capacitances $C_L$ and $C_R$. The effect of a gate is also implemented as a voltage source $V_G$ capacitively coupled via $C_G$.

connected to the dot with potential $V_D$

$$Q_D = \underbrace{(V_D - V_R)C_R}_{\text{Charge on right C}} + \underbrace{(V_D - V_L)C_L}_{\text{Charge on left C}} + \underbrace{(V_D - V_G)C_G}_{\text{Charge connected to gate}} \tag{1.3}$$

and then rewrite it to fit Eq. 1.2.

$$Q_D + V_R C_R + V_L C_L + V_G C_G = C_{sum} V_D. \tag{1.4}$$

We now assume that the charge on the dot is quantized in multiples of the charge quantum $Q_D = Ne^-$. Using

$$U = \frac{1}{2}\vec{V}\boldsymbol{C}\vec{V} = \frac{1}{2}\vec{Q}\boldsymbol{C}^{-1}\vec{Q} \tag{1.5}$$

we can find the energy of the dot for a specific number of electrons $N$

$$U = \frac{(Ne^- + V_R C_R + V_L C_L + V_G C_G)^2}{2C_{sum}}. \tag{1.6}$$

We assumed here that the voltages of the reservoirs and gates do not depend on the dynamics of the dot and will stay fixed for any value $V_D$. Note that for the case of multiple dots we will have to find Eq. 1.3 for each dot and we will end up with several equations. The charges of the different dots however will depend on the occupation of the other quantum dots and we will have to solve a system of equations. We solve a more complex model of three coupled quantum dots in Appendix A.

If we take a closer look at Eq. 1.6, we notice that the energy of the system depends quadratically on the voltages and occupation numbers. If this dependence is plotted for

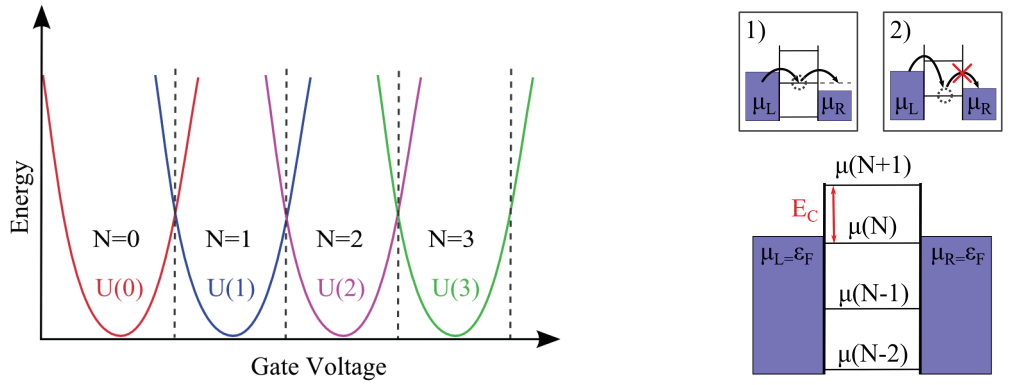


(a) (b)

**Figure 1.4:** (a) Plots of the quantum dot energy from Eq. 1.6 for different values of electron occupation N.(b) Chemical potentials for N electrons of a quantum dot with respect to the chemical potential of the reservoirs. Levels are filled when $\mu(N) < \varepsilon_F$. In the insets we can see a situation where a bias is applied across the dot. Transport through the dot is only possible in situation 1) where the chemical potential of dot is between the chemical potentials of source and drain contacts. Current is blocked in situation 2).

several fixed electron numbers and one of the gate voltages is varied, we obtain Fig. 1.4(a). For very low gate voltages the red branch with zero electrons has minimal energy, which means that the quantum dot is not occupied. By increasing the gate voltage, different branches have minimal energy and we can see that we sequentially populate the quantum dot with electrons. In a situation where the dot is coupled to a reservoir, it can always relax to the ground state by exchanging an electron with the electron reservoir and will therefore always jump to the branch with minimal energy. Then the electrochemical potential becomes a useful concept which is defined as

$$\mu(N) = U(N) - U(N-1) = (N - \frac{1}{2})E_C + \frac{E_C}{e^-}(V_R C_R + V_L C_L + V_G C_G) \tag{1.7}$$

and can be interpreted as the energy needed to add the Nth electron with the charging energy $E_C = \frac{e^2}{C_{sum}}$. This quantity is called the charging energy, as it is equal to the energy needed to add an electron $\mu(N+1) - \mu(N) = E_C$. The electrochemical potential gives a direct relation to the chemical potential of the 2DEG. The 2DEG is an electron reservoir with a chemical potential equal to its Fermi energy $\mu_R = \varepsilon_F$. The reservoir will therefore fill up the quantum dot with electrons until $\mu_{Dot}(N+1) > \varepsilon_F$ as depicted in Fig 1.4(b).

This is possible as long as the coupling between the reservoir and the quantum dot is sufficiently large. The exchange of electrons is hereby mediated by a tunnel barrier. Quantum mechanics allows a particle's spatial probability distribution to extend into and

even beyond a thin potential barrier. We call the event that a particle arrives at the other side of such a barrier a tunnelling event. The probability for such an event depends on the wavefunction overlap of the two charge states involved in the tunnelling event. The penetration of the wavefunction into the barrier resulting in the overlap depends on the height and width of the barrier. This leads to a characteristic mean frequency of events depending on the extent of the barrier which we can influence with the electrostatic profile of the trap. As long as this tunnelling is fast enough, the quantum dot will always be able to achieve equilibrium before we measure its occupancy.

If the chemical potentials of the left and the right reservoirs are not equal, for example due to an applied bias, the quantum dot will mediate electron exchange between the two. This however is only possible in the case where the chemical potential of the dot is between the chemical potentials of the reservoirs as in $\mu_{left} > \mu_{Dot} > \mu_{right}$ depicted in the first inset of Fig. 1.4(b). Then an electron can tunnel from an occupied state in the left reservoir into the quantum dot. As the state in the reservoir will be filled up again very quickly, this process is not reversible. Now as the dot chemical potential is above the Fermi energy of the right reservoir, the electron can tunnel to an unoccupied state in the right reservoir, achieving transport through the dot. On the other hand, if the chemical potential is not in the bias window, then the quantum dot will block electron exchange due to the lack of available reservoir states. This phenomenon is called Coulomb blockade as the charging energy required to increase the dot occupancy by one prevents single electron transfer from one reservoir to the other.

Of course to observe this effect a certain amount of criteria have to be met. Most importantly, the charging energy $E_C$ of the quantum dot has to be bigger than the bias window as well as the temperature broadening of the Fermi distribution $k_BT$. If the temperature is too high, all features of the quantum dot will become washed out by the broad density of states of the reservoir. The broad density of states of the 2DEG then involves multiple chemical potential levels with different electron numbers in the transport. Thus, the current through the dot becomes largely independent of the quantum dot potential and no Coulomb peaks can be observed. In the case of a large bias window $\Delta$, again multiple QD states can participate in the transport. In this case the sum of several transport channels is probed. While this situation is also interesting to study different phenomena in the QD, we shall skip a thorough investigation at this part, as it was not an important situation for our work.

In conclusion, we were able to give a powerful model for the charge dynamics of a quantum dot. Although crude, it gives a good approximation to the experimental findings and serves as an effective tool for the modelling of quantum dot systems of any shape. We

could easily understand the influence of temperature and tunnel-coupling to the Fermi sea and the model gives an intuitive understanding of transport processes. Apart from quantum tunnelling, we neglected here quantum mechanical effects such as orbitals arising in the quantum dot. These will slightly alter the energies of different states similar to the confinement energy we calculated earlier and add excited states for a given configuration of $N$ electrons. While the energy scale for these effects is one order of magnitude below the charging energy, it will have a profound impact on the spin dynamics in the quantum dot that we will investigate later. Yet the predictions of the constant interaction model stay quite accurate and will also be used in the following to understand charge effects in multiple connected quantum dots.

### 1.3.2 Charge measurement in quantum dots

While the working principles of small charge traps created in 2DEGs are relatively straightforward, the task of detecting the individual charges of $1.6 \times 10^{-19}$ C in a semiconductor still remains challenging. As we have shown we can identify the chemical potentials associated with a degeneracy of 2 charge levels with transport of electrons through the dot as long as the temperature broadening is smaller than the charging energy. This was first demonstrated in 1988[42] and clearer by Meirav et al. in 1990.[44] On the other hand this technique requires very large coupling to the reservoirs to generate a measurable current and therefore strongly influences the dynamics of the quantum dot. While many experiments interested in fundamental physics associated with the confined nature of the electrons were performed in the transport regime[50,51,60] and even electron spin manipulation and detection[70] were shown to be possible, we did not employ this technique in this thesis due to its invasive nature. Another technique to detect the charge state of a quantum dot is to use a local electrometer. This has the advantage of being largely independent of the tuning of the quantum dot, but can also be seen as a noninvasive charge measurement. The Coulomb potential of the captured electron diminishes with the distance as $\delta E \propto 1/r$ and is screened by metallic gates and the 2DEG. The detector therefore has to be not only highly sensitive to its electrostatic environment, but it also has to be brought very close to the investigated dot.

The first realisation of such a circuit in lateral quantum dots was already demonstrated in 1993[71] where Field et al. could see a correspondence between the current through the quantum dot and the current through a narrow constriction called quantum point contact(QPC) a few hundred nanometres away. When the electron number decreased(increased) in the quantum dot, the conductance of the QPC would increase(decrease). This is in accordance with the charge in the QD modulating the effective width of the constriction via capacitive

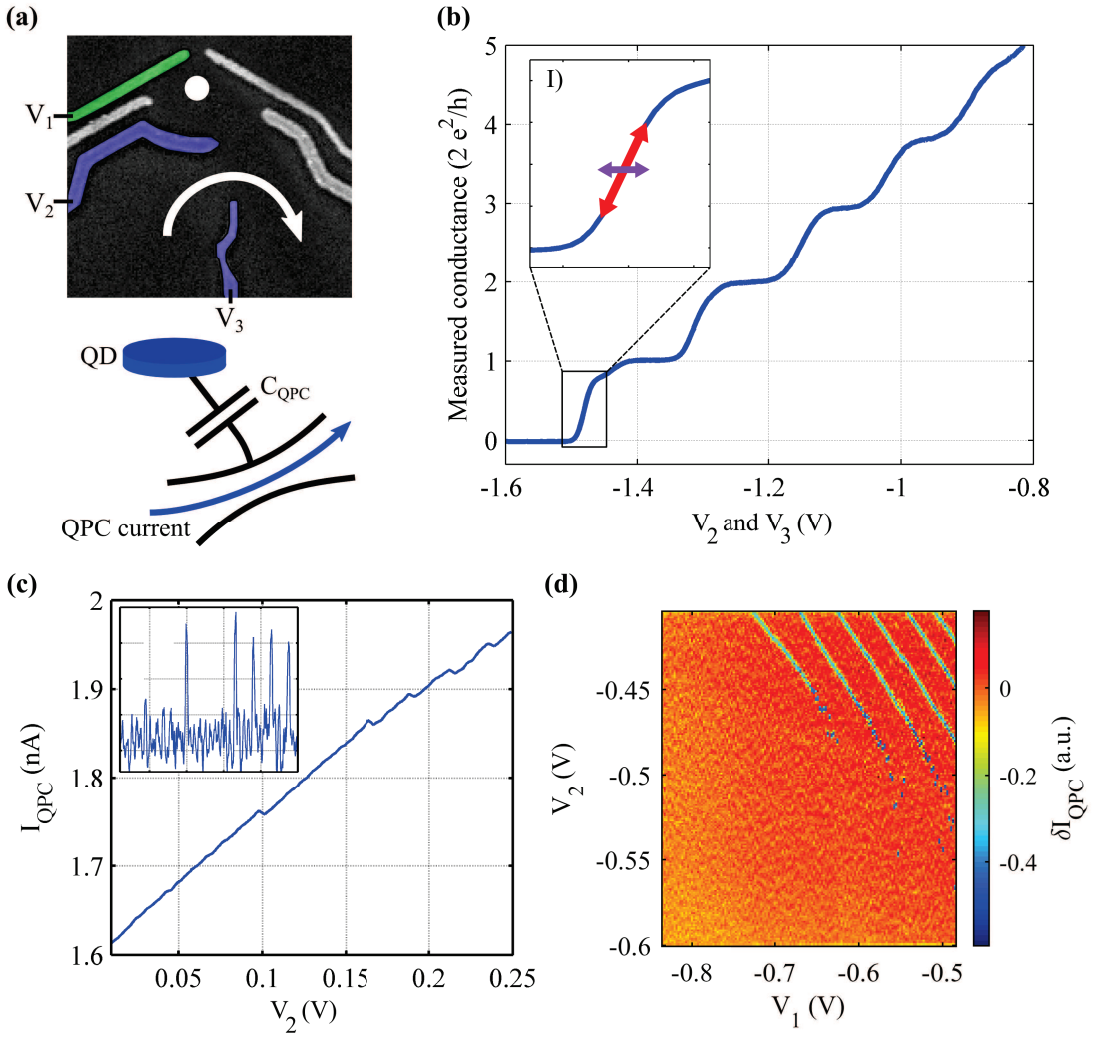


**Figure 1.5:** **(a)** Schematic for the electron detection in a QD with a QPC. The upper side shows a false color electron microscopy image of a sample used in this thesis with the QD and the QPC highlighted by a white dot and a white arrow respectively. The involved QPC gates are colored in blue. The lower side shows the detection principle of a narrow constriction coupled capacitively to a charge island. **(b)** Two-point measurement of the conductance of a narrow constriction measured versus the voltages applied on the QPC gates $V_2$ and $V_3$. The recorded current signal was divided by the applied voltage bias of $V_{bias} \approx 100$ µV. A series resistance of 900 Ohm originating from ohmic contacts, 2DEG sheet resistance, voltage dividers and wires was subtracted from the measured data. The inset shows a zoom of the last conductance transition with arrows indicating the reaction (red) of the detector to a potential variation (violet). **(c)** Current trace when $V_2$ is varied. Steps in the trace indicate a change of the electron number in the dot. Inset: Derivative of the current trace with respect to $V_2$. **(d)** Derivative of the QPC current with respect to $V_2$ when varying $V_1$ and $V_2$. On the left the lines disappear, indicating the zero electron region. On the bottom the reservoir becomes uncoupled from the QD which results in stochastic events.

coupling as shown in Fig. 1.5(a). A similar measurement on one of our samples is shown in Fig. 1.5(c). The current through the QPC shows distinct jumps when the gate voltage connected to the QD $V_2$ is varied. At each jump one electron is removed from the QD and therefore the current that can pass through the QPC rises. In the inset we can see that the derivative of the current with respect to gate voltage shows clear peaks that identify these events. When we vary more than one gate, these peaks form straight lines as can be seen in Fig. 1.5(d). These lines are called charge degeneracy lines and the number of electrons in the QD changes by one when they are crossed. The measured diagram is commonly called a stability diagram, due to the information it gives over the charge state of the QD with respect to the applied gate voltages.

An important fact to note here is that the QPC based detection has another clear advantage over transport measurements besides its non-invasive nature. On the left side of the graph where the gate voltage becomes very negative, we can see that the lines are disappearing. This means that there are no more electrons in the QD which can be kicked out. Now by counting the lines from left to right we can infer the number of electrons in the dot. This is impossible for transport based measurements as with decreasing remaining electron number, the barriers to the leads become thicker resulting in decreasing conductivity. The stability diagram can therefore be used to infer the electron number in the quantum dot.

The remarkable sensitivity of the QPC stems from the effect of conductance quantisation which can be seen in Fig. 1.5(b). At low temperatures, the quantisation energy of a constriction splits the transport of electrons into separate conductance channels as long as the transport is ballistic on the scale of the junction width. One can show that then the conductance has to be quantised in values of $2e^2/h$ where the factor two comes from the spin degeneracy.[41,72,73] Between these plateaus the conductance changes abruptly and is only broadened by temperature and imperfect geometry.[74–76] Small changes in the environmental charge can therefore produce a large current response when the QPC is set to a position close to a charge transition. The sensitivity of such a detector close to a quantum dot when compared to the noise is usually about $0.1e$[77] and with state-of-the-art electronics allows real-time recording of the electron dynamics with a bandwidth of over 10 kHz. This bandwidth is mostly limited by the RC time of the device resistance (50 k$\Omega$) and the capacitance of the cables ($\approx$ 100 pF). In practice the gain bandwidth product of the amplification electronics as well as the parasitic noise from external signals can also reduce the effective bandwidth for sensing. The sensitivity can be further increased by instead using a quantum dot as a sensing device[78] or using radio frequency reflection techniques with an impedance matching circuit to increase the effective bandwidth.[79]

While the latter was not implemented in this thesis, the increased sensitivity of sensing dots allowed the single shot read out of the spin state in the last part of this thesis.

## 1.4 Spin states in quantum dots

When a degree of freedom has to be controlled in any system, there is usually a trade-off between operation speed and lifetime as both tend to depend on the coupling to the environment. While the charge of the electron can be easily manipulated by changing the electrostatic environment, it is also very susceptible to environmental (charge) noise. For charge qubits in 2DEGs the energy relaxation time is of the order of $T_1 \approx 20$ ns and the dephasing time $T_2^*$ below 1 ns[80,81] limiting their usefulness for information storage. However the magnetic moment of the electron (spin) is much better protected, as any process changing it has to conserve the total angular momentum. It turns out, that the energy relaxation of electron spins in QDs can be very long and can exceed 1 s for electrons trapped in a lateral QD in a GaAs/AlGaAs 2DEG.[82] This relative isolation from the environment makes them a possible candidate for qubit implementations.[21]

### 1.4.1 Single electron spins

The most obvious implementation of a 2-level system is the spin of a single electron. For a macroscopic observer a single spin can only take two values: Up $|\uparrow\rangle$ and Down $|\downarrow\rangle$.[83] These degenerate states can be energetically split up by the Zeeman-effect due to the magnetic moment of the electron.[84] This relation between the magnetic field $B$ and the Zeeman energy of the electron

$$E_Z = -\frac{\mu_B g \langle \hat{S} \rangle}{\hbar} B \tag{1.8}$$

depends on the gyromagnetic ratio $g$ and the spin orientation $\langle \hat{S} \rangle$ which can take the values $m_s = \frac{1}{2}$ and $m_s = -\frac{1}{2}$ ($\mu_B$ is the Bohr magneton $\frac{e\hbar}{2m_e}$). The gyromagnetic ratio $g$ for free electrons is approximately 2 whereas it is strongly modified in lateral quantum dots due to the spin-orbit interaction. This factor was found to be $g_{bulk} \approx -0.44$[85] in bulk measurements and $g_{QD} \approx -0.39$ in QDs.[32] This means that at a temperature of 100 mK ($\approx 8$ µeV) we need a magnetic field of several Tesla for $E_Z >> k_B T$ to be fulfilled. One of the problems with high magnetic fields is that the spin relaxation rate due to piezoelectric phonons mediated by the spin-orbit coupling scales with $B^5$[86,87] effectively limiting the measurement time. The energy and phase relaxation rates are also connected via the relation $\frac{1}{T_2} = \frac{1}{2T_1} + \frac{1}{T_2^*}$ and therefore the relaxation time gives an upper limit for the coherence time.[88] However in present experiments this limit has not been reached

for single electron spins and the phase relaxation is dominated by $T_2^*$. A much more serious concern is the possibility to selectively control single electron spins. While coherent driven oscillations of single spins were shown[70] they needed a superconducting stripline to produce an oscillating magnetic field for the (magnetic) manipulation. A two-spin system however can be manipulated electrically by changing the exchange interaction as we will show later.[31] For these reasons we focused in this thesis only on 2-spin systems.

### 1.4.2 Two electron spins

When two electrons are confined in a single quantum dot, they are no longer distinguishable particles and will form 4 product states with different total spin eigenvalues $m_s$. We group them into 3 triplet states

$$\begin{aligned} T_+ &= |\uparrow\uparrow\rangle && (m_s = +1) \\ T_- &= |\downarrow\downarrow\rangle && (m_s = -1) \\ T_0 &= \frac{|\uparrow\downarrow\rangle + |\downarrow\uparrow\rangle}{\sqrt{2}} && (m_s = 0) \end{aligned} \tag{1.9}$$

as well as one singlet state

$$S = \frac{|\uparrow\downarrow\rangle - |\downarrow\uparrow\rangle}{\sqrt{2}} \qquad (m_s = 0). \tag{1.10}$$

As before an applied magnetic field will result in a Zeeman shift for the $T_+$ and $T_-$ states which can be calculated from Eq. 1.8 and is plotted in Fig. 1.6(a). Electrons being fermions the product of the orbital part and the spin part of the wavefunction has to be antisymmetric (exchanging the electrons has to result in a minus sign for the wavefunction). Therefore only in the singlet case can both electrons occupy the ground ($g$) state $\Psi_{orb} = |gg\rangle$ whereas in the triplet case they have to be in a asymmetric combination of ground and excited ($e$) states e.g. $\Psi_{orb} = \frac{|ge\rangle - |eg\rangle}{\sqrt{2}}$ as schematically illustrated in Fig. 1.6(b) (assuming only one excited state). This difference in orbitals results in an energetic splitting of these states that is called the exchange energy $J_{Ex}$ with a magnitude of usually $\approx 300$ µeV and makes the singlet state the ground state.

### 1.4.3 Two spins in double quantum dots

The exchange energy $J_{Ex}$ that defines the quantum axis in one dot is the result of the orbital energy splitting and its size is related to the magnitude of the electron-electron interaction.[89] When however the electrons are pulled apart, this energy will be reduced and eventually go to zero. A way to separate the electron spins is via a charge separation

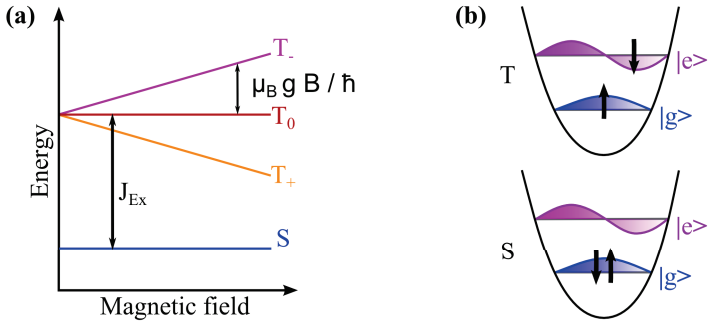


**Figure 1.6:** **(a)** Energy dispersion of the two-electron states in one quantum dot against the magnetic field. The triplet states are split off from the singlet state by the exchange energy $J_{Ex}$. **(b)** Schematic of the orbital occupation for the triplet and singlet state. Upper figure shows the triplet state where one electron has to occupy the energetically higher lying orbital. For the singlet state both electrons can be in the lower orbital resulting in a lower energy.

into different quantum dots. The physical implementation of lateral quantum dots makes it possible to connect several quantum dots via tunnel-barriers. The case of two tunnel-coupled quantum dots is called a double quantum dot (DQD) and its physics have been studied extensively.[61,90,91]

In a DQD the electrons can be separated by changing the potential energy of the two QDs, while making inter-dot charge exchange possible via a tunnel-barrier. We define the detuning $\varepsilon$ as the difference in electrostatic energy of the QDs. Then as we change the detuning we will shift the respective energy levels of the QDs against each other and therefore eventually change the ground state. When tunnelling is allowed between the dots this will result in a change of configuration from two electrons in one dot to one electron in each dot. This situation is schematically depicted in Fig. 1.7 for the separation of two electrons in a double quantum dot.

We can model this system by assuming split electron states $H_{11}$ and electron states where the electrons are confined in the same QD $H_{20}/H_{02}$ (joint) coupled via a tunnel-coupling $t$. The Hamiltonian then takes the form

$$H = \begin{pmatrix} H_{20} & T & 0 \\ T & H_{11} & T \\ 0 & T & H_{02} \end{pmatrix}. \tag{1.11}$$

where $H_{20}$, $H_{02}$, $T$ and $H_{11}$ can be found in Appendix B.1. If we consider only the singlet states for the two configurations $S_{20}$ (both electrons in the first QD) and $S_{11}$ (split) we

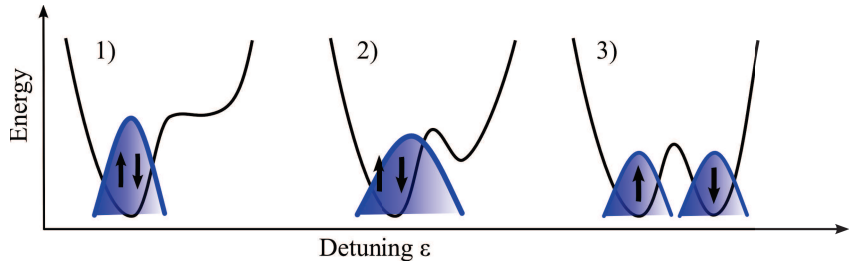


**Figure 1.7:** Schematic of the double dot potential and the effect of the detuning. (1),(2) and (3) show cuts of the electrostatic potential along the x-axis for decreasing detuning from left to right. When the electrostatic energy of the two QDs is the same, the electrons are split into the two dots due to Coulomb repulsion.

obtain after projection

$$H_{singlet} = \begin{pmatrix} \varepsilon & t \\ t & 0 \end{pmatrix}. \tag{1.12}$$

We see that at $\varepsilon = 0$, $S_{20}$ and $S_{11}$ are degenerate and the new eigenstates are symmetric and antisymmetric combinations of the two singlet states with a splitting of $2t$. Therefore at this position the states are hybridized and electron exchange is possible. After diagonalization of the matrix we find the eigenvalues (energies) for all values of $\varepsilon$

$$E_{\pm} = \frac{\varepsilon \pm \sqrt{\varepsilon^2 + 4t^2}}{2} \tag{1.13}$$

which gives the dispersion of the exchange coupled states when the electrostatic potential is varied. For a more complete understanding the eigenvalues of the full Hamiltonian are plotted against the detuning $\varepsilon$ to illustrate the energy dispersion of the coupled system in Fig. 1.8 for different system parameters. We can see that for diminishing tunnel-coupling and no magnetic field as in Fig. 1.8(a) the different states have linear dispersion and the ground state changes with detuning from singlet with both electrons in the left dot (2,0), to the split configuration (1,1) where triplet and singlet are degenerate, to singlet with both electrons in the right dot (0,2). The extent of the split region is given by the charging energy $E_C$. The degenerate triplet states are split off by the Exchange energy $J_{Ex}$ in the joint positions.

When the tunnel-coupling is increased as in Fig. 1.8(b), we see that anti-crossings with splitting $2t$ form at the degenerate positions of the singlet states with different electron configurations. The T(1,1) and S(1,1) states are also no longer degenerate as the singlet state is shifted downwards. A more complete analysis than we did in Eq. 1.13 reveals that

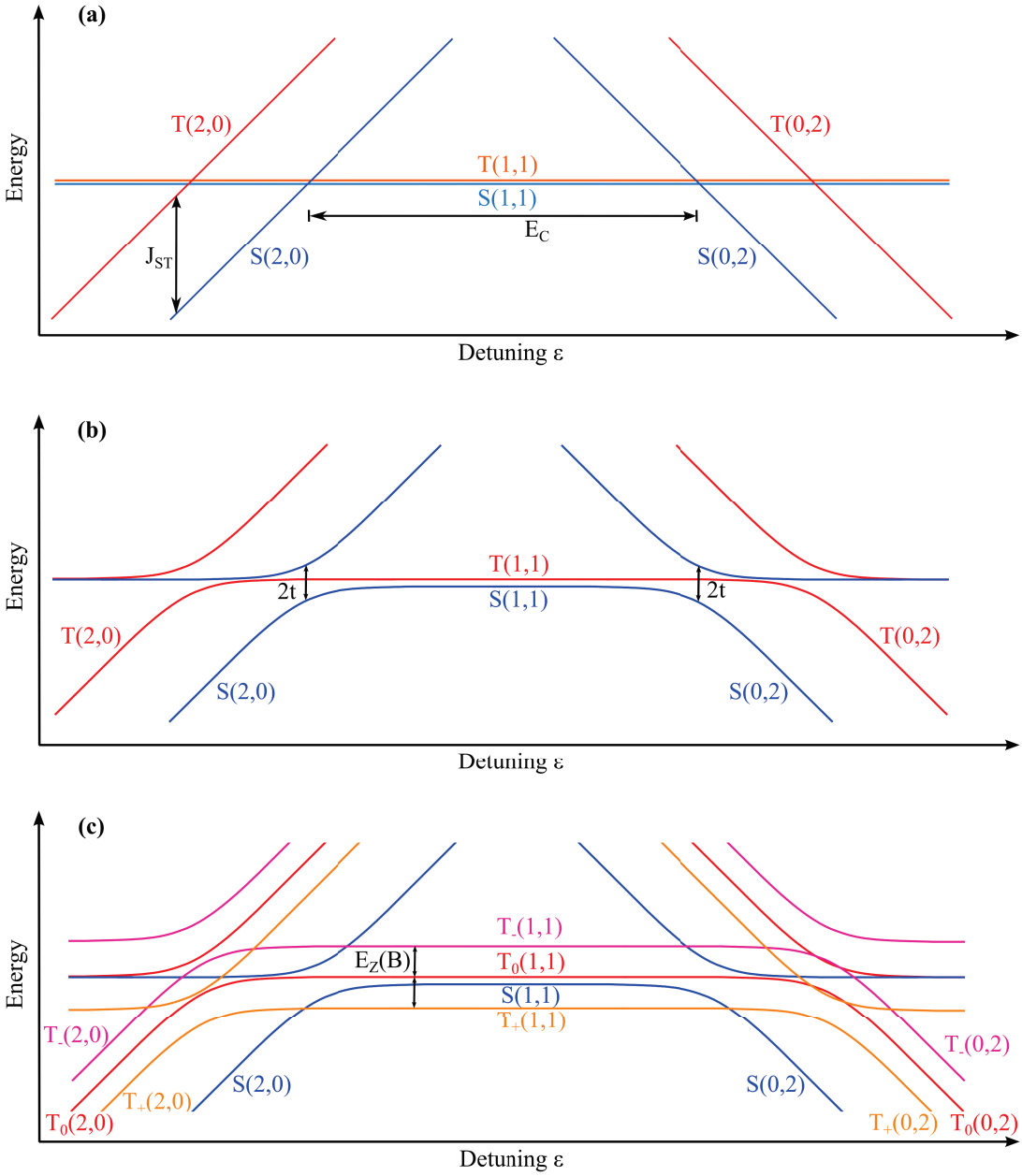


**Figure 1.8:** Energy dispersion of the coupled double dot Hamiltonian for different combinations of magnetic field $B$ and tunnel-coupling $t$ **(a)** Uncoupled Hamiltonian with $t = 0$ and $B = 0$ **(b)** Coupled Hamiltonian with $t \neq 0$ and $B = 0$ **(c)** Coupled Hamiltonian with $t \neq 0$ and finite magnetic field $B \neq 0$

for two spins in two quadratic potential wells, the lowest splitting is given by $J = \frac{4t^2}{E_C}$.[92] Nevertheless our approximations replicate the dispersion well enough to be a useful basis for calculations in experiments.[31]

When we also include a finite magnetic field that introduces the Zeeman energy $E_Z(B)$ as was done in Fig. 1.8(c), we observe a lifting of the degeneracy of the three triplet states. Due to the negative Landé factor $T_-$ is shifted upwards in energy while $T_+$ is shifted down and crosses the singlet branch. This crossing can be used to map out the dispersion of the singlet branch experimentally as was done by Petta et al. in 2006[31] which validates our model of the two spin system. This model is widely used in the literature and we will apply it later to the problem of spin transport across multiple quantum dots. Specifically we will use the $\{S,T_0\}$-subspace as a two-level system or qubit to study coherent evolutions across quantum dots.

## 1.5 Spin measurement in quantum dots

Most of the usefulness of the theory of electron spin dynamics in quantum dots relies on the possibility to measure their spin state. The magnetic moment of the single electron is however so small that it is difficult to detect directly. Most of the measurement techniques therefore rely on the conversion of the spin information to a charge signal which can be detected due to the high sensitivity of quantum point contacts. The measurement has to fulfil several requirements. It has to be faster than the relaxation time $T_1$ of an excited spin state or else the measured information is lost before it is recorded. The measurement also has to have a high fidelity of spin identification to be useful for applications in computation schemes. Finally it has to be highly robust to small perturbations of the electrostatic potential present in our devices. Luckily several implementations of such measurements have already been developed for single spins and spin pairs and fulfil those criteria. In this section we will concentrate on the spin measurement in the $S$-$T$ basis for the case of two electrons that was important for the work performed in this thesis.

### 1.5.1 Energy selective spin measurement

The first possibility is to use the relatively strong (compared to the thermal broadening $k_BT$) energetic splitting between singlet and triplet states to create a single shot spin measurement when the chemical potential is well controlled. The measurement technique is in analogy to the single shot measurement of single spins demonstrated in 2004[93] and was already shown for two-electron states in 2006.[94] As was described earlier, non-invasive charge detectors like a close QPC can detect the number of electrons in a QD with a bandwidth of about 10 kHz. When the QD is brought to a point of charge degeneracy

between one and two electrons, the energetically higher lying triplet states will be allowed to exchange electrons with the reservoir. For the subsequent tunnelling process that adds an electron again, the only available states are at the singlet energy and therefore a singlet state will be produced. This process will dynamically change the electron number from two to one and back to two electrons. It is schematically shown in Fig. 1.9(a) where the Fermi energy is aligned between the singlet and the triplet states. When the tunnelling rate to the 2DEG $\Gamma_{tunnel}$ is varied to be smaller than the measurement bandwidth $W$, these events can be resolved with the current of the QPC when an external voltage bias is applied. The voltage bias is chosen to be around $V_{bias} \approx 200 - 350$ µV to limit excitations while at the same time providing a sufficient current signal. However there is a second restriction on the tunnelling rate to the reservoir for single shot detection which is related to the intrinsic spin relaxation rate $\Gamma_R = 1/T_1$. The tunnelling process has to be the dominant relaxation process to achieve a high visibility and therefore

$$\Gamma_R << \Gamma_{tunnel} << W \tag{1.14}$$

has to be fulfilled to measure spins single-shot.

Several current traces that illustrate this spin measurement performed in a single quantum dot are shown in Fig. 1.9(b). At $t = 0$ we have stochastically loaded the QD with a random spin state by electron exchange with the reservoir. Then the QPC current is measured against time and sampled with a simple threshold algorithm. Several curves show a high plateau at the start of the measurement indicating smaller electron number. We identify these events as the described relaxation process via electron exchange and assign a triplet event. For the yellow and blue curves, no variation is observed and we identify it as a singlet event. This implements a single shot spin to charge conversion measurement in the singlet-triplet basis.

### 1.5.2 Tunnelling rate selective spin measurement

A second observation in Fig. 1.9(b) is the immediate start of the one electron charge signal in the measurement configuration. If the triplet and singlet states had equal tunnel-rates, the time for an electron to leave the quantum dot and to enter it should be the same. We would therefore expect the signal to start at $t_{start} \approx t_{load}$ and not at $t_{start} = 0$. However, this is not the case as the excited states have faster tunnelling rates than the singlet. A simple explanation for this experimental finding is that the excited orbitals can have a higher probability density at the edges of the quantum dot as shown in Fig. 1.6(b).[59] The larger wavefunction overlap between the reservoir and the triplet state results in an

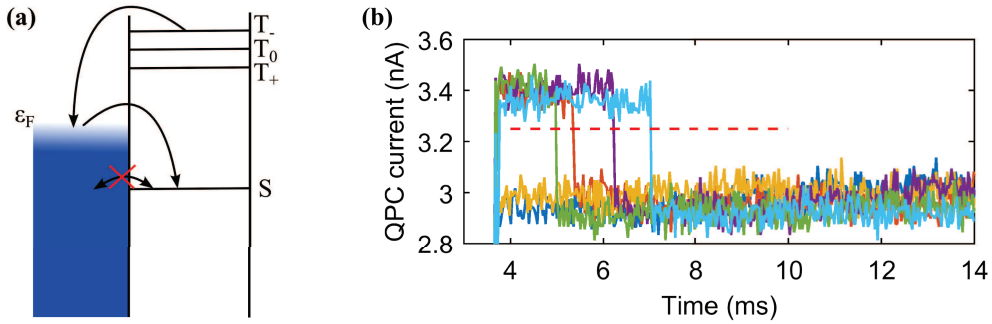


**Figure 1.9:** **(a)** Schematic of the energy alignment of the different spin states in the energy selective detection of two-electron spin states. The Fermi $\varepsilon_F$ lies between the singlet and the triplet states. Electron exchange is only allowed for the triplets. **(b)** Single shot traces for energy selective spin detection. The QPC current is plotted against time where at $t = 0$ we have initialised a random spin state. The yellow curve shows a singlet event while the other curves shows the trace of the triplet relaxation event in (a).

effectively smaller tunnel barrier and therefore faster tunnelling rates. This relaxes our condition in Eq. 1.14 as we only need to fulfil the tunnelling rate of the triplet $\Gamma_T$ to be faster than the relaxation rate and the tunnelling rate of the singlet $\Gamma_S$ to be smaller than the detector bandwidth.

Additionally this allows a second method for the spin measurement in the singlet-triplet basis as we can identify the spin state by the measured tunnelling time to the reservoir which was first demonstrated in 2005.[30]

For that we have to bring the system into the configuration shown in Fig. 1.10(a) where all spin states are above the Fermi energy and the ground state is one electron in the QD. All two-electron states will then show a tunnelling event to one electron, but the time-scales will be slower for the singlet. The resulting current traces for a few events are shown in Fig 1.10(b). A red dashed line was added to clarify the selection process. Every tunnelling event before the red line is counted as a triplet incident while later events are counted as singlets.

The resulting visibility of singlet and triplet events depends on their relative tunnelling rates $\Gamma_T/\Gamma_S$. Late triplet tunnelling will be (erroneously) detected as a singlet with probability $\alpha$ while early singlets will be detected as triplets with probability $\beta$. This results in a visibility $1 - \alpha - \beta$ where the two probabilities are[30]

$$\alpha = 1 - e^{-\Gamma_S \tau} \tag{1.15}$$

$$\beta = \frac{1/T_1 e^{-\Gamma_S \tau} + (\Gamma_T - \Gamma_S) e^{-(\Gamma_T + 1/T_1)\tau}}{\Gamma_T + 1/T_1 - \Gamma_S} \tag{1.16}$$

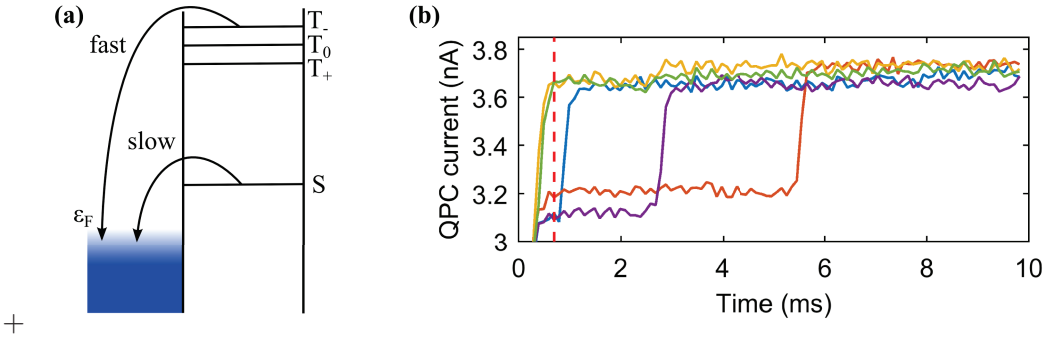


**Figure 1.10:** **(a)** Schematic of the energy alignment of the different spin states in the tunnel rate selective detection of two-electron spin states. The Fermi $\varepsilon_F$ lies below the singlet and the triplet states resulting in relaxation via tunnelling with different rates depending on the state. **(b)** Plot of few exemplary detection traces of tunnelling events. The red dashed line indicates the selection rule for singlet and triplet tunnelling events.

with $\tau$ being the point in time from which the decision is made to assign a singlet event. This usually allows a fidelity of over 90% for values of $\Gamma_T/\Gamma_S \approx 100$ but depends strongly on the difference in wavefunction overlap with the reservoir for singlet and triplet. Nevertheless this implements a high fidelity spin measurement which is largely insensitive to energy fluctuations of the levels (as it does not require well aligned levels), is resistant to QPC noise and does not depend on the magnitude of the splitting $J_{Ex}$.

### 1.5.3 Spin measurement via spin blockade

The last purely electrical spin measurement technique relies on the peculiar shape of the energy dispersion in a double dot shown in Fig. 1.8. Outside of the (1,1) region exists a region where the lowest triplet state is in the (1,1) configuration while the singlet (2,0) state is already energetically favourable. This results in a different charge configuration for the spin states and can therefore be measured with a charge detector. As the triplet is "blocked" from transfer to (2,0) this effect is called Pauli-spin-blockade.[90]

The charge signal is much lower than for the other two measurement methods as it originates only from a displacement of an electron and not a change of the total electron number. It is similarly affected by sample instabilities as the energy selective spin detection scheme as it also relies on the energy splitting given by the exchange energy. However, it conserves the electron number and therefore can be considered a non-destructive spin measurement. Nevertheless, during this thesis all the spin measurements were performed with the other two techniques due to the higher charge signal and the natural integration with isolated quantum dots.

## 1.6 Environmental effects of spins in lateral quantum dots

Until now we have only considered the case of perfectly isolated electrons in an electrostatic trap. However, even though we try hard to reproduce this model system, the electrons are in fact in a crystal where they are subject to many interactions with their environment. While we can deliberately use these couplings to influence the spin state of the electrons in the QD, they are also responsible for a randomization of the information during our manipulation. We discern two mechanisms of information loss. The first is relaxation which describes a loss of energy where an excited state relaxes to the ground state. The second is decoherence or dephasing, which means that we lose information on the phase of our (superposition) state. We can illustrate the difference in the two processes on the Bloch sphere, a representation of a two-level system (TLS) like spin-up and spin-down. For that we write our arbitrary state

$$|\Psi\rangle = \cos\left(\frac{\theta}{2}\right)|e\rangle + \sin\left(\frac{\theta}{2}\right)e^{i\phi}|g\rangle\,. \tag{1.17}$$

as a linear combination of the excited state $|e\rangle$ and the ground state $|g\rangle$. The resulting state can be projected onto the surface of a sphere parametrized by the angles $\theta$ and $\phi$ as depicted in Fig. 1.11(a). In this picture, energy relaxation results in the reduction of the $z$-component of the vector that points onto the surface. The vector $\theta$ therefore approaches $\pi$ as shown in Fig. 1.11(b). It was already stated that the energy relaxation time constant $T_1$ can approach a second in our system. The main relaxation path is relaxation via spin-orbit coupling with piezo-electric phonons.[86] It depends on the orientation and magnitude of the magnetic field and the shape of the dot potential.[95] We will see the origin of the spin-orbit coupling and evaluate the spin relaxation rate in our system later.

Decoherence or dephasing term the loss of information on the angle $\phi$ as in Fig. 1.11(c). For the resulting characteristic decoherence time we differentiate between $T_2$, the decoherence time, and $T_2^*$, the dephasing time. The dephasing time $T_2^*$ is usually smaller and is directly measured in a Ramsey-like experiment. For a two electron spin state split in a double quantum dot it is only 10-20 ns but can be extended to $\approx 100$ ns via dynamical polarization of the nuclei.[37] The coherence time was found to have a lower limit of over 200 µs using a sophisticated echo sequence.[38] Nevertheless the rapid dephasing of the spin information remains one of the biggest challenges in lateral QDs and a deep understanding of the involved processes is required to find possible avenues for improvement.

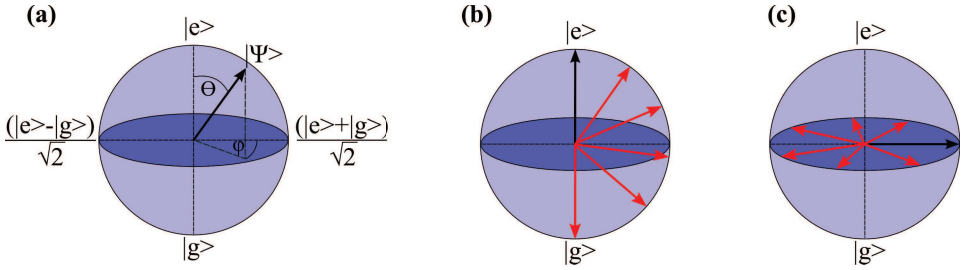


**Figure 1.11:** Graphical representation of two level systems with the Bloch sphere **(a)** Bloch sphere with arbitrary quantum state parametrized by the angles $\theta$ and $\phi$ **(b)** Graphical representation of energy relaxation resulting in $\theta$ approaching $\pi$ **(c)** Graphical representation of dephasing resulting in insecurity over angle $\phi$

### 1.6.1 Hyperfine interaction with the host nuclei

The reason for the fast dephasing of the singlet state is the hyperfine interaction with the nuclei. Hyperfine interaction is a well known phenomenon in atomic physics and results in the hyperfine splitting of atomic levels. In atoms it is the result of the interaction of the magnetic moment of the electron with the magnetic moment of the nucleus. In the quantum dot it arises from the fact that the trapped electron is embedded in a matrix of Gallium, Arsenide and Aluminium atoms which form the crystal. Due to the spatial extent of the electron's wavefunction, its spin interacts with the magnetic moments of all the surrounding nuclei via hyperfine interaction as depicted in Fig. 1.12(a). The Hamiltonian for this interaction is given by

$$H_{HF} = \sum_{k}^{N} A_k \vec{I_k} \vec{S} \tag{1.18}$$

where $\vec{S}$ is the spin operator of the electron, $\vec{I_k}$ the spin operator of one of the nuclei and the sum is over all nuclei in contact.[61] The interaction strength $A_k$ for the respective nucleus depends on its type as well as the electrons waveform overlap with it (and therefore the distance from the center of the dot). Due to their low gyromagnetic ratio, the nuclei are in the high temperature limit and are not ordered. The large number of nuclei ($10^5$) also leads to a reduced back-action of the electron on the individual nuclei.[96] This allows to simplify the (complex) many body problem, by averaging over the interactions with all the surrounding nuclei. The result is mathematically equivalent to a fluctuating magnetic field produced by the spontaneous magnetization of the nuclei.[97] We then simplify the

hyperfine interaction to a Zeeman like interaction

$$\left(\sum_{k}^{N} A_k \vec{I_k}\right) \vec{S} = g\mu_B \vec{B_N} \vec{S} \tag{1.19}$$

where $\vec{B_N}$ is the spontaneous magnetization of the nuclei. Even at low temperatures the total spin orientation in GaAs is mostly random and centred around zero due to the low gyromagnetic ratio of the nuclei. The dynamics of the nuclei bath are at the same time slower than $10^{-4}$ s as indicated by inverse NMR linewidths.[98] As we can perform coherent manipulations within a timescale much shorter than this time ($10^{-8}$ s), we can assume the nuclear field to be constant during one shot of an experiment while varying from realization to realization.

This fluctuating magnetic field induces a precession of a spin around the direction of the magnetic field with the Larmor frequency

$$\omega_L = \frac{eg}{2m_e} B = \frac{g\mu_B}{\hbar} B. \tag{1.20}$$

For the case of the double dot the direction and magnitude of the magnetic field produced by the nuclei will be different in each QD giving different precessions for electrons split into the two dots. We extend Eq. 1.18 to two electrons in two dots[36] and project it onto the $\{|\uparrow\uparrow ,\rangle |\uparrow\downarrow\rangle , |\downarrow\uparrow\rangle |\downarrow\downarrow\rangle\}$ basis and obtain after the substitution in Eq. 1.19

$$H_{HF}^{LR} = \frac{g\mu_B}{2\hbar} \begin{pmatrix} \frac{B_z(L)+B_z(R)}{\sqrt{2}} & B_x(R) - iB_y(R) & B_x(L) - iB_y(L) & 0 \\ B_x(R) + iB_y(R) & \frac{B_z(L)-B_z(R)}{\sqrt{2}} & 0 & B_x(L) - iB_y(L) \\ B_x(L) + iB_y(L) & 0 & \frac{-B_z(L)+B_z(R)}{\sqrt{2}} & B_x(R) - iB_y(R) \\ 0 & B_x(L) + iB_y(L) & B_x(R) + iB_y(R) & \frac{-B_z(L)-B_z(R)}{\sqrt{2}} \end{pmatrix} \tag{1.21}$$

where ($B_x$,$B_y$,$B_z$) indicate the x,y,z-components of the magnetic field produced by the nuclei in the left/right (L/R) dot. We can see that a singlet state will evolve according to the difference of the z-components of the two nuclear fields when we perform the time evolution according to

$$\psi(t) = \exp\left(-\frac{i}{\hbar}\hat{H}t\right)\psi(t=0). \tag{1.22}$$

The magnitude of the hyperfine fields is well established theoretically[99,100] and experimentally[31]

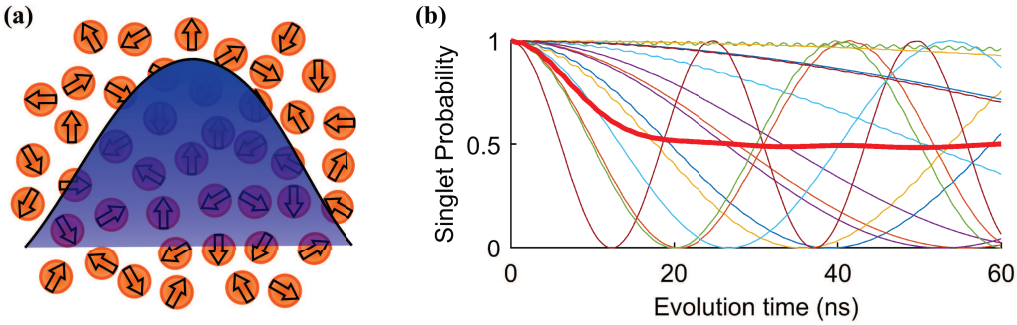


**Figure 1.12:** **(a)** Schematic of the origin of the hyperfine interaction. The electron wavefunction (blue) is spread across $\approx 10^6$ nuclei with whom it interacts **(b)** Plot of coherent evolutions of a singlet state acoording to Eq. 1.22 using the Hamiltonian of Eq. 1.21 with different instantaneous nuclear magnetic fields. The sum of 1000 evolutions is shown in red and gives the dephasing induced decay of a split singlet subject to hyperfine interaction with the host nuclei.

and the nuclear field gradient $B_z(L) - B_z(R)$ is of the order of $\approx 4$ mT which gives an average amount of $N \approx 10^5 - 10^6$ nuclei interacting with the electron. Several coherent evolutions of a singlet according to Eq. 1.22 were calculated for gaussian distributed[34,96] nuclear fields. They are shown in Fig. 1.12(b) as well as the sum of these evolutions that is obtained experimentally when we average many single shot spin measurements. The resulting curve is also measured experimentally and shows a gaussian decay with a decay constant[100]

$$T_2^* = \frac{\hbar\sqrt{2}}{g\mu_B\sqrt{\langle (B_N^z)^2\rangle}} \tag{1.23}$$

that depends on the spread of the distribution of nuclear fields $\langle (B_N^z)^2\rangle$. This spread scales with the square root of the number of nuclei $\propto 1/\sqrt{N}$ and therefore becomes larger with confinement.

The slow evolution of the nuclei makes it possible to use a spin echo to negate the coherent evolution due to the nuclear field. Here a $\pi$-pulse is applied after half the evolution time to refocus the dephased spin. Such experiments have been performed for two-electrons in lateral QDs in 2005[31] and for one electron in 2008[101] and revealed slow decoherence times of a few micro-seconds. Using elaborate echo schemes, the decoherence time could even be extended to $T_2 = 200$ µs.[38] Another way to influence the spin evolution due to the nuclear field is to use the Hyperfine interaction to transfer the magnetic moment of one electron spin to the nuclei bath and thereby polarize it. For two electrons this can be achieved by driving a $|S\rangle$ to $|T_+\rangle$ transition while continuously reinitializing the singlet

with electrons from the 2DEG. Such a scheme was first achieved in 2008[102] and nuclear fields of several hundred millitesla were achieved.[103] When the electrons are in addition used in a feedback loop it was possible to narrow the distribution of the interacting host nuclei by a factor of 10 and thereby obtain a dephasing time $T_2^* = 90$ ns.[37]

### 1.6.2 Spin-orbit interaction

The second important interaction of the trapped electron spins with the environment is the spin-orbit interaction (SOI). The name is originally derived from the picture of an electron orbiting around a nucleus in an atom, resulting in entanglement between spin and angular momentum. In GaAs 2DEGs however we use the term for an interaction that couples a spin to electric fields while it is moving. An intuitive understanding of this process can be obtained when we consider a Lorentz-transformation to the rest-frame of the electron. It results in a transformation of the electric fields into magnetic fields which in turn can influence the spin of the moving electron. In AlGaAs/GaAs heterostructures such electric fields originate from two different sources which results in two different spin-orbit interactions.

The first one is the Dresselhaus spin-orbit interaction which arises from the bulk inversion asymmetry in the zinc-blende crystal structure of the compound. Indeed the local crystal field produced by the different constituents creates varying electric fields depending on the movement direction and gives rise to a Hamiltonian[104]

$$H_{Dr} = \beta(-\hat{p}_x\hat{\sigma}_x + \hat{p}_y\hat{\sigma}_y) \tag{1.24}$$

which couples the momentum $\hat{p}$ to the spin operators $\hat{\sigma}$ with the constant $\beta$ that depends on material properties and $\langle p_z^2 \rangle$.[61] The directions x and y are chosen to be aligned with the (100) and (010) crystallographic directions.

The other origin of spin momentum coupling is called Rashba spin-orbit interaction that originates from the structural inversion asymmetry of our material stack. The triangle shaped potential at the 2DEG position (see Fig. 1.1) results in an electric field along the growth direction. This gives rise to a similar Hamiltonian as for the Dresselhaus SOI

$$H_{Ra} = \alpha(-\hat{p}_y\hat{\sigma}_x + \hat{p}_x\hat{\sigma}_y) \tag{1.25}$$

with the constant $\alpha$ depending on the material and confining potential.[105]

Both interactions are linear in momentum and can be seen as an effective magnetic field whose magnitude and direction depends on the movement of the electron as shown in Fig. 1.13. Note that the direction of the effective fields can amplify or cancel each

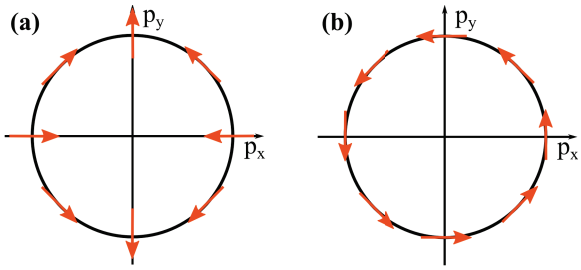


**Figure 1.13:** Effective magnetic field direction representation of the spin-orbit interaction in AlGaAs/GaAs heterostructures depending on the momentum direction shown as orange arrows **(a)** Dresselhaus-type spin-orbit interaction **(b)** Rashba-type spin-orbit interaction

other depending on the movement direction. This variation was actually measured recently and seems to point at a similar magnitude of $|\alpha|$ and $|\beta|$.[95] The linearity of the SOI to momentum means that the rotation that this effective field induces on the spin of an electron depends only on the distance travelled. This makes it useful to define the spin-orbit length $l_{SO}$ which is given by the travelling distance after which a spin has been flipped in the absence of an external magnetic field. It has been directly measured to be $\approx 10$ µm in 2DEGs in an experiment conducted by Sanada et al. using electrons transported with surface acoustic waves.[106]

The effect of the spin-orbit interaction on a confined electron is therefore strongly reduced by the fact that the typical size of a quantum dot is much smaller than the spin-orbit length. However, small movements around the rest position can lead to the coupling of the spin to electric fields that displace the electron. It is this property that leads to the mentioned relaxation time $T_1$ due to piezoelectric phonons in the presence of a magnetic field. This can also be harnessed to induce spin flips when a confining gate is excited resonantly with the external magnetic field as was demonstrated by Nowack et al. in 2007.[32] Additionally the spin-orbit interaction becomes an important influence when the electrons are moved on length-scales which are bigger than the dot as for electrons in moving quantum dots[106,107] or for the tunnelling transport schemes in multiple connected dots as we are going to explore in this thesis.[108]

### 1.6.3 Electron spins in moving quantum dots

The strong localisation of electrons in quantum dots leads to suppressed spin-flip rates.[86,109] However most computational schemes include the necessity to move electrons between sites in large quantum dot arrays. It is therefore necessary to investigate the case where the electron is still confined, but moved in the crystal lattice by a trapping potential. This case of a moving quantum dot has been analytically studied by Huang and Hu[110] and a

short summary of their results will be given here to illustrate the effects of the motion.

### Spin relaxation induced by the disordered crystal potential

An additional decoherence process in the moving quantum dot is induced the fact that the electrostatic potential of the heterostructure is not smooth, but is locally disturbed by the random position of the donor atoms as shown in Fig. 1.14(a). This roughness of the crystal potential leads to a varying electric field when electrons are displaced. The electron spin then couples to the fluctuating electric field via spin-orbit interaction. As a result, the electron will feel a fluctuating effective magnetic field in its rest frame that can lead to spin relaxation.

To arrive at this conclusion, Huang and Hu consider a single electron at position $\boldsymbol{r}$ and with momentum $\boldsymbol{\pi}$ in a quantum dot that is moving in the crystal according to $\boldsymbol{r}_0(t) = \boldsymbol{v}_0 t$. In addition to the moving confinement potential, the electron is also subject to an external magnetic field and spin-orbit interaction. The disorder of the crystal enters via a spatially dependent electric potential. They then calculate the effective Hamiltonian for the spin of the moving electron in the rest-frame of the quantum dot to be

$$H_{eff} = \frac{1}{2} g \mu_B (\boldsymbol{B} + \delta \boldsymbol{B}(t)) \cdot \boldsymbol{\sigma} \tag{1.26}$$

where $\boldsymbol{B} = \boldsymbol{B}_{\text{ext}} + \boldsymbol{\Delta B}$ is the sum of an external magnetic field $\boldsymbol{B}_{\text{ext}}$ and the effective magnetic field due to spin-orbit interaction $\boldsymbol{\Delta B} \approx 10$ µTs/m (which depends on the speed of the electron $\boldsymbol{v}_0$), $\boldsymbol{\sigma}$ are the Pauli matrices and

$$\delta \boldsymbol{B}(t) = 2\boldsymbol{B} \times \boldsymbol{\Omega}(t), \tag{1.27}$$

$$\boldsymbol{\Omega}(t) = \frac{-e}{m^* \omega_d^2} \left[ \varepsilon_y(\boldsymbol{r}_0(t))/\lambda_-, \varepsilon_x(\boldsymbol{r}_0(t))/\lambda_+, 0 \right], \tag{1.28}$$

is the fluctuating effective magnetic field produced by the motion of the quantum dot with orbital excitation energy $\omega_d$ in the crystal. This effective magnetic field depends on the position dependent electric fields field $\varepsilon_{x,y}$ in the lateral plane and the spin-orbit length along different crystal axes $\lambda_\pm$ (here $x$ and $y$ are along the [110] and [$\bar{1}$10] axes). The time dependent dot position $\boldsymbol{r}_0(t)$ transforms the spatial dependence of $\varepsilon_{x,y}(\boldsymbol{r}_0(t))$ into a time dependence. This is the origin of the time dependence of $\delta \boldsymbol{B}(t)$ that leads to decoherence of the spin state via electron spin flips induced by the motion.

To calculate the expected spin-flip rates in our experiments, we estimate the parameters for displacement in a quantum dot array. In the case of high tunnel-coupling, electrons can typically be exchanged between adjacent quantum dots within 1 ns. Assuming an inter-dot

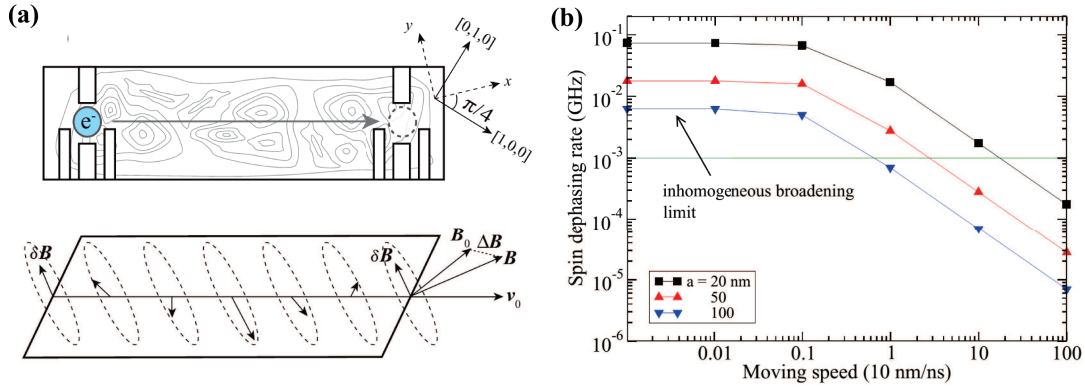


**Figure 1.14:** Coherence in the moving quantum dot **(a)** Schematic of the model of the moving QD that is transported in a disordered potential landscape (equipotential lines). On the bottom, the resulting effective magnetic field in the rest-frame of the electron is given. **(b)** Motional narrowing effect of the nuclei dephasing during motion. Given is the spin dephasing rate as a function of the speed of the electron. The parameter $a$ is the diameter of the quantum dot. Reprinted figures with permission from [110] Copyright (2013) by the American Physical Society

distance of $d \approx 100$ nm, this results in a speed of displacement of $v = 100\ \mathrm{m\,s^{-1}}$. The effective magnetic field due to spin-orbit interaction is then $\boldsymbol{\Delta B} = 1$ mT. Additionally, the device is generally operated at external magnetic fields of 0-200 mT. The spin relaxation rate is then evaluated by

$$\frac{1}{T_1} = \left[\frac{2e\sigma_\varepsilon}{\hbar\omega_d^2}\right]^2 \frac{\omega_Z^2\tau_c}{1+\omega_Z^2\tau_c} F_{SO}(\theta,\phi) \tag{1.29}$$

$$F_{SO}(\theta,\phi) = \left[(\beta^2+\alpha^2)(1+cos^2\theta) + 2\alpha\beta\sin^2\theta\cos 2\phi\right]. \tag{1.30}$$

where $\beta/\alpha$ is the Dresselhaus/Rashba spin-orbit coupling, $\omega_Z$ is the larmor frequency and $\theta/\phi$ are angles corresponding to the direction of the external magnetic field. The constants $\tau_c \approx 1$ ns (at $v_0 = 100\ \mathrm{m\,s^{-1}}$) and $\sigma_\varepsilon \approx 200$ kV/m are the correlation time and the variance of the electric field respectively and are used to quantify the disorder of the crystal potential. The expected displacement induced spin-flip rate in our heterostructure is then $1/T_1 \approx 10^6$ Hz. This spin-flip rate leads to a limit on the coherence time $T_{2,motion} \approx 1$ µs, which is much longer than the dephasing time in static quantum dots $T_2^* \approx 10-20$ ns due to hyperfine interaction. Coherent spin transfer within the previously measured dephasing time should therefore be possible and is not limited by the motion induced spin-flip rate.

Note that here the origin of the term $\delta\boldsymbol{B}(t)$ is the impurity induced disorder along the path in combination with a spin-orbit field. However, lateral nuclear field gradients due

to hyperfine interaction will give rise to a similar effective magnetic field that becomes time dependent during the motion. At $v_0 = 100\ \mathrm{m\,s^{-1}}$, both spin-orbit interaction and lateral field gradients are of similar order of magnitude (1-4 mT)[110] and will both induce similar dephasing rates due to the strong driving agent of the moving quantum dot. The two effects can therefore only be distinguished in experiments when the travelling direction and therefore the relative contributions of Dresselhaus- and Rahsba spin-orbit couplings are controlled.

### Motional narrowing of the nuclear fields during motion

During the motion in the heterostructure, the previously discussed decoherence process due to the hyperfine interaction of the electron with the nuclei is modified. When the quantum dot is displaced, the electron interacts with an increased number of nuclei via contact hyperfine interaction. The larger nuclei bath results in a narrowed distribution of nuclear fields experienced by the electron during a coherent evolution in the time $\tau$. As the variance of the effective nuclear field depends on the number of nuclei $\Delta B_{nuclei} \propto \frac{1}{\sqrt{N_{nuclei}}}$, an increase of the number of nuclei by a factor $\alpha$ results in a reduction of the variance of the nuclear fields by $\sqrt{\alpha}$. This process is called motional narrowing.

In this simple approximation, the motionally narrowed nuclear fields lead to an increase of the coherence time of the electron by the same factor $\sqrt{\alpha}$. Huang and Hu numerically investigated the resulting spin dephasing rate more accurately as a function of the speed of the motion and obtain the dependence shown in Fig. 1.14(b). For low electron velocities, the dephasing time is faster than the rate of narrowing of the nuclear field distribution. However, for higher electron velocities of $v > 1\ \mathrm{m\,s^{-1}}$, the nuclear field distribution is narrowed faster than the dephasing rate and the coherence time is therefore effectively increased. For the estimated speed of $v = 100\ \mathrm{m\,s^{-1}}$ and a quantum dot size of $a \approx 20$ nm, the motional narrowing leads to spin dephasing time of up to 1 µs. As the hyperfine interaction is the dominant decoherence process for electron spins in quantum dots, this enhanced spin dephasing time is assumed to extend the coherence time of an electron spin.

The parameters and timescales for the observation of these two effects are attainable with current technology. The extension of the coherence time via motional narrowing should allow coherent transfer of electron spins in experiments with tunnel-coupled quantum dots. The theoretical understanding of the effect of motion on the quantum dots will be helpful in the interpretation of our results on coherent transport in quantum dots.

## 1.7 State-of-the-art of multiple connected dot manipulation

The control of electrons in one or two quantum dots is already well advanced. Not only is the electron charge routinely measured and manipulated in such structures, but also the spin of the electrons can be readily initialized, controlled and read-out as we showed in this chapter. However, considering the inherent scaling character of lithographically defined solid state systems, controlled quantum dot arrays with more than 2 dots have been surprisingly scarce. While part of it has to do with the demanding fabrication procedures and difficult measurement conditions, it also points at the underlying difficulty of integrating clean potential wells with well controlled couplings in constrained geometries.[111] Most realisations have therefore implemented a linear chain of quantum dots to circumvent the necessity of two-dimensional coupling designs. These difficulties are somewhat illustrated by the first realisation of a charge controlled triple quantum dot by Gaudreau et al. in 2006.[112] It was realised in a supposed double quantum dot where the random impurity concentration gave rise to three discrete potential minima illustrated in Fig. 1.15(a). The stability diagram shows three different slopes of the charge degeneracy lines with respect to the swept gate voltages. This indicates three different dot positions that are differently coupled to the gates. This demonstration was quickly followed by several intentional triple dot designs in many groups for linear chains[113–118] and even few realisations of circular coupling designs.[119,120]

The main advantage of the triple dot system for quantum manipulation is that the quantum states spanned by three electrons distributed in three dots allow for fully electrical 2-axis control of the three-electron spin state.[114,115,117] The qubit identified in this subspace is often called "exchange-only qubit" and is subject of ongoing research. Three recent linear triple-dot designs which featured such coherent three-spin evolutions are shown on the left of Fig. 1.15(g-i). Along I selected stability diagrams for the publications of Laird et al.[114] and Medford et al.[117] as well as the exotic three-spin energy dispersion presented by Gaudreau et al.[115] to illustrate state-of-the-art electron control in such structures. This year in a similar structure to Fig. 1.15(i) Baart et al. also showed successive readout of three one-electron spins as a demonstration of scalable readout of quantum dot matrices.[131] This experiment showed that the electrons can be moved among the quantum dot without the introduction of additional relaxation mechanisms. However no investigation of the coherence of such a process was performed.

Efforts to achieve circular coupling of multiple quantum dot systems led to ambitious design choices as shown by the use of anodic oxidation by Rogge and Haug.[119] Here an AFM tip is used to locally remove the electron gas through oxidation which formed the

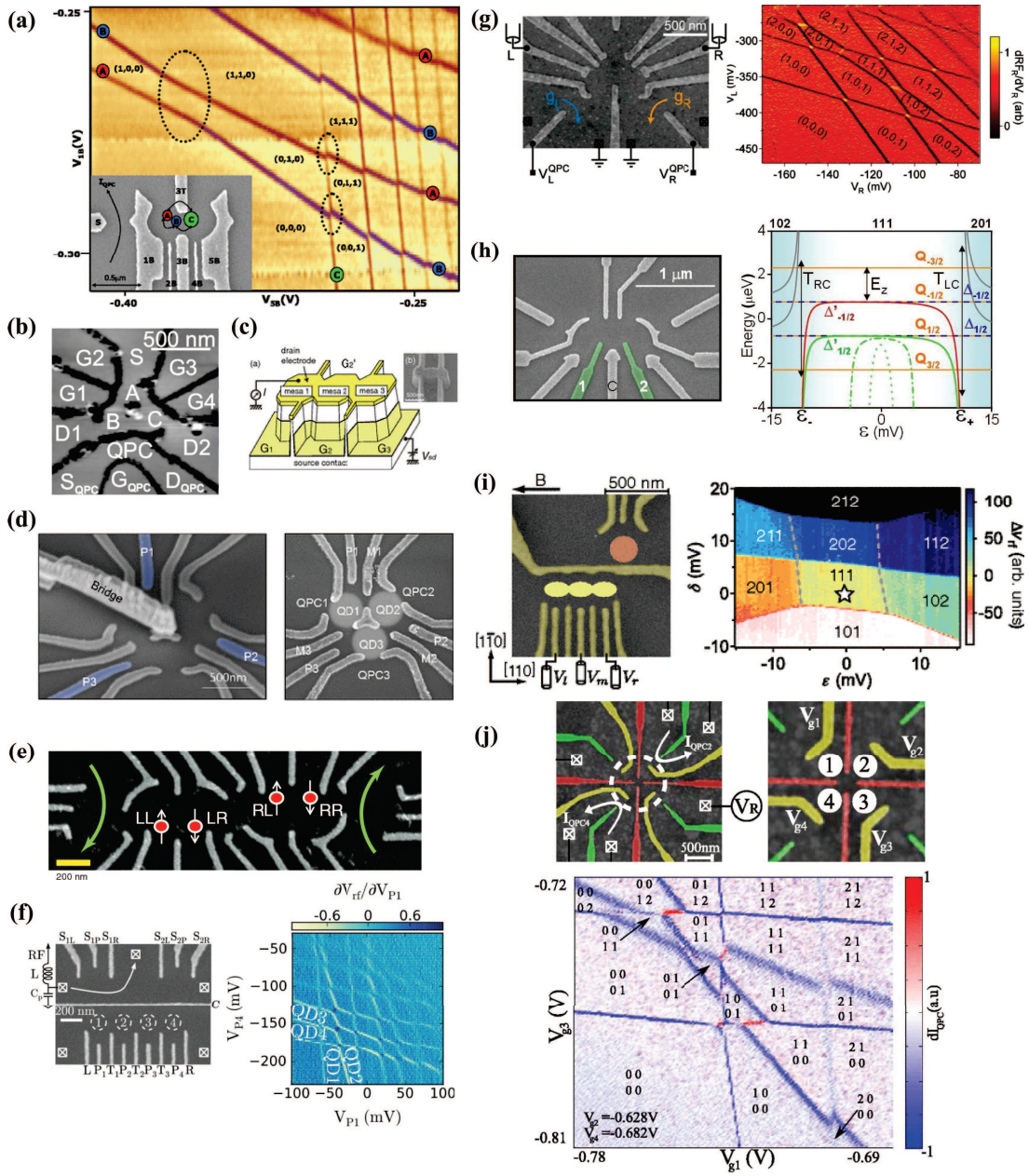


**Figure 1.15:** Selection of stability diagrams of multiple dot systems and secondary electron microscopy (SEM) images of investigated sample designs. **(a)** Stability diagram of the first triple dot, the inset shows a SEM image of the sample with the proposed dot positions.[121] **(b)** SEM image of triangular triple-dot fabricated with anodic oxidation.[122] **(c)** Schematic and SEM image of etched triple quantum dot design.[123] **(d)** Triangular triple-dot design with air bridge.[124] **(e)** SEM image of the sample for a two-qubit C-phase gate in the $\{S,T_0\}$ basis.[125] **(f)** SEM image of sample and stability diagram of a linear quadruple dot with full charge control.[126] **(g-i)** Linear triple dot SEM images, stability diagrams and three-spin energy dispersion ((h) right) used for the coherent control of exchange-only qubits.[127–129] **(j)** SEM images of the circular quadruple dot sample with estimated dot positions 1-4 from the publication of Thalineau et al. and a corresponding stability diagram with electrons in all 4 dots.[130]

structure of Fig. 1.15(b). While this achieves an electron free region in the middle of the structure and therefore a circular layout, the limited amount of gates makes the system not fully tunable. Seo et al.[120] used an air bridge technique to gate the middle of the structure, but the size of their dot structure was large and due to the lack of local charge sensors, they could only perform transport measurements. The lack of control in these structures makes the coherent manipulation and read-out of electron spins impossible. Additionally, many questions about the frustration of the charge and spin of the electrons in a triangular structure have stayed unanswered.

When even larger structures are considered, the number of successful realisations is even smaller. One of the more impressive scaled structures is the electrostatic coupling of two double quantum dots by Shulman et al. in 2012.[33] In their experiment they demonstrated entanglement between two singlet-triplet qubits by implementing a C-phase gate. Efforts to control the tunnel-coupling between four dots were successful in the experiments of Delbecq et al.[132] and Takakura et al.[133] in 2014. They both used linear alignments of quantum dots as shown in Fig. 1.15(f) and demonstrated full charge control while coupling distant dots with the help of intermediate sites.

In our group R. Thalineau showed for the first time charge control over a circularly coupled quadruple quantum dot with the sample shown in Fig 1.15(j) in 2012.[108] He demonstrated that in this structure an electron can be transported along a closed loop but he could not provide proof of the coherence of the process.

In conclusion, commendable progress has been achieved in controlling the spin state of the three-electron exchange-only qubit. Additionally, the work of Shulman et al. showed the first steps towards two-qubit-gates on a lattice with their implementation of the C-phase gate in the $\{S,T_0\}$ basis. However all coherent evolutions have been demonstrated on linear chains of dots with electrons remaining static. While Thalineau et al. presented a pathway for circular coupling strategies, many proposed experiments relying on the topological nature of a circular loop still lack experimental proof.[111]

## 1.8 Conclusion

In this chapter, the general concepts for quantum dot manipulation were introduced. Both the origin of the high-mobility electron gas in the employed heterostructures as well as the control over the electrostatic potential via surface gates were discussed. When the size of a designed electrostatic trap is made small enough, it was shown that few electrons can be isolated in a potential well. This quantum dot was described using the constant interaction model and the expected energy-scales for the confined electrons were given. Furthermore it was shown how the trapped electrons can be detected using close

proximity charge sensors and how their number in the structure can be well controlled. This allowed to theoretically study the dynamics of the spin of one and two electrons in such confined structures. As the spin degree of freedom is used to create controllable two level systems (qubits), this quantity is an active area of research. Electron spin read out in quantum dots is possible via the introduced technique of spin-to-charge conversion. Due to the surrounding crystal potential, the spins are however not optimally protected physical entities. The two main interactions of the isolated spins with the environment were identified as spin-orbit coupling and hyperfine interaction. The resulting decoherence effects as well as manipulation possibilities were analysed with references to state-of-the-art implementations. Finally, a non-exhaustive overview over the implementations of large connected quantum dot systems was given. While the electron spin in linear quantum dot arrays has already become a well accessible entity, no demonstration of coherent electron transport in such structures have appeared in the literature. This demonstration is however critical for the use of quantum dot systems in proposed applications such as quantum computers or quantum simulators. This investigation of the coherent electron transport in quantum dot structures will be the main topic of the following chapters in this thesis.

# CHAPTER 2

## Experimental methods

### 2.1 Introduction

The electrical control of single electrons in lateral quantum dots is a recent achievement, and realizations are limited to a few laboratories in the world. The reasons for that are the high requirements on the sample fabrication, cold temperature technology and measurement control. While ulta-violet (UV) photo-lithography technology is nowadays widely available and made affordable by several companies offering individual shadow mask fabrication, the required electron-beam lithography with resolutions below 100 nm is not available in every research facility. The small energy scales involved in the manipulation of single electrons in quantum dots require sample temperatures below 1 K to allow for an efficient measurement. At the same time, the devices have to be operated on nanosecond timescales and therefore require a good connection to the fast room temperature electronics. These requirements are often contradictory and the experiment therefore has to be performed using a good compromise between high manipulation bandwidth, low noise and low temperature. In this chapter, the core principles of sample fabrication and low temperature generation will be introduced. The techniques for measurement control will be presented starting from the implementation of the electrical connections to a summary of the room temperature experiment control. The limitations on electrical noise, measurement and manipulation bandwidth as well as control parameters will be highlighted during the different sections.

### 2.2 Device fabrication

One of the major difficulties in quantum dot research is the high requirement on the nano-fabrication facilities. The necessary technology, experience and equipment to fabricate high quality heterostructure interfaces with well controlled electron densities and mobilities is only available in a handful of laboratories in the world. Additionally, quantum dots benefit

greatly from dopant engineering, as charge switches between dopant atoms can make highly sensitive experiments impossible. We are fortunate to work in collaboration with the group of Andreas Wieck who provide us with highest quality 2DEGs for the fabrication of our devices. These crystals with a 2DEG located 90 nm below the crystal surface are then used in the nano-fabrication of the lateral quantum dot samples.

The patterning of our devices was done in the nano-fabrication facilities of the Institut Néel and the clean-room facilities of the Plateforme Technologique Amont at the CEA Grenoble. It involves several steps of UV-lithography and one step of electron beam lithography for the fine structure. Photo-lithography in general is a process that projects a two-dimensional structure onto a photosensitive resist that becomes soluble (positive resist) or non soluble (negative resist) to a developer chemical. In principle such a projection process is limited by the Abbe diffraction limit to a resolution given by a smallest point of radius

$$d = \frac{\lambda}{2n \sin\theta} \tag{2.1}$$

where $\lambda$ is the wavelength of the light and $2n \sin\theta$ the numerical aperture of the lens used to create the picture. To circumvent a complex optical apparatus with high numerical aperture the structure to be recreated is usually written on a transparent substrate and brought in close contact with the photo-resist leaving only the non-covered parts to be irradiated. At our institute however we have a laser writing system that can recreate arbitrary designs with a resolution of less than 2 µm on the photo-resist. For smaller structures we use an electron beam writer which uses electromagnetic lenses and deflectors to irradiate a Poly methyl methacrylate (PMMA) layer with high energy electrons. Even though the numerical aperture of electron beam systems is very low, with the small wavelength of $\lambda_{\text{electron}} = 3.9$ pm for electrons with an energy of 100 keV we can achieve a resolution of down to 20 nm.

The sample nano-fabrication process is then as follows

1. Etching of a "mesa", a free standing structure which is electrically isolated
2. Evaporation and annealing of ohmic contacts to electrically connect the 2DEG
3. Definition and evaporation of alignment crosses for electron beam lithography
4. Writing of the fine gate structure by the electron beam
5. Metallic connection of the fine structure to bonding pads for macroscopic access

The mesa etching creates defined current paths for the transport measurements and electrically isolates a small part of the wafer for the fabrication of the device. In addition,

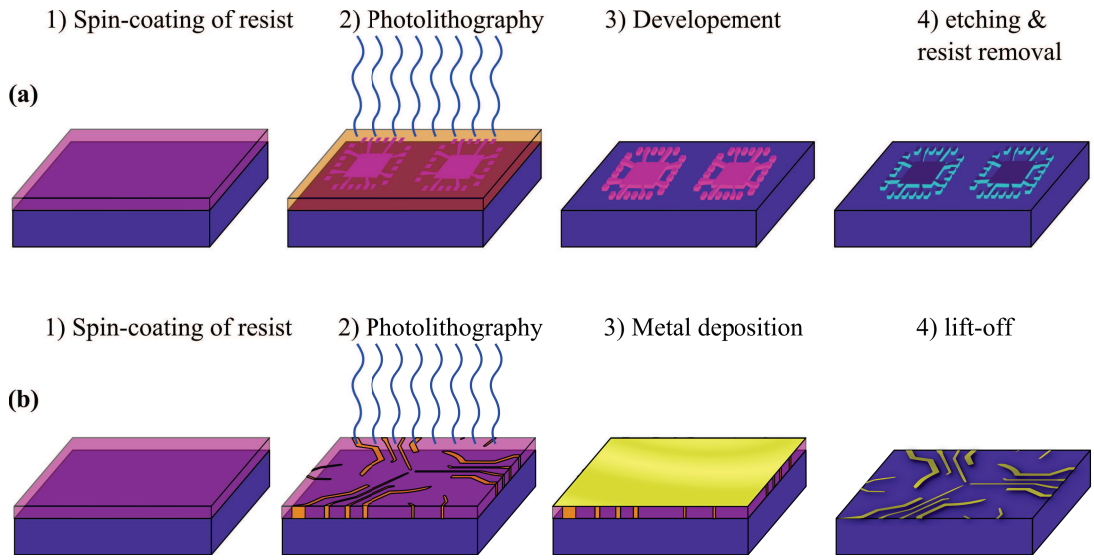


**Figure 2.1:** Schematics of the two fabrication techniques involved in the sample processing **(a)** Steps involved in the etching of the "mesa"-structure using photolithography. **(b)** Metal deposition process involving either optical or electron beam lithography.

the patterning of the mesa also limits the amount of cross-capacitance via the 2DEG. The process is schematically pictured in Fig. 2.1(a). After a spin coating of the optical photo-resist the pattern is irradiated and developed. We use MICROPOSIT$^{TM}$ S1805$^{TM}$ positive photo-resist with a thickness of $\approx 500$ nm. The remaining resist will protect the crystal from the following etching step. We used solutions of either $H_2O_2/H_2SO_4$ and $H_2O_2/H_3PO_4$ for etching of $80-120$ nm to remove the dopant layer. The remaining resist can be removed using Acetone.

In the following step, we create ohmic contacts to the 2DEG using a stack of Au/Ge/Ni/Au. The Germanium and Nickel will form an alloy with the AlGaAs structure when it is annealed and form a low resistance ohmic contact.[134] To deposit the stack of metals, again optical lithography is performed as shown in Fig. 2.1(b), where we irradiate the contact areas followed by resist development. We then evaporate the ≈200 nm thick stack of metals onto the sample in an ultra-high vacuum chamber with electron beam heated metal source cells. The resist hereby protects the underlying crystal from direct contact with the evaporated metal. This is followed by the "lift-off" process where the sample is placed in an Acetone bath and irradiated with ultra-sound. The metals in direct contact to the crystal will stay on the surface whereas metal on the resist will be lifted off with the photo-resist leaving only the light-exposed parts covered. The sample is then brought to an oven and is rapidly ramped up to $\approx 400$ °C and down again to produce a high quality

Ohmic contact. For contact pads with dimensions of 20 µm × 20 µm, we measured a typical contact resistivity of $3 \times 10^{-4}\,\Omega\,\mathrm{cm}^2$.

The following procedures are the definition of alignment crosses via optical lithography and metal deposition with the same lift-off process described above. This allows to accurately position the lateral quantum dot on the crystal during the electron beam writing step of the nanometer sized gates. For the definition of the fine gate structure, a layer of the photo-resist PMMA is used. The PMMA is weakened by the electron beam irradiation where the fine gates are supposed to stick (scission of the polymer chains) and can then be locally removed using a chemical developer. After the development, the necessary metal for the definition of the gates is evaporated. We use a thin layer of only 15 nm Ti/Au to form the actual quantum dot gate pattern. This is again followed by a lift-off in Acetone. The writing process is highly flexible and allows to create arbitrary metal patterns, which are only limited by the resolution of the electron beam writer once the machine is well controlled.

In the last step these fine gates are connected to big bonding pads with optical lithography, metal-deposition and lift-off. A microscope image of the final device is shown in Fig. 2.2(a). The mesa can be identified as the region which the fine-structured gates are placed on. The larger golden metal fingers at the edge of the mesa connect the electrostatic gates to the bonding pads (shown on the right of the image). There are also extensions of the mesa to the bonding pads, which allow to use the bonding pads as an ohmic contact to the sample. This creates an electrical access to the 2DEG for transport measurements. The bonding pads have a macroscopic size of 160 × 110 µm to allow wire bonding to a chip carrier as shown in Fig. 2.2(b). The size of the sample in this picture is 2 mm × 2 mm and it is glued to the chip carrier with varnish. In principle, the orientation of the sample with respect to the crystal orientation is important due to the dependence of the spin-orbit interaction on this parameter. The direction of the edges is naturally given by the easy cleaving directions [110] and [-110]. For the experiments performed in this thesis, we did not further differentiate between the two orientation possibilities. The chip carrier can then be placed into a dilution cryostat and therefore allows to connect the nanometer sized device to macroscopic control electronics. The necessary cold temperature technology and electronics for the measurement will be introduced in the following.

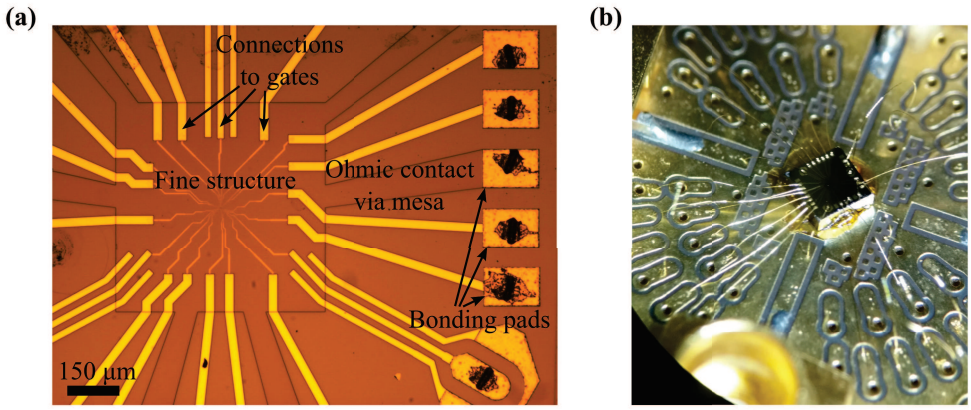


**Figure 2.2:** **(a)** Optical microscope picture of the sample taken at 50x magnification. The black structures on the bonding pads are the remainders of bonding wires previously attached to the sample. **(b)** Picture of the wire-bonded sample glued onto a chip carrier taken through a microscope objective. The sample size is 2 mm by 2 mm.

## 2.3 Cryogenics

The second technological requirement for the measurement of quantum dots is the necessity to work at very low temperatures. The energy scales of the energetic splitting of spin states make temperatures below 1 K necessary. Additionally it has been shown that the QPC sensing of the electron charge becomes inefficient at temperatures above 1 K.[135] Most of the experiments involving quantum dots are therefore performed in dilution cryostats with temperatures as low as few mK. At the Institut Néel we have a long history of cold temperature physics and have access to custom home built dilution cryostats. In the beginning of my thesis a new inverted cryostat was installed, which combines a base temperature of 60 mK with low helium consumption and fast cool-down times (4h-6h to base temperature).

The working principle of a dilution refrigerator relies on the peculiar phase diagram of the Isotope mixture of $He^3$ and $He^4$ at low temperatures shown in Fig. 2.3. It partly arises from the fact, that $He^4$ atoms are Bosons, while $He^3$ atoms are Fermions. Due to its bosonic nature $He^4$ becomes a superfluid liquid below a temperature of 2.177 K. When $He^3$ Fermions are added, the mixture turns back to a normal fluid phase. However below 867 mK the mixture instead separates into two phases, with one superfluid $He^3$ poor phase and the lighter $He^3$ rich phase on top. Now an interesting physical process can happen. Fermionic $He^3$ atoms from the $He^3$ rich phase can diffuse into the superfluid phase and in this way lower the energy of the top phase. This is favourable due to the higher binding energy of $He^3$ atoms in the dilute phase induced by their higher zero point motion.[136] As

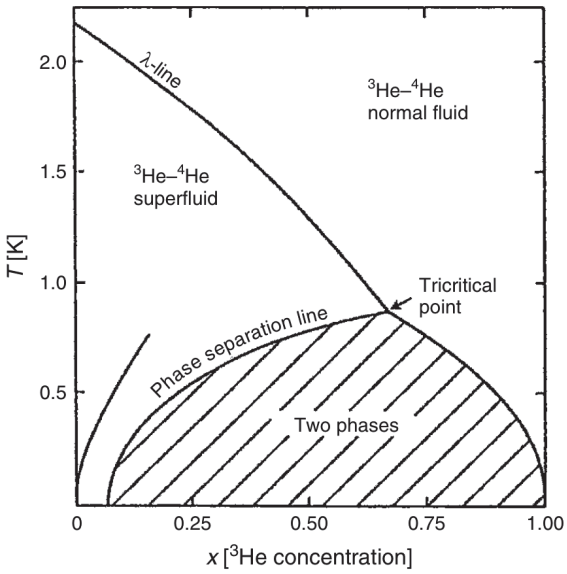


**Figure 2.3:** Phase-diagram of the $He^3$-$He^4$ mixture at low temperatures for varying compositions taken from Pobell [136]. Below 867 mK the system separates into two phases, a superfluid $He^3$ poor and a $He^3$ rich phase.

long as the dilute phase can reduce its $He^3$ concentration, this implements a continuous cooling process at the phase interface which can be kept running by removing $He^3$ atoms on one side and adding $He^3$ atoms at the other side. This is achieved by pumping on the $He^3$ poor phase and reinjecting the extracted gas at the $He^3$ rich phase. The resulting continuous cycle is called dilution cooling and can achieve very low temperatures.

In our inverted dilution cryostat this cycle is implemented as shown in Fig. 2.4. The cryostat consists of five stages which each feature copper radiation shields for thermal insulation. The whole system is under vacuum to reduce heat leaking. In this design, there are two separate circuits to cool the cryostat. The first is a separate $He^4$ circuit that is directly connected to a pressurized liquid helium dewar and illustrated by the light blue line. It provides the cooling power necessary to reduce the temperature of the other circuit. From the Dewar, the $He^4$ mounts up directly to the 4 K stage, where the $He^4$ pot is located. This pot is then filled with liquid $He^4$ which leads to a stable temperature of $\approx$4.5 K at this point in the circuit. The $He^4$ then leaves the cryostat via a counterflow heat exchanger, pre-cooling the second circuit. The circulating $He^4$ leads to a cooling of the bottom two stages and allows to gradually reduce the temperature of the gas in the other circuit from 300 K (room temperature) to 4 K.

The other circuit is filled with a $He^3$-$He^4$ mixture that is used for the implementation of

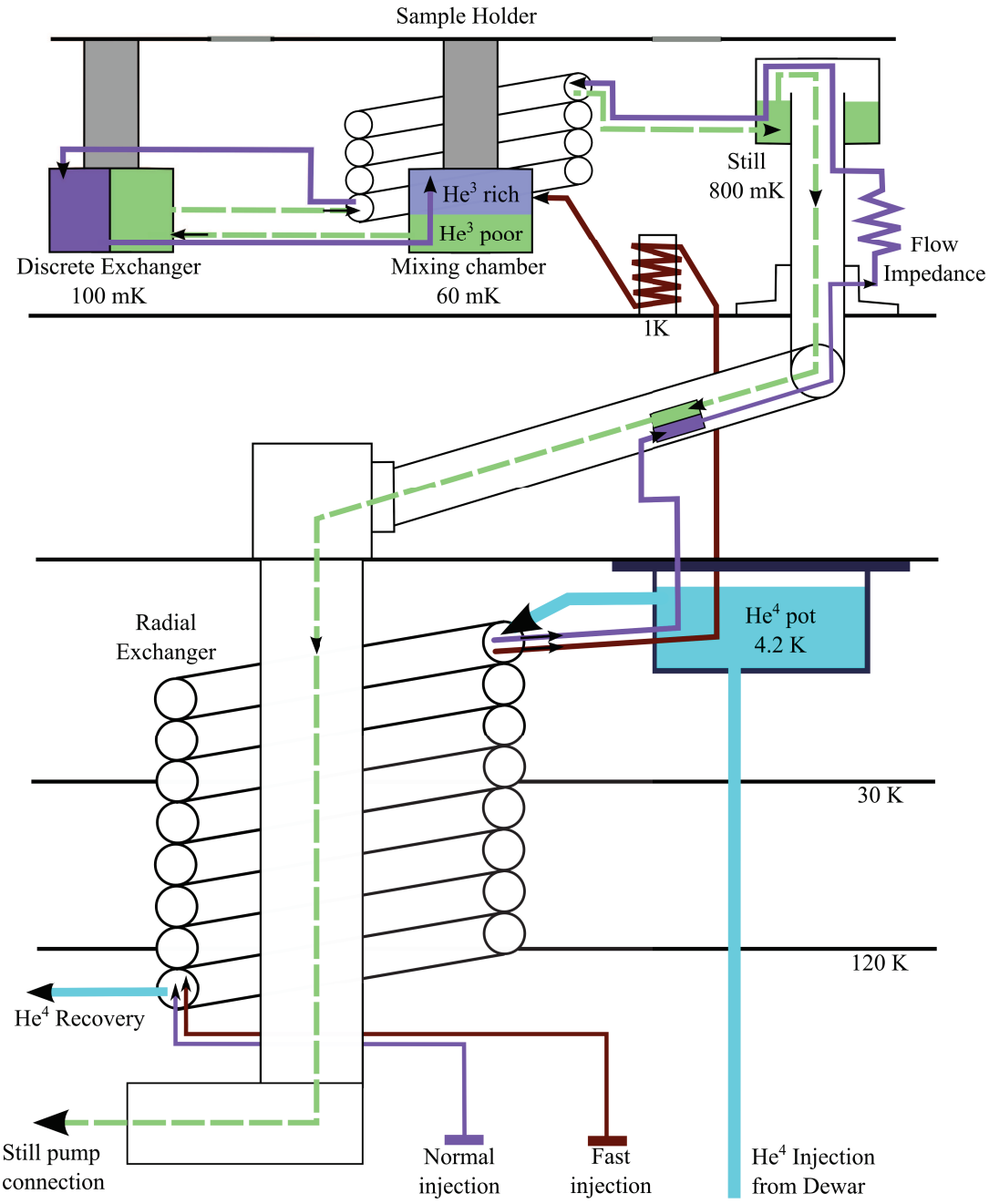


**Figure 2.4:** Schematic of the circulation system of the home-made inverted dilution cryostat "sionludi". Light blue shows the separate $He^4$ circuit. Violet and brown are the normal and rapid injection respectively. The green lines show the path of the now dilute mixing after arriving at the mixing chamber until it arrives at the still pumping connection.

the dilution cooling technique described above. Initially, the upper stages can be cooled to 4 K by the "fast injection"-circuit (brown) which is cooled by the $He^4$ circuit in the counterflow heat-exchanger and thermalized on the still-stage. When the system has been cooled down to 4 K, the "Normal injection" (violet) can be used to start the dilution cooling. Here the mixture is again precooled to 4 K and is then forced through a high flow impedance to cool it via the Joule–Thomson effect. It then passes still, radial counterflow exchanger and a discrete exchanger before it arrives in the mixing chamber to achieve a minimal temperature of the injected $He^3$-$He^4$ mixture. This is important as the cooling power depends strongly on the temperature at the last exchanger $T_{ex}$ by

$$\dot{Q} = \dot{n}_3(95T_{mc}^2 - 11T_{ex}^2) \tag{2.2}$$

where $\dot{n}_3$ is the $He^3$ flow and $T_{mc}$ the temperature of the mixing chamber.[136] At this position, the phase separation happens which leads to the dilution cooling of the cryostat. After passing from the $He^3$ rich phase to the $He^3$ poor phase (green) the mixture is used to cool the arriving mixture before being injected into the still. Here it evaporates due to the low pressure created by pumps outside the cryostat. As the mixture evaporated from the still is mostly composed of $He^3$ ($\approx 97\%$),[137] most of the mixture circulating outside the cryostat and being re-injected is $He^3$. The continuous circulation of the $He^3$ rich mixture leads to a stable cooling of the coldest parts and allows to reach temperatures down to 60 mK.

## 2.4 Wiring and cold temperature experiment parts

While the dilution cryostat provides the necessary low temperatures to observe and manipulate the quantum dots used in this thesis, the experiment heavily relies on an active control of the available parameters. These include the generation of magnetic fields and electrical connections from room temperature electronics to the investigated sample at $\approx 60$ mK. Due to the high bandwidth and low noise requirements, as well as the strong thermal gradients, the implementation of the electrical connections via wires and passive elements can become non-trivial. We therefore give a short summary of the implementation of the magnetic field coil, as well as information about the high- and low-frequency cable connections to the sample. This is complemented by an investigation of the high frequency response of our measurement setup for the nanosecond control of the investigated samples.

### 2.4.1 Magnetic field generation

The low mass and compact design makes the cryostat very practical and allows for fast cooldown times. The separate $He^4$ circuit however induces a few technical restrictions.

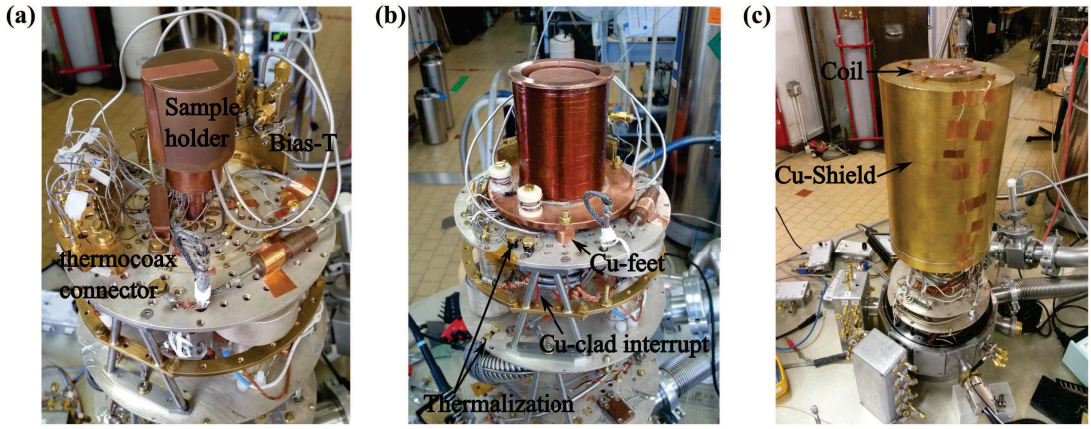


**Figure 2.5:** **(a)** Picture of the top part of the cryostat with the sample holder and the wire connections. **(b)** First coil design which is mounted on top of copper poles directly screwed to the direct exchanger plate. The superconducting wire is thermalized on each stage and had its Cu-matrix interrupted between different temperature stages. **(c)** Picture of the second approach where the coil is screwed onto the reinforced Cu-heat-shield with a temperature of 4 K. The superconducting wire is taped to the screen to avoid a direct touch with the next heat shield.

Most notably the absence of a shielding $He^4$ bath complicates the thermalization of wires and the magnetic field coil.

For the latter we tried two designs where a superconducting Nb-Ti coil mounted on a copper cylinder was in the first edition directly thermalized on the direct exchanger at 100 mK. A picture of this implementation is shown in Fig. 2.5(b) where the coil is screwed onto Cu-feet and thereby thermalized by the stage it rests on. The superconducting wires were removed of their surrounding copper matrix between temperature stages to reduce heat flow and then soldered to copper wires at the 4 K stage. This design worked well for currents of up to 10 A, but it led to a strongly increased cooldown time and was impractical for sample changes.

For the second design the coil therefore is hanging from a reinforced 4 K copper heat-shield to benefit from the larger cooling power. The reinforced shield is shown in Fig. 2.5(c) with the coil screwed to the top. The superconducting wires are guided on the outside of the shield and again connected to copper wires at 4 K. This design reduced the cooldown times for millikelvin operation by 3-4h as the low temperature stages can be cooled down more efficiently.

The magnetic field coil features a low inductance of $\approx 0.7$ H that allows for fast changes of small magnetic fields on the order of $t_{rise} = 80$ µs. At a maximum tested current of 10 A, it allows to generate a magnetic field of $\approx 600$ mT. As the magnetic field requirements for

quantum dot operations are relatively low, this magnetic field coil design was sufficient for the experiments performed in this thesis. The modular design however allows to exchange the coil for a different model with higher inductance to generate higher fields.

### 2.4.2 Wiring of electrical connections

For the electrical connections to the sample, a combination of low thermal noise and high bandwidth are required. To reduce the electron temperature at the sample position, the wires have to be thermalized at each stage of the cryostat. Furthermore, the cables have to be shielded and filtered to limit the impact of the electrical noise on our sensitive samples. As a high bandwidth directly results in increased electrical noise, the bulk of the sample connections are done via low frequency (DC) wires. In the employed cryostat, several different wire-types are used to achieve the necessary control requirements. For the lowest bandwidth requirement, we have constructed a shielded wire bundle as described in Mandal et al. [138]. It consists of 27 constantan wires in a Cu-Ni tube filled with ECCOSORB® CRS 117. It then passes through a copper-powder/Stycast filter before arriving at the the sample holder. These lines have low thermal conduction and are strongly filtered at high frequencies. The close proximity of the wires in the Cu-Ni tube however induced a non-negligible crosstalk. They are therefore only used for constant voltage generation and recovering QPC currents.

The gates that have to be addressed at microsecond timescales are connected via 16 separate coaxial Thermocoax® lines to limit crosstalk during manipulation. These connections have an intermediate bandwidth of 500 MHz and therefore have a negligible effect on the imposed potential changes for microsecond gate movements. At the same time, they efficiently filter radio-frequency radiation and therefore lead to relatively low electron temperatures at the sample.

To manipulate the gate voltages at high frequencies (RF), high bandwidth coaxial cables were installed in the cryostat. They are composed of superconducting Nb-Ti after the 4 K stage to minimize heat conduction. To limit the electron temperature and reduce electronic noise from room temperature electronics we use signal attenuators at 4 K and 100 mK. Depending on the necessary amplitude for manipulation we used 30 dB and 20 dB total attenuation per line for different experiments. To combine high frequency and low frequency manipulation on a gate, RC element bias-T with design parameters of $C = 8$ µF and $R = 1$ kΩ at 300 K were installed on the 100 mK stage (see Fig. 2.5(a)). A schematic of the circuit model is shown in Fig. 2.6(a). This results in a cut-off frequency of 20 Hz at room temperature. Note however, that at low temperatures the used SMD elements tend to have different characteristics and this value is expected to change. Additionally, significant

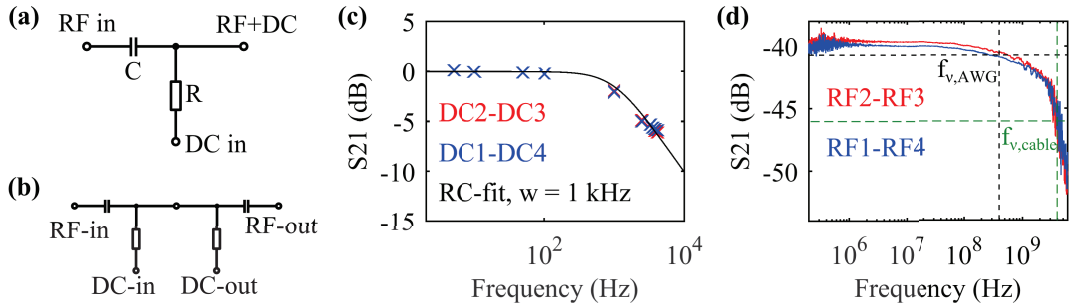


**Figure 2.6:** **(a)** Schematic of the bias-T used in the experiment for 4 Coaxial lines. The parameters are $C = 8$ µF and $R = 1$ kΩ at 300 K. **(b)** Measurement configuration for the determination of the transmission of the bias-T. The output port of the two bias-Ts are connected via a bonding wire at the sample position. **(c)** Low frequency response of the DC connection of the bias-T at low temperature (0.1 K). A square wave of varying frequency is applied on one DC-port and the rms-voltage on the other DC-connection of a second bias-T is probed as shown in (b). In this case, the measured bandwidth $w$ is 2 times higher than for the case of a single bias-T. **(d)** High frequency response of the RF-connection of two coaxial lines connected by bias-Ts at low temperature (0.1 K). The measurement configuration is shown in (b). At the bandwidth of our arbitrary waveform generator (400 MHz) an attenuation of -40.6 dB is measured. For the case of one RF-line, this results in an effective attenuation of -0.3 dB after subtracting the contribution of the attenuators (-20 dB on each line).

signal loss is routinely observed at high frequencies due to the intrinsic bandwidth of the cables, the cable connections and the passive elements.

To accurately measure the characteristics of the RF-connections at low temperature, the output of two bias-Ts were connected with a bonding wire at the sample position as shown in Fig. 2.6(b). For the low frequency response, a square wave of varying frequency was applied on one DC-connection and probed at the DC-port of the other DC-line, while the RF-connections are grounded. The transmission of the signal is shown in Fig. 2.6(c) for two different pairs of RF-connections. The response is fitted with

$$P = \frac{1}{\sqrt{1 + (\omega RC)}} \tag{2.3}$$

and we obtain a bandwidth $f_\nu = \frac{R*C}{2\pi} = 1$ kHz. A numerical analysis of the two circuit models gives the relation $f_{\nu,single} = 0.5 f_\nu$ for the bandwidth of only one Bias-T. We therefore find a high frequency cut-off of 500 Hz for the DC-connection at low temperature.

To analyse the high frequency response of the RF-connection, a network analyser with a maximum frequency of 6 GHz was used. The measurement configuration is again given in Fig. 2.6(b), but this time the signal is applied and recovered on the RF-ports and the DC-ports are grounded. The resulting measurement is given in Fig. 2.6(d) for the same

two pairs of RF-connections. At frequencies below 100 MHz the transmission is fully accounted for by the intentional attenuation of -20 dB per line. At higher frequencies, the response becomes frequency dependent with a value of -46 dB at 4 GHz. Subtracting -40 dB originating from the attenuators, this corresponds to $-3$ dB additional attenuation per line and therefore gives the bandwidth of the RF-connection $f_{\nu,cable} = 4$ GHz.

The bandwidth for manipulation is then limited by the bandwidth of our arbitrary waveform generator of $f_{\nu,AWG} = 400$ MHz. At this frequency, an additional attenuation of -0.3 dB per line is measured (dashed black lines). This corresponds to a reduction of the applied voltage of 4% by the coaxial cables, bias-T, sample holder and bonding wires at the maximum manipulation speed employed in this thesis.

## 2.5 Measurement setup and electronics

Additionally to well filtered and isolated cables that result in a low electron temperature at the sample position, it is also necessary to limit the amount of noise coming from the manipulation electronics. They have to be as quiet as possible, while at the same time providing the required bandwidth and sensitivity for the electrical control of the quantum dot. A schematic of our experiment setup for most experiments is shown in Fig. 2.7.

For the DC voltages we use a home made 16 bit digital to analog converter (DAC) that is capable of producing fast rise times of $t_{rise} < 2$ µs while featuring a bandwidth limited noise floor of $\approx 25$ nV/$\sqrt{\text{Hz}}$ with 1.9 MHz low-pass filters at the connection to the cryostat. This results in a root-mean-squared (rms) noise of 35 µV while still allowing to perform microsecond operations. For the fine control of bias voltages on the QPCs we add 1/1000 voltage dividers which further reduces the noise in the system.

The DAC is controlled via an electrically isolated serial connection by a field-programmable gate array (FPGA) from National Instruments (NI sbRIO-9208). This allows real-time execution of experiments by synchronizing instrument and measurement triggers to gate voltage changes. The experimental sequence can be programmed in advance on a PC and then sent to the FPGA via an ethernet connection allowing for maximum flexibility.

A digital trigger can be used to synch DC and radio-frequency (RF) pulses at real-time. Most of the RF signals were generated by a Tektronics® arbitrary waveform generator (AWG), whose output can be programmed via an ethernet connection. Our model features a sampling frequency of up to 1.2 GSa/s and a pulse rise-time of $\approx 800$ ps. At the same time, the AWG generates a significant amount of high frequency noise which can be evaluated using the bandwidth dependent intrinsic noise of 25 nV/$\sqrt{\text{Hz}}$. Considering the bandwidth of the generator $f_{\nu,AWG} = 400$ MHz and the line attenuation of $-20$ $dB$, the expected rms noise at the sample position due to the AWG is evaluated to be $\approx 100$ µV.

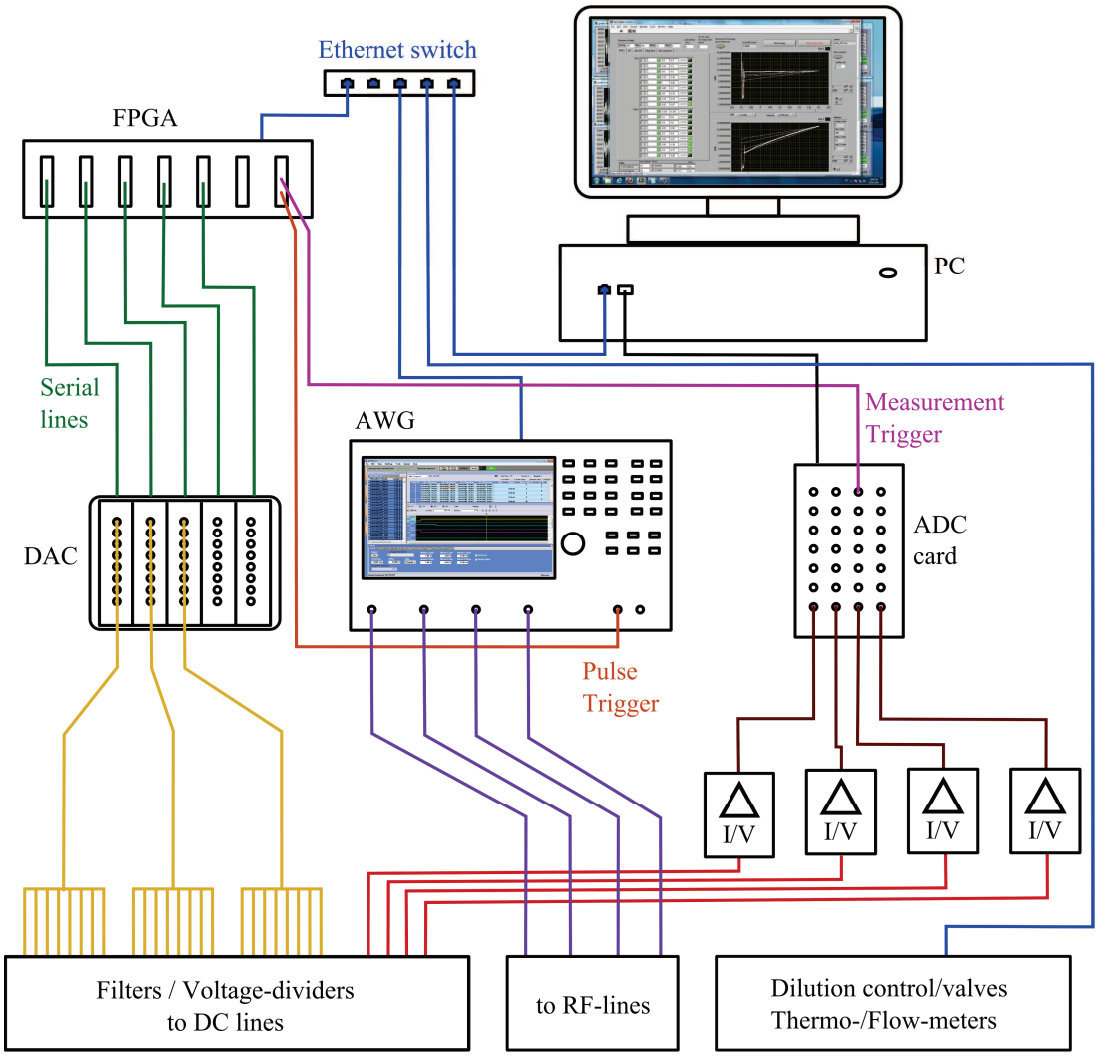


**Figure 2.7:** Schematic representation of the room temperature electronics and measurement equipment. A computer (PC) controls a field-programmable gate array (FPGA) which in turn handles the real-time experiment through serial connections to the Digital-to-Analog (DAC) converters and triggers for measurement and RF apparatus. Current coming from the sample is amplified and then converted to a voltage fed into the analog-to-digital converter (ADC) card. The PC recovers and saves the data acquired in this way.

Finally the QPC current is recovered on custom-made I-V converters based on Texas Instruments® operational amplifiers. They feature low noise of $12\text{nV}/\sqrt{\text{Hz}}$ and variable gain of $10^6 - 10^9$ (1 nA gets converted to 1 mV−1 V respectively) via different feedback resistors. At the lowest gain of $10^6$, an output rise time of $\approx 100$ µs was measured, giving a bandwidth of 10 kHz. The voltage is picked up by a 14 bit analog-to-digital converter (ADC) card from National Instruments. It features a sampling rate of 250 kSa/s which is multiplexed over the measured analog inputs. The acquisition can be triggered by the FPGA to allow the real-time current trace measurements necessary for single shot spin-detection.

The electronics therefore allow the low noise manipulation of the investigated samples. The control voltages can be changed on microsecond to nanosecond timescales. Our measurement chain allows multiplexed recovery of the sample response with a measurement bandwidth of 10 kHz. The experiment is performed in real-time by the FPGA that allows the synchronized control and measurement of the device. All experiment parameters are hereby accessible on a control PC that schedules the experiments and recovers the measured response via a graphical user interface.

## 2.6 Measurement software

To address the acquisition hardware and the FPGA, we have developed a custom measurement suite based on Labview®. Additionally, it can control most instruments in the laboratory (Oscilloscopes, frequency generators, Lock-in detectors etc.) and recover relevant experiment data. The resulting files contain the experimental data as well as information about the experiment parameters which can be read in by a Matlab® based analysis program.

The experiment cycle is adapted to the FPGA based measurement and schematically shown in Fig. 2.8. We first bring all the instruments in the starting position for the current trace. Then the FPGA internal command register is updated via TCP-IP to reflect the next experiment. When the acquisition instruments are ready, the FPGA is triggered to start the experiment. During the following parse of the command register it sends out triggers to instruments and measurement cards while updating the DAC values in a fast real-time command chain. A simple example would be a voltage ramp (staircase) on one DAC output with regular measurement triggers to construct a gate sweep. When the measurement is complete, the data is collected and saved before the program starts the cycle again. As the FPGA command register can be made arbitrarily complex, many experiments can be constructed in this way. The currently implemented commands in the sequentially accessed register are

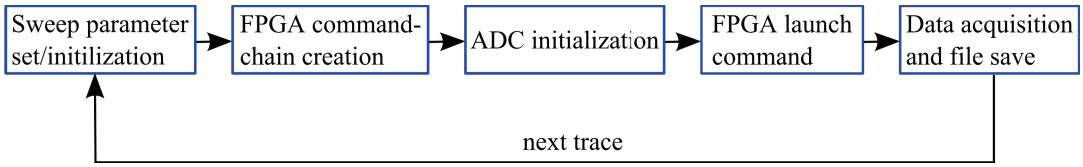


**Figure 2.8:** Simplified schematic of the measurement cycle implemented in the software. The first step includes setting all parameters for the instruments taking part in an experimental realisation. Then the FPGA is programmed and after a measurement instrument initialization, the FPGA runs one instance of an experiment. The last step includes data acquisition and logging. This cycle is repeated for different parameters to obtain the current traces in our experiments.

- Digital **Trigger** status for several digital out connections
- Idle **wait** for a multiple of clock-cycles (here in multiples of 0.45 µs up to several hours)
- **DAC** channel output voltage change
- sequence **jump** command to implement loops

which can be concatenated in arbitrary order. As the triggers synchronize the outputs of several preconfigured instruments these commands combine to allow full control over the real-time execution of the measurement.

The advantage of the FPGA based measurement control are the high timing accuracy used for the synchronization of different instruments. The hardware logic circumvents the usually slow interaction with the operating system of a PC and allows experiment control with nanosecond accuracy. Through the use of a battery, the FPGA can also be made partly immune to the stability of the power grid and in this way protect the sensitive samples.

## 2.7 Conclusion

In this chapter, the experimental requirements for the operation of quantum dots were analysed with respect to the available technology in our laboratory. The sample fabrication techniques and their respective limitations were introduced. They allow to fabricate arbitrary quantum dot designs with resolutions of $\approx 20$ nm and to electrically connect the sample to macroscopic control electronics. The necessary cryogenic cooling for the operation of the device was illustrated for the example of a custom made inverted dilution cryostat. The refrigerator allows to cool the device and the electrical connections down to $\approx 60$ mK and thereby makes the operation of the quantum dot possible. The implementation of the experiment control via magnetic field and electrical connections was

discussed in detail for the same cryostat and the limitations on noise and manipulation bandwidth were given. Finally it was shown how the room temperature electronics and the FPGA based measurement control allow to meet the high requirements for quantum dot operation concerning measurement and control bandwidth, timing resolution and noise. The implemented measurement apparatus makes the manipulation of the fabricated samples at gigahertz frequencies possible. This high level of control will be necessary for the spin manipulation presented in the following chapters.

# CHAPTER 3

## Charge control of Multi-dot systems in the isolated regime

### 3.1 Introduction

The design and the control of multi-dot systems remains challenging up to date as I showed in 1.7. While linear arrangements of triple dots are already used for the implementation of exchange-only qubits, strategies to move and couple electrons in larger systems have still to be presented. Notably, the presence of the reservoirs allows the number of electrons in the system to change. When the number of quantum dots increases, the number of possible charge states increases as well and results in a higher technical difficulty of fixed charge manipulation. For large systems, the exchange of electrons with the reservoir also becomes mediated via nearest neighbour hopping. This exchange can become a slow process due to its dependence on the energy detuning of different quantum dots. The resulting unstable charge state inevitably leads to an increasing difficulty of manipulation with the system size. We will therefore investigate in this chapter a novel regime where the connection to the reservoirs is intentionally cut. It will be shown that in this "isolated regime" the electron number in the quantum dot no longer depends on the chemical potential of the 2DEG, but instead remains constant. The electron number can hereby be deterministically fixed. This process will be used in measurements of isolated quantum dot systems in three different sample designs. The effective removal of the electron bath is demonstrated to result in a subspace of reduced complexity. As the electron number is fixed, the available number of charge states is greatly reduced, leading to simplified analysis and control. This simplification is demonstrated to allow direct access to the inter-dot tunnel-coupling during experiments. Our measurements can be mapped to a simple theory based on the constant interaction model and are explained qualitatively and quantitatively. Finally, measurements of the first fully tunable lateral triple quantum with controlled electron numbers in a closed loop will be presented.

## 3.2 Electrostatic simulation of gate induced potential

To analyse the sample response to certain gate configurations, to obtain a clear picture of the potential in the isolated regime and to streamline the design process of consecutive devices, we implemented a potential calculation for arbitrary gate structures. The requirements were ease of use and natural integration with different design software packages used by different laboratory members. We therefore chose to base it on the GDSII file system, which is shared by common software packages and has free libraries for programmatic creation of sample designs in Python.

The calculation is adapted from the work of Davies et al.[139] who calculated the electrostatic potential created by different geometric shapes in a plane with distance $d$ from the gates. A comparison of the different formulas obtained by Davies et al. is given in Appendix. C.1.

To calculate the potential of arbitrary polygons, we implemented a triangulation method for polygons based on an ear-cutting approach. It decomposes the polygon into triangles by iteratively analysing sets of three connected points of the polygon. If the three points form a triangle with small opening angle ($<\pi$) and without another point of the polygon inside, it is removed until the polygon is fully decomposed. An example of the output of this method is shown in Fig. 3.1(a) for a triple-dot design. Davies et al. calculated the potential of an infinite triangle with its vertex at the origin and an angle of $2\alpha$ with the $x$-axis as

$$\frac{\Phi(x,y,d)}{V_G} = \frac{1}{\pi}\arctan\left(\frac{d\sin\alpha}{(R-x)\cos\alpha - y\sin\alpha}\right) \tag{3.1}$$

where $V_G$ is the gate voltage and $R = \sqrt{x^2+y^2+d^2}$ the distance from the point of observation to the origin (vertex). Due to the linearity of the Maxwell equations we can therefore create an arbitrary finite triangle by adding and subtracting the potentials of three infinite triangles as shown in Fig. 3.1(b). The triangles can hereby be shifted from the point of origin and rotated via simple geometric transformations on the point of observation. By adding the potential of the composing triangles we can generate the potential of the complex gates that form the quantum dot structure.

Note that this electrostatic calculation does not take into account the screening of the potential from the 2DEG, which limits its applicability. The resulting potential profile is therefore less accurate for areas where we expect the presence of the electron gas. However, at the position of the quantum dot, the electron gas is fully depleted by the negative voltages on the gates. Consequently we can expect our calculation to be relatively accurate at the

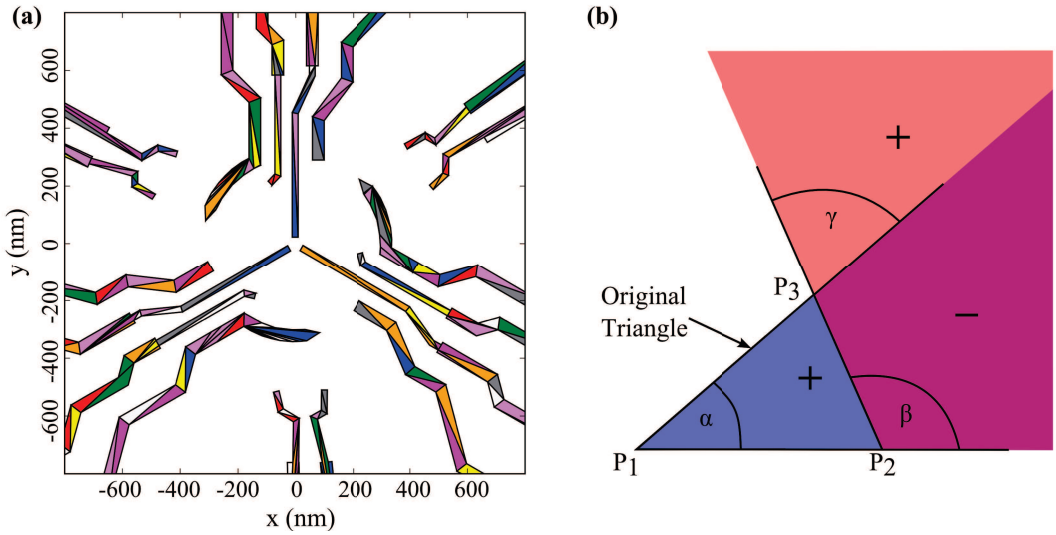


**Figure 3.1:** **(a)** Example of the output of the triangulation method of a gate structure created by the design software. The triangles extracted from the polygons are coloured differently for clarity. **(b)** Illustration of the decomposition of regular triangles into a superposition of infinite Triangles with origins at $P_1$,$P_2$,$P_3$ and angles $\alpha$,$\beta$,$\gamma$ respectively. The signs (+,-) indicate if the potential of the infinite triangles is to be added or subtracted to result in the potential of the original finite triangle.

active area of our device and use it to design the generated potential profile. Additionally, for the calculation of the potential profile of a gate structure by Bautze et al.,[140] he observed a scaling factor of the gate voltages of $\approx 20$ with respect to the experimentally found values. This correction to the potential due to electron screening will be taken into account in the following when a comparison with experimental values is considered. Finally the electron gas is induced by the donor layer approximately 45 nm from the 2DEG. As however their density is relatively low (1 ionized donor per 20 nm) and their exact locations are randomized by the growth process, every sample features a distinctly different potential landscape. Consequently the experimental gate configuration needs to be first adjusted to these initially unknown variations before the intended potential profile can be induced.

## 3.3 Isolation of quantum dots from the electron gas

The main motivation of our pursuit of isolated quantum dot systems lied in the reduced parameter space that it results in. Conceptually for the control of a quantum dot system with $N$ coupled dots, we need to control $N$ chemical potentials as well as $N$ reservoir barriers in addition to the large amount of tunnel-barriers to link the quantum dots. For systems with more than two dots the amount of control parameters can therefore become very big (for a circular triple dot this results in a 9-dimensional optimization

problem originating from 3 QD energies, 3 reservoir-barriers and 3 tunnel-couplings). These parameters are controlled by electrostatic gates in the experiment. To address each control parameter individually, an equal or greater number of gates is needed. Due to the constrained geometry and the finite size of the gates, this leads to a technological hurdle of physical integration.

Isolating the electrons from the reservoirs however frees $N$ degrees of freedom for the barriers to the 2DEG but additionally results in the removal of the 2DEG Fermi energy as a potential reference. As now only the relative potentials of the dot are necessary, we can chose one of them freely and therefore need to only control $N-1$ chemical potentials (making the circular triple dot a 5-dimensional optimization problem, 2 QD energies and 3 tunnel-couplings).

The much larger improvement however is gained when the amount of charge states in the system is considered. When the quantum dots are coupled to a reservoir, the number of available charge states is practically infinite ($N_{\mathrm{electron}} \in \mathbb{N}_0$). Once the number of electrons $N_{\mathrm{electron}}$ is fixed however, the number of available charge states is bounded by

$$N_{\mathrm{states}} = \begin{pmatrix} N_{\mathrm{dot}} + N_{\mathrm{electron}} - 1 \\ N_{\mathrm{dot}} - 1 \end{pmatrix}, \tag{3.2}$$

where $N_{\mathrm{dot}}$ is the number of quantum dots the electrons are distributed to. For example in a triple quantum dot filled with two electrons, only 6 charge configurations are available. This strongly reduced state space is obviously linked to a reduced complexity of charge manipulation. The control of electrons in this regime is therefore greatly simplified.

The isolation also removes a relaxation path for spin information stored in the electrons. As the reservoirs become unavailable for electron exchange, the electron spin can no longer be randomized or re-initialized via a tunnelling event. This becomes especially important when we start to imagine complex paths in the parameter space including multiple tunnelling events. As the parameter space is no longer reduced by the presence of charge degeneracies, this further facilitates the operation of the device.

Additionally, the removal of the reservoirs becomes a natural evolution when no longer all quantum dots can have access to a direct reservoir connection due to the increased system size. Here the exchange of electrons with the reservoir becomes an $M$th order process where $M$ is the number of barriers between the dot and the 2DEG. It is therefore necessary to investigate the dynamics of isolated systems before such a scaling process can be initiated.

Considering a possible application of a scalable quantum dot system, fixing the electron

number in a quantum simulator can be an interesting way of controlling macroscopic parameters without changing the gate voltages that define it. In that way one can imagine to change the chemical potential or the particle density in the same system in a very reproducible way.

## 3.4 Isolated regime for double quantum dots

The first experiments in the isolated regime were performed by Johnson et al. where they exploited the isolated configuration to perform spectroscopy of the excited charge states of a double quantum dot.[142] In our laboratory, the isolated regime was first applied in a sample designed to transfer electrons over large distances with moving quantum dots performed by B. Bertrand.[141,143,144] The isolation from the reservoirs was hereby necessary to initiate the transport process without electron loss. This transition to the isolated regime had several positive side effects that will be highlighted in this section. These results will then be applied for the manipulation of triple dot devices in the following sections.

To guide the electrons during the transfer and isolate them from the environment, a depleted transport channel was implemented in direct contact to a quantum dot. A false color secondary electron microscopy (SEM) image of the sample is shown in 3.2(a). On the channel gates (blue) a voltage $V_{Ch}$ is applied that removes any electrons between them. The quantum dot formed by the metallic gates on the left is controlled via the two voltages $V_L$ (green) and $V_R$ (red). The current through the nearby QPC (bottom) allows to measure the charge state of the quantum dot.

A stability diagram of the quantum dot is shown in Fig. 3.2(b). The diagram features two different regimes depending on the value of $V_L$. On the top, clear charge degeneracy lines are observed in red, with the last one at $V_R \approx -0.57$ V indicating that all the electrons are now removed from the dot. The lines also stop for gate values of $V_L \approx -0.54$ V where they first become stochastic and then end completely. This is the result of the strong coupling of the green gate to the barrier to the reservoir. When it is pushed to more negative values, the tunnelling time to the 2DEG increases until it becomes comparable to the measurement time. Then the charge degeneracy lines become dotted indicating stochastic exchange with the electron gas. Further to the bottom-right of the stochastic charge degeneracy line, the escape time to the reservoir becomes much higher than the measurement time (3 ms/point). The electron can therefore no longer tunnel to the reservoir while the charge degeneracy line is crossed. As the barrier becomes even thicker when $V_L$ is increased more, the system stays with a fixed electron number (indicated on the stability diagram). The trapping time in this position can now easily be increased to be of the order of minutes and we can effectively speak of an isolated system.

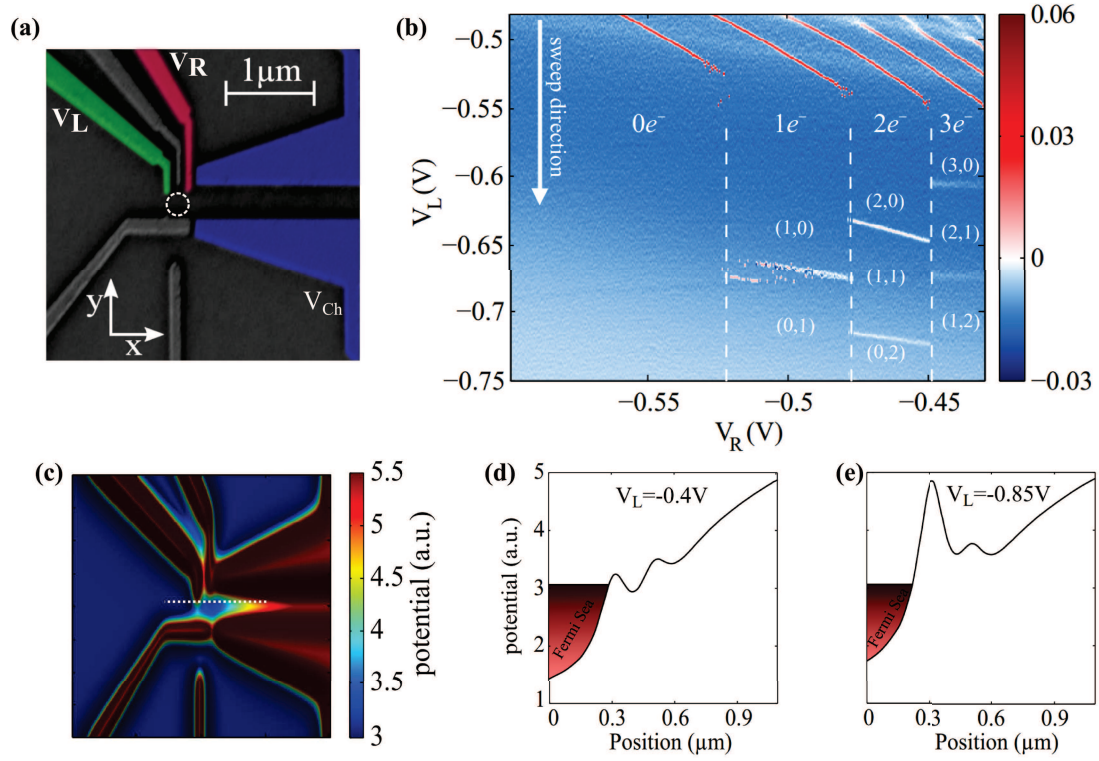


**Figure 3.2:** **(a)** False color SEM image of the sample used for electron transport with surface acoustic waves. The quantum dot is formed by the 4 gates on the left and controlled with the voltages of the red and green gates. A QPC on the bottom allows to measure its charge state. The large blue gates form an elevated channel which is depleted of electrons. **(b)** Stability diagram of the quantum dot from (a) when $V_L$ (green gate) and $V_R$ (red gate) are varied. The QPC current is derived with respect to $V_L$ and encoded by the color scale to the right. The white arrow indicates the sweep direction of the gate $V_L$. The number of electrons trapped in the dot when the coupling to the reservoir is negligible is indicated on the diagram and the different regions separated by dashed lines. In the lower part, the electron configuration is indicated as $(N_L,N_R)$, with $N_L$ ($N_R$) being the number of electrons in the left (right) quantum dot. Figure adapted from the thesis of B. Bertrand.[141] **(c)** Electrostatic simulation of the potential profile with comparable gate voltages as in the experiment from Fig. 3.2. The quantum dot position is clearly visible as a circular blue region separated from the reservoir. **(d)** Potential profile along the dashed white line in (c) for a gate configuration where the quantum dot is well coupled to the reservoir. **(e)** Same potential cut as in (d) but for a gate configuration that corresponds to an isolated regime.

Interestingly when $V_L$ is increased further, faint white lines with a different slope than the charge degeneracy lines and of much lower amplitude are observed. The number of the white lines with comparable slope in a region is observed to be equal to the number of electrons isolated in the system. When the voltage on the channel gates $V_{Ch}$ is made more negative, these lines move to more negative values of $V_L$ (data not shown). The sign of the QPC change indicates that an electron moves away from the QPC. As the connection to the left reservoir has been cut, the only possibility is a displacement towards the channel formed by the blue gates. This assumption is consistent with the voltage dependence on $V_{Ch}$, as this voltage changes the potential energy of the channel.

The calculated potential generated by the gates in the measurement position is plotted in Fig. 3.2(c) to illustrate the alternate position for the electrons. The potential cut along the white line is shown in Fig. 3.2(d,e) for two different voltages on $V_L$. For $V_L = -0.4\ V$, the left dot potential minimum is below the Fermi energy and the barrier separating it from the reservoir is thin. Above the Fermi energy in the channel a small potential minimum is visible, which is located to the right of the red gate in Fig. 3.2(a). As the voltage on $V_L$ is moved to more negative values, the potential barrier to the reservoir becomes higher and thicker. At the same time, the two minima ultimately align and form a double dot separated by a barrier located at the red gate. This underlines our assumption that in the isolated regime electrons can move into the channel and that effectively a double dot is formed with the separation controlled by $V_R$.

To get an intuition of the expected charge configurations in the isolated regime, we derive the emergence of the isolated subspace from the conventional charge stability diagram of a double quantum dot. A typical charge stability diagram in the regime of good coupling to the reservoirs is shown in Fig. 3.3(a). It can be obtained using the constant interaction model including a capacitance between the two dots and has also been measured many times in experiments.[61] The charge transitions are shown in blue and the electron occupation numbers are indicated in each region. Between two regions of equal total electron number, the inter-dot capacitance opens up a small gap for an inter-dot transition that is not mediated by electron exchange with the reservoirs (orange). Instead the exchange across this degeneracy is related to an inter-dot tunnelling event. When however the connection to the electron gas is cut, the blue charge transitions are no longer possible and the only way for electron reorganisation is via inter-dot exchange. For the case of one electron this has to result in only two possible charge regions (0,1) and (1,0) as shown in Fig. 3.3(b). Here the stability diagram is split perpendicular to the detuning axis by a single charge degeneracy line (red) that identifies the inter-dot transition. Initializing the system with a different total electron number will result in a different subspace of available regions. The

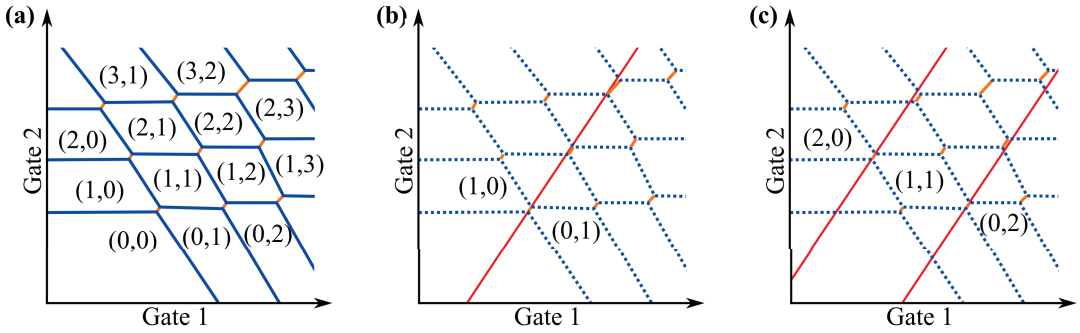


**Figure 3.3:** Schematic of double dot diagrams and the effect of the isolation from the reservoirs. **(a)** Standard double dot stability diagram. The charge degeneracy lines are coloured in blue, while the inter-dot couplings are coloured in orange. The charge occupancies of the two dots L/R are indicated for every region as ($N_L$,$N_R$). **(b)** Same stability diagram as in (a), but reduced to the isolated regime with 1 electron. The blue charge degeneracy lines are no longer available and therefore only the red inter-dot charge transition between (1,0) and (0,1) will be visible. **(c)** Similar diagram as in (b), but for the case of 2 electrons. The diagram reduces to two straight inter-dot transitions (red) that separate the 3 only available configurations (2,0),(1,1) and (0,2).

two-electron case is shown in Fig. 3.3(c) and reveals two straight lines (red) separating the three possible charge configurations (2,0), (1,1) and (0,2). The diagram therefore simplifies greatly and depends only on the initial number of electrons.

To probe this isolated dot, the electron number has to be properly initialised. In Fig. 3.4 a charge stability diagram for positive voltages on $V_L$ is shown. In this position the tunnel rate to the reservoir becomes comparable to the measurement time. This can be identified by the stochastic nature of the charge degeneracy lines. For more positive values of $V_L$, the coupling to the reservoirs becomes larger and the tunnel-rate is on the order of several MHz meaning that an electron can tunnel in and out of the dot within a few microseconds. When we therefore wait in one of the three indicated positions $L_1$, $L_2$ or $L_3$ for a time longer than the tunnelling time, the system will be initialized to 1, 2 or 3 electrons respectively. To now isolate the initialized electron we apply a fast gate pulse on the barrier gate $V_L$ along the white arrow with a rise time of $\approx 2$ µs. As the system passes the charge degeneracy line at a point where the tunnelling time is several milliseconds, the electron has no time to leave the dot and becomes more and more strongly decoupled from the reservoir as $V_L$ is increased. At position A the electron is already well isolated and we can now choose any voltage $V_R$ followed by a sweep on $V_L$ to generate a stability diagram of the isolated configuration.

The resulting stability diagrams for electrons initialized in $L_1$ and $L_2$ are shown in Fig. 3.5. We used the procedure outlined above and reinitialized the electron number after

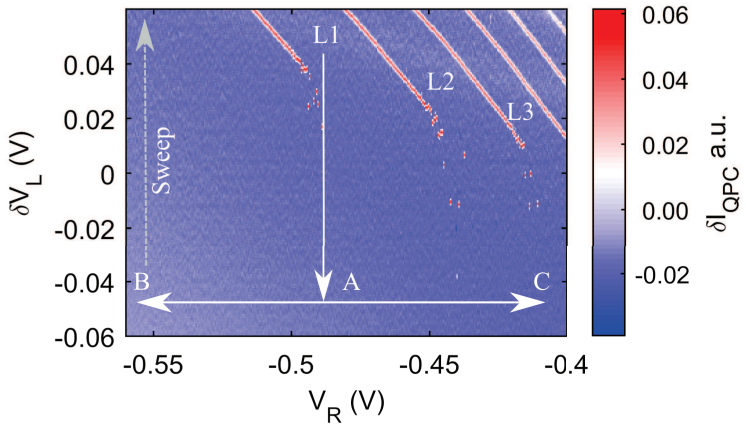


**Figure 3.4:** Measurement protocol to obtain a stability diagram of the isolated system illustrated on a stability diagram taken close to the position where the tunnel rate to the reservoir becomes comparable to the measurement time. Derivative of the detector current with respect to $V_L$ as a function of $V_L$ and $V_R$. $V_L$ is swept from more positive values to more negative values. Electrons can be first initialized in the positions $L_1$,$L_2$ and $L_3$ to a fixed electron number (1,2,3) within a few microseconds. A voltage pulse on $V_L$ raises the electrons in energy up to the channel and disconnects the dot from the reservoir. In this position $V_R$ is adjusted to values between B and C followed by a sweep on $V_L$ to construct a stability diagram of the isolated configuration with fixed electron number.

every sweep of $V_L$ from negative to positive values (indicated by arrow). For initialization in $L_1$ we expect a single electron in the dots and therefore expect a single charge degeneracy line as in Fig. 3.3(b). Indeed, in Fig. 3.5(a) we see a single line in the bottom of the diagram which is almost parallel to the $x$-axis at $V_L \approx -0.73$ V. The blue color indicates, that the electron comes closer to the QPC. It is therefore interpreted as the transition from the charge configuration (0,1) to (1,0), where the electron enters the dot closer to the reservoir. When $V_L$ is made more positive again, the system gets progressively reconnected to the reservoirs and electrons are leaving the quantum dot (stochastic red dots on the left) for negative voltages of $V_R$. For more positive values of $V_R > -0.45$ V, blue stochastic events are observed, indicating additional electrons entering the quantum dot. For the case of more negative $V_L$ these processes are however forbidden and lead to the observation of only the single inter-dot exchange line over a large area of the parameter space. We can therefore conclude, that the quantum dots are disconnected from the leads as long as $V_L \ll -0.55$. In this parameter region we can treat the system as an isolated double dot with only two possible charge configurations for the trapped electron. These configurations are separated by a single inter-dot exchange line that is clearly visible in the stability diagram.

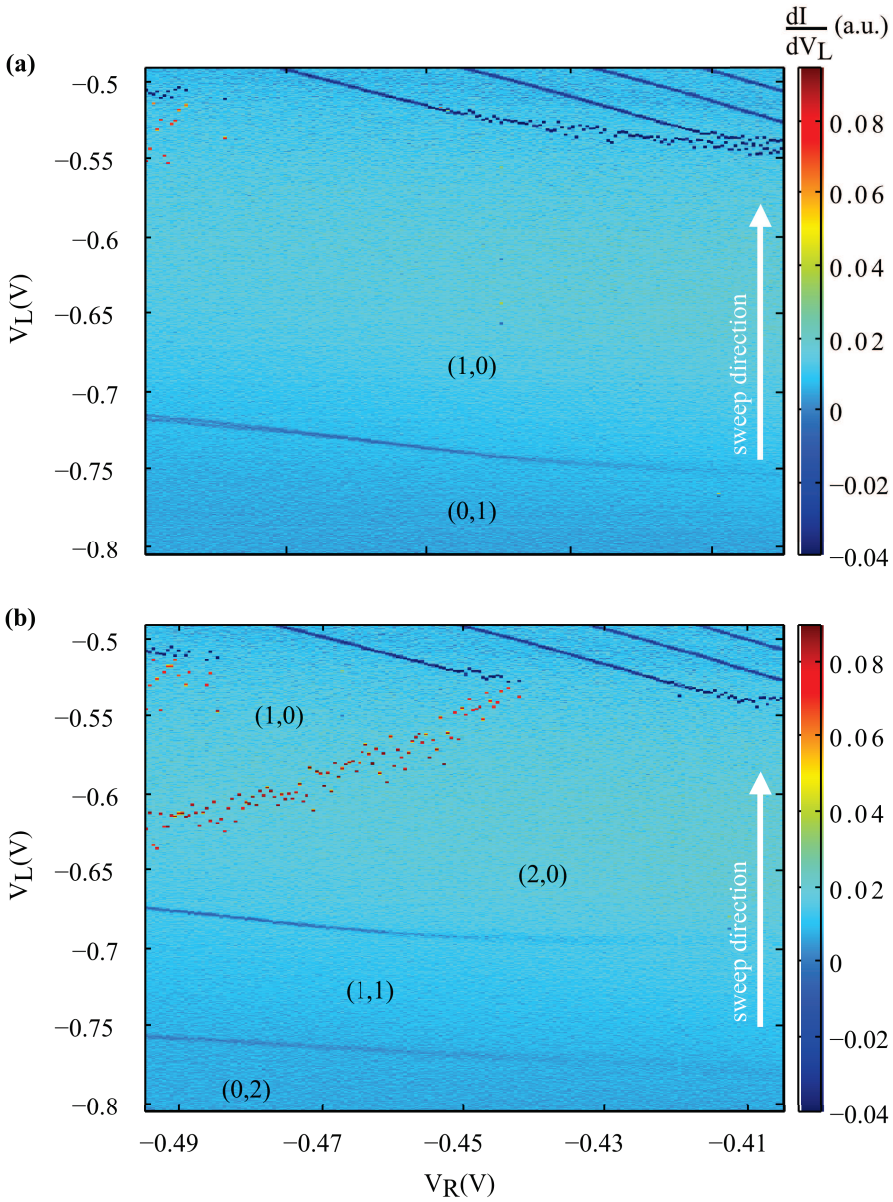


**Figure 3.5:** Stability diagrams obtained using the procedure outlines in Fig. 3.4. Derivative of the detector QPC current as a function of $V_L$ and $V_R$. At $V_L = -0.8$, $V_R$ is adjusted to a position given by the diagram's limits and then $V_L$ is swept to more positive values.**(a)** Case of a single electron initialized in the dot close to the reservoir and then isolated from the electron gas. **(b)** Same stability diagram as in (a) but for the case of two electrons initialized in the dot.

The shape of the inter-dot exchange line is observed to not be uniform across all values of $V_R$, but seems to broaden and faint for more positive values. The slope of the line is almost parallel to the $x$-axis, which means that $V_R$ affects the chemical potential of both dots almost equally. These features can be explained with the position of the gate corresponding to $V_R$ with respect to the two quantum dot locations. The potential simulation revealed that it is located between the two potential minima. The voltage on $V_R$ will therefore influence the height of the potential barrier between the dots and/or their spatial separation, but not their detuning. When $V_R$ is made more positive, the potential barrier will then decrease resulting in an increased tunnel-coupling. As the tunnel-coupling becomes stronger than the energy associated with the temperature $k_BT \approx 8$ µeV, it will induce a notable broadening of the charge degeneracy line. This effect is observed for $V_R \approx -0.43$ V revealing a trivial way to change the tunnel-coupling parameter during an experiment, which we will use later for spin manipulations. The coupling can also be increased to be on the order of GHz and allows to perform operations within the coherence time of electron spins.

The case of initialization with two electrons in the left dot is demonstrated in a stability diagram in Fig. 3.5(b). After initialization in $L_2$, the same diagram as before is taken, first varying $V_R$ and then sweeping $V_L$ from negative to positive values. Here two parallel lines on the bottom of the diagram are observed, which are again identified as the transitions from the left to the right dot based on the polarity of the signal. They correspond to the configurations (0,2), (1,1) and (2,0) and are located symmetrically around the previous (0,1)-(1,0) transition.

For more positive values of $V_L$ in the (2,0) region, a dotted red line appears which ends at the charge degeneracy line of the transition (2,0)-(1,0). This line indicates loss of one electron to the reservoir. Towards the upper-left, the reservoir barrier becomes too low to trap both electrons and one electron is lost with a characteristic time close to the measurement time. Towards the lower-right of the stochastic line, the electrons become more decoupled from the reservoir and the electron number is conserved. The electron loss line is therefore the boundary of the isolated regime with fixed electron number. The slope of the electron loss line hereby gives information about the relative effect of the two gate voltages on the height of the barrier to the reservoir and the potential of the quantum dots.

In conclusion, these measurements demonstrate the isolation of electrons from the reservoirs for the case of two tunnel-coupled dots. Clean measurements of the resulting charge stability diagrams were presented, probing the reorganisation of the charges for the case of one and two electrons. The isolation from the reservoirs drastically reduces the complexity of the system. Full control of a double quantum dot system in a large gate voltage space is demonstrated. Additionally, easy access to the tunnel-coupling with

a simple variation of a single gate corresponding to $V_R$ was revealed. This effect will be probed more quantitatively in Chapter 4 and used to perform coherent exchange of one quantum of spin between two electrons.

## 3.5 A linear triple-dot chain in the isolated regime

Given the obvious advantages in reduced complexity, we wanted to apply the isolated manipulation scheme to a multi-dot system that had already been investigated in our group. R. Thalineau had already shown that his quadruple dot design can be brought into a circular coupling regime.[108] Due to an improved fabrication processes it was possible to fabricate an enhanced design with 4 additional gates as shown in Fig. 3.6(a). The new gates are shown in green and act mostly on the chemical potential of the quantum dot. The blue gates define the dot shape, chemical potential and the connection to the reservoir. The red gates are responsible for separating the 4 charge traps and should therefore allow to tune the inter-dot tunnel-coupling. Four QPC gates (violet) each define a constriction that can act as a charge sensor.

Sadly though all measured samples exhibited a 5th dot in the center of the structure when the red gates were not made very negative. On the other hand, for gate configurations where the center dot was unfavourable, the inter-dot couplings were found to be very low. A more concise analysis of the circular coupling situation is given in Appendix C.2.

In this section we will instead focus on the case where the center potential minimum is used to form a linear chain of quantum dots. The approximate positions of the quantum dots in the device are emphasized by white circles in Fig. 3.6(a). This chain will be brought into the isolated regime and the control over the charge state in the linear triple dot is demonstrated. It will be shown that in the isolated regime, the path of the electrons in the device can be easily controlled. Finally, a model for the analysis of our measurements is discussed and used to extract quantitative information about the quantum dots.

### 3.5.1 Regime of a linear chain of quantum dots

A linear chain of quantum dots can be constructed in the investigated device by forming an asymmetric trap with the gate potentials. This situation can be obtained by increasing the voltage of the top and bottom barrier gates (blue in Fig. 3.6). The upper and lower dot will then be made unavailable in energy. This leads to the definition of a linear array of quantum dots that are oriented along the $x$-direction. An electrostatic simulation of this configuration is shown in Fig. 3.6(b). The cut along the black dashed line in the inset of Fig 3.6(b) reveals the distinct minima along a straight line with the center dot in the middle.

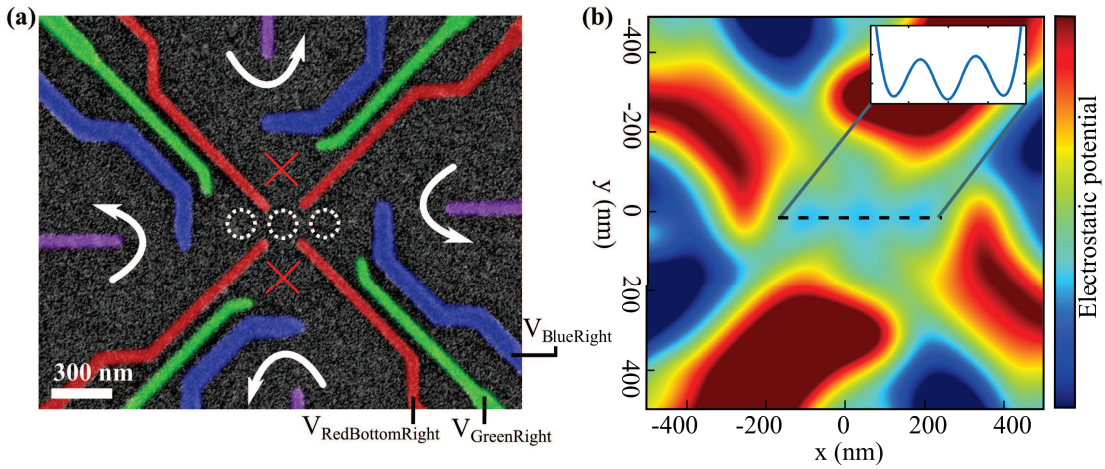


**Figure 3.6:** **(a)** False color SEM image of the fabricated sample design. The tunnel gates are colored in red, the barrier defining gates in blue and the added plunger gates are colored in green. The QPCs are defined by the violet gates. The expected dot positions are indicated by dashed white circles. **(b)** Electrostatic simulation of the sample in (a). The coloring encodes the potential height as shown on the bar to the right. Red corresponds to high potential while blue corresponds to low potential. The inset shows the potential profile along the black dashed line.

To transform the system into an isolated chain, first the energy of the quantum dots is raised above the Fermi energy, so that no electron is left in the structure. The tunnel-barriers to the 2DEG on the left, bottom and top are closed by applying negative voltages on the blue barrier gates. This leads to an isolated situation, where electron exchange with the reservoir is only possible in the right dot. The right barrier can then be controlled to pump electrons from the 2DEG into the isolated quantum dot system.

This situation is achieved in Fig. 3.7 where for positive voltages of the right barrier gate $V_{\mathrm{BlueRight}}$, the right quantum dot is still well coupled to the leads and shows clear charge degeneracy lines. The right quantum dot is then prepared at $V_{\mathrm{BlueRight}} = -0.5$ V for different voltages of the right plunger gate $V_{\mathrm{GreenRight}}$. A microsecond pulse to $V_{\mathrm{BlueRight}} = -1.1$ V isolates the quantum dot from the electron gas and prepares an electron number that depends on $V_{\mathrm{GreenRight}}$. When $V_{\mathrm{BlueRight}}$ is now swept in the indicated direction, we observe straight parallel lines similar to the isolated double dot in the previous chapter. For more positive values of $V_{\mathrm{BlueRight}}$, dotted red lines become visible corresponding to the stochastic loss of electrons to the reservoir when the barrier becomes too low. The diagram can therefore be interpreted as the measurement of an isolated double dot, where the number of parallel lines give the number of electrons inside the structure after loading. The electrons are hereby transferred to the center dot. The left quantum dot is found to be unavailable

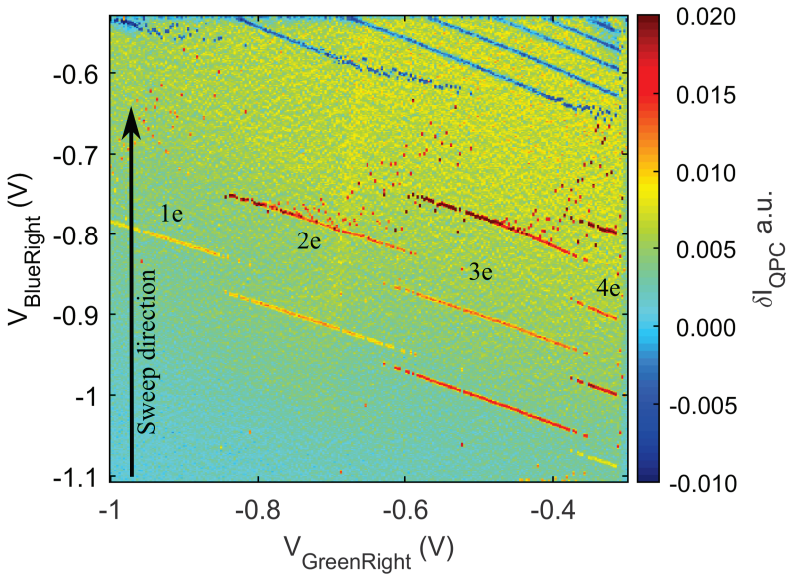


**Figure 3.7:** Stability diagram for the right dot with a loading step in the beginning. Derivative of the left QPC current with respect to $V_{\mathrm{BlueRight}}$ as a function of $V_{\mathrm{BlueRight}}$ and $V_{\mathrm{GreenRight}}$. First the plunger voltage $V_{\mathrm{GreenRight}}$ is adjusted and then the barriers is opened for 20 ms at $V_{\mathrm{BlueRight}} = -0.5$ V. This is followed by a microsecond pulse to $V_{\mathrm{BlueRight}} = -1.1$ V to isolate the right quantum dot from the barriers. $V_{\mathrm{BlueRight}}$ is then swept in the indicated sweep direction. As $V_{\mathrm{GreenRight}}$ is adjusted before the isolation, this leads to a different number of electrons loaded into the dot (illustrated in the diagram by 1e, 2e, 3e and 4e) along the diagram.

in energy in this situation, which is consistent with the large negative voltage applied on the left blue barrier gate $V_{\mathrm{BlueLeft}}$.

Contrary to the case of the previous section, the polarity (color) of the current jump observed for the isolated inter-dot transition is now inverse. This is due to the fact that the diagram is taken with the left QPC which is closer to the center dot than to the right dot. Consequently it detects a rise in current when the electron moves from the center to the right dot.

Similar to our previous measurements it is also possible to isolate a fixed electron number following the procedure outlined already in Fig. 3.3. Starting with two electrons in the right quantum dot, the electrons are again isolated by pulsing $V_{\mathrm{BlueRight}}$ to more negative values. Then, $V_{\mathrm{GreenRight}}$ is adjusted and $V_{\mathrm{BlueRight}}$ is varied from negative to more positive values. The resulting stability diagram is shown in Fig. 3.8(a). It shows two distinct parallel lines in the full isolated configuration space. The dot occupation numbers that follow from the tunnelling processes were added to the graph to illustrate the position of each electron.

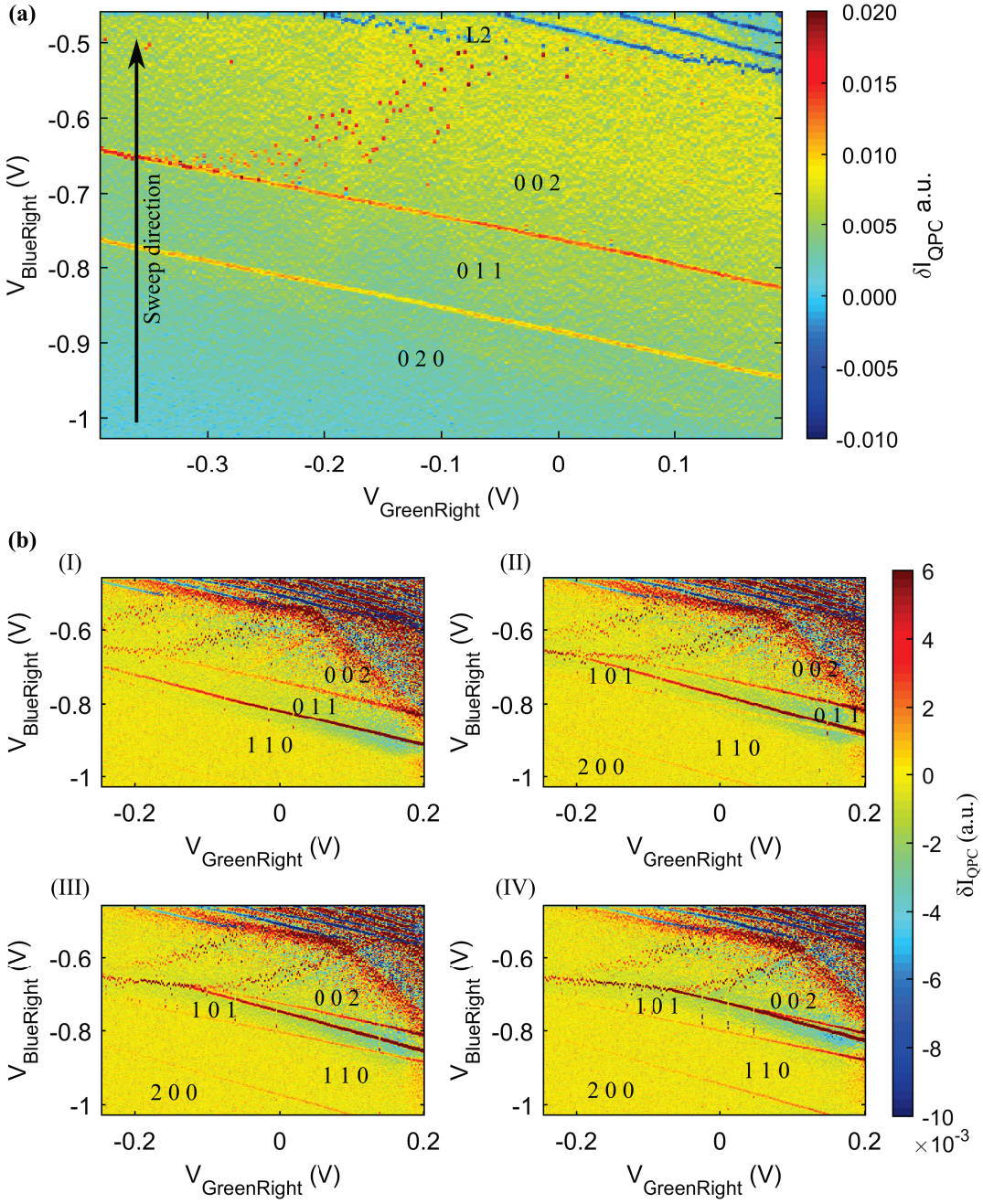


**Figure 3.8:** **(a)** Stability diagram of the isolated triple dot with 2 electrons loaded before the sweep of $V_{\mathrm{BlueRight}}$ as a function of $V_{\mathrm{GreenRight}}$. The derivative of the left QPC current with respect to $V_{\mathrm{BlueRight}}$ is encoded by the colorbar. **(b)** Gradual change along (I)-(IV) of the respective energy of the third dot with 2 electrons loaded into the isolated system exemplified on stability diagrams taken with $V_{\mathrm{BlueRight}}$ and $V_{\mathrm{GreenRight}}$. We can clearly see two new parallel lines move with respect to the measurement from (a) as the potential of the third dot is decreased. The respective electron configuration is indicated for the different regions assuming a chain of dots.

The diagram resembles the previously measured double dot diagram in Fig. 3.5 but features fixed width of the inter-dot exchange line. We therefore deduce, that the swept gates only affect the chemical potential of the dots and not their tunnel-coupling. In this case the tunnelling time is adjusted to be shorter than the measurement time, but not important with respect to temperature broadening. We can also conclude that in this sample it is possible to reach the regime of an isolated double dot with very similar characteristics to the previously measured sample.

A second observation is that the dotted line, which was previously identified as electron loss to the 2DEG, stops at the first inter-dot crossing. Thus, the condition for electron loss is only fulfilled when two electrons are present in the right quantum dot. Indeed, electrons that enter the right quantum dot have to occupy a state that is higher in energy than the other electrons. As a result, the last electron has a higher probability to tunnel to the reservoir and in this case is immediately lost. The tunnel-barrier height requirement to preserve the isolated state therefore depends on the electron number. Additionally, we note that electron loss only occurs via the reservoir connection of the right dot.

In the next step, the potential of the left dot was adjusted to align with the potential of the center dot. Fig. 3.8(b) shows a variation of the left dot energy after it had already been lowered compared to the measurement in Fig. 3.8(a). The left dot energy is decreasing along the different stability diagrams from (I) to (IV). We observe that a new set of two parallel lines with slightly different slope have appeared on the diagrams. With decreasing energy of the left dot, they move up on the diagrams. This means that it becomes easier to shuffle electrons from the center into the left dot when decreasing the gate voltage $V_{\mathrm{BlueRight}}$. The respective dot occupation numbers can be inferred from the slopes of the inter-dot charge degeneracies. They were added to the graphs assuming a linear chain of dots following the scheme (Left,Center,Right). While decreasing $V_{\mathrm{BlueRight}}$, the electrons are one by one first moved to the center dot and then to the left. Indeed, the gates on the right affect the right and center dots strongly, but are only weakly coupled to the left dot. All three quantum dots have been made available for charge transfer in the isolated regime. The resulting diagrams allow clear discrimination of the electron positions. The charge configuration can hereby be deduced from the efficiency of potential variation of the electrostatic gates and their geometric position.

### 3.5.2 Stability diagrams of the isolated triple-dot chain

Using one of the tunnel gates (red color, bottom right of Fig. 3.6), the potential of the center dot can be changed more independently to access the full configuration space. Such diagrams for different numbers of electrons are shown in Fig. 3.9. Different numbers of

electrons were initialized in the different diagrams to demonstrate the degree of control in such a system. We start by analysing the dynamics of the triple dot for the simplest case of one electron.

### One electron

The stability diagram for one electron initialized in the quantum dots is shown in Fig. 3.9(a). We note only three charge configurations and three different slopes for the inter-dot exchange degeneracy lines which correspond to exchange from right to center (001)-(010), exchange from center to left dot (010)-(100) on the bottom and the direct exchange from right to left (001)-(100). The different transitions are indicated in the diagram and can be directly identified from their slope and the height of the QPC current change, which will be explicitly shown in the following.

For very positive voltages on $V_{\mathrm{BlueRight}}$, the electron is found in the loading dot on the right. The exchange from the right to the center dot (001)-(010) corresponds to the slope that is almost unaffected by the value of the varied tunnel gate (red gate on the bottom right in Fig. 3.6(a)). This finding signifies that the potential energy of the two dots is equally affected upon variation of $V_{\mathrm{RedBottomRight}}$. At the same time this gate has a severe effect on the tunnel barrier between the two dots. We deduce this from the gradual broadening of the inter-dot exchange line when $V_{\mathrm{RedBottomRight}}$ is made more positive, as the energy associated with the tunnel-coupling becomes comparable to $k_B T$ ($\approx 8$ µeV) at $V_{\mathrm{RedBottomRight}} \approx -0.53$ V.

The inter-dot exchange line corresponding to a transition from the center to the left dot (010)-(100) can also be identified from its slope. As neither of the two varied gates should have a sizeable effect on the potential of the left dot and as $V_{\mathrm{BlueRight}}$ should only weakly affect the center dot, this transition should be mostly mediated by $V_{\mathrm{RedBottomRight}}$. The width of the inter-dot exchange line is also largely unaffected by either of the two gates and remains sharp across the diagram. This independence of the tunnel-coupling on either gate-voltage is also expected from the geometric position of the gates and the location of the minima of the potential simulation.

The exchange from the right to the left dot (001)-(100) is easily identifiable by its stochastic nature. We also observe, that close to the crossing of all inter-dot exchange lines, the line becomes sharp and the exchange is no longer slower than the measurement time. Farther to the left, the line changes to a broad region where the electron tunnels back and forth as indicated by an equal number of differential conductance peaks with reverse polarity (red and blue dots) but at random intervals. We interpret this experimental finding as an indirect coupling via the center dot. Such a coupling is expected to depend

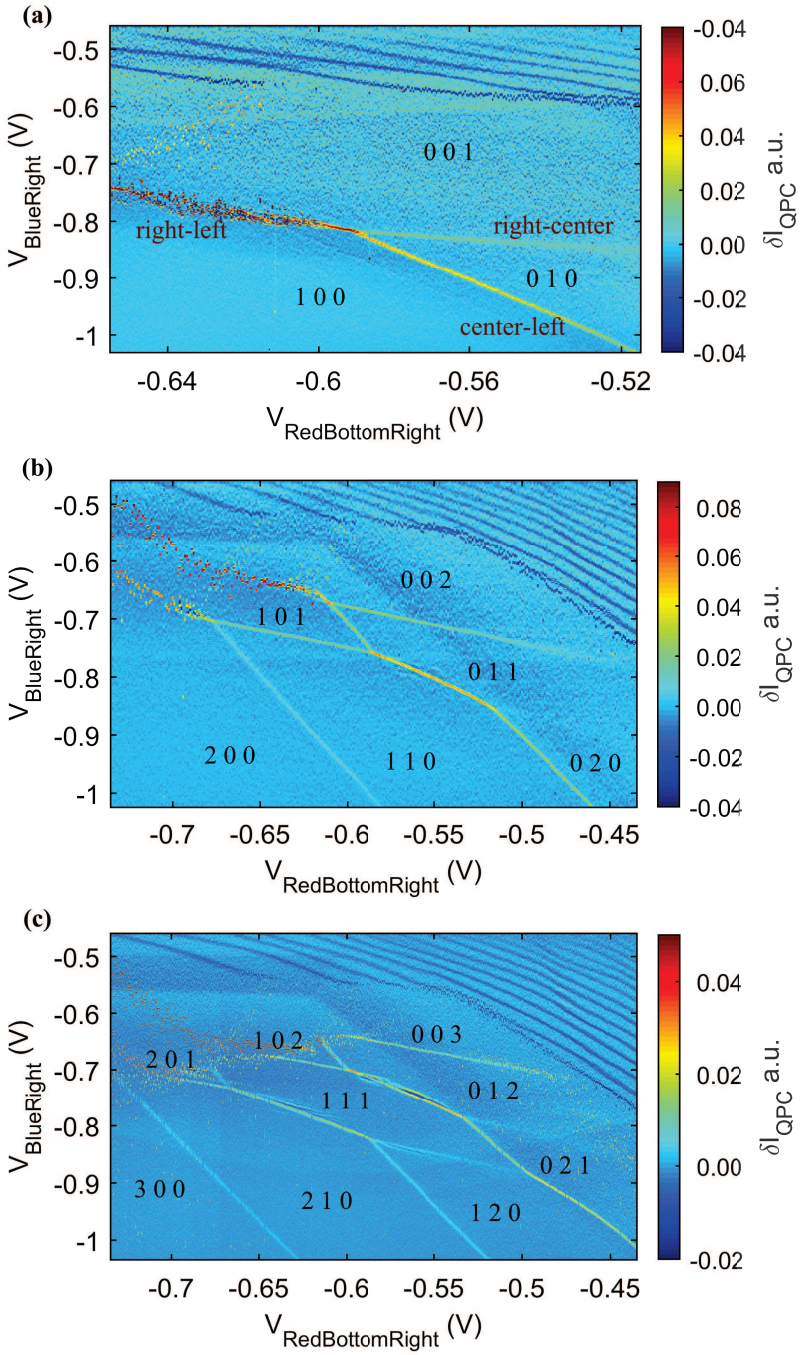


**Figure 3.9:** Stability diagrams of the isolated linear triple quantum dot for different numbers of electrons initialized in the isolation step. The derivative of the left QPC current as a function of $V_{\mathrm{BlueRight}}$ is encoded in the colorbars. After the isolation of the system, $V_{\mathrm{RedBottomRight}}$ is adjusted. Then the voltage $V_{\mathrm{BlueRight}}$ is swept from negative to more positive values to construct the two-dimensional maps. The electron occupation of the quantum dots is indicated in the graphs. **(a)** Stability diagram for one electron initialized in the dots. **(b)** Stability diagram for two electrons initialized in the dots. **(c)** Stability diagram for three electrons initialized in the dots.

on the potential position of the center dot and the two tunnel-couplings associated with this dot following

$$t_{13} \approx \frac{t_{12} \cdot t_{23}}{\Delta}, \tag{3.3}$$

where $\Delta$ is the energy separation of the center dot from the two outer quantum dots and $t_{12}/t_{23}$ are the tunnel-couplings of the center dot to the left/right dot respectively.[145] As $V_{\mathrm{RedBottomRight}}$ is made more negative, $\Delta$ increases while $t_{23}$ decreases, leading to a very strong change in the effective tunnelling rate. This agrees well with the observed dependence of the tunnel-rate with $V_{\mathrm{RedBottomRight}}$. Due to the strong variation of the coupling with $V_{\mathrm{RedBottomRight}}$, this explanation with mediated exchange is favoured over a direct exchange. The stochastic behaviour of the charge state close to the crossing is discussed in Appendix C.3. All findings support the picture of a linear chain of quantum dots with a center dot between the right and left dots. Their positions are well approximated by the location of the potential minima in the electrostatic calculation of the potential profile.

### Two electrons

The number of electrons in the structure can be increased by changing the loading position in the initialization stage. The case of two initialized electrons is shown in Fig. 3.9(b)). The resulting diagrams grow slightly in complexity, but stay clear and consistent with the first measurement. Specifically, we observe six different charge configurations separated by inter-dot exchange lines with the same three slopes as in the one electron case. The electron configuration can be inferred by an analysis of the slopes of the transitions that were crossed from the initialization in (002). The resulting configurations are given in the diagram. In addition to the three regions of both electrons in one of the three quantum dots, we observe three distinct configurations where the electrons are split between the quantum dots. The split configuration (101) for relatively negative values of $V_{\mathrm{RedBottomRight}}$ is not very well protected against electron loss. There exist two slopes and colors for the loss events, corresponding to electron loss to the left and to the right reservoirs respectively. The left dot is closer to the measuring QPC, which results in the higher conductance change associated with the deep red color. We can therefore discriminate two paths for electron loss via different barriers depending on the slope of the electron loss lines or the size of the current change.

### Three electrons

For the case of three electrons shown in Fig. 3.9(c)), the diagram develops a central hexagonal structure which identifies the case of equal electron distribution across the three quantum dots (111). While it is still possible to fill each quantum dot with the maximum number of three electrons, we observe that the split configurations with an empty center dot have become increasingly unfavourable. The high potential in the center does not allow for a good compromise in gate voltages, that keeps the electrons in the quantum dots. Also, the high coupling between the center dot and the right dot results in barely visible exchange lines on the right of the diagram. It was difficult to improve the situation due to the strong influence of the tunnel gates on the center dot's energy as well as its coupling to the two outer dots.

However, the different configurations are still clearly separated and allow the full identification of the different regions. From the three measured diagrams we can clearly see, that different numbers of electrons can be transported into arbitrary configurations using only two gates. The different regions are clearly separated by inter-dot exchange lines that are associated with one electron movement through a specific barrier, allowing full control over the path of every single electron. The observed charge dynamics will allow to improve future device designs to be immune to electron loss and have fully tunable inter-dot couplings, which will be demonstrated at the end of this chapter.

## 3.6 Simulation of the charge diagrams with the constant interaction model

For a validation of our analysis and a quantitative understanding of the measured data, we wanted to replicate the experimental data with the constant interaction model of a triple quantum dot. The basic principles and constraints of the constant interaction model were already outlined for a simple system in 1.3.1. We now apply it to the triple quantum dot in the isolated regime.

A rough model of the situation is schematically shown in Fig. 3.10. To reduce the complexity, only one gate independently coupled to each quantum dot is shown, while in reality every gate affects the energy of each dot. The full derivation for the system is made in Appendix A.1. Here we will only consider a simplified system that neglects inter-dot capacitive coupling between the quantum dots and therefore set $C_1 = C_2 = C_3 = 0$. This approximation is valid in the limit of low inter-dot coupling, where the charging energies of the different quantum dots dominate the charge dynamics. The equations then reduce significantly in complexity and we end up with the sum of the three individual dot energies

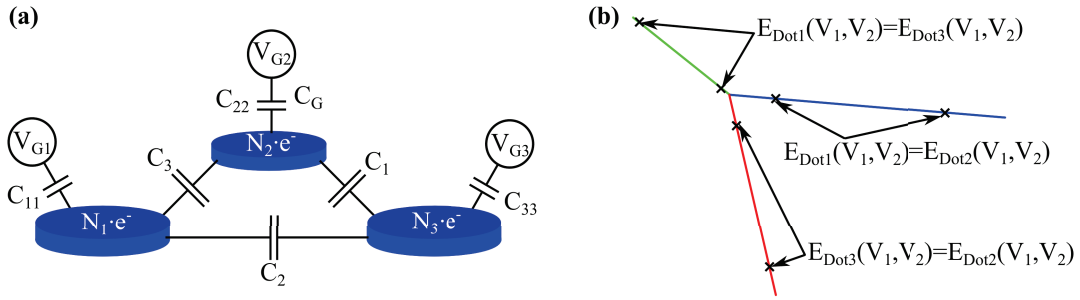


**Figure 3.10:** **(a)** Simplified scheme of the triple dot in the constant interaction model. The charge islands (dots) are coupled by the capacitances $C_1$,$C_2$ and $C_3$, which can be varied to go from a linear to a triangular configuration. Each dot is coupled to gates (only one gate per dot is shown here) with different voltages $V_{G1}$,$V_{G2}$ and $V_{G3}$. **(b)** Schematic of the determination of the coupling parameters $\alpha_{xj}$ from the isolated stability diagram. The inter-dot transitions are colored differently and for each slope we take two points for which the energy of the involved dots has to be equal.

$$E_k = \sum_x \frac{\{\sum_j C_{xj} V_j + [k_x - N_0]e\}^2}{2C_{sum}}, \tag{3.4}$$

where the index $x$ specifies the respective dot and the index $j$ the respective gate. $k$ is a specific configuration of electrons for which we calculate the energy $E_k$ and gives the number of electrons in each dot. However, the gate capacitances $C_{xj}$ and the sum of all capacitances connected to a dot $C_{sum}$ are not directly measured in the experiment. Instead the energy needed to add an electron $E_C = \frac{e^2}{C_{sum}}$ and the effect of a gate voltage on the respective quantum dot energy $\alpha_{xj} = e\frac{C_{xj}}{C_{sum}}$ are measured.

In general, extracting these energies usually requires a reference energy scale. One way is to measure the size of coulomb diamonds as a function of applied bias in transport measurements.[59] The bias window can then be used to directly quantify the gate efficiency $\alpha_{xj}$ or the charging energy $E_C$. Another way is to induce level transitions via microwave excitation with a reference frequency.[146] This photon assisted tunnelling (PAT) process also provides a direct energy scale via the photon energy. Such a measurement in the isolated regime is presented in Appendix C.4.

In this section we will however fix one of the gate coefficients $\alpha_{xj}$ to an approximate value consistent with PAT measurements and then determine the other parameters from an investigation of the measured stability diagram. First, we rewrite Eq. 3.4 for the energy

of a charge configuration in terms of $\alpha_{xj}$ and the respective charging energies $E_{C,x}$

$$E_k = \sum_x \frac{1}{E_{C,x}} \{\mu_x + [k_x - N_0] E_{C,x}\}^2, \tag{3.5}$$

where the summation is again over all dots $x$ and

$$\mu_x = \sum_j \alpha_{xj} V_j \tag{3.6}$$

is the influence of the gates $j$ on the respective dot energy as given by the gate voltages $V_j$ and the coefficients $\alpha_{xj}$.

Second, we bound the coefficients by equations derived from the direct evaluation of the stability diagram. A schematic of the process is shown in Fig. 3.10(b). For each crossing we obtain an equation for the equality of the involved dot energies. Then the slope of each charge degeneracy is directly connected to the gate capacitances. The extracted slopes that were used for the following calculations are given in the upper part of Table 3.1. We end up with only three equations for 6 variables and therefore we have to guess three of them to construct a stability diagram. We choose $\alpha_{\text{BlueRight,right}} = 0.05$ and neglect any influence of the gates on the left quantum dot $\alpha_{\text{BlueRight,left}} = \alpha_{\text{RedBottomRight,left}} = 0$ and then obtain the values given in the lower part of Table 3.1. Even though these coefficients may not be perfectly accurate, they allow us to model the system and observe the influence of unequal charging energies, inter-dot capacitances and other effects on the resulting stability diagram.

Finally, we have to calculate the energies of the charge configurations according to Eq. 3.5 for all different configurations $k_x$ and find the one with minimal energy to reconstruct the stability diagram. A Matlab function that implements this calculation and finds the configuration with minimal energy is given in Appendix A.2.

For the one electron case, the charging energies of the quantum dots are not needed to replicate the stability diagram and we can therefore test our system using this case. The output of the simulation of one electron in three quantum dots is shown in 3.11(a) and agrees well with the measured data in Fig. 3.9(a).

For two or more electrons in the system, the charging energies of the quantum dots are necessary to obtain quantitative agreement. To determine them, we measure the distance (in voltage space) of the 4 charge degeneracy crossings for the two-electron case for the

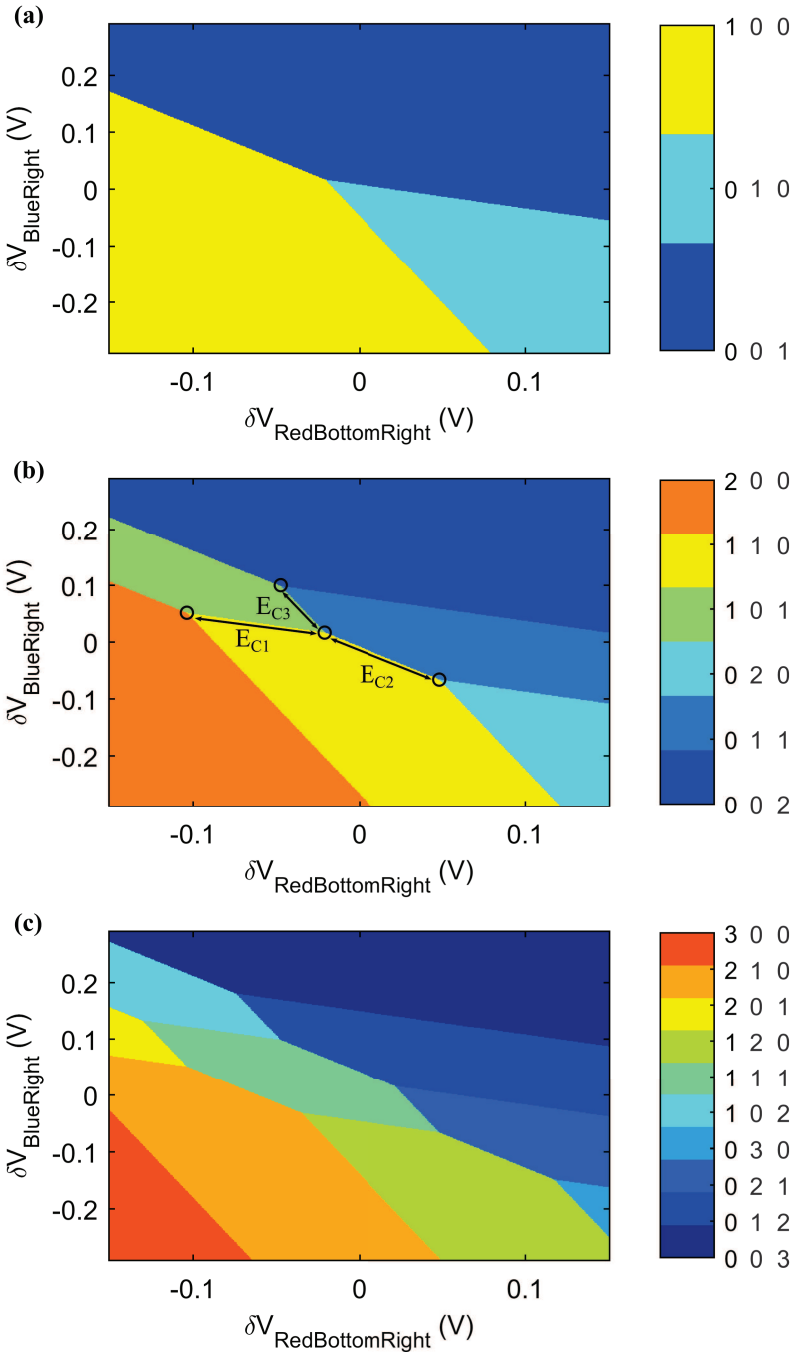


**Figure 3.11:** Simulation of the isolated triple dot stability diagram based on the constant interaction model of Eq. 3.5. The necessary constants are given in Table 3.1. The color encodes the electron configuration with minimal energy. The Matlab function used for the calculation is given in Appendix A.2. **(a)** Stability diagram for one electron. **(b)** Stability diagram for two electrons. The position of the charge degeneracy crossings and the measured distances for the calculation of the charging energies are indicated by black circles and arrows respectively. **(c)** Stability diagram for three electrons.

| | Right-Center | Center-Left | Right-Left |
|---|---|---|---|
| Measured slope | -0.60 | -3.45 | -1.37 |
| | $\mathrm{QD}_{left}$ | $\mathrm{QD}_{center}$ | $\mathrm{QD}_{right}$ |
| $\alpha_{\mathrm{BlueRight}}$ $(e)$ | **0** | 0.0147 | **0.05** |
| $\alpha_{\mathrm{RedBottomRight}}$ $(e)$ | **0** | 0.04527 | 0.06 |
| $E_C$ (meV) | 2.43 | 2.1 | 2.6 |

**Table 3.1: (Upper)** Slopes extracted from the measured diagram for the determination of the coefficients $\alpha$. **(Lower)** Fit-Coefficients for the replication of the stability diagram for the gate coefficients $\alpha$ acting on the three quantum dots $\mathrm{QD}_{left}$, $\mathrm{QD}_{center}$ and $\mathrm{QD}_{right}$. Note that the influence of the blue right gate on the right dot $\alpha_{\mathrm{BlueRight}}(\mathrm{QD}_{right})$ is guessed (bold). The other values follow deterministically.

simulated and experimentally obtained diagram (see 3.11(b)). As these quantities are each linearly related to one of the charging energies, we can easily determine the charging energies which are given in Table 3.1. Using these charging energies, the simulated charge stability diagrams with 2 and 3 electrons in the triple-dot system shown in Fig. 3.11(b,c) also agree quantitatively with the experimentally obtained diagrams in Fig. 3.9(b,c). We can therefore be confident in our determination of the relative constants for the gate capacitances and charging energies.

Note that we have considered the case of uncoupled quantum dots. In fact there exists a significant inter-dot capacitance between adjacent quantum dots. A Matlab function that includes inter-dot capacitances is given in Appendix A.3. Surprisingly, this addition has no influence on the geometric shape of the diagram, but results only in a renormalisation of the capacitances and charging energies. This is unlike the case of good coupling to the reservoir, where the shape of the stability diagram can change drastically when the inter-dot capacitances are varied. As we can therefore not deduce the inter-dot capacitance value from the diagram, we will not include this case in the discussion.

We could show that the measured diagrams are indeed the manifestation of a triple quantum dot with fixed number of electrons. All features are reproduced and therefore allow to use the model for the investigation of systems of more quantum dots. The diagrams can be used to extract quantitative information about the investigated system when an energy reference is given and the obtained values are consistent with previously measured values in similar systems.[59] Finally the arrangement of the quantum dots is not of particular importance for the geometric shape of the measured stability diagram. This information can only be extracted from the couplings of the gates to the energies of the quantum dots and from the magnitude of the inter-dot tunnel-couplings.

## 3.7 Full charge control of a circularly coupled triple-dot

Using the insights gained from the experiment on the linear chain of quantum dots, we decided to adjust our device to realise a triple dot that is circularly coupled with adjustable and high inter-dot tunnel-coupling.

Our fabricated sample is shown in a false color SEM image in Fig. 3.12(a). The length of the tunnel-gates (red) in the middle was increased to disfavour the formation of a center dot. Inter-dot tunnelling is now supposed to occur below the 20 nm thin gates. Additionally we added the light-blue coloured barrier definitions, that decouple the tunnel-gates from the barrier to the reservoir and allow for efficient isolation of the system. The blue curved gates shape the potential minima and define their positions, while the green plunger gates are connected to high bandwidth bias-Ts and allow fast control of the chemical potentials. Due to the increased space of the triple dot design, it was possible to add a sensing dot (violet gates) to each side of the device to improve the sensitivity of the charge detectors.

A potential simulation for realistic gate voltages is shown in Fig. 3.12(b). It reveals the clear separation of three potential minima and the absence of a center dot even for low voltages on the tunnel-gates. Relatively negative voltages on the barrier gates (light-blue) can create a high potential barrier to the reservoir without having a significant effect on the potential depth at the dot position.

The effect of the light-blue gate can be seen in the stability diagram in Fig. 3.13. Here the curved blue gate of the bottom dot is swept from positive to negative values while we vary the corresponding light-blue barrier gate. The slope of the charge degeneracy line is almost parallel to the x-axis, indicating a weak coupling of the light-blue gate to the chemical potential of the dot. However, the stochastic nature of the degeneracy lines reveals, that the tunnelling time to the reservoir is strongly affected as $V_{\mathrm{LightBlueBottom}}$ is made more negative. Electrons can therefore be efficiently loaded into the isolated position by initializing in $L_1$, $L_2$ or $L_3$ and then applying a fast pulse on the light-blue gate. A following pulse on the curved gate then raises the potential of the dot with respect to the Fermi energy while keeping the electrons confined.

Such a sequence was performed and followed by a variation of the chemical potentials of the quantum dots with two of the curved blue gates in Fig. 3.14. The cases of one and two electrons initialized in the beginning of the sequence are presented in the two resulting stability diagrams. Similar to the previous case of the linear chain of dots, three distinct charge configurations separated by three inter-dot charge degerenacy lines are observed for the case of one electron in Fig. 3.14(a). The sensing QPC is located on the right side of the sample. It therefore detects only a small signal for the electron tunnelling from the bottom

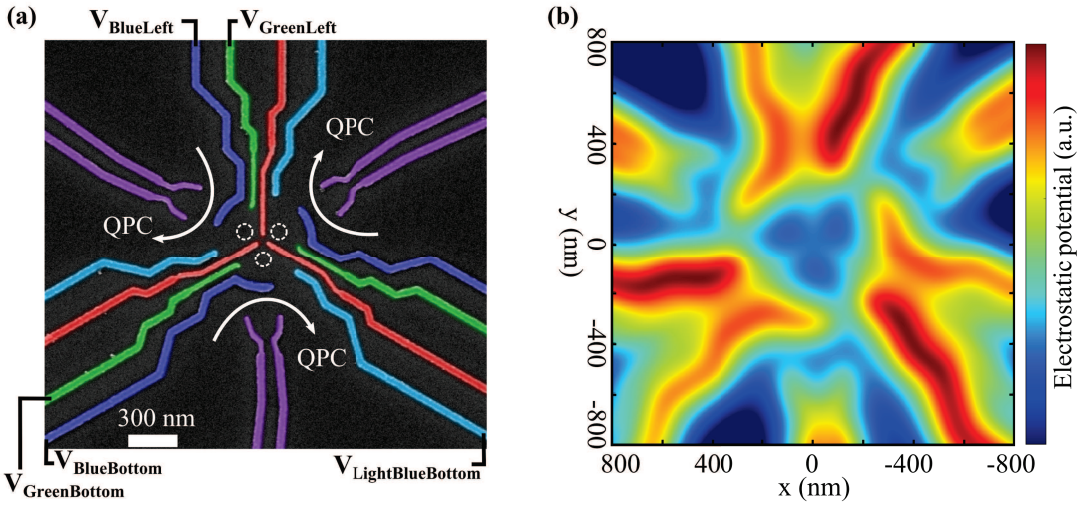


**Figure 3.12:** **(a)** False color SEM image of the fabricated triple-dot device. The suspected dot positions are indicated by white dashed circles. Three QPCs (white arrow) allow highly sensitive charge read-out of each dot and a sensing dot can be formed with the violet gates. The gates are coloured with respect to their function. **(b)** Electrostatic simulation of the potential profile of the sample in (a). The three clearly separated potential minima at the dot positions are clearly visible.

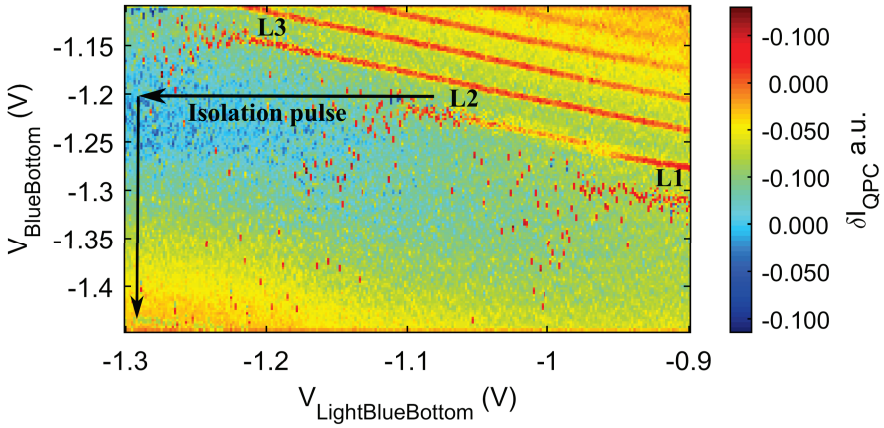


**Figure 3.13:** Stability diagram of the bottom dot with the other dots raised in potential. The sweep direction is from positive to negative voltages on $V_{\mathrm{BlueBottom}}$ after adjustement of $V_{\mathrm{LightBlueBottom}}$. The sensing QPC is on the top-right side and its derivative with respect to $V_{\mathrm{BlueBottom}}$ is encoded in the colorbar to the right. The different loading positions ($L_1$,$L_2$,$L_3$) for several electron numbers and the pulse sequence used to isolate the electrons in the case of $L_2$ are indicated in black.

to the left dot as shown by the faint blue line in the top right of the diagram. However as expected it detects a strong signal for electron tunnelling from the left to the right dot and from the bottom dot to the right dot. Unlike the case of the linear chain, all inter-dot exchange lines are sharp and show no stochastic events or broadening. This similarity of the inter-dot coupling strengths hints at the fact that the quantum dots are indeed coupled in a circle.

For the case of two electrons in Fig. 3.14(b), we see the same geometric pattern for the inter-dot charge degeneracy lines that we had already observed for the linear chain and in our simulation of the stability diagram. All exchange barriers are fast and transport in a circle is indeed possible. No electron loss events are observed, showing the effectiveness of the barrier gates on the insulation of the three-dot system. The fact that the slope of the transition from the bottom to the right dot is largely unaffected by $V_{\mathrm{BlueLeft}}$ indicates, that the involved quantum dots are symmetrically located with respect to this gate. We also observe an almost unity slope for the transition of the bottom to the left dot, affirming our assumption of the triangular placement of the quantum dots.

The same analysis of the slopes as in 3.6 was performed to replicate the measured diagrams and to obtain the relative charging energies of the quantum dots. From the three slopes of the inter-dot charge degeneracies, again three equations are obtained for the gate efficiencies $\alpha_{xj}$. The system is simplified by implying circular border conditions and we

| | Bottom-Left | Right-Left | Bottom-Right |
|---|---|---|---|
| Measured slope | 1.2848 | -3.48 | 0.22 |
| Calculated slope | **1.2848** | -3.51 | 0.22 |
| | $\mathrm{QD}_{\mathrm{Bottom}}$ | $\mathrm{QD}_{\mathrm{Left}}$ | $\mathrm{QD}_{\mathrm{Right}}$ |
| $\alpha_{\mathrm{BlueBottom}}$ $(e)$ | **0.05** | 0.0228 | **0.015** |
| $\alpha_{\mathrm{BlueLeft}}$ $(e)$ | 0.015 | 0.05 | 0.0228 |
| Charging energy (meV) | 2.4 | 2.7 | 1.7 |

**Table 3.2: (Upper)** Measured and calculated slopes of the transitions in the stability diagram for the isolated circularly-coupled triple-quantum-dot. The value of the slope for the transition from the bottom to the left dot is used for the calculation of the other two slopes (bold). **(Lower)** Coefficients $\alpha_{xj}$ for the simulation of the stability diagram. The initial guesses are emphasized in bold font. The charging energies for each dot as obtained from the analysis of the stability diagram are also given below.

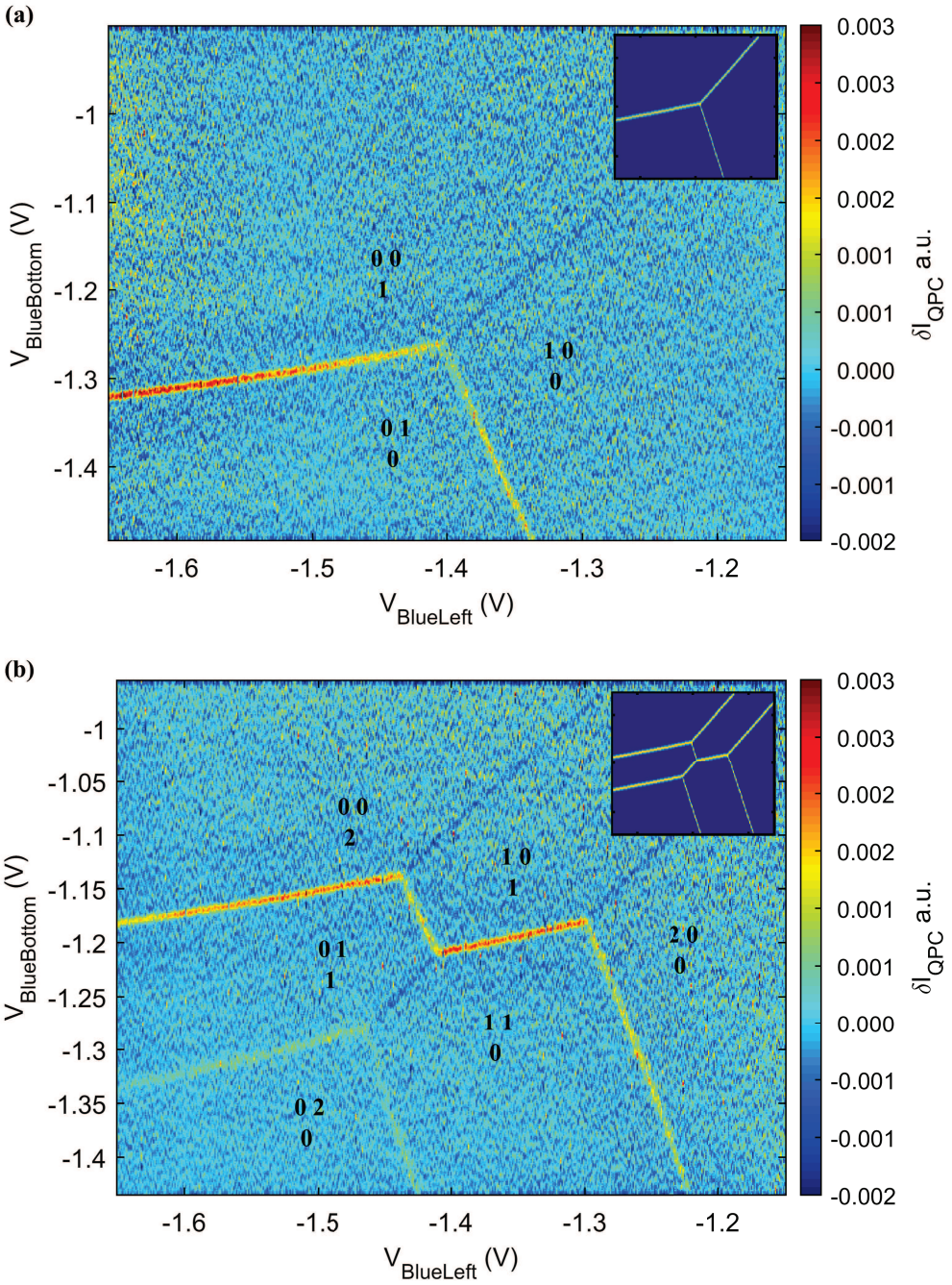


**Figure 3.14:** Stability diagrams of the isolated triple-dot after the tunnel barriers were adjusted for roughly equal coupling strengths. The derivative of the detector QPC is plotted as a function of $V_{\mathrm{BlueBottom}}$ and $V_{\mathrm{BlueLeft}}$. The sensing QPC is on the top-right side and its derivative with respect to $V_{\mathrm{BlueBottom}}$ is encoded in the colorbar to the right. The respective dot-occupation is noted for every region. The insets show the expected stability diagrams calculated with the constant interaction model using the constants given in Table 3.2. **(a)** Case of one electron initialized in the system. **(b)** Case of two electrons initialized in the system.

therefore set

$$\begin{aligned}
&\alpha_{\mathrm{BlueBottom}}(\mathrm{QD}_{\mathrm{Bottom}}) = \alpha_{\mathrm{BlueRight}}(\mathrm{QD}_{\mathrm{Right}}) = \alpha_{\mathrm{BlueLeft}}(\mathrm{QD}_{\mathrm{Left}}),\\
&\alpha_{\mathrm{BlueBottom}}(\mathrm{QD}_{\mathrm{Left}}) = \alpha_{\mathrm{BlueRight}}(\mathrm{QD}_{\mathrm{Bottom}}) = \alpha_{\mathrm{BlueLeft}}(\mathrm{QD}_{\mathrm{Right}}),\\
&\alpha_{\mathrm{BlueBottom}}(\mathrm{QD}_{\mathrm{Right}}) = \alpha_{\mathrm{BlueRight}}(\mathrm{QD}_{\mathrm{Left}}) = \alpha_{\mathrm{BlueLeft}}(\mathrm{QD}_{\mathrm{Bottom}})
\end{aligned} \tag{3.7}$$

where $\alpha_{\mathrm{x}}(\mathrm{QD}_{\mathrm{y}})$ is the influence of the gate $x$ on the quantum dot located at $y$.

The resulting system of equations is however not independent and the measurement of one slope fixes the values of the other two slopes independent of the exact values of $\alpha_{xj}$. This allows to test the validity of the assumption of circular quantum dot positions. We therefore fix the slope of the transition from the bottom to the left dot to the measured value and then find the other two slopes that are consistent with the circular border conditions. The measured and calculated values for the slopes of the inter-dot transitions from the stability diagram are given in Table 3.2. The remarkable agreement shows that the assumption of circular symmetry of gate efficiencies is valid. The quantum dots are therefore circularly placed with respect to the gate positions.

To calculate the charging energies we again fix two gate efficiencies $\alpha_{\mathrm{BlueBottom}}(\mathrm{QD}_{\mathrm{Bottom}}) = 0.05$ and $\alpha_{\mathrm{BlueBottom}}(\mathrm{QD}_{\mathrm{Right}}) = 0.015$ and obtain the values shown in Table 3.2. To determine the charging energies, we measure the distance of the charge degeneracy crossings in the two-electron stability diagram as previously introduced in section 3.6. The calculated diagrams then agree quantitatively with the experimentally obtained diagrams.

Having confirmed that the quantum dots are circularly placed and their coupling is roughly equal, we have to prove variability of the tunnel-barriers to use the triple dot system for quantum manipulation and coherent transport. Such a variation of the inter-dot coupling strength is performed in Fig. 3.15. This is exemplified by three stability diagrams taken for different configurations of the red tunnel gates. The coupling is hereby increasing from the left diagram to the right diagram. On the outer left diagram, the coupling is chosen to be lower than the measurement frequency as indicated by the dotted transitions. All transitions hereby occur stochastically at random positions in energy. In the center diagram, the coupling becomes comparable to the measurement frequency. Excitations that move an electron from one dot to the other are clearly visible as pairs of red and blue dots in the vicinity of the sharp transitions. Some exchange transitions are also doubled, hinting at the possibility of resonances with excited states.[142] Finally on the right diagram a situation is shown where the splitting associated with the coupling becomes comparable to the effect of temperature. The strongly broadened lines are barely visible only at positions where the detector sensitivity is exceptionally good. The tunnel-rate in this diagram is

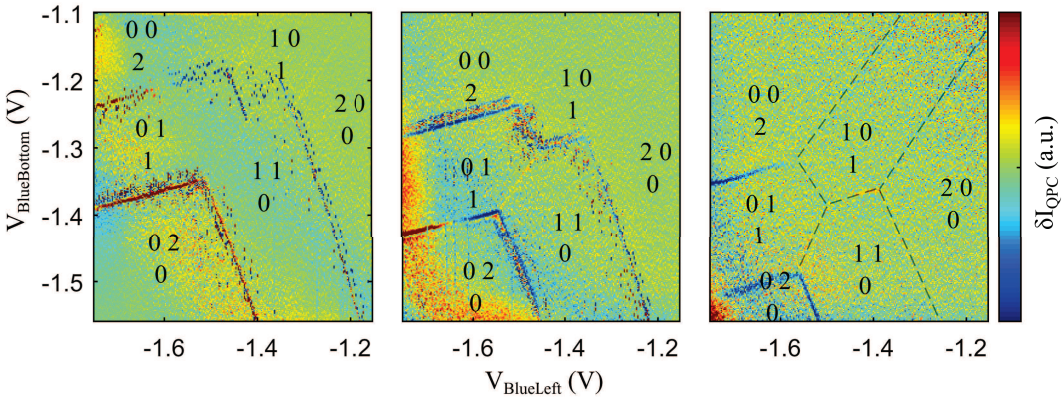


**Figure 3.15:** Stability diagrams of the isolated triple dot with two electrons initialized in the loading sequence. Derivative of the top-right QPC current with respect to $V_{\mathrm{BlueBottom}}$ as a function of $V_{\mathrm{BlueBottom}}$ and $V_{\mathrm{BlueLeft}}$. From left to to the right the inter-dot coupling is increased. **(Left)** Case of coupling lower than the measurement frequency (few Hz). **(Center)** Case of coupling mostly comparable to the measurement frequency (50 Hz). **(Right)** Effect of tunnel-coupling on degeneracy-line broadening greater than temperature (GHz). Visual guides were added for clarity (dashed lines).

therefore several GHz.

This possibility to adjust the tunnel-coupling over a wide range and to achieve tunnelling rates of several GHz opens up several manipulation schemes and is a requirement for spin manipulation. The fact that the quantum dots are circularly coupled with well controlled tunnel-barriers between each quantum dot and controlled electron number is demonstrated for the first time. This control over the barriers will be used for the manipulation of spin qubits in the next chapter. Additionally, it will allow to bring the system into a situation with balanced and fast tunnel-barriers that allow charge manipulation on the order of nanoseconds. This enables the coherent transport of electrons along a closed path studied in this thesis.

## 3.8 Conclusion

In this chapter, the control over the charge degree of freedom in three different sample geometries was demonstrated. To facilitate the operation of the device, a novel manipulation scheme was introduced. It consists in the isolation of the electrons in the quantum dots from the surrounding 2DEG via thick potential barriers. It was shown, that in this system the electron number is then fixed, leading to a reduced subspace of charge configurations. The reduced complexity allows to access the tunnel-coupling as a tunable parameter, which was previously fixed during experiments. Additionally, the simplification of the charge

space allows to scale up the system size, while giving full control over the path of the electrons in the structure. The manipulation of single electrons in multiple quantum dots was demonstrated for the case of a linear chain of three quantum dots, as well as for a circular triple quantum dot device. The enhanced manipulation possibilities of the quantum dots in the isolated regime allows to access a large parameter space of inter-dot couplings. The inter-dot tunnel-rates can hereby be changed from a few hertz to several gigahertz. Our measurements are quantitatively reproduced by a simple theory based on the constant interaction model. This allows to extract relevant experiment parameters like the charging energy or the position of the quantum dots. The high level of control over the charge state demonstrated in the isolated regime will allow novel spin manipulation protocols in the next chapter. We will make use of the variability of the tunnel-coupling to perform coherent evolutions of electrons spin pairs in an isolated double dot. Finally, the increased control over the path of an electron in the isolated regime paves the way for an investigation of the electron transport in quantum dot arrays.

# CHAPTER 4

## Spin control in isolated Multi-dot systems

### 4.1 Introduction

While the control over the charge of a trapped electron is a remarkable technological achievement, its applicability to quantum simulation or computation schemes is usually limited by the many electrical noise sources that couple to this degree of freedom. These noise sources include electrical perturbations from the gates and ohmic contacts, charge reorganisation in the surface and donor layer, piezoelectric phonons as well as noise from the nearby charge detectors. On the other hand, the spin of an electron is protected by selection rules that impose the conservation of angular momentum. Additionally, the strength of magnetic fields in a semiconductor crystal is usually low and their variation in time is slow, making the spin information a well protected entity. In this chapter our recently developed technique of isolated charge manipulation that was presented in the last section will be used for the control over the isolated electron spin degree of freedom. In comparison to previous experiments, the full control over the double-dot potential in the isolated configuration allows to directly control the tunnel-coupling between dots. This control will be used to implement a novel manipulation scheme to perform the coherent exchange of one quantum of spin between two electrons, initially proposed by Loss and DiVincenzo.[21] The control scheme is then shown to lead to a lowered susceptibility of the coherence time to charge noise.

Secondly, the spin of the electrons will be used to probe the inter-dot coupling of a double dot and the circular triple dot device introduced in the last chapter. The measured spin mixing dynamics in the triple dot will be analysed and allow to infer the effective exchange energy of electrons in the three coupled dots. This information will be employed to bring this multi-dot system into a state of large balanced inter-dot couplings. In this regime, nanosecond electron transfer between quantum dots becomes possible.

Finally, our results on coherent transport of electrons in a quantum dot array over distances up to several micrometers will be presented. The transport is found to induce novel dynamics on the spin of the travelling electrons. We will use an extensive set of experimental evidence to discuss the dominant decoherence processes during the transport. Our results will be compared to theoretical predictions found in the literature to deduce the underlying dynamics.

## 4.2 Spin read-out of an electron pair in the isolated regime

The charge state of a quantum dot system can be routinely measured with a QPC acting as a local electrometer. In the last chapter it was shown that also the reorganization of charges in isolated quantum dots can be directly probed. The spin of the isolated electrons is however more difficult to determine. One way to differentiate the spin states is to create an energy difference, that is larger than thermal broadening ($k_BT \approx 8$ µeV). Fortunately, the degeneracy of the singlet and triplet states of two electrons in a quantum dot is lifted by the exchange energy of $J_{ST} \approx 300$ µeV. This large energy splitting allows to convert the spin information of two electrons into a measurable charge signal via the concept of spin-to-charge conversion introduced in section 1.5. The technique was previously used in the regime of good coupling to the reservoirs, but its applicability to the isolated regime will be shown here. The spin-to-charge conversion is hereby implemented in the loading dot of the isolated system, where the tunnelling rate to the reservoir can be made comparable to the detector bandwidth. In this situation, single-shot spin read-out can be performed as shown in the following.

To characterise the spin-to-charge conversion process, the electron tunnelling time to the reservoir is first adjusted to a few milliseconds. This allows to observe single electron tunnelling events in real time with our electronics. Next, the chemical potential of the single dot connected to the 2DEG is brought close to the charge degeneracy between one and two electrons. In this position, the charge dynamics are expected to depend on the two-electron spin state due to the large exchange energy. This effect can be analysed with the following protocol which is also schematically presented in Fig 4.1(a) :

- The quantum dot is prepared in the single electron region with an unknown single spin by a tunnelling event to remove any influence of previous spin measurements.
- The system is brought to the two electron region where the tunnelling rate is of the order of $\approx 100$ kHz for the loading time $\tau_1 = 30$ µs. This initializes a random two-electron spin state in the quantum dot via an electron tunnelling event from the reservoir.

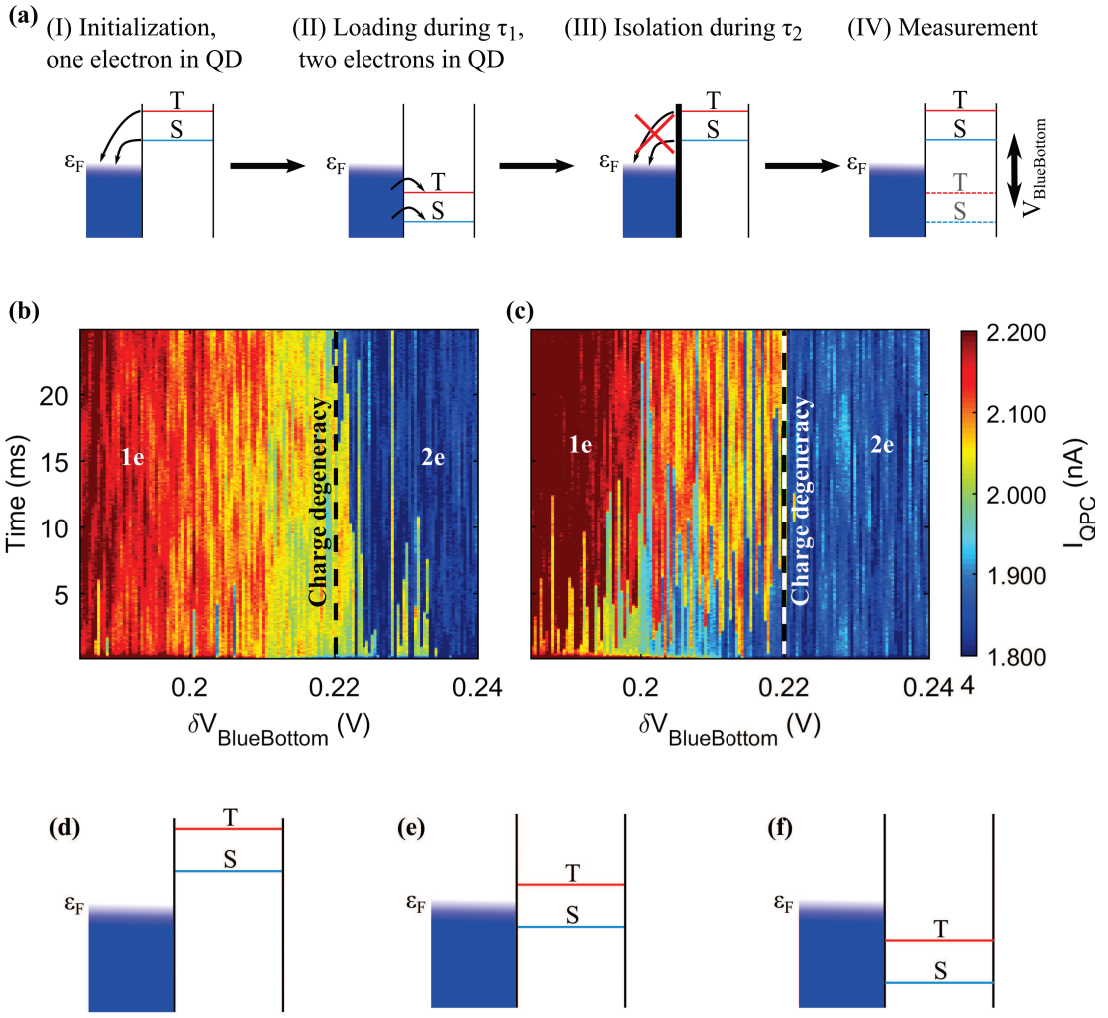


**Figure 4.1:** **(a)** Schematic of the characterisation of the spin measurement as described in the main text. For each step, the chemical potential alignment of the Singlet (S) and Triplet (T) states with respect to the Fermi energy $\varepsilon_F$ is given. Tunnelling processes are indicated by arrows. **(b)** Characterisation of the spin-to-charge conversion process (see text). The QPC current is plotted as a function of $V_{\mathrm{BlueBottom}}$ and the time after the last step of the sequence in (a). After two electrons are loaded into the dot, $V_{\mathrm{BlueBottom}}$ is immediately moved to a certain value close to the charge transition and the current trace is recorded versus time. The red color encodes high current, corresponding to one electron left in the dot. The blue color encodes low current, identified with two electrons localised in the dot. **(c)** Same diagram as in (b), but with a waiting time of 10 ms after the electrons were loaded into the isolated state and before the current trace is recorded. **(d)** Chemical potential of the two electron states above the Fermi energy. The charge ground state is one electron in the dot; all two-electron spin states tunnel out of the dot. **(e)** Fermi energy aligned between the singlet and triplet states (only one shown). Only a triplet state can tunnel to the reservoir if there are two electrons in the dot. **(f)** Fermi energy above the two-electron states.

- The electrons are then pulsed to the isolated regime where no electron exchange with the reservoir is possible (introduced in chapter 3) and remain for a variable relaxation time $\tau_2$.
- Finally, the chemical potential of the quantum dot is adjusted to a position close to the charge transition and the potential barrier to the electron reservoir is again lowered. In this configuration, the electrons are allowed to tunnel to the reservoir. By monitoring the current through a nearby QPC we can therefore observe the influence of the spin state on the charge dynamics.

When the chemical potential is scanned through the charge transition in the last step of the procedure described above, we obtain the charge dynamics as a function of the alignment of the chemical potentials of the singlet and triplet states. This investigation was performed for two different values of the relaxation time in the isolated position $\tau_2$.

#### Case of short relaxation time $\tau_2$

In Fig. 4.1(b) the previously introduced characterisation method is performed for $\tau_2 = 0$, such that the loaded spin state is not allowed to relax. The color coded current level is used to distinguish between one electron in the quantum dot (red) or two electrons in the quantum dot (blue).

For very positive values of $V_{\mathrm{BlueBottom}}$, the system is in the configuration given in Fig. 4.1(f) where both spin states lie below the Fermi energy. Consequently, no electron exchange with the reservoir is possible and two electron occupancy (blue) of the quantum dot is observed independent of time.

For more negative values of $V_{\mathrm{BlueBottom}}$, the system is brought into the situation shown in Fig. 4.1(e) where the the singlet state lies below the Fermi energy, while the triplet state is above it. As a result, a triplet state can effectively be transformed to a singlet state, by exchanging one electron with the reservoir and therefore occupying a one electron-state for a short time. This event can be witnessed in the diagram as a short red step at the beginning of the scan. The step is followed by a low current signal (blue), indicating that a second electron tunnels back in. As the singlet state is the charge ground state in this position, no further electron tunnelling event is observed.

Farther to the left for even more negative voltages on $\delta V_{\mathrm{BlueBottom}} < 0.22$ V, the charge degeneracy line is crossed. Then the system is in the situation depicted in Fig. 4.1(d) where both spin states are above the Fermi energy and one electron will in all cases leave the dot. Accordingly, a mostly red one-electron region is observed, with only few visible instances of occupation by two electrons at the beginning of the current trace. The timescale for

the majority of these tunnelling events is observed to be below 200 µs (below the detector bandwidth).

### Case of long relaxation time $\tau_2$

This diagram changes dramatically, when the relaxation time $\tau_2$ in the isolated position after the two electron loading is increased up to 10 ms. The obtained diagram is shown in Fig. 4.1(c). Unlike before, the blue region where no electrons are exchanged with the reservoir has increased and ends only at the position of the charge degeneracy line at $\delta V_{\mathrm{BlueBottom}} = 0.22$. Specifically, no steps are observed in the beginning of the current trace for the region that was identified with the position depicted in Fig. 4.1(e). We interpret this as the relaxation of the initialized triplet fraction to the singlet state during the waiting time $\tau_2$. As there are no triplets remaining in the dot, the electron exchange in the potential situation from Fig. 4.1(e) is no longer possible, which explains the extended blue region in the right side of the graph.

Additionally, the previously red region shows long instances of two-electron occupation (blue) at the beginning of the current trace for almost all values of $V_{\mathrm{BlueBottom}}$. The timescale for these events is several milliseconds and depends on the height of the tunnel-barrier to the electron reservoir. The observation of these events can be explained by the different tunnelling times of the singlet and triplet states. Due to the different orbital wavefunction of these two states, the triplet has a higher probability to be at the edge of the quantum dot. This different spatial distribution leads to a higher probability to tunnel to the reservoir within a given time $\tau$. A singlet state is therefore expected to result in a longer two-electron occupancy before one electron is exchanged with the reservoirs. This is consistent with the measured slow tunnelling time for $\tau_2 = 10$ ms. The longer two-electron occupancy is hardly observed for the case of short waiting time $\tau_2 \approx 30$ µs. The electron tunnelling time for the case of a triplet state is therefore very short and below 200 µs. This experimental finding also indicates that mostly triplets are loaded into the quantum dot during the loading time $\tau_1$ due to their faster tunnelling time. We can therefore initialize the spin of the two electrons just by changing the waiting time $\tau_2$ to either be a triplet state or a singlet state.

This also reveals two possibilities for spin detection. One is to detect one-electron occupation in the situation of Fig. 4.1(e). This implements the energy-selective detection scheme already discussed in 1.5.1 as only a triplet state will produce such events.[94] The other method is the detection of two-electron occupation in the situation of Fig. 4.1(d) that was introduced in section 1.5.2. Given the difference in the tunnel-rates between singlet and triplet, the spin state of the electrons in the quantum dot can be effectively

determined.[30] This procedure is implemented by identifying the measured tunnelling time with a spin state in the quantum dot. The condition for the state identification then has to be optimised such that $\frac{1}{\Gamma_{\text{triplet}}} << t_{\text{decision}} << \frac{1}{\Gamma_{\text{singlet}}}$, where $t_{\text{decision}}$ is the time used for the discrimination of the spin states and $\Gamma_{\text{singlet}}/\Gamma_{\text{triplet}}$ are the tunnel-rates of the singlet/triplet states respectively.

To characterize the spin life time in the quantum dot and the measurement visibility, the quantum dot is initialised with a triplet state and the time $\tau_2$ is varied in the above mentioned scheme. Then the chemical potential is aligned for one of the two detection schemes. The single-shot spin measurement is repeated to accurately determine the triplet fraction with respect to the waiting time. We chose to perform this measurement for a tunnel-rate selective spin measurement shown in Fig. 4.2. An exponential fit in black was added and fits the data well. The resulting visibility is 63% and the fit reveals a triplet decay time of 1.6 ms. This value is in good agreement with literature values[30,61,94] and similar values were measured in multiple samples ranging from 1.4 ms to 2.6 ms for the triple dot device in the isolated configuration.

There are several reasons for the reduced visibility of the measurement. First of all, the initialization of triplet states is limited by the tunnel-rate difference between singlet and triplet states and therefore usually not all of the initial states are triplets. Secondly, the finite operation time of gate movements of 15 µs per gate movement results in a time in which triplet state decay can occur before read-out, which reduces the maximum triplet probability that we can obtain. Finally, the finite tunnel-rate difference leads to the possibility of erroneously identifying a late tunnelling triplet as a singlet state.

The lower bound of the triplet probability is given by the misidentification of a fast tunnelling singlet state as a triplet. The exact dependence of the different error contributions on the tunnelling rates, relaxation rates and the point in time for state discrimination was already discussed in 1.5.2. From the observed visibility and the measured values of $\Gamma_S$ and $T_1$, we estimate a tunnelling rate difference of $\Gamma_T/\Gamma_S \approx 10$.

The lower bound for the triplet probability was consistently between 10-20% in different linear and circular triple dot samples for tunnel-rate readout. The reproducible minimal measurement error for the lower bound on the triplet probability shows that in these sample designs, the tunnel-rate difference $\Gamma_T/\Gamma_S$ was of similar magnitude. This parameter is very difficult to optimize experimentally and depends on the spatial form of the confinement potential. By shaping the electrostatic potential with the gate voltages it can usually be varied between 1-10 in the circular triple quantum dot samples. These values are in good agreement with values obtained in other laboratories.[30]

All measurements were preformed with a 10 kHz detection chain which limits the time

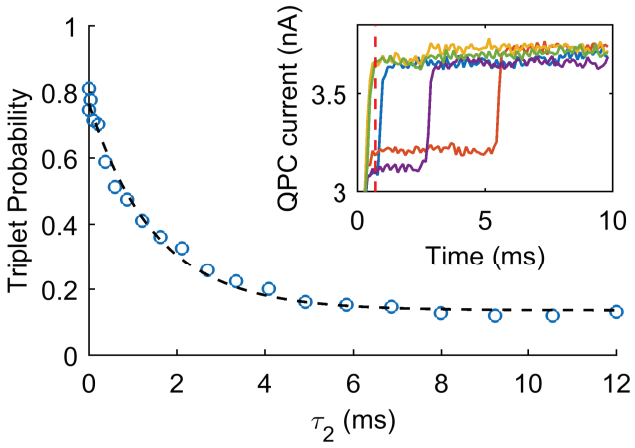


**Figure 4.2:** Measurement of the averaged triplet probability in the isolated regime as a function of the relaxation time $\tau_2$ without external magnetic field in a triple dot device. After the initialization of a triplet state, the electrons are isolated from the reservoirs for a varied time $\tau_2$. Then the spin is measured by the tunnel-rate dependent spin measurement technique at $\delta V_{\mathrm{BlueBottom}} < 0.22$ V and averaged over several realisations (see inset). The size of the blue dots represents the statistical errorbars on the probability. The exponential fit (dashed black) gives a visibility of 63% and a decay time of 1.6 ms. This corresponds to a fidelity of the measurement of $1 - \frac{\alpha+\beta}{2} = 82\%$, where $\alpha$ and $\beta$ are the error probabilities for state misidentification of singlet and triplet respectively. They are given by the upper and lower limits of the measured probabilities in this scheme. **Inset** : Exemplary single-shot current traces used for the measurement. Plotted is the QPC current as a function of the time after the last step in the procedure of Fig. 4.1(a). The red dashed line gives the threshold for triplet-singlet state discrimination.

used for singlet and triplet discrimination to $\tau > 200$ µs. This time is not negligible with respect to the relaxation time of the triplet states. An improvement of the measurement bandwidth could therefore result in a better visibility. The bandwidth can be improved by using high-sensitivity detectors like sensing-dots and improving the detection chain by using higher bandwidth amplifiers or implementing RF reflection techniques as mentioned earlier.

Note that for energy selective detection, higher visibilities can generally be achieved,[94] but the drawback is the need for the exact alignment of the singlet and triplet levels with the Fermi energy. This varies over time due to charge reorganization in the semiconductor structure and leads to decreasing fidelity with measurement time on the order of hours. For the long measurement times needed for the investigation of the multi dot devices, we therefore mostly opted to use the tunnel-rate dependent spin measurement technique, while we switched to the energy selective detection scheme to improve our signal to noise ratio. Both measurement techniques can easily be integrated at the loading position and

therefore allow to probe the spin dynamics in the isolated regime.

## 4.3 Coherent exchange oscillations in an isolated double quantum dot

In the last section it was shown, that conventional spin measurement techniques are fully viable to readout the spin state in the isolated configuration. At the same time, no detrimental effects on the spin readout and initialization from the isolation were observed. It is therefore possible to apply the introduced single-shot spin-detection technique for the investigation of the spin dynamics in the isolated system. We can hereby exploit the direct access to the height of the inter-dot tunnel-barrier during a single experiment in the isolated regime. This acquired degree of freedom over the tunnel-coupling can be used as a manipulation tool, which will be demonstrated in this section.

### 4.3.1 Electrical control over the two-electron spin state

To realise a two level system with two electrons, we will focus on the $m_s = 0$ subspace of the two electron spins. The relevant states are depicted on the Bloch sphere in Fig. 4.3(a) and are $|T_0\rangle$, $|S\rangle$, $|\uparrow\downarrow\rangle$ and $|\downarrow\uparrow\rangle$. As was shown in 1.4.3, the exchange energy $J(\varepsilon)$ responsible for the $|T_0\rangle$-$|S\rangle$ energy splitting depends on the detuning of the two quantum dots $\varepsilon$. At the same time, in our system there exists a second energy scale associated with the difference of nuclear fields experienced by the electrons $\Delta B_Z$, which will be called the nuclear field gradient. It arises due to the hyperfine interaction with the nuclei and was identified in 1.6.1 as a source of decoherence for electrons separated in two quantum dots.

However, it is also possible to use this energy scale for the manipulation of the two electron spin state as it creates an energy splitting between $|\uparrow\downarrow\rangle$ and $|\downarrow\uparrow\rangle$. When the electrons are separated into two quantum dots, the exchange interaction $J(\varepsilon)$ can become negligible compared to the nuclear field gradient $\Delta B_Z$. Then the eigenstates of the system are $|\uparrow\downarrow\rangle$ and $|\downarrow\uparrow\rangle$ as shown in the schematic representation of the energy dispersion in Fig. 4.3(b). When the detuning $\varepsilon$ is increased, $J(\varepsilon)$ is also also increased and allows to change the eigenstates of the two-spin system electrically from the $\{|\uparrow\downarrow\rangle,|\downarrow\uparrow\rangle\}$ basis to the $\{|T_0\rangle,|S\rangle\}$ basis.

In the last section, we showed how a singlet state can be prepared in one quantum dot by waiting in the isolated configuration. In Fig. 4.3(b) we observe, that it is possible to transform this singlet state into an eigenstate of the nuclear field gradient $\Delta B_Z$ by adiabatically separating the electrons. A transition is hereby called adiabatic if the eigenfunctions are transformed slowly enough that no excitation to a higher level can occur and the system therefore stays in the instantaneous eigenstates. To estimate the appropriate speed of separation to induce an adiabatic transition, one can use the Landau-

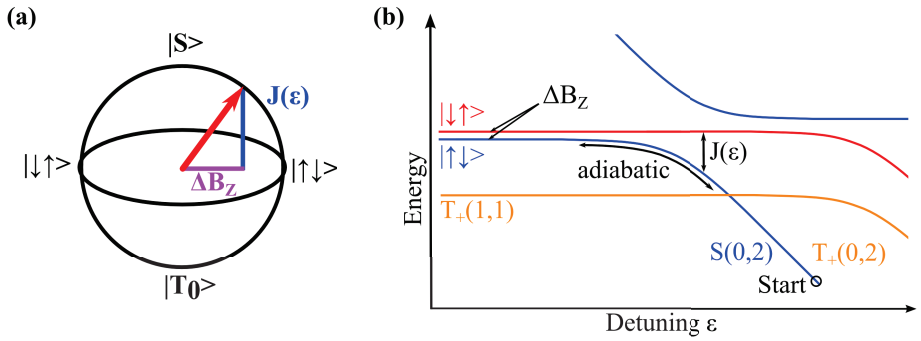


**Figure 4.3:** **(a)** Bloch sphere representation of the $m_s = 0$ states of two electron spins. The quantum axis that gives the eigenstates of the system is shown by a red arrow and depends on the relative magnitudes of the exchange interaction (blue) and the nuclear field gradient (violet). **(b)** Schematic of the energy dispersion of the two electron double dot as a function of the detuning $\varepsilon$. The adiabatic transformation from the $\{|T_0\rangle,|S\rangle\}$ basis to the $\{|\uparrow\downarrow\rangle,|\downarrow\uparrow\rangle\}$ basis is indicated by a black arrow.

Zener formula[147–150]

$$P_{LZ} = 1 - \exp\left(-2\pi \frac{a^2/\hbar}{\delta E/\delta t}\right) \tag{4.1}$$

which calculates the probability for an adiabatic transition in an anti-crossing of two states with linearly varying energies at the speed of $\delta E/\delta t$ which are coupled by a matrix element $a$. For realistic values we obtain the adiabaticity criterion for a transition time of 1 µs. However, due to the fact that the exchange coupling varies non-linearly, this value usually underestimates the necessary separation time. It is however close to experimentally found values for the adiabaticity criterion.[31]

On the other hand, the spin state is conserved during the separation of the electrons when the detuning is changed at a higher speed than the one given by the adiabaticity criterion. In this case the state is not transformed into an eigenstate of the system and will therefore evolve coherently in the instantaneous eigenbasis. This possibility to initialize the spin state and manipulate the eigenbasis by changing the detuning has been previously used to induce coherent exchange oscillations between the $|\uparrow\downarrow\rangle$ and $|\downarrow\uparrow\rangle$ states.[31] However, these oscillations decayed quickly due to the high susceptibility to charge noise in the exchange position.[151] We will show in the following, that the direct control over the tunnel-barrier eliminates this noise susceptibility and allows a higher amount of coherent oscillations within the coherence time.

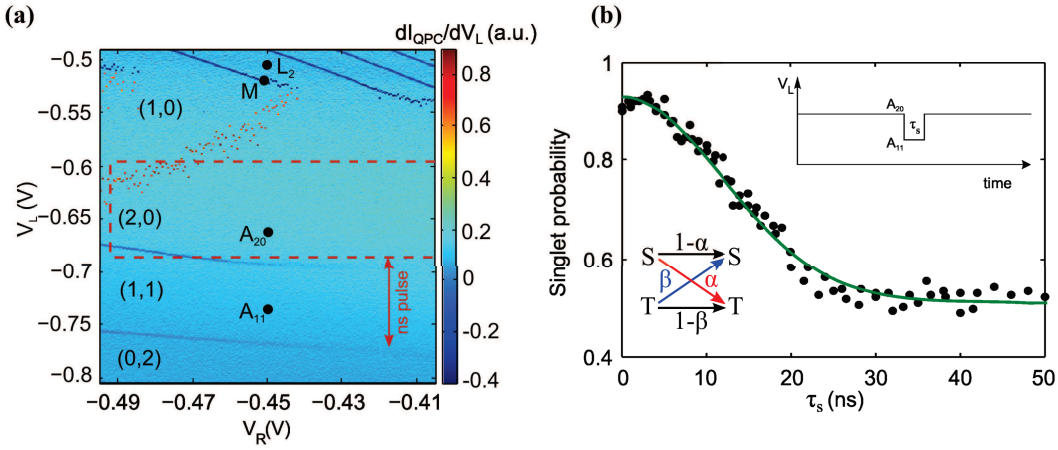


**Figure 4.4:** **(a)** Stability diagram of the isolated two-electron double dot introduced in 3.4. The spin measurement positions and nanosecond pulse origins for the spin manipulation are added to the graph. Electrons are initialized in $L_2$ and their spin state is measured with an energy selective detection scheme in M. The red dashed area shows the parameter space for the investigation of the exchange coupling. **(b)** Measurement of the influence of crossing the (2,0)-(1,1) charge degeneracy on an initialized singlet state at a magnetic field of $B = 100$ mT. Averaged single shot singlet probability as a function of the duration $\tau_s$ of a nanosecond pulse from point $A_{20}$ to point $A_{11}$. The inset on the top-right shows the pulse shape. The averaged single shot singlet probability (black dots) is fitted with a gaussian decay (green curve) that reveals a dephasing time $T_2^* = 15$ ns. From the initial value of the Singlet probability and the final mixing value we can estimate the fidelity of the spin measurement to be $1 - \frac{\alpha+\beta}{2} \approx 92\%$ (see inset on the bottom-left). Figure adapted from [141].

### 4.3.2 Spin mixing in the isolated double quantum dot

The demonstration of the coherent spin oscillations was performed in the isolated double dot close to the transfer channel from 3.4 and conducted in collaboration with B. Bertrand.[141,152] To perform coherent spin manipulations in a double dot, the electrons have to be strongly coupled in two separate dots by a fast tunnel-barrier. Then the influence of the nuclei and the variable exchange coupling on the spin state becomes observable and can be used to coherently manipulate the electron pair.

The effect of the electron separation on the spin state is first investigated in the region depicted in the two-electron isolated diagram in Fig. 4.4(a). Before the electrons are brought to this region, the two electrons are initialized in point $L_2$, which is followed by a long wait time (20 ms) to initialize a singlet state in the left dot. Then a fast nanosecond pulse on $V_L$ from point $A_{20}$ to $A_{11}$ is performed to split the electrons into different quantum dots. When the electrons are in the (1,1) configuration, their exchange energy is reduced and their spin state becomes affected by the hyperfine interaction with the random nuclei orientations. The singlet state is therefore expected to dephase on a timescale given by the

variance of the nuclear fields in the two dots. To probe this effect, the spin state is read out with an energy-selective spin measurement at point M at the end of the measurement sequence.

The measurement is presented in Fig. 4.4(b). The inset shows the pulse shape and the varied pulse duration $\tau_S$. The averaged single-shot singlet probability ($P_S$) is represented by black dots and varies from an initial high value of $P_S \approx 90\%$ to $P_S \approx 50\%$ for long pulse times. The measurement is fitted with a gaussian decay shown by the green curve and reveals a dephasing time of the singlet state of $T_2^* \approx 15$ ns. The final value at $\tau_S = 50$ ns shows that the singlet probability has dropped to 50% indicating, that $|T_0\rangle$ and $|S\rangle$ have been completely mixed. This is in excellent agreement with the literature and our previously presented dephasing mechanism of the slowly varying nuclear field gradient. It means that the eigenstates of the split electrons are $|\uparrow\downarrow\rangle$ and $|\downarrow\uparrow\rangle$ and the exchange coupling is negligible in this position just as we expected. Using Eq. 1.23 we extract a spread of the nuclear field gradient of $\sqrt{\langle (B_N^z)^2 \rangle} \approx 2.7$ mT.

The information, that the singlet state is fully mixed by the nuclei after a pulse duration of 50 ns can be used as a probe for the residual exchange interaction $J$. At point $A_{11}$ it is approximately given by $J_{Split} = \frac{4t^2}{E_C}$ and therefore depends on the tunnel-coupling as was shown in 1.4.3. When the exchange interaction becomes bigger than the nuclear field gradient $\Delta B_Z$, the eigenbasis is given by $\{|T_0\rangle,|S\rangle\}$ and no mixing is expected for the prepared singlet state. We therefore conclude, that if the mixing does not occur, then the exchange coupling has to be larger than the nuclear field gradient $\Delta B_Z$.

To perform this measurement with the fast risetime of our pulse generator, the region outlined by the dashed red rectangle in Fig. 4.4(a) is scanned with the addition of a 50 ns pulse of fixed amplitude on $V_L$ of $\approx 80$ mV. The effectively probed area during the pulse is then the one shown in the upper part of Fig. 4.5. When the triplet probability is plotted as a function of the two gates defining the pulse start position, the diagram in the middle of Fig. 4.5 is obtained.

We observe, that for relatively negative values on $V_R$ and $V_L$, the prepared singlet state indeed mixes with the $|T_0\rangle$ state and after 50 ns the triplet probability has risen to 50% as indicated by the yellow color. However for more positive values of $V_R$ little mixing is observed as indicated by the blue color. As we have seen before in 3.4, $V_R$ controls the height of the tunnel-barrier between the two dots and therefore the tunnel-coupling $t$. For more positive values of $V_R$, $t$ is increased until $\frac{4t^2}{E_C} >> \Delta B_Z \approx 100$ neV. At this point, the increasing effect of the exchange coupling leads to the discussed basis change from $\{|\uparrow\downarrow\rangle,|\downarrow\uparrow\rangle\}$ to $\{|T_0\rangle,|S\rangle\}$. In this basis, the prepared singlet state experiences no mixing any more, explaining the large blue region in the diagram. We can therefore conclude, that

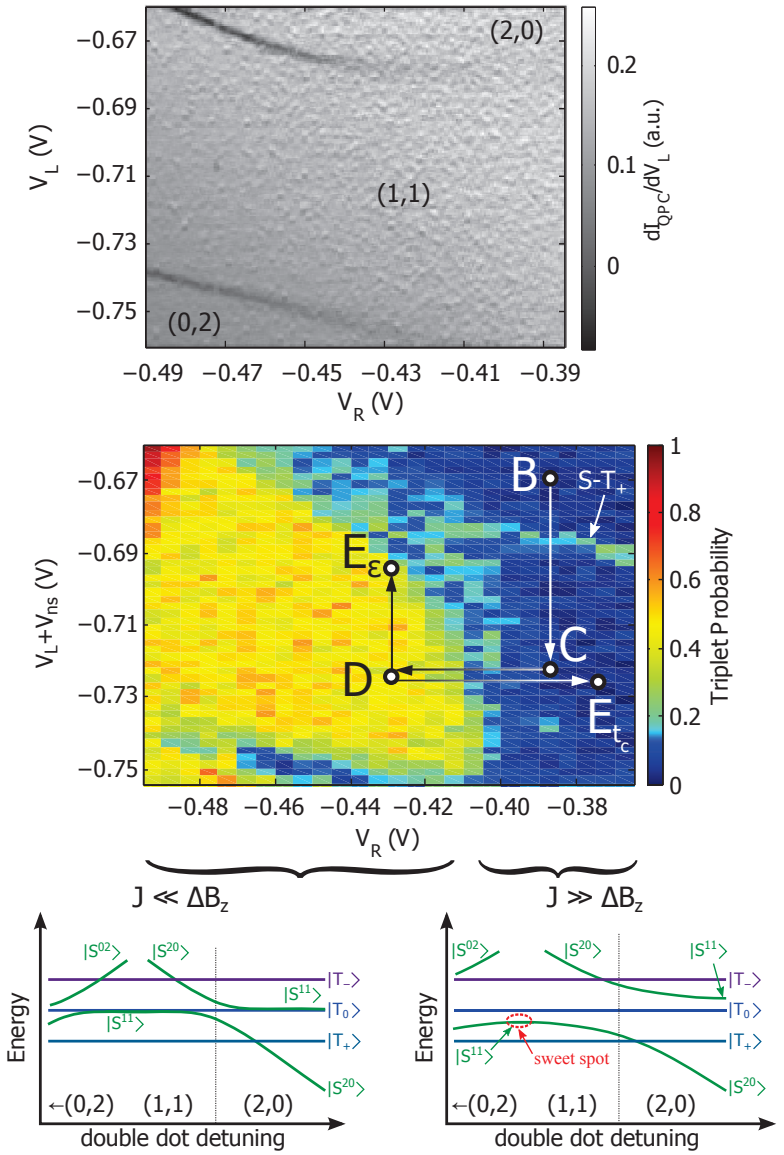


**Figure 4.5: (Upper)** Effectively probed area of the stability diagram of Fig. 4.4(a), when a fixed amplitude pulse on $V_L$ is applied in each position of the dashed red rectangle. **(Middle)** Averaged triplet probability plotted as a function of the starting position of the 50 ns pulse applied on $V_L$. The starting position is varied along $V_R$ and $V_L$ and the singlet probability is recorded via energy selective spin-to-charge conversion. **(Bottom)** Schematic of the energy dispersion of the spin states when the tunnel-coupling is increased. The left diagram shows the situation for low tunnel-coupling, where $|S\rangle$ and $|T_0\rangle$ are mixed by the nuclei and $|\uparrow\downarrow\rangle$ and $|\downarrow\uparrow\rangle$ are the eigenstates of the system. The diagram on the right shows the situation where a large tunnel-coupling overcomes the effect of the nuclei, the eigenstates are $|S\rangle$ and $|T_0\rangle$ and no mixing is therefore observed. Figure adapted from [141].

it is possible to effectively vary the exchange coupling $J$ with $V_R$. We attribute it to a change of the tunnel-coupling $t$ due to a varied tunnel-barrier height controlled by the gate voltage. This variation allows to perform a change of the eigenstates from $\{|\uparrow\downarrow\rangle,|\downarrow\uparrow\rangle\}$ to $\{|T_0\rangle,|S\rangle\}$ which can be used to induce coherent spin oscillations.

At the same time, a sharp line is observed for $V_L \approx -0.69$ V and $V_R > -0.41$ V where the singlet state is also mixed. It can be attributed to the crossing of the $|T_+\rangle$ and $|S\rangle$ state. As we saw in 1.4.3, the $|T_+\rangle$ state is split off from the $|S\rangle$ and $|T_0\rangle$ states by the Zeeman energy. Due to the singlet dispersion, the $|S\rangle$ state and $|T_+\rangle$ state are crossing close to the charge degeneracy. As was shown before, the nuclear field gradients transverse to the externally applied magnetic field will mediate mixing between those two spin states in the degenerate position. The size of the lateral nuclear field gradient $\Delta B^N_{x,y} \approx 100$ neV leads to a relatively sharply defined mixing area and therefore explains the observed signal. When the pulse ends after the crossing for $V_L < -0.69$ V, no mixing is observed. It can be attributed to the fast rise time of the nanosecond pulse and the resulting low probability to mix with the $|T_+\rangle$ state. The mixing probability can be calculated with the Landau-Zener probability given in Eq. 4.1 assuming an anti-crossing of the states mediated by the hyperfine interaction. The identification of the line as a $|T_+\rangle$-$|S\rangle$ crossing can be confirmed by varying the magnetic field and detecting the movement of the crossing position which can be found in Appendix D.1.

### 4.3.3 Coherent exchange oscillations via the control of the tunnel-coupling

The variability of the exchange coupling by pulsing the single gate $V_R$ opens up a new possibility for spin manipulation. In the original demonstration of coherent exchange oscillations, the exchange energy $J$ was changed along the detuning axis $\varepsilon$. However, due to the energy dispersion of the singlet state, charge noise along the detuning axis $\delta\varepsilon$ will directly influence the manipulation via a change of $J(\varepsilon + \delta\varepsilon)$ as can bee seen close to the vertical grey line in the bottom part of Fig. 4.5. The randomization of the exchange coupling leads to a randomization of the oscillation frequency. This results in a rapid decay of the coherent oscillations. Now the tunnel-coupling can be directly used as a variable parameter as initially proposed by Loss and DiVincenzo.[21] The advantage of such a scheme is shown in the lower part of Fig. 4.5. As we can see from the energy dispersion of the singlet state in the two-electron double dot for low (left) and high (right) tunnel-coupling, changing the tunnel-coupling increases the exchange coupling at the split (1,1) position. However in contrary to the previously used manipulation schemes, the exchange coupling is almost unaffected by charge noise on the detuning axis at the so called "sweet spot" (indicated in the diagram). This promises a higher coherence, as we can eliminate one

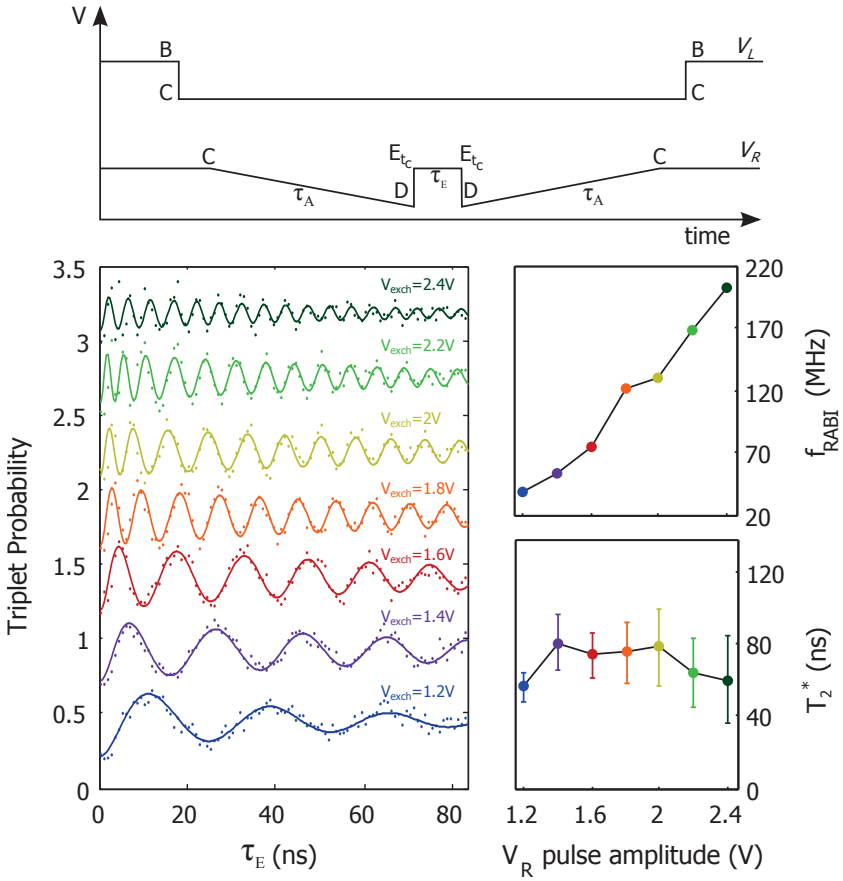


**Figure 4.6:** Coherent spin oscillations using the tunnel-coupling as a control parameter. **(Upper)** Pulse shapes for the two gates controlling the spin manipulation. The upper curve shows the transfer of the initialized singlet into the (1,1) region performed by $V_L$. The lower curve shows the pulse applied on $V_R$ and the control parameters that dictate the coherent manipulation. **(Lower)** Averaged triplet probability for the pulse sequence shown above as a function of the pulse length $\tau_E$. On the left we can see the raw data as coloured points depending on the amplitude of the exchange pulse $V_{exch}$ (indicated in the diagram). The measured points were offset for clarity. An exponentially damped sine fit is applied to each curve. On the right we can see the extracted Rabi-frequencies $f_{Rabi}$ (top) and decoherence times $T_2^*$ (bottom) for the different values of $V_{exch}$. Figure adapted from [141].

dephasing source for the manipulation scheme.

The experimental pulse sequence for this operation is as follows and shown in the upper part of Fig. 4.6.

- First a singlet is initialized in the quantum dot and brought to point B on Fig. 4.5.
- Then a fast pulse on $V_L$ skips the $|T_+\rangle$ crossing non-adiabatically to preserve the singlet state in point C.
- A slow ramp of $\tau_A = 1$ µs transforms the prepared singlet state adiabatically into the ground state of the nuclear field dominated region in D ($|\uparrow\downarrow\rangle$ or $|\downarrow\uparrow\rangle$).
- Then a fast pulse on $V_R$ to point $\mathrm{E}_{t_C}$ increases the exchange coupling and changes the eigenstates non-adiabatically to $|S\rangle$ and $|T_0\rangle$ for a certain time $\tau_E$.
- Now the inverse pulse sequence is performed to project the resulting state onto the singlet-triplet basis and read out the spin state.

The resulting averaged triplet probabilities as a function of the duration $\tau_\mathrm{E}$ and amplitude of the exchange pulse $V_\mathrm{exch}$ are shown on the left in the lower part of Fig. 4.6. We can see that the triplet probability at the end of the pulse sequence oscillates as a function of the time spent in the region of high exchange coupling $\tau_\mathrm{E}$. The frequency of oscillation is hereby dependent on the amplitude of the exchange pulse $V_\mathrm{exch}$. We observe, that for lower amplitudes, the frequency is slower than for higher amplitudes. This is consistent with a higher exchange coupling for more positive values of $V_R$ as also indicated by the diagram in Fig. 4.5. To extract more quantitative information about the evolution, we fit the curves with a Sine function and a Gaussian decay of the form $P(t) = A * \exp\left(-\frac{t^2}{(T_2^*)^2}\right) * \sin\left(2\pi f_{RABI} * t + B\right) + C$. The values $A$,$B$ and $C$ are free fit parameters, $T_2^*$ is the decay constant and $f_{RABI}$ is the oscillation frequency. The extracted fit parameters are given to the right of the measured data. The oscillation frequency $f_\mathrm{Rabi}$ seems to increase linearly with the pulse amplitude of $V_\mathrm{exch}$.

On the other hand, the extracted damping time constant $T_2^*$ is almost unaffected by the pulse amplitude. This means that more oscillations (operations) can be performed, before the coherence of the state is lost. This is in stark contrast to previously measured exchange oscillations which showed a decrease of the coherence time when the oscillation frequency was increased. The quality of the oscillations can be quantified by using the formula introduced by Dial et al. $Q = JT_2^*/2\pi$ for an easy comparison with other schemes.[151] We find an improvement for $Q$ from 2 up to 12 for the largest investigated oscillation frequency. An explanation for this improvement can be given by our operation of the system in the

mentioned "sweet spot" regime and the resulting immunity to charge noise on the detuning. In fact for the previous measurements where the exchange coupling was varied along the detuning axis, this sensitivity to charge noise increased with increasing pulse amplitudes due to the singlet and triplet energy dispersion. As a consequence, a constant quality of the oscillations was observed for different values of the pulse amplitude.

We can show the effectiveness of the sweet spot operation and the difference of the two schemes by fixing the exchange oscillation position at $V_{\mathrm{exch}} = 1.6$ V and then varying the detuning with $V_L$. Then the system will again become sensitive to charge noise along the detuning axis and we expect a reduction of the quality of the oscillations. The preparation of the eigenstate of the nuclei mediated magnetic field gradient is performed as before and only the starting position of the exchange pulse controlled by the microsecond pulse on $V_L$ is changed. The nanosecond exchange pulse controlled by $V_{ns}$ is kept the same. The resulting measurement is shown on the left part of Fig. 4.7.

Again we observe clear oscillations of the triplet probability as a function of the pulse duration $\tau_{\mathrm{E}}$. When $V_L$ is varied, the frequency of the oscillation $f_{\mathrm{Rabi}}$ also increases similar to the previous case. An analysis of the exponentially damped sine fits applied to the data on the left however reveals a different behaviour. The oscillation frequency $f_{\mathrm{Rabi}}$ seems to now vary non-linearly with the pulse amplitude as shown by the graph. More importantly however, the damping time constant which is associated with the coherence time $T_2^*$ is clearly decreasing with the pulse amplitude and results in less oscillations within the coherence time for higher values of the exchange coupling.

This difference in the relation of the oscillation frequency to the coherence time shows a great advantage of the manipulation of the tunnel-coupling at the sweet spot. This manipulation is greatly simplified in the isolated regime as the gate movement to change the tunnel-coupling can not result in electron exchange with the reservoir. However, the same experiment was also performed later by two different groups without the necessity of isolated regime manipulation.[153,154] Additionally, it is possible to use large pulse amplitudes along the detuning axis to reach another sweet spot regime as shown by Dial et al. in a recent publication.[151] On the other hand, the investigation of the singlet mixing in the (1,1) region as a continuous function of the tunnel-coupling has been performed for the first time and shows a great simplification for the tuning of the inter-dot barrier. The coherent manipulation of the spins by this new accessible parameter was directly probed here. The demonstrated simplicity promises additional improvements in terms of manipulation possibilities and coherence times for spin qubits.

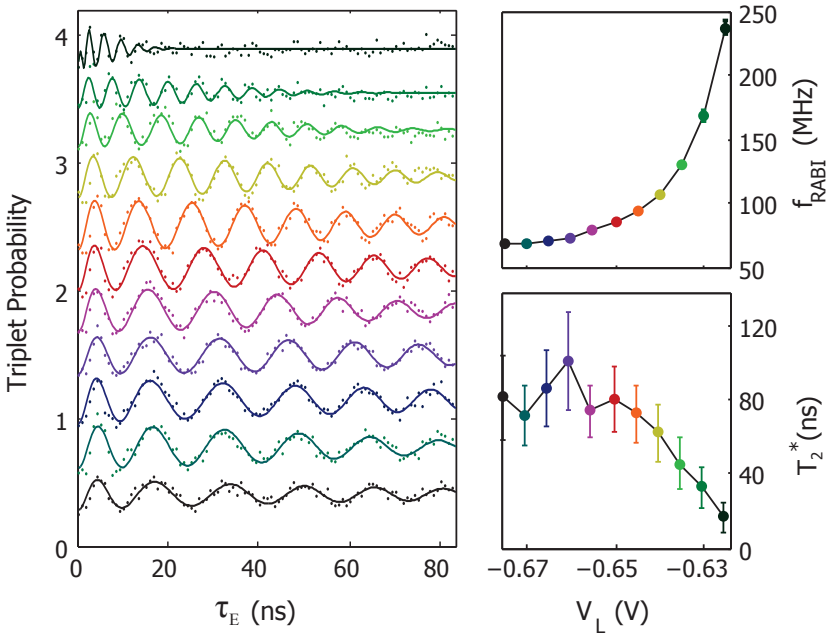


**Figure 4.7:** Coherent spin oscillations varying the detuning to illustrate the importance of the sweet spot operation. The same scheme as in Fig. 4.6 is used, but $V_{\mathrm{exch}} = 1.6$ V is fixed while $V_L$ is varied for the different curves. **(left)** Averaged single-shot triplet probability as a function of the pulse length $\tau_{\mathrm{E}}$ for increasing values of $V_L$ from the bottom to the top. The data points were differently coloured and offset for clarity. An exponentially damped sine fit is applied to the data. **(right)** Extracted fit parameters as a function of $V_L$. $f_{\mathrm{Rabi}}$ is the extracted oscillation frequency, while the coherence time $T_2^*$ is the damping time constant. Figure adapted from [141].

## 4.4 Spin as a probe for exchange coupling in a circular triple quantum dot

In the last section it was demonstrated, that the exchange coupling between two quantum dots can be directly probed by the evolution of a prepared singlet state using rapid voltage pulses. This tool can also be used to probe the inter-dot coupling of several quantum dots, as will be shown in this section. In our analysis of the charge dynamics of the quantum dot, only a rough estimate of the inter-dot tunnel-coupling could be obtained. Using the spin of a two-electron state, we will now demonstrate the full control of the inter-dot exchange coupling in a precise manner. To show the advantages of the manipulation in the isolated regime, we will demonstrate that the inter-dot coupling can be moved over orders of magnitudes. The resulting energy dispersion can be probed as a function of the detuning by an analysis of the mixing dynamics. This direct investigation of the inter-dot coupling allows to balance the tunnel-coupling strengths between the quantum dots and thereby realize a circularly coupled triple dot device. The mixing dynamics in the circular system will be analysed as a function of the coupling strength, which allows to prepare the

triple quantum dot for the investigation of electron transport in a closed loop.

### 4.4.1 Probing the split electron state with a two-electron singlet

To probe the spin mixing dynamics in the triple dot system, a single shot spin measurement is again implemented in the loading position of the isolated system with two electrons. The sample that showed the more interesting spin dynamics was the circularly coupled triple quantum dot whose charge control was introduced in 3.7. This was due to the high level of control over the inter-dot coupling that was possible with respect to the linear triple-dot explored beforehand.

Unlike the previous case of the isolated double dot, where only a single inter-dot coupling was controlled, we now have to gain control over three different inter-dot couplings. However, the influence of the exchange coupling on the two-electron spin state can again be used to probe each of these couplings individually.

The circular triple dot is first loaded with two electrons in the bottom dot followed by a relaxation time of 20 ms to initialize a singlet state. This state is then brought to one of the positions indicated by the white dashed rectangle in Fig. 4.8(a). Then single shot read-out is performed at each position 150 times and the resulting diagram of the averaged single-shot triplet probability for each scanned point is plotted in Fig. 4.8(d). The obtained diagram roughly replicates the charge stability diagram for the microsecond movements of the gates. No mixing is obtained for the doubly occupied charge region and strong mixing occurs once the electrons are split into different quantum dots.

The slow rise time of 2 µs of the varied gates however masks any features with fast timescales, such as the $|S\rangle$-$|T+\rangle$ crossing. Indeed, the slow voltage pulse creates a mixture of $|S\rangle$ and $|T_+\rangle$ when the degeneracy is passed. It is therefore necessary to decrease the rise time of the probe pulse by applying RF-pulses on the green gates as shown in Fig. 4.8(b). The sum of the two pulses can then reveal the fast dynamics of the triple dot system on nanosecond timescales similar to the measurement of the isolated double dot in the last section. The involved RF gates are in the following identified by their respective dot positions $V_{\mathrm{Left}}$, $V_{\mathrm{Right}}$ and $V_{\mathrm{Bottom}}$ as shown in Fig. 4.8(b). The pulses are schematically shown in Fig. 4.8(c) for their respective gates.

The same measurement as in Fig. 4.8(d) is performed with the addition of the RF-pulse to obtain the diagrams of Fig. 4.8(e,f) for the two different pulses. In the region where before singlet states were not mixing, broad regions with a triplet probability of $P_{\mathrm{triplet}} \approx 0.4$ appear as well as the appearance of sharp lines farthest away from the inter-dot crossings. The broad regions are identified as $|T_0\rangle$-$|S\rangle$ mixing similar to the case of the isolated double dot investigated before.

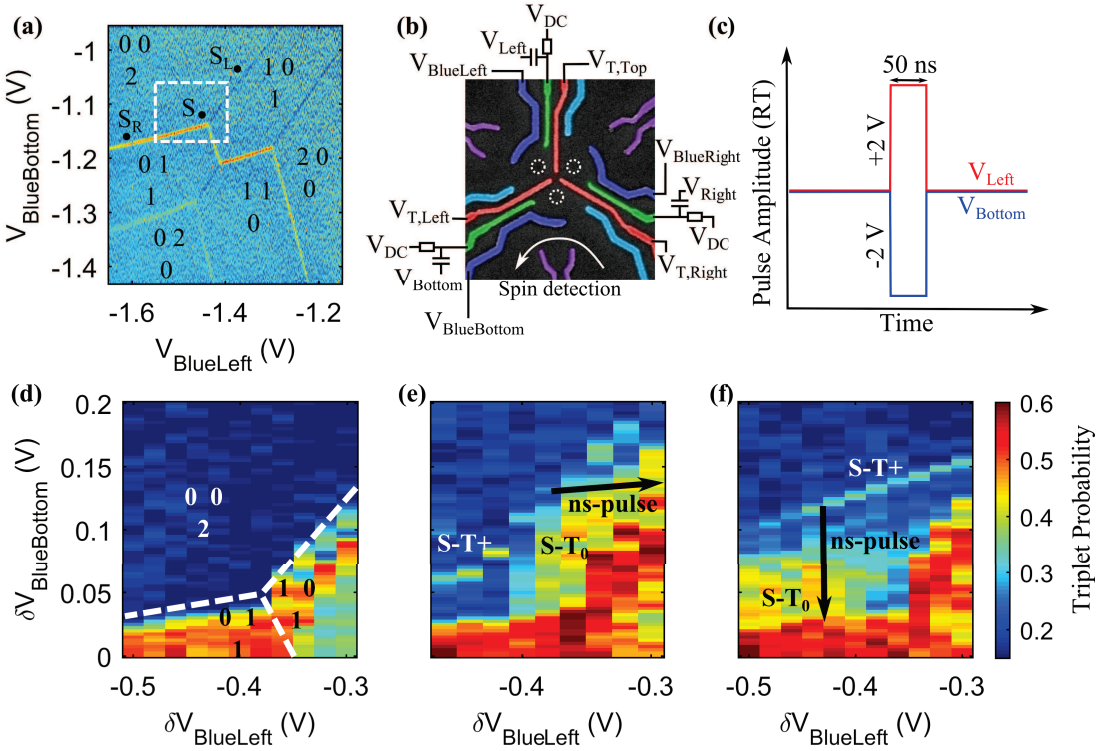


**Figure 4.8:** **(a)** Stability diagram of the circular triple quantum dot that was introduced in 3.7. The probed region for the spin detection is shown as a white dashed rectangle. Pulse starting positions S, $S_L$ and $S_R$ as well as electron occupation numbers were also added to the graph. **(b)** False color image of the triple dot sample showing the RF-connections to the gates as well as the position of the spin detector. **(c)** Pulses applied on the green RF-plunger gates $V_{Left}$ and $V_{Bottom}$ for (e) and (f). **(d)** Averaged single-shot triplet probability as a function of $V_{BlueBottom}$ and $V_{BlueLeft}$ without any applied pulse. The position of the charge degeneracy lines are indicated by white dashed lines and the electron occupation numbers were added. **(e)** Similar measurement as in (d), but with a 50 ns long 0.4 V pulse applied on the left green gate $V_{Left}$ at each data point. The direction and amplitude of the pulse is indicated by a black arrow in the diagram. **(f)** Same measurement as in (e), but with a -0.4 V pulse applied on the bottom green gate $V_{Bottom}$. The direction and amplitude of the pulse is indicated by a black arrow in the diagram.

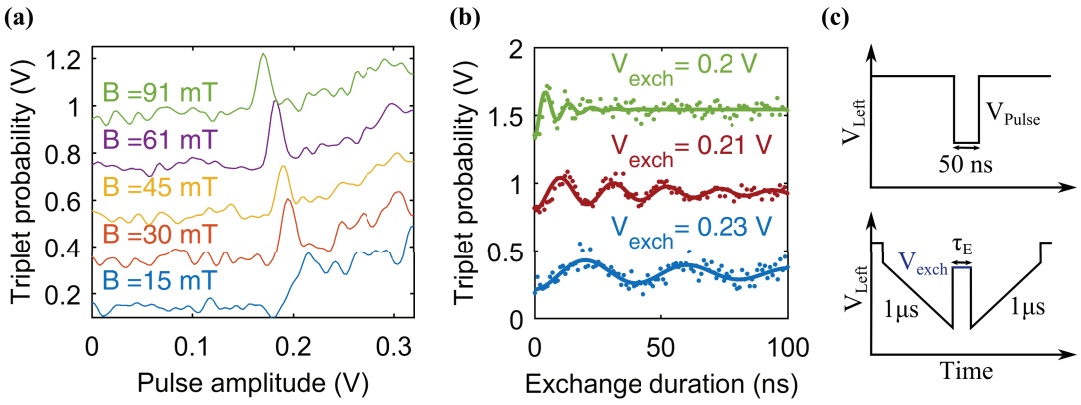


**Figure 4.9:** **(a)** Averaged single-shot triplet probability as a function of the amplitude of a 50 ns pulse on $V_{\mathrm{Left}}$ applied at $\mathrm{S_{Left}}$. The pulse is shown in the upper part of (c). The magnetic field $B$ is varied and the resulting curves are offset and coloured for clarity. **(b)** Averaged single-shot triplet probability as a function of $\tau_{\mathrm{E}}$ for the pulse in the lower part of (c) applied at point $\mathrm{S_L}$ in Fig. 4.8(a). The coherent exchange oscillations performed at the crossing to the left quantum dot for different exchange pulse amplitudes are offset and differently coloured for clarity. An exponentially damped sine fit was added to the data. **(c)** Schematic of the used pulses for the experiments in (a) and (b). The upper curve shows the probe pulse used to track the position of the $|S\rangle$-$|T_+\rangle$ crossing. The bottom curve shows the pulse used to measure the coherent exchange oscillations. The exchange duration $\tau_{\mathrm{E}}$ is varied to change the time spent in the region of high exchange coupling.

The sharp mixing lines are again identified as the crossing of the $|S\rangle$ state with the $|T+\rangle$ state by modifying the Zeeman energy splitting of the triplet state with the external magnetic field. Such a measurement is presented in Fig. 4.9(a). Here we start in the position $\mathrm{S_L}$ indicated in Fig. 4.8(a) and apply a 50 ns pulse of varying amplitude on $V_{\mathrm{Left}}$ before recovering the triplet probability. At low magnetic field $B = 15$ mT, only the region of $|T_0\rangle$ mixing is clearly observable. For higher magnetic fields, a peak appears, which is moved to lower pulse amplitudes when the magnetic field is increased. The peak becomes clearly separated for the $|T_0\rangle$-$|S\rangle$ mixing region at $B = 61$ mT. This dependence on the applied magnetic field allows to identify the observed peak with the $|S\rangle$-$|T+\rangle$ crossing.

When the $|T_0\rangle$-$|S\rangle$ mixing region and the $|S\rangle$-$|T+\rangle$ peak are separated by a region without mixing of the singlet state, it becomes possible to initialize the spin in the eigenstates of the nuclear field gradient. This allows to perform the coherent exchange oscillations discussed before. Note that due to the limited number of RF-connections on the sample, the exchange coupling is changed along the detuning axis as in the initial experiments of Petta et al.[31] For that the pulse shown in the lower part of Fig. 4.9(c) is applied in the same position $S_{\mathrm{L}}$. The first sharp rise crosses the $|S\rangle$-$|T+\rangle$ degeneracy and the

following adiabatic ramp transforms the singlet into an eigenstate of the $\{|\uparrow\downarrow\rangle, |\downarrow\uparrow\rangle\}$ basis at $V_{\mathrm{Left}} = 0.32$ V, where the electrons are split. Then the exchange pulse lets the system evolve under a finite exchange coupling $J(\varepsilon)$ controlled by the exchange pulse amplitude $V_{\mathrm{exch}}$ for the duration $\tau_{\mathrm{E}}$. Three coherent exchange oscillations for different values of $V_{\mathrm{exch}}$ are shown in Fig. 4.9(b) and reveal our ability to coherently change the exchange coupling of the two spins and observe their rotations as a function of time. This behaviour is identical to the one obtained for double quantum dots. This observation demonstrates, that the triple-dot can be transformed into a system of three different double dots when the energy levels of the third dot have been slightly raised and are not available. This shows the possibility to apply previously developed spin manipulation techniques to the circular triple-dot system.

A second deduction is that the system is in a strongly coupled regime for the electrons. Both of these experiments, be it the movement of the $|S\rangle$-$|T+\rangle$ position with magnetic field and the possibility to perform coherent oscillations rely on a very specific coupling condition. The $|S\rangle$-$|T+\rangle$ crossing becomes discernible only at coupling strengths of a few micro-electronvolt, due to the singlet energy dispersion induced by the tunnel-coupling that was introduced in 1.4.3. The small energy shift of the $|T+\rangle$ state $E_{\mathrm{Zeeman}}(60\ \mathrm{mT}) = 1.5\ \mu\mathrm{eV}$ then gets translated to a much bigger shift in detuning, which leads to the observable movement of the crossing with magnetic field. This indicates tunnel-rates of a few gigahertz which is a requirement for coherent operations.

Similarly the possibility to initialize the electrons in the $\{|\uparrow\downarrow\rangle, |\downarrow\uparrow\rangle\}$ basis and to observe coherent oscillations not only ascertains the strong coupling assumption, but also gives an upper limit for the coupling strength. As was shown in 1.4.3, the tunnel-coupling leads to a finite exchange coupling even in the middle of the (1,1) region, where the electrons are maximally split. This value is approximated by $J = \frac{4t^2}{E_C}$ and is required to be smaller than the nuclear field gradient $\Delta B_Z = 4$ mT ($\approx 100$ neV) of the two dots when the eigenstate is supposed to be in the $\{|\uparrow\downarrow\rangle, |\downarrow\uparrow\rangle\}$ basis. Using a charging energy $E_C = 2$ meV, an upper limit of $t < 7$ µeV is obtained. When the coupling is further increased, the eigenstate produced by the adiabatic is no longer in the $\{|\uparrow\downarrow\rangle, |\downarrow\uparrow\rangle\}$ basis and the oscillation amplitude will reduce. Similarly, the singlet states will no longer mix fully with the $|T_0\rangle$ state in this region, and the broad yellow $|T_0\rangle$-$|S\rangle$ mixing regions in a measurement such as in Fig. 4.8(e,f) has a reduced triplet probability.

The triple dot system is therefore found to be in the regime of high inter-dot coupling with tunnel-rates of the order of a few gigahertz. The measured behaviour is found to be analogous to the double dot case. To confirm the analogy, the possibility to perform coherent spin oscillations in this configuration was demonstrated. The transition to other

charge configurations also exhibited $|S\rangle$-$|T+\rangle$ crossings, that could be manipulated with the application of an external magnetic field. The demonstrated similarity to double quantum dot experiments will be helpful for the theoretical understanding of the performed spin transfer experiments in later sections.

### 4.4.2 Tunnel-coupling between different dots as a variable control parameter

The effect of different tunnel-coupling conditions on the spin dynamics can be directly inferred in our system when the voltages of the tunnel-barrier defining gates $V_{\mathrm{T,Left}}$, $V_{\mathrm{T,Right}}$ and $V_{\mathrm{T,Bottom}}$ are changed while probing the singlet mixing. This allows to determine the tunnel-coupling between adjacent quantum dots and thereby adjust the three different tunnel barriers for balanced coupling.

A measurement where the tunnel-coupling between the bottom and left dot is systematically varied is shown in Fig. 4.10(a). The measurement starts in point $S_{\mathrm{L}}$ in Fig. 4.8(a) from which the chemical potential of the bottom dot is varied with $V_{\mathrm{BlueBottom}}$ while the tunnel-coupling is varied with $V_{\mathrm{T,Left}}$. For positive voltages on $V_{\mathrm{BlueBottom}}$ in the doubly occupied region, again no mixing is obtained. However, when the charge degeneracy (black dashed line) is crossed, the singlet state mixes with the triplet states for values of $V_{\mathrm{T,Left}} < -0.27$ V. For more positive values of $V_{\mathrm{T,Left}}$ no mixing is observed any more. We therefore deduce, that for high values of inter-dot coupling, the microsecond gate movement no longer leads to an efficient mixing process with the triplet states.

To again probe the spin mixing dynamics, the same diagram was taken with an added 50 ns pulse of $V_{\mathrm{Pulse}} = 0.3$ V on $V_{\mathrm{Left}}$ in Fig. 4.10(b). The area of mixing due to the microsecond pulse is indicated by the black dashed region for clarity. Outside this region, the observed mixing effects are due to the added pulse with a fast rise time of $\approx 0.9$ ns. For negative voltages on $V_{\mathrm{T,Left}}$, a broad region with $P_{\mathrm{triplet}} \approx 0.4$ is observed and identified with the previously discussed $|T_0\rangle$-$|S\rangle$ mixing process. This region however ends for more positive voltages of $V_{\mathrm{T,Left}} > -0.32$ V. As $V_{\mathrm{T,Left}}$ affects the tunnel-coupling of the two dots, it therefore changes the exchange energy between the two electrons. In analogy to the case of the isolated double dot, this leads to a change of the eigenbasis when the exchange coupling $J$ becomes bigger than the nuclear field gradient $\Delta B_Z$. In this case, no mixing is observed any more. We can therefore identify the coupling configuration, where the $|T_0\rangle$-$|S\rangle$ mixing ceases with a tunnel-coupling value of 7 µeV by direct comparison with the measured nuclear field gradient $\frac{4t^2}{E_C} = E(\Delta B_Z) = 100$ neV.

When the tunnel-coupling is increased for more positive voltages on $V_{\mathrm{T,Left}}$, the previously identified $|S\rangle$-$|T+\rangle$ crossing emerges with rising amplitude. To the right, for very high tunnel-coupling, a second line appears, which joins the $|S\rangle$-$|T+\rangle$ crossing at $V_{\mathrm{T,Left}} \approx -0.21$.

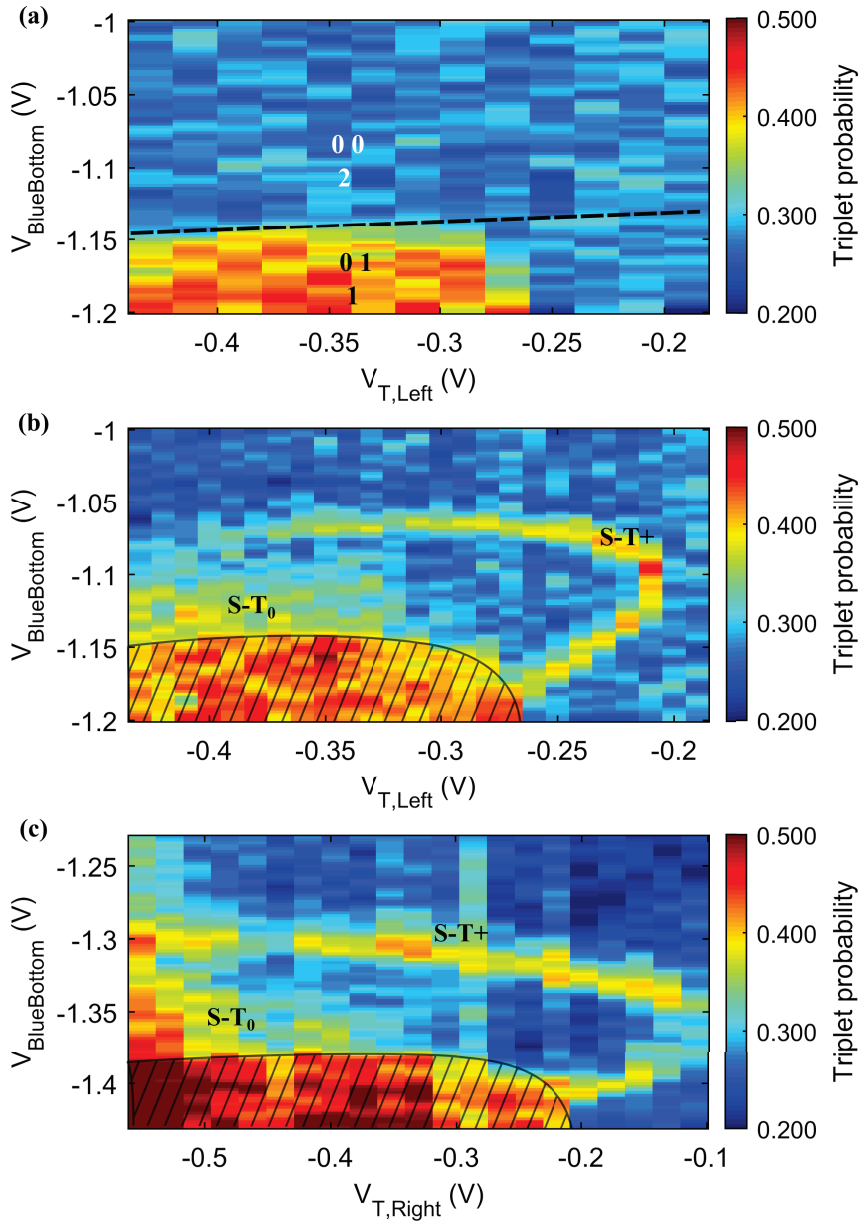


**Figure 4.10:** Influence of the tunnel-coupling on the singlet-probe when the electrons are split at a magnetic field of $B = 90$ mT. **(a)** Reference measurement for the exchange probe. The system is brought into position $S_{\mathrm{L}}$ in Fig. 4.8(a) and the potential of the bottom dot is increased with $V_{\mathrm{BlueBottom}}$ while the left tunnel-gate $V_{\mathrm{T,Left}}$ is varied to change the exchange coupling. The single-shot averaged triplet probability is encoded in the color-bar. **(b)** Same measurement as in (b) but with the addition of a 50 ns pulse of $V_{\mathrm{Pulse}} = 0.3$ V on $V_{\mathrm{Left}}$. **(c)** Similar measurement as in (b), but the connection to the right dot is probed at $S_{\mathrm{R}}$ in Fig. 4.8(a) by a 50 ns pulse of $V_{\mathrm{Pulse}} = -0.3$ V on $V_{\mathrm{Bottom}}$, while the right tunnel barrier $V_{\mathrm{T,Right}}$ is varied.

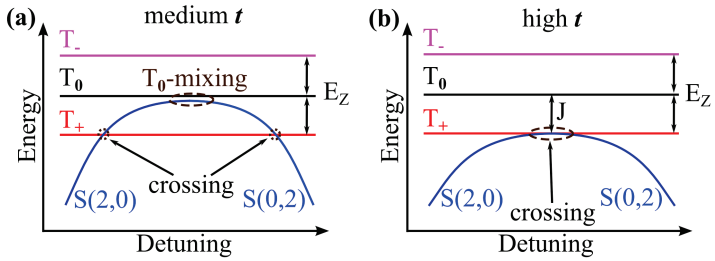


**Figure 4.11:** Schematics of the energy dispersion of a double quantum dot filled with two electrons illustrating the influence of the tunnel-coupling on the position of the $|T+\rangle$-$|S\rangle$ crossing. The third dot is raised in energy and not available. **(a)** Case of medium tunnel-coupling where two $|S\rangle$-$|T+\rangle$ crossings can be observed on each side of the region where the electrons are split into two dots. **(b)** Special case of high tunnel-coupling where only one $|S\rangle$-$|T+\rangle$ crossings can be observed. The exchange coupling in the center is then equal to the Zeeman energy $E_Z$.

This other mixing line is the $|S\rangle$-$|T+\rangle$ crossing associated with the singlet state with two-electron occupation of the left dot. The origin of the two crossings is illustrated in a schematic of the energy dispersion of the involved states in Fig. 4.11(a). At the point where the two meet, the exchange coupling in the center of the (1,1) region is equal to the magnetic field splitting $E_{\mathrm{Zeeman}}(90\ \mathrm{mT}) = 2.25\ \mu\mathrm{eV}$. Then the energy of the singlet state and the triplet state are degenerate at this position and only a single point of mixing is observed. This situation is schematically depicted in Fig. 4.11(b). Note that this configuration indicates that the tunnel-coupling is on the order of $t \approx \sqrt{E_{\mathrm{Zeeman}} \cdot E_C/4} = 32\ \mu\mathrm{eV}$.

The same measurement can be performed at the position $S_{\mathrm{R}}$ in Fig. 4.8(a) to demonstrate control over the coupling to the right dot which is shown in Fig. 4.10(c). The influence of the microsecond gate movement on the spin mixing is again indicated by a black dashed region. The coupling between the bottom and the right dot is changed with $V_{\mathrm{T,Right}}$ while the potential of the bottom dot is varied with $V_{\mathrm{BlueBottom}}$. We observe the same pattern of the joining of the two $|S\rangle$-$|T+\rangle$ crossings and the appearance of a $|T_0\rangle$-$|S\rangle$ mixing area for smaller couplings.

We can therefore deduce, that we are able to move the tunnel-coupling energy continuously from nano-electronvolt to several micro-electronvolt and infer the exchange coupling from the observed mixing of a prepared singlet state. This is possible for both crossings connected to the probe dot and demonstrates the direct and easy control over the exchange coupling. As both couplings can be very high, the device also meets the prerequisites for more advanced measurements that rely on coherent transfer of the electrons.

### 4.4.3 Spin mixing diagram of the full circular triple-dot for different coupling configuration

Having gained quantitative control over the exchange coupling of two pairs of adjacent dots when the third dot potential is elevated in energy, we can continue to probe the yet unexplored region where all three dots have approximately equal potential energy.

To perform this investigation, a singlet state is again initialized in the bottom dot. The state is then brought to point $S$ in Fig. 4.8(a), where the two charge degeneracies corresponding to the left and right dot align. Simultaneous 50 ns long gate pulses of varying amplitude on $V_{\mathrm{Left}}$ and $V_{\mathrm{Bottom}}$ then allow to probe the vicinity of the degeneracy of the three (1,1) configurations. The outcome of the spin measurement is then averaged over several iterations for different values of $V_{\mathrm{Left}}$ and $V_{\mathrm{Bottom}}$ and allows to construct a diagram of the spin mixing probability. The interaction time of 50 ns was chosen to neglect any influence of the initial dynamics. This measurement is performed for different values of inter-dot couplings in Fig. 4.12 and will in the following be called a spin mixing map.

In Fig. 4.12(a), the case for relatively high inter-dot coupling is shown. For small pulse amplitudes on $V_{\mathrm{Left}}$ and $V_{\mathrm{Right}}$, the electrons stay in the bottom quantum dot and no mixing is observed (top left). When the pulse crosses one of the two charge degeneracies, two lines with high mixing probability and different slopes are observed. They are identified as the $|S\rangle$-$|T+\rangle$ crossings with the configurations where one electron is transferred to either the left or right quantum dot.

For even larger amplitudes, the pulse reaches the center of the charge configurations with the electrons split between two different dots. They can be identified on the mixing map with the broad areas where the measured triplet probability has risen to $P_{\mathrm{triplet}} \approx 0.4$. In these regions, $|T_0\rangle$-$|S\rangle$ mixing is an efficient process and the singlet state is mixed on nanosecond timescales. All three charge configurations with split electrons can be clearly identified with distinct mixing regions in the diagram.

The $|T_0\rangle$-$|S\rangle$ mixing areas are observed to be separated by regions of lower mixing probability. They appear as light blue areas close to the expected positions of the charge degeneracies. The mixing probability at the end of the probe pulse depends on the ratio of the nuclear field gradient $\Delta B_Z$ and the exchange coupling $J$ of the two electrons. We therefore infer that at the position of the charge degeneracies, the exchange coupling in the two different configurations is added. The sum of the two $J$ can then be larger than the nuclear field gradient $\Delta B_Z$ between the two charge configurations. In the changed eigenbasis of $\{|T_0\rangle,|S\rangle\}$, the eigenstate is then closer to the singlet state and no mixing is observed. This observation is a strong indicator for the coherent transfer of the electrons between the dots. As we observe three clearly separated regions, the couplings are also

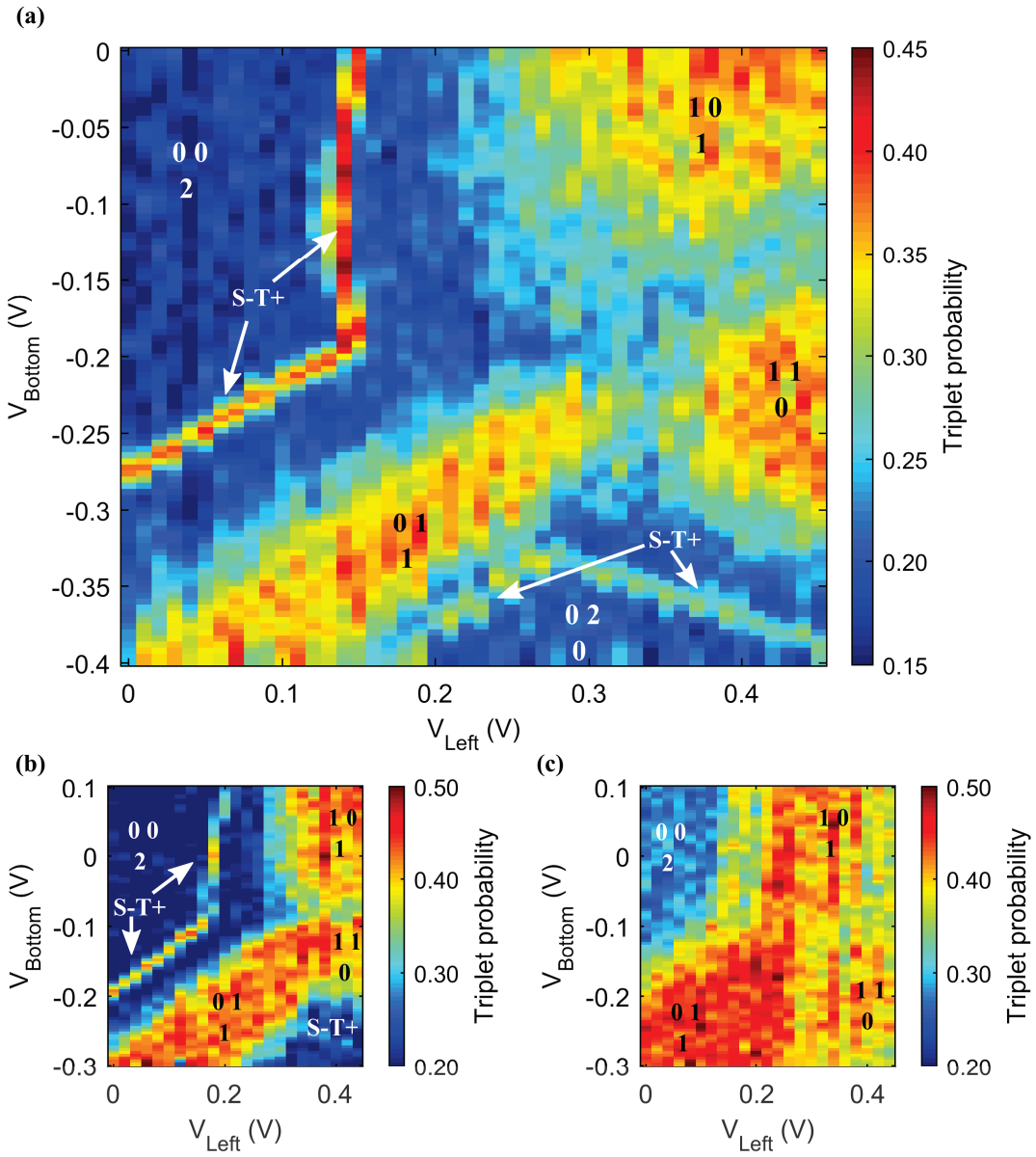


**Figure 4.12:** Spin mixing map with a singlet-probe state for the circular triple-dot with balanced tunnel-couplings. Averaged single-shot triplet probability as a function of the respective amplitudes of simultaneous 50 ns pulses on $V_{\mathrm{Bottom}}$ and $V_{\mathrm{Left}}$. Shown is the data for three different inter dot coupling strengths. All measurements were taken at a magnetic field of $B = 100$ mT. **(a)** Spin mixing map for high coupling. **(b)** Spin mixing map for medium coupling. **(c)** Spin mixing map for (relatively) low coupling.

almost perfectly balanced at a high coupling strength.

For very large pulse amplitudes on both gates, two additional mixing lines are observed, which are followed by a region without mixing. This region is identified as the configuration where both electrons are transferred to the right quantum dot. The sharp lines of strong mixing are again identified as crossings between the $|S\rangle$ and $|T+\rangle$ states. The fact, that both electrons can be transferred into another dot without inducing mixing via the transfer indicates, that the pulse rise time at the sample position is short and the induced electron transfer is fully coherent.

For smaller inter-dot coupling strength, a similar diagram is observed. The corresponding spin mixing map is shown in Fig. 4.12(b). The $|S\rangle$-$|T+\rangle$ crossings can still be identified, but are closer to the enlarged $|T_0\rangle$-$|S\rangle$ mixing regions. At the positions of the charge degeneracies of the configurations where the electron are split, the mixing probability is no longer clearly reduced. Indeed, the three different mixing regions are observed to merge for decreasing coupling. This finding affirms our analysis of the addition of the different exchange couplings at the position of the charge degeneracies.

When the inter-dot coupling is further reduced, a merging of the $|S\rangle$-$|T+\rangle$ crossings and the $|T_0\rangle$-$|S\rangle$ mixing regions is observed. The different charge configurations can therefore no longer be identified in the spin mixing map.

The different diagrams allow to clearly distinguish different coupling conditions. Note that the couplings had already been optimized for balanced inter-dot coupling. Measurements and an analysis of a slightly unbalanced tunnel-coupling configuration are given in Appendix D.2.

In this section, variable and symmetric circular inter-dot coupling of a triple quantum dot was demonstrated for the first time. The electron exchange between the quantum dots appears to be coherent, making it possible to use this model system to investigate the transport process further. The spin mixing maps can hereby be used as a tool of investigation that give information about charge configuration and exchange coupling at the same time.

## 4.5 Coherent spin transfer in a closed loop

Our prime focus with the circularly coupled triple dot was the transport of the electrons on a circular path. Firstly, it allows to study the evolution of the electron spin during the transport in our semiconductor structure with respect to the path it has taken and as a function of the distance it has been moved. The transport of individual electrons in such structures is currently an actively followed research topic. It resulted in several approaches to determine its viability and the effect it has on the electron's spin for several quantum

computing or quantum simulation schemes. In our circular triple-dot, the path of the electrons can be controlled with a high amount of precision and the travelled distance can be related to the number of tunnelling events between dots. Additionally, the circular coupling can be used to induce more complex movement strategies than previous experiments limited to linear chains of quantum dots. The implemented spin measurement hereby allows to measure the coherence of an initialized electron pair during the transfer. The manipulation in the isolated regime permits to minimize any influence of the surrounding 2DEG and gives access to a large parameter space. We will therefore be able to use our high level of control over the experiment parameters to gain insights into the transfer process as well as obtain information about environmental effects on the electrons during the path.

### 4.5.1 Transport of a coherent state in the circular triple dot system

To transport the electron spins in a closed loop, the voltage pulse scheme shown in Fig. 4.13(a) is implemented. The schematic shows the spin mixing map for the circularly coupled triple dot with the addition of markers for the start position of the two electrons localised in the bottom dot $S$ and three locations with different charge configurations 1, 2 and 3. The black arrows indicate the movement in gate voltage space. Fig. 4.13(b) illustrates the resulting movement of the two electrons in the three quantum dots for an exemplary $|\downarrow\uparrow\rangle$ state. It emphasizes the fact that the gate movements result in a series of single electron movements when the charge degeneracies are crossed. This allows to move the electrons one-by-one among the quantum dots and consequently follow a closed loop spanned by the dots.

As a reference measurement for the coherent evolution, first the nuclei induced dephasing is measured in the three charge configurations 1, 2 and 3. Recall that in this situation, the electrons are going to be split into two dots. For this measurement, an initialised singlet state is brought to each configuration by a nanosecond pulse and the spin state is then measured with spin-to-charge conversion. The averaged singlet probability as a function of the separation time $\tau_s$ in any of the three charge configurations is shown in Fig. 4.14(a). A fast decay in all three positions is observed, which was fitted with a Gaussian envelop of the form $f(x) = a * \exp\left(-\frac{x^2}{(T_2^*)^2}\right) + c$. The extracted decay constant is of the order of $T_2^* \approx 10$ ns, which is consistent with results for electrons split into double quantum dots reported in literature.[31] In the three positions we see very comparable dephasing times $T_2^*$ as well as the same final value for mixing. The dephasing time is related to the variance of the nuclear field gradient $\Delta B_Z$ as was shown in 1.6.1. This variance depends on the number of nuclei the electron interacts with and therefore the spatial extent of the electron wavefunction. We can therefore infer that the effective size of the quantum dots is very

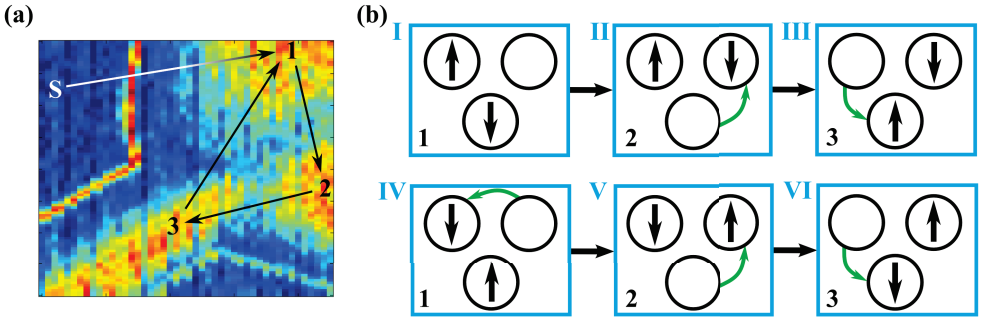


**Figure 4.13:** Schematic of the circular transport with the influence of the spin state. **(a)** Spin mixing map for the circularly coupled case that was introduced earlier. The starting and end positions of the gate movements for circular transport are indicated by $S$, 1, 2 and 3. The gate movements are shown as black arrows. **(b)** Illustration of the influence of the circular gate movements on the spin of an exemplary $|\downarrow\uparrow\rangle$ state. The different positions are marked in the bottom left and the spin positions and directions are indicated by black arrows in the respective dots (black circles). The last tunnelling event is illustrated by a green arrow.

similar. The decay constant also allows to obtain a value for the nuclear field gradient of $\Delta B_Z \approx 4$ mT using the calculation introduced in 1.6.1.

The final mixing value of the three reference measurements is related to the residual exchange coupling $J$ in the three positions. If $J$ becomes larger than $\Delta B_Z$, the final mixing value will be reduced due to the change of eigenstates observed before in 4.4.2. This measurement therefore confirms that $J$ is negligible or at least equal in the three probed positions.

The next step is the measurement of the influence of a rotational motion on the electron coherence. After electron separation, the three electron configurations are visited in rapid succession and the singlet probability is recorded at the end of each full turn. The corresponding voltage pulse sequence is shown in Fig. 4.14(b). Naturally, the effective pulse will be smoothed by the finite bandwidth of the arbitrary waveform generator and slightly affected by the influence of the high bandwidth RF-cables in the dilution cryostat and we expect a finite rise time of $\tau_{\text{rise}} = 0.9$ ns. A measurement of the output of the arbitrary waveform generator is shown in Appendix D.4 and shows that the intended movement is reproduced reasonably well for $\tau_{dwell} > 1.7$ ns. The synchronization of the pulses is investigated in Appendix D.5. We can therefore assume that the electrons will be transported on nanosecond timescales between the three charge configurations.

The resulting measurement of the singlet probability as a function of the time spent turning/separated $\tau_s$ is given alongside a stationary decay in Fig. 4.14(c) for $\tau_{\text{turn}} = 5$ ns and a magnetic field of $B = 200$ mT. Interestingly, the coherence time of the singlet

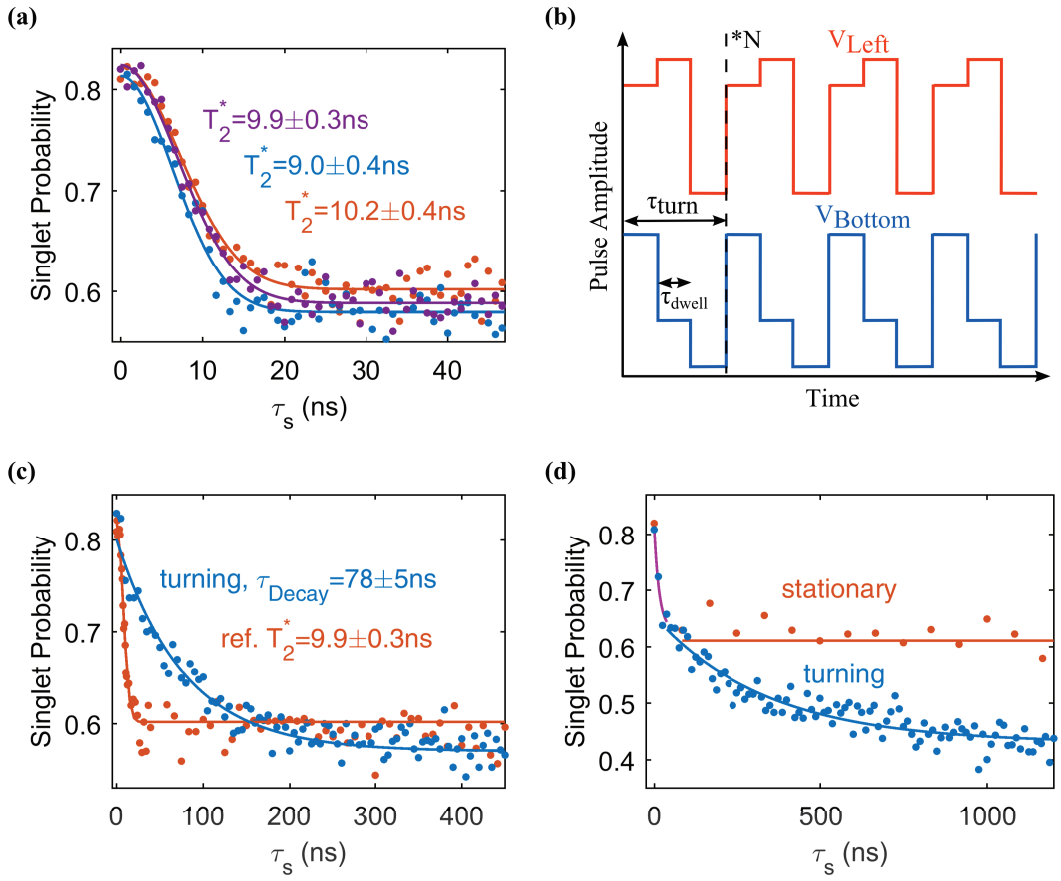


**Figure 4.14:** Decoherence in the circularly coupled spin system. **(a)** Singlet dephasing measured in each charge configuration. Averaged single-shot singlet probability as a function of the duration $\tau_s$ of a simultaneous nanosecond pulse on $V_{\mathrm{Left}}$ and $V_{\mathrm{Bottom}}$ towards positions 1 (violet), 2 (blue) and 3 (orange) shown in Fig. 4.13. The curves are fitted with the Gaussian decay given in the main text. The extracted decay times $T_2^*$ including the error of the fitting procedure are indicated in the graph and coloured according to the respective curve. **(b)** Pulse sequence applied on the two RF-plungers. The curves are offset and coloured differently for clarity. One turn is composed of visiting 3 positions in parameter space for an equal time. This sequence is repeated to construct the rotation. **(c)** Averaged single-shot singlet probability probability as a function of time spent turning $\tau_s$ in the triple dot system (blue) using the pulse sequence shown in (b). The rotation is performed with a time per turn $\tau_{\mathrm{turn}} = 5$ ns and at a magnetic field of $B = 200$ mT. The curve is fitted with the exponential decay given in the main text and the resulting time constant $\tau_{\mathrm{Decay}}$ is given in the graph including the error of the fitting procedure. A stationary singlet decay in one position is also shown for comparison (orange). **(d)** Similar measurement as in (c), but for a lower turning frequency with $\tau_{\mathrm{turn}} = 12.5$ ns and a magnetic field of $B = 90$ mT (blue). The data is fitted with two exponential decays shown in different colors (violet,blue). A stationary singlet decay in one position is also shown for comparison (orange).

state is strongly increased during the turning motion. An exponential fit of the form $f(x) = a * \exp\left(-\frac{x}{\tau_{\text{Decay}}}\right) + c$ was added to the data and reveals a decay time of $\tau_{\text{Decay}} = 78$ ns. This value is an increase of a factor of 8 with respect to the stationary coherence time. The increased coherence time leads to the deduction that the coherence is no longer limited by the hyperfine interaction with the nuclei in the three different charge configurations. The exponential behaviour is also different from the Gaussian decay observed for the reference measurements in the endpoints of the pulse sequence. This exponential decay therefore hints at a different decoherence process, that now limits the decay time of the moving electrons.

When the same measurement is performed for a lower turning frequency with $\tau_{\text{turn}} = 12.5$ ns and a lower magnetic field of $B = 90$ mT, a different behaviour is observed (see Fig. 4.14(d)). The resulting curve is no longer purely exponential, but appears to be composed of two decay times. The first decay (violet) is characterised by a fast decay time and ends approximately at the mixing value of the reference measurement $P_{\text{singlet}} = 0.6$, as observed in Fig. 4.14(a). The reference value is interpreted as the threshold for $\{|S\rangle$-$|T_0\rangle\}$-mixing corresponding to an equal mixture of the two states. The second decay (blue) features a much longer decay time and goes below the measured reference value for stationary mixing. The low singlet probability is an indication that the state leaves the $\{|S\rangle$-$|T_0\rangle\}$-subspace. We can therefore conclude, that the second decay results in a mixing with the $|T_+\rangle$ and/or $|T_-\rangle$ states during the turning motion.

The observation of two different decays leads to the conclusion that the resulting curves are a convolution of two different effects. We interpret this finding as the influence of the non-trivial dynamics of the electron transfer process. Indeed, the necessary pulse amplitudes for the change of the charge configuration are of the order of the charging energy of the quantum dot. This leads to a strong modification of the trapping potential during the transfer. Due to the finite rise time of our function generator, this potential perturbation results in a finite time window of real space movement of the quantum dot position before and after the tunnelling process. The dynamics will then be composed of a static phase where the electrons are stationary in two quantum dots, and a transfer phase where they are displaced in moving quantum dots similar to the case outlined in section 1.6.3. This real space movement of the quantum dot positions is illustrated in the schematic shown in Fig. 4.15.

This transfer phase can be identified as the origin of the enhancement of the coherence time, as well as the source of the now dominating decoherence mechanism. Huang and Hu calculated for the case of moving quantum dots, that a real space movement of a quantum dot should induce spin-flip processes that are mediated by either spin-orbit or

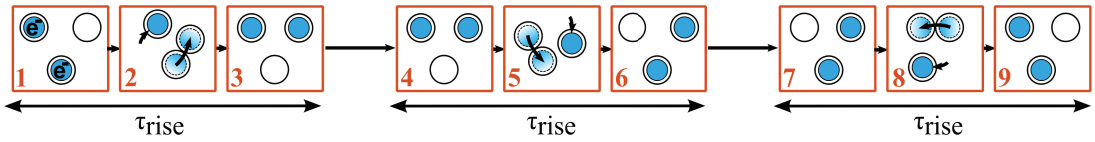


**Figure 4.15:** Schematic of the real space movement of the quantum dot positions during the transfer phase. The three single electron transfer possibilities induced by the three repeating segments of the pulse shown in Fig. 4.14(b) with a characteristic time $\tau_{\mathrm{dwell}}$ are shown by the panels 1-3, 4-6 and 7-9 respectively. The quantum dot positions are indicated by black circles and the position of the electrons are shown as blue filled circles. Black arrows indicate the quantum dot movements and electron tunnelling events. The characteristic time for the electron transfer via moving quantum dots is identified with the rise time of the pulse generator $\tau_{\mathrm{rise}}$.

transverse hyperfine couplings.[110] The energy for the spin-flip can hereby be provided by the strong driving agent, in this case the electron motion. This process explains the observed departure from a Gaussian decay envelope that would be expected for a nuclei induced dephasing mechanism. The experimentally observed exponential decay that leaves the $\{|S\rangle$-$|T_0\rangle\}$-subspace therefore signifies, that the decoherence is limited by single electron spin-flips during the motion.

At the same time, the hyperfine-induced decoherence time that was previously limiting the coherence is expected to be increased up to the µs-timescale in moving quantum dots.[110] The underlying process is considered to be similar to motional narrowing observed in liquid nuclear magnetic resonance experiments.[155] The efficiency of the motional narrowing process is expected to depend on the relation of the time spent in the stationary positions and the time spent moving. When the gate pulses are not allowed to reach their end-positions before the initiation of the next movement, the quantum dot position will no longer be static at any point in time. This explains why the coherence time can be increased beyond the stationary value for a high turning frequency with $\tau_{\mathrm{turn}} = 5$ ns where the pulse shape is found to be dominated by the pulse rise time (see Appendix D.4). The increased number of nuclei the electrons interact with then leads to a narrowing of the nuclear field gradients as introduced in section 1.6.3. We saw that the motional narrowing is only efficient as long as the speed of the electron is greater than 1 $\mathrm{m\,s^{-1}}$. In our experiment, the speed of the electrons approaches $v \approx 330$ nm/5 ns $= 65$ $\mathrm{m\,s^{-1}}$ which should lead to coherence times of several hundred nanoseconds (distance extracted from the electrostatic potential calculation). However, in the case of the circular triple quantum dot, the maximum surface area of the quantum dot structure can also limit the enhancement of the coherence time. It limits the maximum amount of nuclei that an electron can interact with. This increase of the coherence time can be estimated using the

surface area of the quantum dot $A_{\mathrm{dot}} = 20 \times 20$ nm$^2$ and the approximate surface of the quantum dot structure $A_{\mathrm{structure}} \approx 200 \times 200$ nm$^2$. The enhancement is then approximated by the ratio of the two surfaces $\sqrt{\frac{A_{\mathrm{structure}}}{A_{\mathrm{dot}}}} \approx 10$. This decoherence process should however show Gaussian dynamics and can therefore not be the limiting mechanism.

To analyse the contribution of the two decoherence effects in the different phases of the transfer, we will first isolate the effect of the static phase in the limit of low turning frequency. In the following, we will probe the electron coherence during the moving phase and measure its dependence on the external parameters. The analysis will be complemented by a discussion that excludes alternative explanations for the observed behaviour during the motion.

### 4.5.2 Direct observation of motional narrowing in the circular triple quantum dot

To isolate the effect of the static phase on the electrons, we have to limit as much as possible the turning motion while visiting the three charge configuration for an equal amount of time. A pulse sequence that achieves this requirement is shown in Fig. 4.16(a). The pulse performs a single turn in the structure, but the time spent in each charge configuration is changed for different experiments. This allows to probe the spin dephasing as a function of the separation time $\tau_s$ in the three quantum dots.

The resulting measurement of the singlet probability is presented in Fig. 4.16(b) as a function of time required for the turn. The data fits well with a Gaussian decay with a decay constant of $T_2^* = 16$ ns. It has to be compared to the timescale of a stationary decay in one of the charge configurations and is observed to be significantly longer. This improvement of the coherence time is explained by the fact that several charge configurations are visited. Indeed, when considering the interaction with a three times larger amount of nuclei, the variance of the nuclear field gradients should be reduced by a factor of $\sqrt{3}$. The exceptional agreement of the experimentally found enhancement with the theoretically predicted factor of $\sqrt{3}$ can be considered a "smoking-gun" for a motional narrowing process due to the displacement in the triple dot structure. The Gaussian decay is also expected from a nuclei induced dephasing process and supports our interpretation. Not only does this affirm our assumption of the enhancement of the coherence time via a motional narrowing process, but it also shows that each electron visits the three distinct quantum dots during the pulse sequence.

However, this leads to only an enhancement of the coherence time by $\sqrt{3}$, which is significantly lower than the one observed in the experiment when continuously turning. The enhancement can therefore not be explained only by the increased configuration space of the three charge configurations and must therefore be attributed to the real space

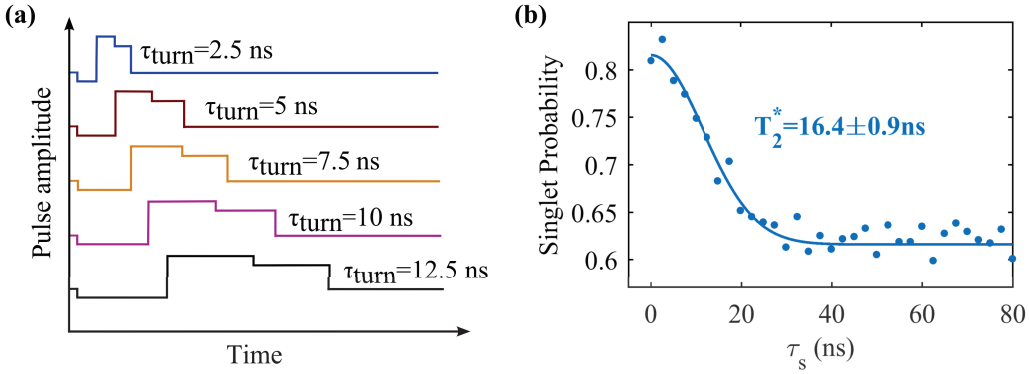


**Figure 4.16:** **(a)** Pulse shape for the investigation of the motional narrowing process. Only the voltage pulse on $V_{\text{Left}}$ is shown (see Fig. 4.14(b) for the corresponding voltages applied on $V_{\text{Bottom}}$). The pulse performs one turn on the spin mixing map with different turn times $\tau_{\text{turn}}$ to change the time spent in each configuration. **(b)** Averaged single-shot singlet probability as a function of $\tau_s$ using the gate pulse introduced in (a). A Gaussian fit was performed on the data and the extracted decay time constant is given in the graph. The error is given by the fitting procedure.

motion discussed earlier. Additionally, no decay below the reference value of $P_{\text{singlet}} = 0.6$ attributed to the $\{|S\rangle$-$|T_0\rangle\}$-subspace is observed. The consideration of the transfer phase is therefore vital for the explanation of the enhanced coherence time as well as the observed decay.

### 4.5.3 Variation of the turning frequency

The investigation of the static phase revealed a hyperfine limited coherence time identified by a gaussian decay of the singlet probability as a function of separation time. During the turning motion however, the coherence time showed an exponential dependence on the time spent turning. This decoherence process associated with the motion of the electrons during the transfer phase will now be investigated in greater detail.

First, a systematic variation of the turning frequency at a fixed magnetic field of $B = 90$ mT was performed for the continuous turning motion. This allows to discriminate between a process that depends on the travelled distance and a process that depends on the travelling time. The singlet probability for continuous turning motion is given as a function of number of turns in Fig. 4.17. The turning frequency is varied and indicated in the graph via the time necessary to complete one turn $\tau_{\text{turn}}$. All decays are fitted with a single exponential. It is evident, that the quality of the fit is good for the two highest turning frequencies with $\tau_{\text{turn}} = 2.5$ ns and $\tau_{\text{turn}} = 5$ ns. Here the singlet probability therefore exponentially decays as a function of time.

For lower turning frequencies, a single exponential no longer fits the data well. The

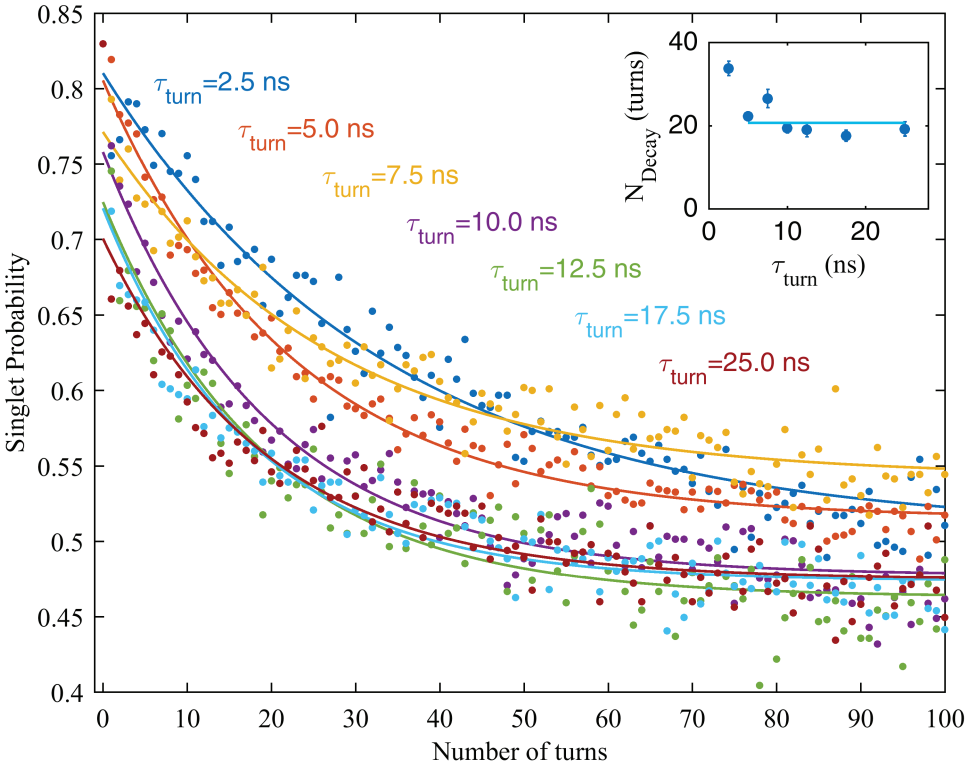


**Figure 4.17:** Averaged single-shot singlet probability during the turning motion as a function of number of turns. The different curves were taken for different values of $\tau_{\mathrm{turn}}$ which are indicated in the graph and are coloured differently for clarity. The external magnetic field is $B_Z = 90$ mT. Exponential fits were applied to the data and are coloured equally as the respective data points. **Inset :** Decay constant $N_{\mathrm{Decay}}$ in units of performed turns as a function of $\tau_{\mathrm{turn}}$. The statistical errorbars of the fit procedure were added to the extracted decay constants. The linear fit (light blue line) emphasizes the independence of the decay constant of $\tau_{\mathrm{turn}}$.

singlet probability drops sharply in the beginning followed by a slow exponential decay that was identified with leaking out of the $\{|S\rangle$-$|T_0\rangle\}$-subspace. The first decay is identified with the influence of the static phase and will be disregarded in the following. The second slow decay shows a strong dependence on the number of turns and dominates the performed fitting procedure for all values of $\tau_{\mathrm{turn}}$. The performed exponential fit therefore reveals information about the slow decoherence process associated with the transfer phase.

The extracted fit parameters for the decay constant $N_{\mathrm{Decay}}$ are given in the inset of Fig. 4.17 as a function of $\tau_{\mathrm{turn}}$. A constant fit was added to the data to emphasize that the decay constant in units of the number of turns is almost independent of the turning

frequency and is therefore not related to the time spent separated. On the contrary, the observed dependence on the number of turns indicates, that the process leading to the leaking out from the $\{|S\rangle$-$|T_0\rangle\}$-subspace is mostly related to the travelled distance. The number of turns can be converted to a path length using the distance of the estimated potential minima positions in the electrostatic calculation of $d_{dot} = 110$ nm. For a decay constant of $N_{\mathrm{Decay}} = 20$ turns this results in a travelled distance of $l_{\mathrm{travelled}} \approx 6$ µm. This distance is comparable to the spin-orbit length measured in similar hetero-structures.[61,156]

For the fastest investigated turning frequency with $\tau_{\mathrm{turn}} = 2.5$ ns, the decay time in units of completed turns is significantly increased. However at this frequency, the effect of the finite rise-time of the pulse generator strongly warps the pulse shape. The resulting pulse is then confined to the center of the spin mixing diagram. This reduced pulse amplitude can reduce the effective distance travelled by the electrons. This justifies to disregard this point for the analysis of the turning frequency dependent mixing process.

It was therefore shown that the second decay that leads to a leaking-out of the $\{|S\rangle$-$|T_0\rangle\}$-subspace depends only on the travelled distance of the electrons. From an estimation of the distance between the quantum dots, the characteristic length associated with the decoherence process is estimated to be $l_{\mathrm{travelled}} \approx 6$ µm. For high turning frequencies with $\tau_{\mathrm{turn}} < 7.5$ ns, this process is found to become the dominant decoherence process resulting in a single exponential decay of the singlet probability. We interpret this finding as the regime where the evolution is dominated by the transfer phase which is consistent with the rise time of our pulse generator. This finding allows to isolate this decoherence process in the following measurements.

### 4.5.4 Magnetic field dependence of the coherence time during circular motion

Having isolated the transfer phase in the measurements by an increase of the turning frequency, we can study the dependence of the distance dependent decoherence process on the external magnetic field. While the coupling to the nuclei should be hardly influenced by this control parameter, the magnetic field would act as comparative energy scale for effects such as the spin-orbit coupling or lateral field gradients.

The measured curves are shown in Fig. 4.18(a) and were fitted with exponential decays. We chose to perform the measurement with characteristic turning time of $\tau_{\mathrm{turn}} = 5$ ns to limit the influence of pulse rise time and at the same time remain dominated by the distance dependent decoherence process. The extracted fit parameters for the decay time constant are given in Fig. 4.18(b) and a linear fit has been added to the data.

The measured data shows a clear tendency and seems to agree very well with a single exponential decay in the full measurement window. For the curve at zero magnetic field, the

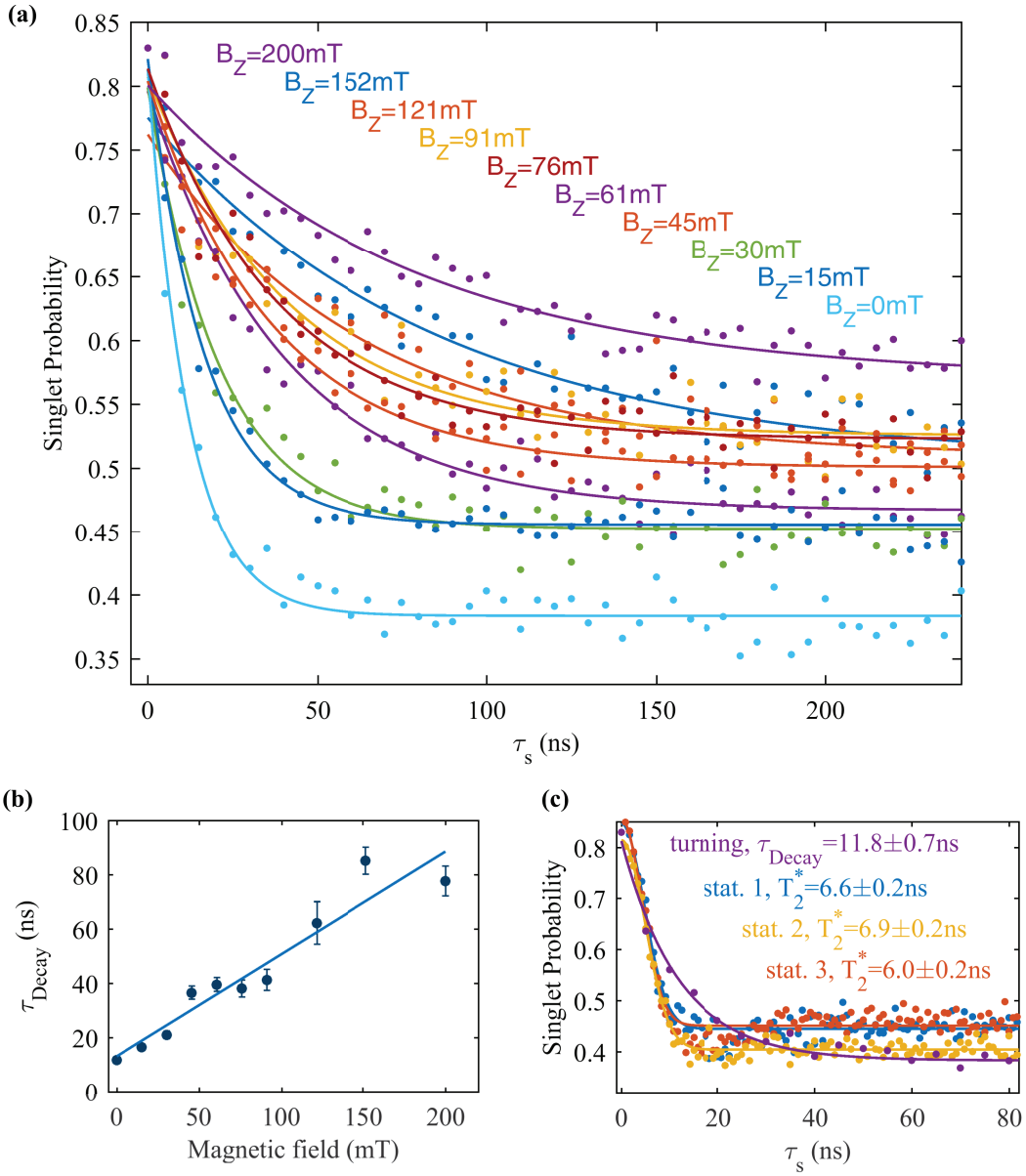


**Figure 4.18:** **(a)** Averaged single-shot singlet probability during the turning motion as a function of turning time. The magnetic field is varied between curves with different colors and the corresponding values are given in the graph. The time per turn is $\tau_{\text{turn}} = 5$ ns during the rotation. All curves were fitted with an exponential decay. **(b)** Extracted decay-time $\tau_{\text{Decay}}$ as a function of magnetic field. The errorbars associated with the fitting procedure were added to the data. The linear fit (dashed blue line) emphasizes the linear dependence of the decay time with magnetic field. **(c)** Zero field measurement of the influence of the turning motion on the singlet probe and the corresponding stationary reference decays for all three dot combinations. The data has been fitted with exponential decays and the decay constants are given in the graph.

singlet probability drops to 0.4 almost immediately on a timescale very much comparable to the reference decay. In fact it is almost indiscernible from the reference measurements performed at zero magnetic field in a stationary split electron position shown in Fig. 4.18(c). While the dephasing time is reduced for low magnetic fields to about $T_2^* \approx 6$ ns in all stationary cases and the zero field rotation still protects the singlet state, the improvement is only a factor of 2.

The final mixing value of the reference measurements at zero field also gives the threshold for equal probability of measuring any of the two electron spin states $\{|S\rangle,|T_0\rangle,|T_+\rangle,|T_-\rangle\}$. Comparing this threshold with the final mixing value of the measured decays allows to determine the nature of the mixing process. Mixing with both the $|T_+\rangle$ or the $|T_-\rangle$ states is found. This excludes the possibility of erroneously anticrossing the $|T_+\rangle$ state during the displacement with a Landau-Zener type process. This supports our identification of the observed mixing process that leads to singlet probabilities below 0.6 with a spin-flip of one electron.

When the magnetic field is increased, the decay time seems to increase linearly up to a maximal value at the highest investigated field. The improvement is measured for the decay constant of the exponential fit as well as for the projected final mixing value for infinite turns. Additionally the improvement in the dephasing time with magnetic field is also evident for short timescales. The absence of different timescales indicates, that the application of a higher magnetic field both reduces the $\{|S\rangle$-$|T_0\rangle\}$ mixing, as well as the mixing with the $|T_+\rangle$ and/or $|T_-\rangle$ states within the given parameter space. Sadly, at higher magnetic fields, the implemented spin read-out technique became inefficient because of the application of the magnetic field perpendicular to the 2DEG plane. It should however be possible to overcome this technical restriction in future experiments by changing the magnetic field direction to determine if the decay time would saturate for higher magnetic field values.

The magnetic field dependence of the decoherence process is consistent with the assumption of single spin-flips during the transfer phase mediated by lateral nuclear field gradients or spin-orbit interaction. The Zeeman energy of the electron spin then has to be overcome by the external excitation and is expected to reduce the spin-flip probability. A magnetic field dependent spin-flip rate associated with a tunnelling process was recently observed by Maisi et al. in double dot experiments and attributed to spin-orbit coupling.[157] In their experiment, they similarly observed a reduction of the spin-flip rate with increasing magnetic field. While the dependence was not linear, the difference can be explained by different excitation energy spectra in the two experiments. In their case the tunnelling was excited by thermal effects in a stationary quantum dot configuration. In our case however,

the quantum dots are excited by the strong driving agent necessary to induce the circular motion. The excitation spectrum is then expected to be related to the specifics of the pulse and can therefore lead to qualitatively different dynamics.

In conclusion, the coherence of a singlet state that is subject to a turning motion is demonstrated to be protected by a large external magnetic field. An enhancement of the coherence time was observed for magnetic fields that are significantly larger than the effective magnetic field of lateral nuclear field gradients and spin orbit interaction. It is attributed to a protection from incoherent spin-flips via the increasing Zeeman energy. The origin of the spin-flips is associated with an excitation induced by a motion/deformation of the quantum dot potential during the performed path and is mediated via spin-orbit coupling or transverse nuclear field gradients. The energy necessary to perform the spin-flip is provided by the external driving agent that induces the motion.[110] The observed linear dependence of the coherence time with magnetic field is hereby attributed to the specifics of the excitation spectrum of the external driver.

### 4.5.5 Discussion of alternative explanations for the observed spin evolution

The enhancement of the coherence time was identified with the presence of motional narrowing in our experiment, while the dominant decoherence process is attributed to single spin-flips induced by a real space motion of the quantum dot. In this section we will discuss alternative explanations for the observed behaviour which have to be excluded for the clear identification of the physical processes.

#### Effect of the inter-dot coupling on the adiabatic passage of the electrons

First, we will exclude the possibility of non-adiabatic transfer via a variation of the inter-dot coupling strength. To investigate the possibility of non-adiabatic electron transfer, the turning motion was also performed for different values of the inter-dot tunnel-coupling $t$. The corresponding measurement is shown in Fig. 4.19 for the coupling conditions that were shown before in Fig. 4.12 and correspond to three conditions from relatively weak tunnel-coupling to relatively strong tunnel-coupling. The fourth curve is for the case of very weak inter-dot coupling strength (green). A spin mixing map for this case can be found in Appendix D.3.

For the three conditions with higher coupling, the previously seen enhancement of the coherence time during the turning motion is observed. A small differences in the decay constant $\tau_{\mathrm{Decay}}$ is extracted by the fits and the coherence time seems to be increased for the case of high tunnel-coupling (blue). The measured increase of the coherence time with increasing tunnel-coupling is consistent with the two decoherence processes that we

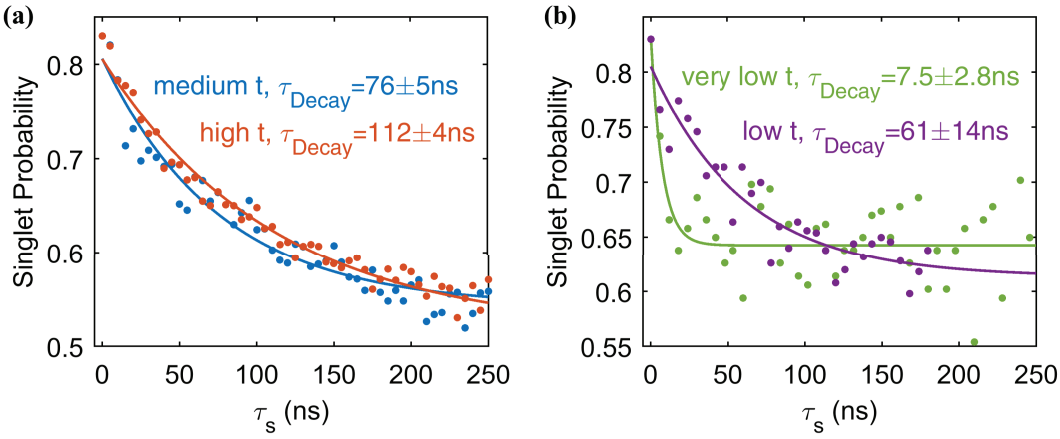


**Figure 4.19:** Averaged single-shot singlet probability during the continuous turning scheme for different configurations of the inter-dot tunnel-coupling $t$. The curves in (a) and (b) were taken on different thermal cycles of the same sample and have slightly different turning frequency. The magnetic field is B=90 mT in all configurations. **(a)** Cases of high (orange) and medium (blue) tunnel-coupling $t$ corresponding to the situations from Fig. 4.12(a,b). The time per turn is $\tau_{\text{turn}} = 5$ ns. **(b)** Cases of very low $t$ (green) and low $t$ (violet). The spin mixing map for the case of very low $t$ can be found in Appendix D.3. The spin mixing map for the case of low $t$ can be found in Fig. 4.12(c). The time per turn is $\tau_{\text{turn}} = 6$ ns.

proposed. For higher tunnel-coupling, the barrier between the quantum dots is lower and the inter-dot distance is expected to be reduced.[92] We can therefore relate the increase of the coherence time to a reduced effect of the distance dependent decoherence process during a fixed amount of turns.

The curves corresponding to low $t$ (violet) and to very low $t$ (green) in Fig. 4.19(b) were taken on a different thermal cycle of the same sample and have different measurement visibilities compared to the cases of high and medium $t$ shown in Fig. 4.19(a). The extracted decay time can however be compared to the cases of higher coupling strength due to the very similar rotation procedure and external parameters. Most importantly, we observe a strongly reduced decay constant when the tunnel-coupling is very low compared to the case of low $t$.

This experimental finding is important as the inter-dot coupling strength is related to the adiabaticity of the electron movement around the circle. We believe, that the relatively small influence of the tunnel-coupling parameter on the resulting decay of the three curves with higher coupling is an indicator for the adiabaticity of the electron tunnelling process for the three parameter spaces. Specifically we see no sharp drop of the dephasing time that would be expected if the electrons can no longer follow movement imposed by the gate pulses. However in the case of very low tunnel-coupling (green), the singlet probability drops

very fast and only decays slowly afterwards. We therefore conclude, that the adiabaticity criterion is fulfilled for the higher coupling strengths. This finding excludes incoherent tunnelling events as a source of decoherence.

Additionally this investigation excludes an alternative way of protecting the singlet from the nuclei induced dephasing. For the case of high coupling shown in Fig. 4.5(a), a reduced mixing probability is observed for gate voltage positions close to the inter-dot charge degeneracies. For high turning frequencies, the warping of the effective path leads to an increasing amount of time spent in these low mixing probability regions. This can lead to an improvement of the coherence time. This possible explanation is however contradicted by the observation of an enhancement of the coherence time for lower coupling strengths. Especially for the case of low tunnel-coupling, no regions where no mixing occurs can be observed. However this case also led to a significant increase of the coherence time. This possible explanation for the enhanced coherence time via a variation of the exchange energy can therefore be excluded.

#### Influence of varied path dynamics on the coherence time

In the previous sections we proposed an enhancement of the coherence time via a motional narrowing process due to the real space movement of the quantum dot positions. Another possibility for such an enhancement was recently proposed by Drummond et al. who considered an electron spin pair moving on a circular path.[158] They noted that the spatial exchange of the two electrons after a full circle should lead to a reversal of the interaction with the nuclear spins. This effect is similar to echo sequences already performed in lateral quantum dots that led to extensions of the coherence time exceeding 1 microsecond.[31] This enhancement of the coherence time would however be constrained to circular motion. We will therefore investigate the influence of varied path dynamics on the spin coherence.

Firstly, the extension of the coherence time did not depend on the turning direction (clockwise/anticlockwise). A direct comparison between clockwise turning and a succession of clockwise (CW) and anticlockwise (ACW) turns that are sequenced together is given in Fig. 4.20(a). No significant dependence of the decay constant on the turning direction is observed.

Secondly, the turning motion was compared to a one-dimensional movement within a charge configuration and between two different charge configurations. The investigated pulses are schematically shown on the spin mixing map in Fig. 4.20(b). The position of the electrons is hereby repeatedly changed between the endpoints of the arrows. For a good comparison, the dwell time in each pulse end-position is set to a time $\tau_{\mathrm{dwell}} = 2.5$ ns for a constant ratio of pulse rise time to stationary waiting period. The averaged single-shot

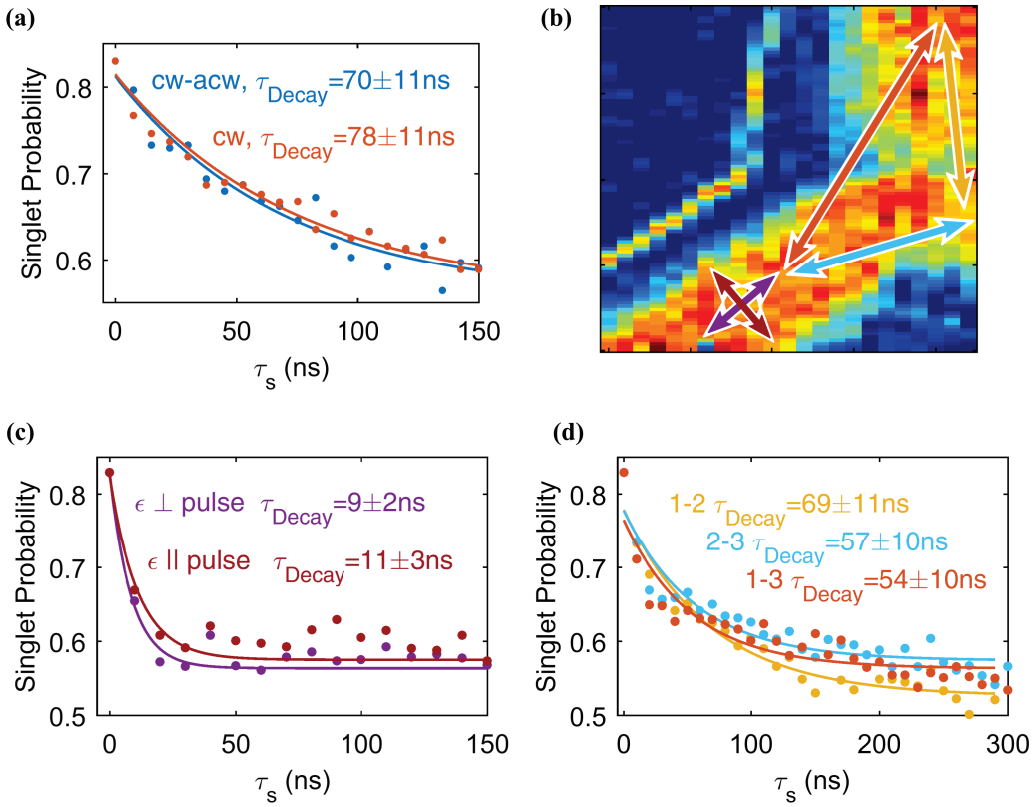


**Figure 4.20:** **(a)** Averaged single-shot probability as a function of separation time $\tau_s$ for different turning directions. Comparison of alternating clockwise-anticlockwise (cw-acw) rotation to constant clockwise (cw) rotation. The magnetic field is $B = 90$ mT and the time per turn is $\tau_{\text{turn}} = 7.5$ ns. **(b)** Spin-mixing map for the medium coupling regime to exemplify different movement strategies. The arrows show the end-positions of the different pulses in (c) and (d) and are equally coloured as the corresponding curve. **(c)** Averaged single-shot probability as a function of separation time $\tau_s$ while moving within one charge configuration as shown in (b). The direction of the movement is either perpendicular ($\varepsilon$ $\perp$) or parallel ($\varepsilon||$) compared to the detuning axis (indicated in the graph and in (b)). The dwell time at the endpoints of the pulses is kept constant at $\tau_{\text{dwell}} = 2.5$ ns. **(d)** Averaged single-shot probability as a function of separation time $\tau_s$ while moving between two charge configuration as illustrated by the arrows in (b). The dwell time in each charge configuration is kept constant at $\tau_{\text{dwell}} = 2.5$ ns.

probabilities as a function of separation time $\tau_s$ are shown in Fig. 4.20(c,d) and are coloured equally as the corresponding arrow in Fig. 4.20(b) for clarity. All curves were fitted with a single exponential decay and the decay time $\tau_{\mathrm{Decay}}$ alongside the error from the fitting procedure are given in the graphs.

For the case of movement within one of the charge configurations shown in Fig. 4.20(c), the singlet probability drops fast to a value close to the previously established reference $\{|S\rangle$-$|T_0\rangle\}$-mixing threshold. The time scale for this decay is of the same order or faster than the previously established reference decay value $T_2^* \approx 10$ ns. This seems to not depend much on the direction of the movement, as either movement perpendicular to the detuning axis $\varepsilon$ or parallel to the detuning axis results in mostly the same curve. The coherence time is therefore not increased when the electrons are shaken in their stationary positions. We interpret this observation as the strongly reduced surface area that is visited in this scheme and the resulting small effect of motional narrowing.

However, a significant improvement of $T_2^*$ is observed when the pulse sequence changes between two charge configurations and electron tunnelling is involved as evidenced by the measurements presented in Fig. 4.20(d). For all three cases, dephasing times below the one for the turning motion are observed, but more than a factor of two larger than in the case of the stationary dephasing. This observation directly contradicts the proposed scheme by Drummond et al. that should not show an enhancement of the coherence time for such a motion.

This large improvement is also inconsistent with motional narrowing due to (instantaneous) tunnelling. As in principle only one electron should be involved in the tunnelling process between two configurations, only a small contribution of motional narrowing is expected. In fact the situation is considered similar to a case of two dots with unequal sizes, of which one has a narrowed nuclear field distribution of a factor of $\sqrt{2}$. In this case an improvement of the coherence time of around 15% is expected. The observed dephasing time is however much greater than this expected value.

This measurement can however be explained with the motional narrowing during the transfer phase. Due to the large pulse amplitudes used to transfer an electron and the resulting change in the potential landscape both electrons experience a real space movement. Then the extension of the decay time is consistent with the process of motional narrowing observed before. The potential variation imposed by the gate movements thus leads to a significant displacement of the quantum dot potential even in the case of the one-dimensional movement.

We therefore conclude, that the enhancement of the coherence time is not constrained to circular movement. One-dimensional movements similarly lead to improvements of the

coherence time. This allows to reject the spin echo scheme proposed by Drummond et al. for the explanation of the observed behaviour during the turning motion and supports the assumption of a motional narrowing process.

### 4.5.6 Summary of the obtained results on the coherent transfer

In this section, results on electron transfer between three tunnel-coupled quantum dots were presented. A significant increase of the coherence time upon movement was observed that demonstrates a suppression of the hyperfine interaction with the nuclei. The origin of the enhancement is attributed to motional narrowing due to the displacement of the electrons. The observed large increase of the coherence time for continuous turning motion is identified as real space movement of the quantum dot positions during the electron transfer. For low turning frequencies (limit of one turn) we find an enhancement of $\sqrt{3}$ of the coherence time, which is consistent with a motional narrowing process in the limit of instantaneous transfer.

For high turning frequencies, the dominant decoherence process was observed to depend mostly on the travelled distance of the electrons. This decoherence process showed strong dependence on the externally applied field. The dependence of the coherence time on high external magnetic fields indicates an incoherent single electron spin-flip process as the source for the observed behaviour. Qualitative agreement is found with a theory of spin relaxation in moving quantum dots subject to a disordered path, that was proposed in the literature.[110] For the highest applied field of $B = 200$ mT, a maximal value of the coherence time of up to 80 ns was observed. This corresponds to an estimated displacement of $l_{\mathrm{travelled}} = 5$ µm.

Several sources of systematic errors can be excluded for the interpretation of our results. Due to the behaviour of the coherence time with respect to the inter-dot coupling strength, it can be assumed that the electrons traverse the circle in a adiabatic manner and that the rise time of our gate pulse is slow enough with respect to the tunnelling time between dots. We could also exclude gate synchronization errors when the phase between the two motion inducing gate sequences was varied and a pattern that matches well with the expected behaviour was observed. Furthermore, the dependence of the measured singlet coherence time on the varied control parameters allowed to exclude other possible explanations for the enhancement of the coherence time.

We can therefore conclude that we indeed performed a rotational motion on the electrons. The observed decoherence is fully explained by considering a movement of the quantum dot positions during electron transfer. This motion induces an enhancement of the coherence time via motional narrowing, while at the same time opening a new decoherence channel

via an observed spin-flip mechanism. Other proposed explanations found in the literature could be excluded based on the dependence of the coherence time on the varied parameters. Specifically, the enhancement of the coherence time seems to not be related to the exchange of the electron positions during the circular motion, as similar enhancements were observed for one-dimensional motion. The coherent evolution in the triple quantum dot and the resulting decoherence processes are therefore well identified. This first observation of coherent electron spin transport in a two-dimensional array is expected to pave the way for the investigation of long range coherent electron transfer.

## 4.6 Conclusion

In this chapter, our results on the spin manipulation in the isolated regime were presented. A spin read-out technique for a two-electron spin state was introduced that is compatible with the isolated manipulation. This allowed to perform coherent spin evolutions in the investigated structures and measure the resulting spin state. The reduced subspace of charge configurations is found to allow novel spin manipulation schemes. Specifically, the simplified access to the tunnel-coupling between two quantum dots was shown to allow coherent oscillations of a two-electron spin state at the position of a "sweet spot". The resulting dynamics revealed an increase of the number of coherent oscillations within the limited coherence time. It was shown, that this is the result of a decoupling of the coherent evolution from charge noise along the detuning axis, which previously limited similar experiments.

In the second part, the spin of electrons in an isolated triple-quantum dot was investigated. It was shown, that the two-electron spin-state can be used as probe for the exchange coupling via the observation of the mixing probabilities in different charge configurations. This characterisation method allowed to fine tune the quantum dot array for balanced high inter-dot coupling. The transport of electron spins in this regime was then investigated. We observed an enhancement of the coherence time during transport that was identified to originate from a motional narrowing process. The magnitude of the enhancement revealed the non-trivial exchange of the electrons between the quantum dot. Specifically, it was found that during the transfer process, the variation of the gate voltages induces a motion of the quantum dot position. This moving quantum dot is observed to explore a large surface in the quantum dot structure during an induced circular motion. The real space motion is also identified as the origin for a newly introduced decoherence mechanism via single electron spin-flips. This mechanism is found to depend mostly on the travelled distance and is explained with a theoretical model of moving quantum dots subject to spin-orbit coupling or transverse hyperfine gradients from the literature.

This is the first demonstration of coherent electron transfer in a quantum dot array over distances of several micrometers. The observed enhancement of the coherence time promises a path to increase the system size of quantum dot structures. Additionally, it is expected to allow long range coherent transfer between distant quantum dot systems. Finally, the introduced tools for the characterisation of the exchange coupling and spin coherence are expected to facilitate the coherent operation of multi-dot systems in future experiments.

# CHAPTER 5

## Conclusion and perspectives

In this thesis, the charge and spin dynamics of electrons in multiple coupled semiconductor quantum dots were explored. The utilized fabrication methods of the gate defined nanostructures used to trap the electrons create a link to the highly developed field of information technology. This connection and the small size of the structures has been regarded as an indicator for a good scaling behaviour of qubit implementations based on the spin of electrons in such structures.[21] Indeed, the lifetime of spin states in the investigated structures can approach seconds,[95] while nanosecond spin rotations have been demonstrated in this thesis as well as in other laboratories.[31–33,114] However, there still remain great challenges to increase the spin coherence time, to find suitable manipulation protocols for large systems and to integrate a scalable qubit on a two-dimensional lattice.

We therefore focused on the investigation of quantum dot structures where the electrons can be transported within an artificial lattice to investigate the physical processes that appear when the system size is increased. Our focus hereby lied on the implementation of circular coupling of quantum dots that allows to extend present manipulation schemes in linear arrays to a scalable system. To cope with the increasing complexity of higher quantum dot numbers, we developed a manipulation approach, that we call the isolated regime. Here the electrons are completely decoupled from the surrounding electrons and confined to an artificial structure. The electron number in this configuration is fixed and can be deterministically initialized. We showed that this regime allows to simplify the charge control in quantum dots via the reduction of the number of available charge states. At the same time, the tunnel-coupling is introduced as an effective new control parameter for the interaction between electrons. We showed how the variation of the tunnel-coupling can be identified from the charge and spin dynamics. Then we used this parameter to implement the initially proposed spin rotation scheme by Loss et al.[21] and showed its

superiority over conventional spin rotation schemes relying on changes of the detuning. Previous schemes were limited by charge noise along the manipulation axis and therefore showed a reduction in the coherence time when the manipulation speed was increased. The newly developed manipulation is no longer limited by this process and therefore promises further improvements regarding the viability of electron spins as qubits. The developed technique is also not dependent on the technical implementation of the quantum dot and should be fully applicable to next generation quantum dot systems such as in isotopically purified silicon.

An equal improvement in the control of quantum dot systems in the isolated regime was observed for larger quantum dot systems. In this work we showed the implementation of two triple quantum dot systems in a linear and a circular arrangement. In both cases, the isolated regime proved to allow control over the path of each electron in the gate defined structure. This demonstrated simplification of the charge control is expected to render the operation of larger quantum dot structures feasible. The measured system response is still compatible with the established theory of the constant interaction model. This allowed to extract quantitative information about the charge positions and energy scales in the system. The direct experimental access to the tunnel-coupling allowed to define a circularly coupled triple quantum dot with balanced inter-dot barriers for the first time. Using the spin state of a two-electron pair as a probe, the coupling energy can be analysed and tuned with a high accuracy. The coupling speed could be increased to gigahertz frequencies, which allows nanosecond control over the charge state and therefore the electron path.

This well defined coupling condition was the prerequisite for an analysis of the coherence of spin transfer processes in gate defined structures. Indeed, due to the short coherence times of electron spins in the investigated AlGaAs/GaAs quantum dots, the coherent electron transport was supposed to be limited to timescales below 10 ns. However, in our investigation of the coherence of the electron transfer of a two-electron pair we could show that the coherence time was effectively increased during movement. We measured a coherence time of $T_2^* = 78$ ns corresponding to a travelled path of 5 µm at 100 $\mathrm{m\,s^{-1}}$. This means that the previously dominant decoherence mechanism due to the hyperfine interaction is reduced for the travelling electrons.

We proceeded to identify the two now limiting decoherence mechanisms and their dependence on the control parameters. The first process is shown to be related to a motional narrowing of the hyperfine interaction with the nuclei. The nuclei generate an effective magnetic field in the quantum dots, which is broadened by their intrinsic dynamics. This broadening has been found to limit the coherence time in previous experiments. Increasing the number of nuclei is therefore expected to reduce the variance of the nuclear

magnetic field and should lead to longer coherence times. We could experimentally show that this leads to the expected $\sqrt{3}$ improvement of the spin coherence time when the electrons are mostly confined to three stationary quantum dots. However, during continuous tunnelling events, the improvement was greatly enhanced. This experimental finding can be explained with a real space movement of the quantum dot positions during the electron exchange. This movement lets the electron explore a large surface area in the artificial structure and therefore narrows the effectively explored nuclear field distribution.[110] The tunnelling of the electrons between quantum dots is therefore found to be not an instantaneous process, but related to a significant real space movement of the electron during the external gate voltage modulation. This insight into the tunnelling process is expected to influence future control schemes.

The observed enhancement of the coherence time during movement hints at the possibility to use electrons as a quantum mediator between distant quantum systems. In such a scheme, information is encoded onto the electron spin, which is then transferred via tunnelling events in an array to a distant site. The motional narrowing during movement then allows to preserve the spin information over distances that were previously not expected. At the target position, the information can then be directly exchanged and preserved via echo schemes for several microseconds.[38]

At the same time, the second observed decoherence process is found to limit the viability of such a scheme. It was identified as a process that depended mostly on the number of tunnelling events and therefore on the distance of the travelled electrons. The mechanisms also showed a strong dependence on magnetic field, which increased the coherence of the electrons almost linearly even for high magnetic fields of $\approx 200$ mT. The experimental findings support a process involving single electron spin flips mediated via transverse effective magnetic fields. These fields have their origin in the spin-orbit or the hyperfine interaction and are expected to limit the coherence of travelling electrons in disordered systems.[110] The disorder is hereby introduced by the strong driving of the electrostatic potential during the imposed path by the variation of the gate voltages in the presence of a random donor potential.

Both decoherence mechanisms are therefore related to the real space movement of the electron in the strongly driven potential landscape. While the hyperfine interaction is found to be reduced with increasing movement speed and distance, the other has the inverse dependence. These experimental findings are expected to be critical for the development of large interconnected quantum systems based on electron spin qubits. The transport of spin information via electron tunnelling events in quantum dot arrays has been shown to be a viable process. The limitations concerning the coherence of this process were experimentally

observed and allow to develop strategies to counter the underlying mechanisms.

As the disorder of the potential is considered to be an important part in the distance dependent decoherence process, dopant engineering of the heterostructure could result in longer coherent transport distances. A promising scheme would hereby be the removal of the dopant atoms while at the same time inducing the electron gas via electrostatic gating. The resulting smooth potential should allow long range transport over distances exceeding the measured limit of $l_{\mathrm{travel}} \approx 6$ µm. Similarly, using semiconductor structures with weaker nuclear field gradients and no spin orbit coupling like silicon removes the coupling of the spin to its real space movement and is expected to lead to an even greater improvement of the coherent transfer distance.

When the electrostatic disorder of the system is reduced, a larger loop is also expected to lead to non-abelian phases when the electrons are subject to a turning motion. Such schemes were proposed and evaluated by San-Jose et al.[159] and Golovach et al.[160] and rely on the geometric phases that are acquired during transport on a closed loop. These phases stem from the spin-orbit interaction present in the material and should lead to coherent spin evolutions at zero magnetic field. While they were not observed in our experiments, the demonstrated possibility to coherently displace electrons on a loop should allow their investigation in future experiments.

The enhanced control over the charge states in the isolated regime also allows to increase the controllable system size of quantum dot structures. Based on the results obtained in the investigated artificial quantum dot structures, we designed a large rectangular quantum dot array featuring a total of nine tunnel-coupled quantum dots. Such a system is expected to give valuable insights into the viability of spin qubits as a base for quantum simulators. At the same time it allows to investigate transport phenomena which are based on a rectangular grid. This permits to identify effects related to the direction of the movement, which are expected for spin-orbit coupling in our structure. Finally, it will allow to develop techniques for the control of increasingly large quantum dot systems. First preliminary results have already shown the control over 7 different quantum dots in the structure. Improvements in the control of the sample are expected to increase the available number of controllable quantum dots to include the full structure.

Concluding, we can say that we were able to give a first demonstration of coherent electron spin transport in semiconductor quantum dots for the case of single electrons over a distance of $l_{\mathrm{travel}} \approx 6$ µm. The coherence time of the travelling electrons was found to be increased and the limiting mechanisms were identified. The obtained results allow to asses the viability of electron spins as quantum mediators between distant quantum dot systems. The experimental findings are expected to influence the development of future

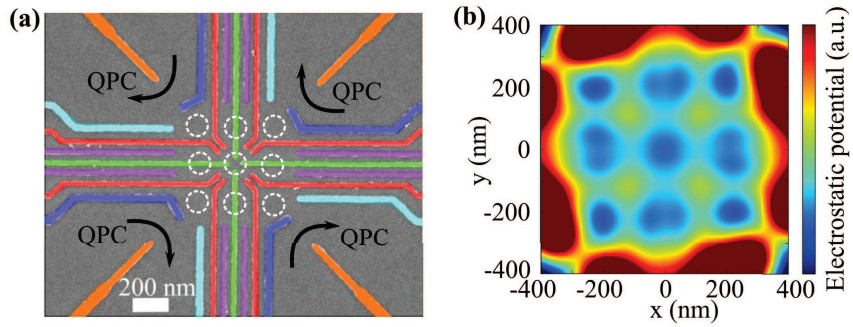


**Figure 5.1:** **(a)** False color image of the as fabricated 9-dot array. The expected quantum dot positions are indicated by white dashed circles. **(b)** Calculation of the electrostatic potential profile of the active region of the 9-dot array for realistic gate voltages. Nine clear potential minima are visible.

structures via the information over the disorder induced decoherence mechanism. The introduced charge manipulation technique in the isolated regime is found to greatly improve the control over the quantum dot system. Its implementation for the manipulation of large quantum dot arrays is already ongoing. These results are expected to stimulate further experiments on the electron transport in quantum dot structures and open the possibility to investigate geometrical phases related to the path of the electrons. Considering the recent emergence of quantum dot systems based on silicon heterostructures, the results and techniques obtained in this thesis are expected to facilitate the development of large spin qubit architectures.

# Bibliography


1. Millikan, R. A.: 'A Direct Photoelectric Determination of Planck's "$h$"'. *Phys. Rev.* (3 Mar. 1916), vol. 7: pp. 355–388 (cit. on p. 1).
2. de Broglie, Louis: 'La mécanique ondulatoire et la structure atomique de la matière et du rayonnement'. *J. Phys. Radium* (1927), vol. 8(5): pp. 225–241 (cit. on p. 1).
3. Davisson, C. J. and L. H. Germer: 'Reflection of Electrons by a Crystal of Nickel'. *Proc Natl Acad Sci U S A* (Apr. 1928), vol. 14(4). 16587341[pmid]: pp. 317–322 (cit. on p. 1).
4. Aoyama, T., M. Hayakawa, T. Kinoshita, and M. Nio: 'Revised value of the eighth-order QED contribution to the anomalous magnetic moment of the electron'. *Phys. Rev. D* (5 2008), vol. 77: p. 053012 (cit. on p. 1).
5. Gabrielse, G., D. Hanneke, T. Kinoshita, M. Nio, and B. Odom: 'New Determination of the Fine Structure Constant from the Electron $g$ Value and QED'. *Phys. Rev. Lett.* (3 July 2006), vol. 97: p. 030802 (cit. on p. 1).
6. Jacques, Vincent, E Wu, Frédéric Grosshans, François Treussart, Philippe Grangier, Alain Aspect, and Jean-François Roch: 'Experimental Realization of Wheeler's Delayed-Choice Gedanken Experiment'. *Science* (2007), vol. 315(5814): pp. 966–968 (cit. on p. 1).
7. Guerlin, Christine, Julien Bernu, Samuel Deleglise, Clement Sayrin, Sebastien Gleyzes, Stefan Kuhr, Michel Brune, Jean-Michel Raimond, and Serge Haroche: 'Progressive field-state collapse and quantum non-demolition photon counting'. *Nature* (Aug. 2007), vol. 448(7156): pp. 889–893 (cit. on p. 1).
8. Planck, Max: 'Über das Gesetz der Energieverteilung im Normalspectrum'. *Annalen der Physik* (1901), vol. 309(3): pp. 553–563 (cit. on p. 1).

9. Einstein, A.: 'Über einen die Erzeugung und Verwandlung des Lichtes betreffenden heuristischen Gesichtspunkt'. *Annalen der Physik* (1905), vol. 322(6): pp. 132–148 (cit. on p. 1).

10. Schrödinger, E.: 'An Undulatory Theory of the Mechanics of Atoms and Molecules'. *Phys. Rev.* (6 Dec. 1926), vol. 28: pp. 1049–1070 (cit. on p. 1).

11. Bloch, Felix: 'Über die Quantenmechanik der Elektronen in Kristallgittern'. *Zeitschrift für Physik* (1929), vol. 52(7): pp. 555–600 (cit. on p. 1).

12. Sommerfeld, A. and H. Bethe: 'Aufbau Der Zusammenhängenden Materie'. Berlin, Heidelberg: Springer Berlin Heidelberg, 1933. Chap. Elektronentheorie der Metalle: pp. 333–622 (cit. on p. 1).

13. Bardeen, J., L. N. Cooper, and J. R. Schrieffer: 'Theory of Superconductivity'. *Phys. Rev.* (5 Dec. 1957), vol. 108: pp. 1175–1204 (cit. on p. 1).

14. Grünberg, P., R. Schreiber, Y. Pang, M. B. Brodsky, and H. Sowers: 'Layered Magnetic Structures: Evidence for Antiferromagnetic Coupling of Fe Layers across Cr Interlayers'. *Phys. Rev. Lett.* (19 Nov. 1986), vol. 57: pp. 2442–2445 (cit. on p. 1).

15. Einstein, A., B. Podolsky, and N. Rosen: 'Can Quantum-Mechanical Description of Physical Reality Be Considered Complete?' *Phys. Rev.* (10 May 1935), vol. 47: pp. 777–780 (cit. on p. 1).

16. Freedman, Stuart J. and John F. Clauser: 'Experimental Test of Local Hidden-Variable Theories'. *Phys. Rev. Lett.* (14 Apr. 1972), vol. 28: pp. 938–941 (cit. on p. 1).

17. Hensen, B. et al.: 'Loophole-free Bell inequality violation using electron spins separated by 1.3 kilometres'. *Nature* (2015), vol. 526(7575). Letter: pp. 682–686 (cit. on p. 1).

18. Giustina, Marissa et al.: 'Significant-Loophole-Free Test of Bell's Theorem with Entangled Photons'. *Phys. Rev. Lett.* (25 2015), vol. 115: p. 250401 (cit. on p. 1).

19. Shalm, Lynden K. et al.: 'Strong Loophole-Free Test of Local Realism*'. *Phys. Rev. Lett.* (25 2015), vol. 115: p. 250402 (cit. on p. 1).

20. Deutsch, D.: 'Quantum Theory, the Church-Turing Principle and the Universal Quantum Computer'. *Proceedings of the Royal Society of London A: Mathematical, Physical and Engineering Sciences* (1985), vol. 400(1818): pp. 97–117 (cit. on pp. 1, 2).

21. Loss, Daniel and David P. DiVincenzo: 'Quantum computation with quantum dots'. *Phys. Rev. A* (1 Jan. 1998), vol. 57: pp. 120–126 (cit. on pp. 1, 2, 16, 87, 99, 133).

22. Deutsch, David and Richard Jozsa: 'Rapid Solution of Problems by Quantum Computation'. *Proceedings of the Royal Society of London A: Mathematical, Physical and Engineering Sciences* (1992), vol. 439(1907): pp. 553–558 (cit. on p. 2).

23. Grover, Lov K.: 'A Fast Quantum Mechanical Algorithm for Database Search'. *Proceedings of the Twenty-eighth Annual ACM Symposium on Theory of Computing*. STOC '96. Philadelphia, Pennsylvania, USA: ACM, 1996: pp. 212–219 (cit. on p. 2).

24. Shor, Peter W.: 'Polynomial-Time Algorithms for Prime Factorization and Discrete Logarithms on a Quantum Computer'. *SIAM J. Comput.* (Oct. 1997), vol. 26(5): pp. 1484–1509 (cit. on p. 2).

25. Feynman, Richard P.: 'Simulating physics with computers'. *International Journal of Theoretical Physics* (1982), vol. 21(6): pp. 467–488 (cit. on p. 2).

26. Monroe, C., D. M. Meekhof, B. E. King, W. M. Itano, and D. J. Wineland: 'Demonstration of a Fundamental Quantum Logic Gate'. *Phys. Rev. Lett.* (25 Dec. 1995), vol. 75: pp. 4714–4717 (cit. on p. 2).

27. Vandersypen, Lieven M. K., Matthias Steffen, Gregory Breyta, Costantino S. Yannoni, Mark H. Sherwood, and Isaac L. Chuang: 'Experimental realization of Shor's quantum factoring algorithm using nuclear magnetic resonance'. *Nature* (2001), vol. 414(6866): pp. 883–887 (cit. on p. 2).

28. Waldherr, G., Y. Wang, S. Zaiser, M. Jamali, T. Schulte-Herbruggen, H. Abe, T. Ohshima, J. Isoya, J. F. Du, P. Neumann, and J. Wrachtrup: 'Quantum error correction in a solid-state hybrid spin register'. *Nature* (2014), vol. 506(7487). Letter: pp. 204–207 (cit. on p. 2).

29. Barends, R. et al.: 'Superconducting quantum circuits at the surface code threshold for fault tolerance'. *Nature* (2014), vol. 508(7497). Letter: pp. 500–503 (cit. on p. 2).

30. Hanson, R., L. H. Willems van Beveren, I. T. Vink, J. M. Elzerman, W. J. M. Naber, F. H. L. Koppens, L. P. Kouwenhoven, and L. M. K. Vandersypen: 'Single-Shot Readout of Electron Spin States in a Quantum Dot Using Spin-Dependent Tunnel Rates'. *Phys. Rev. Lett.* (19 May 2005), vol. 94: p. 196802 (cit. on pp. 2, 23, 92).

31. Petta, J. R., A. C. Johnson, J. M. Taylor, E. A. Laird, A. Yacoby, M. D. Lukin, C. M. Marcus, M. P. Hanson, and A. C. Gossard: 'Coherent Manipulation of Coupled Electron Spins in Semiconductor Quantum Dots'. *Science* (2005), vol. 309(5744): pp. 2180–2184 (cit. on pp. 2, 17, 21, 27, 28, 95, 106, 114, 127, 133, 172).

32. Nowack, K. C., F. H. L. Koppens, Yu. V. Nazarov, and L. M. K. Vandersypen: 'Coherent Control of a Single Electron Spin with Electric Fields'. *Science* (2007), vol. 318(5855): pp. 1430–1433 (cit. on pp. 2, 16, 30, 133).

33. Shulman, M. D., O. E. Dial, S. P. Harvey, H. Bluhm, V. Umansky, and A. Yacoby: 'Demonstration of Entanglement of Electrostatically Coupled Singlet-Triplet Qubits'. *Science* (2012), vol. 336(6078): pp. 202–205 (cit. on pp. 2, 36, 133, 151).

34. Coish, W. A. and Daniel Loss: 'Hyperfine interaction in a quantum dot: Non-Markovian electron spin dynamics'. *Phys. Rev. B* (19 Nov. 2004), vol. 70: p. 195340 (cit. on pp. 2, 28).

35. Johnson, A. C., J. R. Petta, J. M. Taylor, A. Yacoby, M. D. Lukin, C. M. Marcus, M. P. Hanson, and A. C. Gossard: 'Triplet-singlet spin relaxation via nuclei in a double quantum dot'. *Nature* (June 2005), vol. 435(7044): pp. 925–928 (cit. on p. 2).

36. Hung, Jo-Tzu, Lukasz Cywiński, Xuedong Hu, and S. Das Sarma: 'Hyperfine interaction induced dephasing of coupled spin qubits in semiconductor double quantum dots'. *Phys. Rev. B* (8 Aug. 2013), vol. 88: p. 085314 (cit. on pp. 2, 27).

37. Bluhm, Hendrik, Sandra Foletti, Diana Mahalu, Vladimir Umansky, and Amir Yacoby: 'Enhancing the Coherence of a Spin Qubit by Operating it as a Feedback Loop That Controls its Nuclear Spin Bath'. *Phys. Rev. Lett.* (21 Nov. 2010), vol. 105: p. 216803 (cit. on pp. 2, 25, 29).

38. Bluhm, Hendrik, Sandra Foletti, Izhar Neder, Mark Rudner, Diana Mahalu, Vladimir Umansky, and Amir Yacoby: 'Dephasing time of GaAs electron-spin qubits coupled to a nuclear bath exceeding 200 μs'. *Nat Phys* (Feb. 2011), vol. 7(2): pp. 109–113 (cit. on pp. 2, 25, 28, 135).

39. Muhonen, Juha T., Juan P. Dehollain, Arne Laucht, Fay E. Hudson, Rachpon Kalra, Takeharu Sekiguchi, Kohei M. Itoh, David N. Jamieson, Jeffrey C. McCallum, Andrew S. Dzurak, and Andrea Morello: 'Storing

quantum information for 30 seconds in a nanoelectronic device'. *Nat Nano* (2014), vol. 9(12). Letter: pp. 986–991 (cit. on p. 3).

40. Veldhorst, M., C. H. Yang, J. C. C. Hwang, W. Huang, J. P. Dehollain, J. T. Muhonen, S. Simmons, A. Laucht, F. E. Hudson, K. M. Itoh, A. Morello, and A. S. Dzurak: 'A two-qubit logic gate in silicon'. *Nature* (2015), vol. 526(7573). Letter: pp. 410–414 (cit. on p. 3).

41. Wees, B. J. van, H. van Houten, C. W. J. Beenakker, J. G. Williamson, L. P. Kouwenhoven, D. van der Marel, and C. T. Foxon: 'Quantized conductance of point contacts in a two-dimensional electron gas'. *Phys. Rev. Lett.* (9 Feb. 1988), vol. 60: pp. 848–850 (cit. on pp. 5, 15).

42. Smith, C G, M Pepper, H Ahmed, J E F Frost, D G Hasko, D C Peacock, D A Ritchie, and G A C Jones: 'The transition from one- to zero-dimensional ballistic transport'. *Journal of Physics C: Solid State Physics* (1988), vol. 21(24): p. L893 (cit. on pp. 5, 13).

43. Meirav, U., M. A. Kastner, M. Heiblum, and S. J. Wind: 'One-dimensional electron gas in GaAs: Periodic conductance oscillations as a function of density'. *Phys. Rev. B* (8 Sept. 1989), vol. 40: pp. 5871–5874 (cit. on p. 5).

44. Meirav, U., M. A. Kastner, and S. J. Wind: 'Single-electron charging and periodic conductance resonances in GaAs nanostructures'. *Phys. Rev. Lett.* (6 Aug. 1990), vol. 65: pp. 771–774 (cit. on pp. 5, 13).

45. Beenakker, C. W. J.: 'Theory of Coulomb-blockade oscillations in the conductance of a quantum dot'. *Phys. Rev. B* (4 1991), vol. 44: pp. 1646–1656 (cit. on p. 5).

46. Beenakker, C. W. J. and A. A. M. Staring: 'Theory of the thermopower of a quantum dot'. *Phys. Rev. B* (15 1992), vol. 46: pp. 9667–9676 (cit. on p. 5).

47. Tarucha, S., D. G. Austing, T. Honda, R. J. van der Hage, and L. P. Kouwenhoven: 'Shell Filling and Spin Effects in a Few Electron Quantum Dot'. *Phys. Rev. Lett.* (17 1996), vol. 77: pp. 3613–3616 (cit. on p. 5).

48. Staring, A. A. M., L. W. Molenkamp, B. W. Alphenaar, H. van Houten, O. J. A. Buyk, M. A. A. Mabesoone, C. W. J. Beenakker, and C. T. Foxon: 'Coulomb-Blockade Oscillations in the Thermopower of a Quantum Dot'. *EPL (Europhysics Letters)* (1993), vol. 22(1): p. 57 (cit. on p. 5).

49. Kouwenhoven, Leo P, Charles M Marcus, Paul L McEuen, Seigo Tarucha, Robert M Westervelt, and Ned S Wingreen: 'Electron transport in quantum dots'. *Mesoscopic electron transport*. Springer, 1997: pp. 105–214 (cit. on p. 5).

50. Goldhaber-Gordon, D., Hadas Shtrikman, D. Mahalu, David Abusch-Magder, U. Meirav, and M. A. Kastner: 'Kondo effect in a single-electron transistor'. *Nature* (Jan. 1998), vol. 391(6663): pp. 156–159 (cit. on pp. 5, 13).

51. Cronenwett, Sara M., Tjerk H. Oosterkamp, and Leo P. Kouwenhoven: 'A Tunable Kondo Effect in Quantum Dots'. *Science* (1998), vol. 281(5376): pp. 540–544 (cit. on pp. 5, 13).

52. Sasaki, S., S. De Franceschi, J. M. Elzerman, W. G. van der Wiel, M. Eto, S. Tarucha, and L. P. Kouwenhoven: 'Kondo effect in an integer-spin quantum dot'. *Nature* (June 2000), vol. 405(6788): pp. 764–767 (cit. on p. 5).

53. Takada, S., C. Bäuerle, M. Yamamoto, K. Watanabe, S. Hermelin, T. Meunier, A. Alex, A. Weichselbaum, J. von Delft, A. Ludwig, A. D. Wieck, and S. Tarucha: 'Transmission Phase in the Kondo Regime Revealed in a Two-Path Interferometer'. *Phys. Rev. Lett.* (12 Sept. 2014), vol. 113: p. 126601 (cit. on p. 5).

54. Schuster, R., E. Buks, M. Heiblum, D. Mahalu, V. Umansky, and Hadas Shtrikman: 'Phase measurement in a quantum dot via a double-slit interference experiment'. *Nature* (Jan. 1997), vol. 385(6615): pp. 417–420 (cit. on p. 5).

55. Henny, M., S. Oberholzer, C. Strunk, T. Heinzel, K. Ensslin, M. Holland, and C. Schönenberger: 'The Fermionic Hanbury Brown and Twiss Experiment'. *Science* (1999), vol. 284(5412): pp. 296–298 (cit. on p. 5).

56. Ji, Yang, Yunchul Chung, D. Sprinzak, M. Heiblum, D. Mahalu, and Hadas Shtrikman: 'An electronic Mach-Zehnder interferometer'. *Nature* (Mar. 2003), vol. 422(6930): pp. 415–418 (cit. on p. 5).

57. Bocquillon, E., V. Freulon, J.-M Berroir, P. Degiovanni, B. Plaçais, A. Cavanna, Y. Jin, and G. Fève: 'Coherence and Indistinguishability of Single Electrons Emitted by Independent Sources'. *Science* (2013), vol. 339(6123): pp. 1054–1057 (cit. on p. 5).

58. Kouwenhoven, Leo P., Charles M. Marcus, Paul L. McEuen, Seigo Tarucha, Robert M. Westervelt, and Ned S. Wingreen: 'Mesoscopic Electron Transport'. Ed. by Sohn, Lydia L., Leo P. Kouwenhoven, and Gerd Schön. Dordrecht: Springer Netherlands, 1997. Chap. Electron Transport in Quantum Dots: pp. 105–214 (cit. on p. 5).

59. Kouwenhoven, L P, D G Austing, and S Tarucha: 'Few-electron quantum dots'. *Reports on Progress in Physics* (2001), vol. 64(6): p. 701 (cit. on pp. 5, 22, 75, 78).

60. Wiel, W. G. van der, S. De Franceschi, J. M. Elzerman, T. Fujisawa, S. Tarucha, and L. P. Kouwenhoven: 'Electron transport through double quantum dots'. *Rev. Mod. Phys.* (1 Dec. 2002), vol. 75: pp. 1–22 (cit. on pp. 5, 9, 13).

61. Hanson, R., L. P. Kouwenhoven, J. R. Petta, S. Tarucha, and L. M. K. Vandersypen: 'Spins in few-electron quantum dots'. *Rev. Mod. Phys.* (4 Oct. 2007), vol. 79: pp. 1217–1265 (cit. on pp. 5, 9, 18, 26, 29, 61, 92, 122).

62. Manfra, Michael J.: 'Molecular Beam Epitaxy of Ultra-High-Quality AlGaAs/-GaAs Heterostructures: Enabling Physics in Low-Dimensional Electronic Systems'. *Annual Review of Condensed Matter Physics* (2014), vol. 5(1): pp. 347–373 (cit. on p. 6).

63. Gehrsitz, S., H. Sigg, N. Herres, K. Bachem, K. Köhler, and F. K. Reinhart: 'Compositional dependence of the elastic constants and the lattice parameter of $Al_xGa_{1-x}As$'. *Phys. Rev. B* (16 Oct. 1999), vol. 60: pp. 11601–11610 (cit. on p. 6).

64. Nakata, S., M. Tomizawa, M. Yamamoto, K. Ikuta, and T. Mizutani: 'Electrical transport properties and confinement potential analysis of buried AlGaAs/GaAs quantum wires'. *Journal of Applied Physics* (1994), vol. 76(4): pp. 2330–2335 (cit. on p. 7).

65. Umansky, V., M. Heiblum, Y. Levinson, J. Smet, J. Nübler, and M. Dolev: 'MBE growth of ultra-low disorder 2DEG with mobility exceeding $3510^6$ cm2/V s'. *Journal of Crystal Growth* (2009), vol. 311(7). International Conference on Molecular Beam Epitaxy (MBE-XV)The 15th International Conference on Molecular Beam Epitaxy (MBE-XV): pp. 1658–1661 (cit. on p. 7).

66. Esfarjani, Keivan, Henry R. Glyde, and Virulh Sa-yakanit: 'Disorder, screening, and quantum Hall oscillations'. *Phys. Rev. B* (2 1990), vol. 41: pp. 1042–1053 (cit. on p. 7).

67. Iqbal, M. J., D. Reuter, A. D. Wieck, and C. H. van der Wal: 'Robust recipe for low-resistance ohmic contacts to a two-dimensional electron gas in a GaAs/AlGaAs heterostructure'. *ArXiv e-prints* (July 2014), vol. (cit. on p. 8).

68. Oosterkamp, T.H., W.G. van der Wiel, L.P. Kouwenhoven, D.G. Austing, T. Honda, and S. Tarucha: 'Electron ground states in a few-electron quantum dot'. English. *Advances in Solid State Physics 38*. Ed. by Kramer, Bernhard. Vol. 38. Advances in Solid State Physics. Springer Berlin Heidelberg, 1999: pp. 139–152 (cit. on p. 9).

69. Stopa, M.: 'Quantum dot self-consistent electronic structure and the Coulomb blockade'. *Phys. Rev. B* (19 Nov. 1996), vol. 54: pp. 13767–13783 (cit. on p. 9).

70. Koppens, F. H. L., C. Buizert, K. J. Tielrooij, I. T. Vink, K. C. Nowack, T. Meunier, L. P. Kouwenhoven, and L. M. K. Vandersypen: 'Driven coherent oscillations of a single electron spin in a quantum dot'. *Nature* (Aug. 2006), vol. 442(7104): pp. 766–771 (cit. on pp. 13, 17).

71. Field, M., C. G. Smith, M. Pepper, D. A. Ritchie, J. E. F. Frost, G. A. C. Jones, and D. G. Hasko: 'Measurements of Coulomb blockade with a noninvasive voltage probe'. *Phys. Rev. Lett.* (9 Mar. 1993), vol. 70: pp. 1311–1314 (cit. on p. 13).

72. Büttiker, M., Y. Imry, R. Landauer, and S. Pinhas: 'Generalized many-channel conductance formula with application to small rings'. *Phys. Rev. B* (10 May 1985), vol. 31: pp. 6207–6215 (cit. on p. 15).

73. Wharam, D A, T J Thornton, R Newbury, M Pepper, H Ahmed, J E F Frost, D G Hasko, D C Peacock, D A Ritchie, and G A C Jones: 'One-dimensional transport and the quantisation of the ballistic resistance'. *Journal of Physics C: Solid State Physics* (1988), vol. 21(8): p. L209 (cit. on p. 15).

74. Beenakker, C.W.J. and H. van Houten: 'Quantum Transport in Semiconductor Nanostructures'. *Semiconductor Heterostructures and Nanostructures*. Ed. by Ehrenreich, Henry and David Turnbull. Vol. 44. Solid State Physics. Academic Press, 1991: pp. 1–228 (cit. on p. 15).

75. Maaø, Frank A., I. V. Zozulenko, and E. H. Hauge: 'Quantum point contacts with smooth geometries: Exact versus approximate results'. *Phys. Rev. B* (23 Dec. 1994), vol. 50: pp. 17320–17327 (cit. on p. 15).

76. Cronenwett, Sara Marie: 'COHERENCE, CHARGING, AND SPIN EFFECTS IN QUANTUM DOTS AND POINT CONTACTS'. PhD thesis. Stanford University, 2001 (cit. on p. 15).

77. Elzerman, J. M., R. Hanson, J. S. Greidanus, L. H. Willems van Beveren, S. De Franceschi, L. M. K. Vandersypen, S. Tarucha, and L. P. Kouwenhoven: 'Few-electron quantum dot circuit with integrated charge read out'. *Phys. Rev. B* (16 Apr. 2003), vol. 67: p. 161308 (cit. on p. 15).

78. Barthel, C., M. Kjærgaard, J. Medford, M. Stopa, C. M. Marcus, M. P. Hanson, and A. C. Gossard: 'Fast sensing of double-dot charge arrangement and spin state with a radio-frequency sensor quantum dot'. *Phys. Rev. B* (16 Apr. 2010), vol. 81: p. 161308 (cit. on p. 15).

79. Reilly, D. J., C. M. Marcus, M. P. Hanson, and A. C. Gossard: 'Fast single-charge sensing with a rf quantum point contact'. *Applied Physics Letters* (2007), vol. 91(16), 162101 (cit. on p. 15).

80. Petta, J. R., A. C. Johnson, C. M. Marcus, M. P. Hanson, and A. C. Gossard: 'Manipulation of a Single Charge in a Double Quantum Dot'. *Phys. Rev. Lett.* (18 Oct. 2004), vol. 93: p. 186802 (cit. on p. 16).

81. Li, Hai-Ou, Gang Cao, Guo-Dong Yu, Ming Xiao, Guang-Can Guo, Hong-Wen Jiang, and Guo-Ping Guo: 'Conditional rotation of two strongly coupled semiconductor charge qubits'. *Nat Commun* (July 2015), vol. 6. Article (cit. on p. 16).

82. Amasha, S., K. MacLean, Iuliana P. Radu, D. M. Zumbühl, M. A. Kastner, M. P. Hanson, and A. C. Gossard: 'Electrical Control of Spin Relaxation in a Quantum Dot'. *Phys. Rev. Lett.* (4 Jan. 2008), vol. 100: p. 046803 (cit. on p. 16).

83. Gerlach, Walther and Otto Stern: 'Der experimentelle Nachweis der Richtungsquantelung im Magnetfeld'. *Zeitschrift für Physik* (1922), vol. 9(1): pp. 349–352 (cit. on p. 16).

84. Uhlenbeck, G.E. and S. Goudsmit: 'Spinning Electrons and the Structure of Spectra'. *Nature* (Feb. 1926), vol. 117: pp. 264–265 (cit. on p. 16).

85. Weisbuch, Claude and Claudine Hermann: 'Optical detection of conduction-electron spin resonance in GaAs, $Ga_{1-x}In_xAs$, and $Ga_{1-x}Al_xAs$'. *Phys. Rev. B* (2 Jan. 1977), vol. 15: pp. 816–822 (cit. on p. 16).

86. Khaetskii, Alexander V. and Yuli V. Nazarov: 'Spin-flip transitions between Zeeman sublevels in semiconductor quantum dots'. *Phys. Rev. B* (12 Sept. 2001), vol. 64: p. 125316 (cit. on pp. 16, 25, 30).

87. Amasha, Sami: 'Electron tunneling and spin relaxation in a lateral quantum dot'. PhD thesis. Massachusetts Institute of Technology. Dept. of Physics., 2008 (cit. on p. 16).

88. Golovach, Vitaly N., Alexander Khaetskii, and Daniel Loss: 'Phonon-Induced Decay of the Electron Spin in Quantum Dots'. *Phys. Rev. Lett.* (1 June 2004), vol. 93: p. 016601 (cit. on p. 16).

89. Gindikin, Yasha and Vladimir A Sablikov: 'Electron-electron interaction effect on the singlet-triplet transitions in one-dimensional quantum dots'. *Journal of Physics: Condensed Matter* (2011), vol. 23(17): p. 175601 (cit. on p. 17).

90. Johnson, A. C., J. R. Petta, C. M. Marcus, M. P. Hanson, and A. C. Gossard: 'Singlet-triplet spin blockade and charge sensing in a few-electron double quantum dot'. *Phys. Rev. B* (16 2005), vol. 72: p. 165308 (cit. on pp. 18, 24).

91. Taylor, J. M., J. R. Petta, A. C. Johnson, A. Yacoby, C. M. Marcus, and M. D. Lukin: 'Relaxation, dephasing, and quantum control of electron spins in double quantum dots'. *Phys. Rev. B* (3 2007), vol. 76: p. 035315 (cit. on p. 18).

92. Burkard, Guido, Daniel Loss, and David P. DiVincenzo: 'Coupled quantum dots as quantum gates'. *Phys. Rev. B* (3 Jan. 1999), vol. 59: pp. 2070–2078 (cit. on pp. 21, 126).

93. Elzerman, J. M., R. Hanson, L. H. Willems van Beveren, B. Witkamp, L. M. K. Vandersypen, and L. P. Kouwenhoven: 'Single-shot read-out of an individual electron spin in a quantum dot'. *Nature* (July 2004), vol. 430(6998): pp. 431–435 (cit. on p. 21).

94. Meunier, T., K.-J. Tielrooij, I. T. Vink, F. H. L. Koppens, H. P. Tranitz, W. Wegscheider, L. P. Kouwenhoven, and L. M. K. Vandersypen: 'High fidelity measurement of singlet-triplet state in a quantum dot'. *physica status solidi (b)* (2006), vol. 243(15): pp. 3855–3858 (cit. on pp. 21, 91–93).

95. Scarlino, P., E. Kawakami, P. Stano, M. Shafiei, C. Reichl, W. Wegscheider, and L. M. K. Vandersypen: 'Spin-Relaxation Anisotropy in a GaAs Quantum Dot'. *Phys. Rev. Lett.* (25 Dec. 2014), vol. 113: p. 256802 (cit. on pp. 25, 30, 133).

96. Klauser, D.J.: 'Hyperfine Interaction and spin decoherence in quantum dots'. PhD thesis. Universit ät Basel, 2008 (cit. on pp. 26, 28).

97. D'yakonov, MI and VI Perel: 'Optical orientation in a system of electrons and lattice nuclei in semiconductors. Theory'. *Soviet Journal of Experimental and Theoretical Physics* (1974), vol. 38: p. 177 (cit. on p. 26).

98. Paget, D., G. Lampel, B. Sapoval, and V. I. Safarov: 'Low field electron-nuclear spin coupling in gallium arsenide under optical pumping conditions'. *Phys. Rev. B* (12 June 1977), vol. 15: pp. 5780–5796 (cit. on p. 27).

99. Khaetskii, Alexander V., Daniel Loss, and Leonid Glazman: 'Electron Spin Decoherence in Quantum Dots due to Interaction with Nuclei'. *Phys. Rev. Lett.* (18 Apr. 2002), vol. 88: p. 186802 (cit. on p. 27).

100. Merkulov, I. A., Al. L. Efros, and M. Rosen: 'Electron spin relaxation by nuclei in semiconductor quantum dots'. *Phys. Rev. B* (20 Apr. 2002), vol. 65: p. 205309 (cit. on pp. 27, 28).

101. Koppens, F. H. L., K. C. Nowack, and L. M. K. Vandersypen: 'Spin Echo of a Single Electron Spin in a Quantum Dot'. *Phys. Rev. Lett.* (23 June 2008), vol. 100: p. 236802 (cit. on p. 28).

102. Petta, J. R., J. M. Taylor, A. C. Johnson, A. Yacoby, M. D. Lukin, C. M. Marcus, M. P. Hanson, and A. C. Gossard: 'Dynamic Nuclear Polarization with Single Electron Spins'. *Phys. Rev. Lett.* (6 Feb. 2008), vol. 100: p. 067601 (cit. on p. 29).

103. Foletti, Sandra, Hendrik Bluhm, Diana Mahalu, Vladimir Umansky, and Amir Yacoby: 'Universal quantum control of two-electron spin quantum bits using dynamic nuclear polarization'. *Nat Phys* (Dec. 2009), vol. 5(12): pp. 903–908 (cit. on p. 29).

104. Dresselhaus, G.: 'Spin-Orbit Coupling Effects in Zinc Blende Structures'. *Phys. Rev.* (2 Oct. 1955), vol. 100: pp. 580–586 (cit. on p. 29).

105. Bychkov, Yu A and EI Rashba: 'Properties of a 2D electron gas with lifted spectral degeneracy'. *JETP lett* (1984), vol. 39(2): p. 78 (cit. on p. 29).

106. Sanada, H., T. Sogawa, H. Gotoh, K. Onomitsu, M. Kohda, J. Nitta, and P. V. Santos: 'Acoustically Induced Spin-Orbit Interactions Revealed by Two-Dimensional Imaging of Spin Transport in GaAs'. *Phys. Rev. Lett.* (21 May 2011), vol. 106: p. 216602 (cit. on p. 30).

107. Bertrand, B., S. Hermelin, S. Takada, M. Yamamoto, S. Tarucha, A. Ludwig, A. D. Wieck, C. Bäuerle, and T. Meunier: 'Long-range spin transfer using individual electrons'. *ArXiv e-prints* (Aug. 2015), vol. (cit. on p. 30).

108. Thalineau, Romain, Sylvain Hermelin, Andreas D. Wieck, Christopher Bäuerle, Laurent Saminadayar, and Tristan Meunier: 'A few-electron quadruple quantum dot in a closed loop'. *Applied Physics Letters* (2012), vol. 101(10), 103102 (cit. on pp. 30, 36, 66, 166).

109. Khaetskii, Alexander V. and Yuli V. Nazarov: 'Spin relaxation in semiconductor quantum dots'. *Phys. Rev. B* (19 2000), vol. 61: pp. 12639–12642 (cit. on p. 30).

110. Huang, Peihao and Xuedong Hu: 'Spin qubit relaxation in a moving quantum dot'. *Phys. Rev. B* (7 Aug. 2013), vol. 88: p. 075301 (cit. on pp. 30, 32, 33, 118, 125, 130, 135).

111. Hsieh, Chang-Yu, Yun-Pil Shim, Marek Korkusinski, and Pawel Hawrylak: 'Physics of lateral triple quantum-dot molecules with controlled electron numbers'. *Reports on Progress in Physics* (2012), vol. 75(11): p. 114501 (cit. on pp. 34, 36).

112. Gaudreau, L., S. A. Studenikin, A. S. Sachrajda, P. Zawadzki, A. Kam, J. Lapointe, M. Korkusinski, and P. Hawrylak: 'Stability Diagram of a Few-Electron Triple Dot'. *Phys. Rev. Lett.* (3 July 2006), vol. 97: p. 036807 (cit. on pp. 34, 151).

113. Schröer, D., A. D. Greentree, L. Gaudreau, K. Eberl, L. C. L. Hollenberg, J. P. Kotthaus, and S. Ludwig: 'Electrostatically defined serial triple quantum dot charged with few electrons'. *Phys. Rev. B* (7 Aug. 2007), vol. 76: p. 075306 (cit. on p. 34).

114. Laird, E. A., J. M. Taylor, D. P. DiVincenzo, C. M. Marcus, M. P. Hanson, and A. C. Gossard: 'Coherent spin manipulation in an exchange-only qubit'. *Phys. Rev. B* (7 Aug. 2010), vol. 82: p. 075403 (cit. on pp. 34, 133, 151).

115. Gaudreau, L., G. Granger, A. Kam, G. C. Aers, S. A. Studenikin, P. Zawadzki, M. Pioro-Ladriere, Z. R. Wasilewski, and A. S. Sachrajda: 'Coherent control of three-spin states in a triple quantum dot'. *Nat Phys* (Jan. 2012), vol. 8(1): pp. 54–58 (cit. on pp. 34, 152).

116. Amaha, S., T. Hatano, H. Tamura, S. Teraoka, T. Kubo, Y. Tokura, D. G. Austing, and S. Tarucha: 'Resonance-hybrid states in a triple quantum dot'. *Phys. Rev. B* (8 Feb. 2012), vol. 85: p. 081301 (cit. on pp. 34, 151).

117. Medford, J., J. Beil, J. M. Taylor, E. I. Rashba, H. Lu, A. C. Gossard, and C. M. Marcus: 'Quantum-Dot-Based Resonant Exchange Qubit'. *Phys. Rev. Lett.* (5 July 2013), vol. 111: p. 050501 (cit. on pp. 34, 152).

118. Sánchez, R., G. Granger, L. Gaudreau, A. Kam, M. Pioro-Ladrière, S. A. Studenikin, P. Zawadzki, A. S. Sachrajda, and G. Platero: 'Long-Range Spin Transfer in Triple Quantum Dots'. *Phys. Rev. Lett.* (17 May 2014), vol. 112: p. 176803 (cit. on p. 34).

119. Rogge, M. C. and R. J. Haug: 'Noninvasive detection of molecular bonds in quantum dots'. *Phys. Rev. B* (15 Oct. 2008), vol. 78: p. 153310 (cit. on pp. 34, 151).

120. Seo, M., H. K. Choi, S.-Y. Lee, N. Kim, Y. Chung, H.-S. Sim, V. Umansky, and D. Mahalu: 'Charge Frustration in a Triangular Triple Quantum Dot'. *Phys. Rev. Lett.* (4 Jan. 2013), vol. 110: p. 046803 (cit. on pp. 34, 36, 151).

121. *Reprinted figure with the permission of* Gaudreau, Studenikin, Sachrajda, Zawadzki, Kam, Lapointe, Korkusinski, and Hawrylak *[: 112] Copyright 2006 by the American Physical Society.* (Cit. on p. 35).

122. *Reprinted figure with permission from* Rogge and Haug *[: 119] Copyright 2008 by the American Physical Society.* (Cit. on p. 35).

123. *Reprinted figure with permission from* Amaha, Hatano, Tamura, Teraoka, Kubo, Tokura, Austing, and Tarucha *[: 116] Copyright 2012 by the American Physical Society.* (Cit. on p. 35).

124. *Reprinted figure with permission from* Seo, Choi, Lee, Kim, Chung, Sim, Umansky, and Mahalu *[: 120] Copyright 2013 by the American Physical Society.* (Cit. on p. 35).

125. *From* Shulman, Dial, Harvey, Bluhm, Umansky, and Yacoby *[: 33]. Reprinted with permission from AAAS.* (Cit. on p. 35).

126. *Reprinted with permission from* Delbecq, Nakajima, Otsuka, Amaha, Watson, Manfra, and Tarucha *[: 132]. Copyright 2014, AIP Publishing LLC.* (Cit. on p. 35).

127. *Reprinted figure with permission from* Laird, Taylor, DiVincenzo, Marcus, Hanson, and Gossard *[: 114] Copyright 2010 by the American Physical Society.* (Cit. on p. 35).

128. *Reprinted by permission from Macmillan Publishers Ltd: Nature Physics* Gaudreau, Granger, Kam, Aers, Studenikin, Zawadzki, Pioro-Ladriere, Wasilewski, and Sachrajda *[: 115], copyright 2012* (cit. on p. 35).

129. *Reprinted figure with permission from* Medford, Beil, Taylor, Rashba, Lu, Gossard, and Marcus *[: 117] Copyright 2013 by the American Physical Society.* (Cit. on p. 35).

130. *Reprinted from* Thalineau *[: 161] . with the permission of AIP Publishing* (cit. on p. 35).

131. Baart, A. T, M. Shafiei, T. Fujita, C. Reichl, W. Wegscheider, and L M.K. Vandersypen: 'Single-spin CCD'. *Nat Nano* (2016), vol. advance online publication. Letter (cit. on p. 34).

132. Delbecq, M. R., T. Nakajima, T. Otsuka, S. Amaha, J. D. Watson, M. J. Manfra, and S. Tarucha: 'Full control of quadruple quantum dot circuit charge states in the single electron regime'. *Applied Physics Letters* (2014), vol. 104(18), 183111 (cit. on pp. 36, 151).

133. Takakura, T., A. Noiri, T. Obata, T. Otsuka, J. Yoneda, K. Yoshida, and S. Tarucha: 'Single to quadruple quantum dots with tunable tunnel couplings'. *Applied Physics Letters* (2014), vol. 104(11), 113109 (cit. on p. 36).

134. Koop, E J, M J Iqbal, F Limbach, M Boute, B J van Wees, D Reuter, A D Wieck, B J Kooi, and C H van der Wal: 'On the annealing mechanism of AuGe/Ni/Au ohmic contacts to a two-dimensional electron gas in GaAs/$Al_xGa_{1-x}As$ heterostructures'. *Semiconductor Science and Technology* (2013), vol. 28(2): p. 025006 (cit. on p. 41).

135. Colless, J. I., A. C. Mahoney, J. M. Hornibrook, A. C. Doherty, H. Lu, A. C. Gossard, and D. J. Reilly: 'Dispersive Readout of a Few-Electron Double Quantum Dot with Fast rf Gate Sensors'. *Phys. Rev. Lett.* (4 Jan. 2013), vol. 110: p. 046805 (cit. on p. 43).

136. Pobell, Frank: *Matter and Methods at Low Temperatures*. Springer, 2007 (cit. on pp. 43, 44, 46).

137. Thiele, Stefan: 'Read-out and coherent manipulation of an isolated nuclear spin using a single-molecule magnet spin-transistor'. Theses. Université de Grenoble, Jan. 2014 (cit. on p. 46).

138. Mandal, Soumen, Tobias Bautze, Rémi Blinder, Tristan Meunier, Laurent Saminadayar, and Christopher Bäuerle: 'Efficient radio frequency filters for space constrained cryogenic setups'. *Review of Scientific Instruments* (2011), vol. 82(2), 024704 (cit. on p. 48).

139. Davies, John H., Ivan A. Larkin, and E. V. Sukhorukov: 'Modeling the patterned two-dimensional electron gas: Electrostatics'. *Journal of Applied Physics* (1995), vol. 77(9): pp. 4504–4512 (cit. on pp. 56, 165, 166).

140. Bautze, Tobias, Christoph Süssmeier, Shintaro Takada, Christoph Groth, Tristan Meunier, Michihisa Yamamoto, Seigo Tarucha, Xavier Waintal, and Christopher Bäuerle: 'Theoretical, numerical, and experimental study of a flying qubit electronic interferometer'. *Phys. Rev. B* (12 Mar. 2014), vol. 89: p. 125432 (cit. on p. 57).

141. Bertrand, Benoit: 'Transport d'information de spin à l'échelle de l'électron unique'. Theses. Université Grenoble Alpes, Mar. 2015 (cit. on pp. 59, 60, 96, 98, 100, 103, 171).

142. Johnson, A. C., C. M. Marcus, M. P. Hanson, and A. C. Gossard: 'Charge sensing of excited states in an isolated double quantum dot'. *Phys. Rev. B* (11 2005), vol. 71: p. 115333 (cit. on pp. 59, 83).

143. Hermelin, Sylvain, Shintaro Takada, Michihisa Yamamoto, Seigo Tarucha, Andreas D. Wieck, Laurent Saminadayar, Christopher Bauerle, and Tristan Meunier: 'Electrons surfing on a sound wave as a platform for quantum optics with flying electrons'. *Nature* (Sept. 2011), vol. 477(7365): pp. 435–438 (cit. on p. 59).

144. Bertrand, Benoit, Sylvain Hermelin, Pierre-André Mortemousque, Shintaro Takada, Michihisa Yamamoto, Seigo Tarucha, Arne Ludwig, Andreas D Wieck, Christopher Bäuerle, and Tristan Meunier: 'Injection of a single electron from static to moving quantum dots'. *arXiv preprint arXiv:1601.02485* (2016), vol. (cit. on p. 59).

145. Braakman, F. R., P. Barthelemy, C. Reichl, W. Wegscheider, and L. M. K. Vandersypen: 'Long-distance coherent coupling in a quantum dot array'. *Nat Nano* (June 2013), vol. 8(6). Article: pp. 432–437 (cit. on p. 73).

146. Oosterkamp, TH, T Fujisawa, WG Van Der Wiel, K Ishibashi, RV Hijman, S Tarucha, and Leo P Kouwenhoven: 'Microwave spectroscopy of a quantum-dot molecule'. *Nature* (1998), vol. 395(6705): pp. 873–876 (cit. on pp. 75, 169).

147. Landau, L. D.: 'Zur Theorie der Energieübertragung. II'. *Physikalische Zeitschrift der Sowjetunion* (1932), vol. 2: pp. 46–51 (cit. on p. 95).

148. Zener, Clarence: 'Non-Adiabatic Crossing of Energy Levels'. *Proceedings of the Royal Society of London. Series A, Containing Papers of a Mathematical and Physical Character* (1932), vol. 137(833): pp. 696–702 (cit. on p. 95).

149. Stueckelberg, E. C. G.: 'Theorie der unelastischen Stösse zwischen Atomen'. *Helvetica Physica Acta* (1932), vol. 5: p. 369 (cit. on p. 95).

150. Majorana, Ettore: 'Atomi orientati in campo magnetico variabile'. *Il Nuovo Cimento (1924-1942)* (1932), vol. 9(2): pp. 43–50 (cit. on p. 95).

151. Dial, O. E., M. D. Shulman, S. P. Harvey, H. Bluhm, V. Umansky, and A. Yacoby: 'Charge Noise Spectroscopy Using Coherent Exchange Oscillations in a Singlet-Triplet Qubit'. *Phys. Rev. Lett.* (14 Apr. 2013), vol. 110: p. 146804 (cit. on pp. 95, 101, 102).

152. Bertrand, Benoit, Hanno Flentje, Shintaro Takada, Michihisa Yamamoto, Seigo Tarucha, Arne Ludwig, Andreas D. Wieck, Christopher Bäuerle, and Tristan Meunier: 'Quantum Manipulation of Two-Electron Spin States in Isolated Double Quantum Dots'. *Phys. Rev. Lett.* (9 2015), vol. 115: p. 096801 (cit. on p. 96).

153. Martins, Frederico, Filip K. Malinowski, Peter D. Nissen, Edwin Barnes, Saeed Fallahi, Geoffrey C. Gardner, Michael J. Manfra, Charles M. Marcus, and Ferdinand Kuemmeth: 'Noise Suppression Using Symmetric Exchange Gates in Spin Qubits'. *Phys. Rev. Lett.* (11 2016), vol. 116: p. 116801 (cit. on p. 102).

154. Reed, M. D. et al.: 'Reduced Sensitivity to Charge Noise in Semiconductor Spin Qubits via Symmetric Operation'. *Phys. Rev. Lett.* (11 2016), vol. 116: p. 110402 (cit. on p. 102).

155. Bloembergen, N., E. M. Purcell, and R. V. Pound: 'Relaxation Effects in Nuclear Magnetic Resonance Absorption'. *Phys. Rev.* (7 Apr. 1948), vol. 73: pp. 679–712 (cit. on p. 118).

156. Stotz, James A. H., Rudolf Hey, Paulo V. Santos, and Klaus H. Ploog: 'Coherent spin transport through dynamic quantum dots'. *Nat Mater* (Aug. 2005), vol. 4(8): pp. 585–588 (cit. on p. 122).

157. Maisi, V. F., A. Hofmann, M. Röösli, J. Basset, C. Reichl, W. Wegscheider, T. Ihn, and K. Ensslin: 'Spin-Orbit Coupling at the Level of a Single Electron'. *Phys. Rev. Lett.* (13 2016), vol. 116: p. 136803 (cit. on p. 124).

158. Drummond, David, Leonid P. Pryadko, and Kirill Shtengel: 'Suppression of hyperfine dephasing by spatial exchange of double quantum dots'. *Phys. Rev. B* (24 Dec. 2012), vol. 86: p. 245307 (cit. on p. 127).

159. San-Jose, Pablo, Burkhard Scharfenberger, Gerd Schön, Alexander Shnirman, and Gergely Zarand: 'Geometric phases in semiconductor spin qubits: Manipulations and decoherence'. *Phys. Rev. B* (4 Jan. 2008), vol. 77: p. 045305 (cit. on p. 136).

160. Golovach, Vitaly N., Massoud Borhani, and Daniel Loss: 'Holonomic quantum computation with electron spins in quantum dots'. *Phys. Rev. A* (2 2010), vol. 81: p. 022315 (cit. on p. 136).

161. Thalineau, Romain: 'Qubits de spin : de la manipulation et déplacement d'un spin unique à son utilisation comme détecteur ultra sensible'. PhD thesis. Université de Grenoble, Institut Néel-CNRS, 2012 (cit. on p. 152).

162. Biesinger, D. E. F., C. P. Scheller, B. Braunecker, J. Zimmerman, A. C. Gossard, and D. M. Zumbühl: 'Intrinsic Metastabilities in the Charge Configuration of a Double Quantum Dot'. *Phys. Rev. Lett.* (10 2015), vol. 115: p. 106804 (cit. on pp. 167, 169).

# APPENDIX A

## Constant interaction model of a coupled triple dot

### A.1 Calculation of the energy for three circularly coupled dots

In this Appendix we calculate the electrostatic energies for a coupled tripledot. In our model we assume three charge islands with potentials $V_{D1}$,$V_{D2}$ and $V_{D3}$ which are coupled to each other via capacitances $C_{M1}$,$C_{M2}$ and $C_{M3}$ aswell as to several gates $V_\nu$ with capacitances $C_{\mu\nu}$, where $\mu$ denotes the quantum dot the capacitance is associated to. Fig. A.1 shows such an arrangement.

We can then find the equivalent system of equations to 1.3 which includes interdot couplings

$$\begin{aligned} Q_{D1} &= \underbrace{\sum_\nu (V_{D1}-V_\nu)C_{1\nu}}_{\text{gate dependent charge}} + \underbrace{(V_{D1}-V_{D2})C_{M3}}_{\text{influence of Dot2}} + \underbrace{(V_{D1}-V_{D3})C_{M2}}_{\text{influence of Dot3}} \\ Q_{D2} &= \sum_\nu (V_{D2}-V_\nu)C_{2\nu} + (V_{D2}-V_{D1})C_{M3} + (V_{D2}-V_{D3})C_{M1} \\ Q_{D3} &= \sum_\nu (V_{D3}-V_\nu)C_{3\nu} + (V_{D3}-V_{D1})C_{M2} + (V_{D3}-V_{D2})C_{M1} \end{aligned} \tag{A.1}$$

which we can rewrite in terms of vectors $\vec{Q}$ and $\vec{V}$ and the capacitance matric $\boldsymbol{C}$:

$$\begin{pmatrix} Q_{D1}+\sum_\nu C_{1\nu}V_\nu \\ Q_{D2}+\sum_\nu C_{2\nu}V_\nu \\ Q_{D3}+\sum_\nu C_{3\nu}V_\nu \end{pmatrix} = \begin{pmatrix} \sum_\nu C_{1\nu} & -C_{M3} & C_{M2} \\ C_{M3} & \sum_\nu C_{2\nu} & C_{M1} \\ C_{M2} & C_{M1} & \sum_\nu C_{3\nu} \end{pmatrix} \begin{pmatrix} V_{D1} \\ V_{D2} \\ V_{D3} \end{pmatrix}. \tag{A.2}$$

To find the energy of our system we use Eq. 1.5 ($U = \frac{1}{2}\vec{Q}\,\boldsymbol{C}^{-1}\,\vec{Q}$) for which we need to

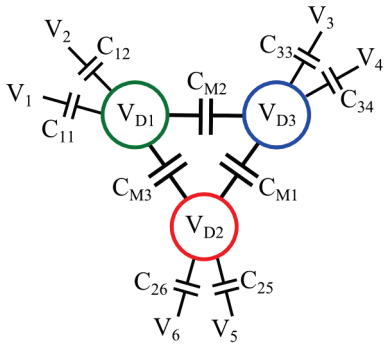


**Figure A.1:** Constant interaction scheme for three coupled quantum dots.

find the inverse of $\boldsymbol{C}$:

$$\boldsymbol{C}^{-1} = \frac{1}{|A|}\begin{pmatrix} C_2C_3 - C_{M1}^2 & C_{M2}C_{M1} + C_{M3}C_3 & C_{M3}C_{M1} + C_{M2}C_2 \\ C_{M2}C_{M1} + C_{M3}C_3 & C_1C_3 - C_{M2}^2 & C_{M2}C_{M3} + C_{M1}C_1 \\ C_{M3}C_{M1} + C_{M2}C_2 & C_{M2}C_{M3} + C_{M1}C_1 & C_1C_2 - C_{M3}^2 \end{pmatrix} \tag{A.3}$$

where $C_1 = \sum_\nu C_{1\nu}$, $C_2 = \sum_\nu C_{2\nu}$, $C_3 = \sum_\nu C_{3\nu}$ and

$$A = C_1C_2C_3 - 2C_{M1}C_{M2}C_{M3} - C_{M3}^2C_3 - C_{M2}^2C_2 - C_{M1}^2C_1 \tag{A.4}$$

Finally we obtain

$$U = \frac{1}{2}N_1^2E_{C1} + \frac{1}{2}N_2^2E_{C2} + \frac{1}{2}N_3^2E_{C3} + N_1N_2E_{CM12} + N_1N_3E_{CM13} + N_2N_3E_{CM22} + f(V_\nu) \tag{A.5}$$

where we again substituted $Q_{D1} = N_1e^-$,$Q_{D2} = N_2e^-$,$Q_{D3} = N_3e^-$ and further simplified

$$E_{C1} = \frac{(C_2C_3 - C_{M1}^2)e^2}{|A|}; E_{C2} = \frac{(C_1C_3 - C_{M2}^2)e^2}{|A|}; E_{C3} = \frac{(C_1C_2 - C_{M3}^2)e^2}{|A|}; \tag{A.6}$$

$$E_{CM12} = \frac{e^2(C_{M1}C_{M2} + C_{M3}C_3)}{|A|}; E_{CM13} = \frac{e^2(C_{M1}C_{M3} + C_{M2}C_2)}{|A|}; \\ E_{CM23} = \frac{e^2(C_{M2}C_{M3} + C_{M1}C_1)}{|A|} \tag{A.7}$$

and where we combined the terms that depend on the gate voltages into $f(V_\nu)$.

## A.2 Matlab function: Simplified tripledot configuration with minimal energy

In this appendix I give the Matlab function that calculates the energy of a specific triple-dot system for an input of two gate voltages and a list of dot occupations. The dot occupations *permutations* give the allowed subspace of electron configurations (i.e. 001 010 and 001). The output is the configuration with minimal energy.

```
function index=find_minimal_configuration(E07,E10,permutations)
Ec=[0.00325 ,0.0019,0.0025]; %charging energy in eV
alpha=-0.05*[0 0.294 1; %07
    0 0.905 1.2]; %10

%% main code
[n,m]=size(permutations);
E=(permutations).*repmat(sqrt(Ec),n,1); % influence of dot occupation
Evoltage=([E07,E10]*alpha)./sqrt(Ec);
Eg=repmat(Evoltage,n,1); % gate influence

Energies=E+Eg; % sum of contributions of gate influence and electron occupation
Esum=sum(Energies.*Energies,2); %sum up squared contributions of the different
dots
[C,index]=min(Esum); % find minimal configuration
end
```

## A.3 Matlab function: Tripledot configuration with minimal energy

The following Matlab function calculates the minimal configuration with equal input parameters as in Appendix A.2, but for the calculation from Eq. A.5 that includes inter dot capacitances.

```
function index=find_minimal_configuration_coupleddots(E07,E10,permutations)
Ec=[0.00325 ,0.0019,0.0025]; %charging energy in eV
alpha=-0.05*[0 0.294 1; %07
    0 0.905 1.2]; %10
electroncharge=1.6*(10^-19);
Evoltage=electroncharge*([E07,E10]*alpha)./Ec; %in Coulomb (capacitance times
voltage)
Egs=repmat(Evoltage,n,1);%in C
C1=electroncharge/Ec(1);%in Farad
C2=electroncharge/Ec(2);%in Farad
C3=electroncharge/Ec(3);%in Farad
CM1=0.5*C1; %inter-dot capacitance 1
CM2=0.1*C1; %inter-dot capacitance 2
CM3=0.1*C1; %inter-dot capacitance 3
A=abs(C1*C2*C3-2*CM1*CM2*CM3-CM3*CM3*C3-CM2*CM2*C2-CM1*CM1*C1);
permutations=electroncharge*permutations;% in Coulomb
E=0.5/A*((C2*C3-CM1*CM1)*(Egs(:,1)+permutations(:,1)).*(Egs(:,1)+permutations
(:,1)) ...
+(C1*C3-CM2*CM2)*(Egs(:,2)+permutations(:,2)).*(Egs(:,2)+permutations(:,2))...
+(C1*C2-CM3*CM3)*(Egs(:,3)+permutations(:,3)).*(Egs(:,3)+permutations(:,3))...
+2*(CM1*CM2-C3*CM3)*(Egs(:,1)+permutations(:,1)).*(Egs(:,2)+permutations(:,2))...
+2*(CM1*CM3-C2*CM2)*(Egs(:,1)+permutations(:,1)).*(Egs(:,3)+permutations(:,3))...
+2*(CM2*CM3-C1*CM1)*(Egs(:,2)+permutations(:,2)).*(Egs(:,3)+permutations(:,3))...
); %sum up squared contributions of the different dots
[C,index]=min(E); % find minimal configuration
end
```

# APPENDIX B

## Effective Hamiltonian including the spin degree of freedom in double and triple quantum dot systems

### B.1 Double quantum dot Hamiltonian

In this appendix we give the explicit operators of the simple model of two spins in a double quantum dot discussed in 1.4.3. The Hamiltonian introduced previously was given by

$$H = \begin{pmatrix} H_{20} & T & 0 \\ T & H_{11} & T \\ 0 & T & H_{02} \end{pmatrix} \tag{B.1}$$

In the basis of the three charge configurations $|20\rangle$ (both electrons left), $|11\rangle$ (electrons split) and $|02\rangle$ (both electrons right). The Hamiltonian for two spins in the left quantum dot is given by

$$H_{20} = \begin{pmatrix} 2\varepsilon_L + E_C - E_Z + J_{Ex} & 0 & 0 & 0 \\ 0 & 2\varepsilon_L + E_C & J_{Ex} & 0 \\ 0 & J_{Ex} & 2\varepsilon_L + E_C & 0 \\ 0 & 0 & 0 & 2\varepsilon_L + E_C + E_Z + J_{Ex} \end{pmatrix} \tag{B.2}$$

where $\varepsilon_L$ is the energy of the left dot, $E_C$ the charging energy, $E_Z$ the Zeeman energy due to an externally applied magnetic field and $J_{Ex}$ the exchange energy of the electrons.

Similarly the Hamiltonian for two spins in the right quantum dot is given by

$$H_{02} = \begin{pmatrix} 2\varepsilon_R + E_C - E_Z + J_{Ex} & 0 & 0 & 0 \\ 0 & 2\varepsilon_R + E_C & J_{Ex} & 0 \\ 0 & J_{Ex} & 2\varepsilon_R + E_C & 0 \\ 0 & 0 & 0 & 2\varepsilon_R + E_C + E_Z + J_{Ex} \end{pmatrix} \tag{B.3}$$

where $\varepsilon_R$ is the energy of the right quantum dot, while charging energy and exchange energy are considered to be equal. For the case of two electrons split between the two quantum dots the Hamiltonian is given by

$$H_{11} = \begin{pmatrix} -E_Z + \varepsilon_L + \varepsilon_R & 0 & 0 & 0 \\ 0 & \varepsilon_L + \varepsilon_R & 0 & 0 \\ 0 & 0 & \varepsilon_L + \varepsilon_R & 0 \\ 0 & 0 & 0 & E_Z + \varepsilon_L + \varepsilon_R \end{pmatrix}. \tag{B.4}$$

Finally the three charge configurations are coupled by a tunnel-coupling $t$ leading to the coupling matrix

$$T = \begin{pmatrix} t & 0 & 0 & 0 \\ 0 & t & 0 & 0 \\ 0 & 0 & t & 0 \\ 0 & 0 & 0 & t \end{pmatrix}. \tag{B.5}$$

## B.2 Spin Hamiltonians for the tunnelcoupled triple quantum dot

In this Appendix, we give a simple spin Hamiltonian for the tunnel-coupled triple quantum dot. It was obtained by extending the established model for double quantum dot presented in the previous section. We hereby consider two spins in three tunnel-coupled quantum dots that experience an instantaneous magnetic field gradient (i.e. due to hyperfine interaction). The quantum dos are tunnel-coupled one-by-one and only single electron tunnelling events are considered. The reduced state space is given by the product space of 4 possible spin configurations $\{|\uparrow\uparrow\rangle, |\uparrow\downarrow\rangle, |\downarrow\uparrow\rangle, |\downarrow\downarrow\rangle\}$ and the 6 possible charge configurations for the electrons $\{|LL\rangle, |RR\rangle, |DD\rangle, |LR\rangle, |RD\rangle, |LD\rangle\}$. The charge positions are hereby identified by the positions of the electrons in the left ($L$), right ($R$) and bottom ($D$) quantum dots.

In the basis of the charge states our model Hamiltonian is then given by

$$H = \begin{pmatrix} H_{LL} & 0 & 0 & T & 0 & T \\ 0 & H_{RR} & 0 & T & T & 0 \\ 0 & 0 & H_{DD} & 0 & T & T \\ T & T & 0 & H_{LR} + H_{LR}^* & T_i & T \\ 0 & T & T & T_i & H_{RD} + H_{RD}^* & T \\ T & 0 & T & T & T & H_{LD} + H_{LD}^* \end{pmatrix} \tag{B.6}$$

where $H_{ij}$ are the spin Hamiltonians for the electrons in the quantum dots $i$,$j$ and $T/T_i$ are tunnel matrices coupling the different charge states with a given tunnel-coupling.

The spin Hamiltonian for double occupancy of one quantum dot is given by

$$H_{ii} = \begin{pmatrix} 2\varepsilon_i + E_C - E_Z(B) + J_{Ex} & 0 & 0 & 0 \\ 0 & 2\varepsilon_i + E_C & J_{Ex} & 0 \\ 0 & J_{Ex} & 2\varepsilon_i + E_C & 0 \\ 0 & 0 & 0 & 2\varepsilon_i + E_C + E_Z(B) + J_{Ex} \end{pmatrix} \tag{B.7}$$

where $\varepsilon_i$ is the energy of the dot in position $i$, $J_{Ex}$ the exchange energy, $E_Z(B)$ the Zeeman energy due to an external magentic field applied along the $z$-direction and $E_C$ the charging energy.

For the split configurations the spin Hamiltonian is given by

$$H_{ij} = \begin{pmatrix} \varepsilon_i + \varepsilon_j - E_Z(B) & 0 & 0 & 0 \\ 0 & \varepsilon_i + \varepsilon_j & 0 & 0 \\ 0 & 0 & \varepsilon_i + \varepsilon_j & 0 \\ 0 & 0 & 0 & \varepsilon_i + \varepsilon_j + E_Z(B) \end{pmatrix} \tag{B.8}$$

and is perturbed by the presence of the instantaneous hyperfine induced nuclear field

$$H_{ij}^* = \begin{pmatrix} E_{dBz}(i) + E_{dBz}(j) & E_{dBx}(j) - iE_{dBy}(j) & E_{dBx}(i) - iE_{dBy}(i) & 0 \\ E_{dBx}(j) + iE_{dBy}(j) & E_{dBz}(i) - E_{dBz}(j) & 0 & E_{dBx}(i) - iE_{dBy}(i) \\ E_{dBx}(i) + iE_{dBy}(i) & 0 & -E_{dBz}(i) + E_{dBz}(j) & E_{dBx}(j) - iE_{dBy}(j) \\ 0 & E_{dBx}(i) + iE_{dBy}(i) & E_{dBx}(j) + iE_{dBy}(j) & -E_{dBz}(i) - E_{dBz}(j) \end{pmatrix} \tag{B.9}$$

where $E_{dBz}(i)$ gives the effective instantaneous magnetic field acting on the electron in position $i$ along $z$ ($x$,$y$).

Finally the tunnel-matrices are given by

$$T = \begin{pmatrix} t & 0 & 0 & 0 \\ 0 & t & 0 & 0 \\ 0 & 0 & t & 0 \\ 0 & 0 & 0 & t \end{pmatrix} \tag{B.10}$$

and

$$T_i = \begin{pmatrix} t & 0 & 0 & 0 \\ 0 & 0 & t & 0 \\ 0 & t & 0 & 0 \\ 0 & 0 & 0 & t \end{pmatrix} \tag{B.11}$$

where $t$ is the tunnel-coupling energy. $T_i$ hereby implements circular boundary conditions, such that a single spin traversing in a circle is not flipped after one turn due to the parametrisation.

# APPENDIX C

## Charge control of multi-dot systems

### C.1 Discrepancies in the electrostatic potential calculation of polygons

During an analysis of the calculation of Davies et al.[139] performed to calculate the electrostatic gate potential at the quantum dot position discussed in 3.2, we found a discrepancy in their calculation for the polygon shape. This is highlighted by a calculation of the potential from a rectangular gate in Fig. C.1. The calculation is performed once with the result by Davies et al. for rectangles in Fig. C.1(a) and once for the result of a polygon with the same shape in Fig. C.1(b). The two potentials are observed to differ at positions below the gate and close to the vertices of the structure. The rectangle can also be formed with a combination of 2 triangles and the same calculation result as for the rectangle calculation is obtained. The fact that the potential generated by the "polygon calculation" is not differentiable along projections of the sides of the polygon is another hint at a problem with the calculation. We therefore implemented the triangulation method discussed in 3.2 to decompose polygons and calculated the electrostatic potential from the composing triangles. This allowed to circumvent the presented inconsistencies without the need to simplify the complex gate structures used to form the quantum dots for the calculation of the electrostatic potential.

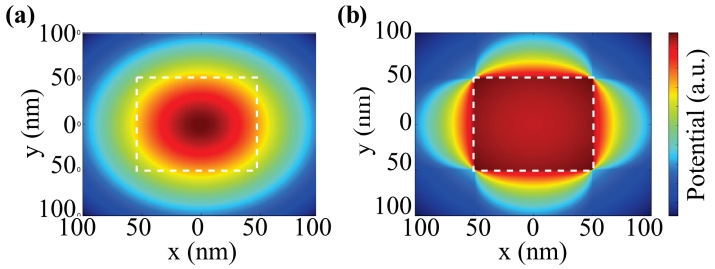


**Figure C.1:** Simulation of the electrostatic potential generated by a square gate with different methods. The calculation is based on the numerical result obtained by Davies et al.[139] for different geometric shapes. The dashed white lines indicate the position of the gate. **(a)** Simulation of the potential by calculating the potential of the polygon formed by the corners of the square gate. **(b)** Simulation of the potential by calculating the potential of the rectangular shape of the square gate.

## C.2 Circular coupling in the quadruple dot device

Following the demonstration of R. Thalineau of a circularly coupled quadruple quantum dot device,[108] we intended to use an improved version of his original design to show coherent transport in a closed loop. In this appendix, we give an analysis of the difficulties to realize circular coupling in the device that was already discussed in 3.5. The sample is given in Fig. C.2(a) with the expected quantum dot positions for the circular coupling case indicated by dashed white circles. An electrostatic simulation for the case of symmetric gate voltages is shown in Fig. C.2(b). The electrostatic simulation reveals a clover like potential structure with a slightly elevated potential in the middle.

In this symmetric gate configuration, the sample was measured in a regime where the quantum dots are well coupled to the reservoirs. A stability diagram close to zero electrons in the structure is shown in the upper part of Fig. C.3. The charge degeneracy lines are highlighted with black dashed lines to highlight different slopes. Unlike our assumption of only 4 quantum dots in the structure, we can clearly observe 5 different slopes for the charge degeneracy lines. This corresponds to 5 different quantum dot positions that have different couplings to the varied gates. By moving different gate voltages and from an analysis of the slopes, all lines can be related to a position in the quantum dot structure. We hereby make use of the fact, that the influence on the potential minima depends on the distance to the respective gates. The occupation numbers for the 5 quantum dots are given in the diagram assuming the clover like structure evident in the electrostatic simulation of the potential profile.

To realize circular coupling with only four quantum dots, the voltage on all red gates needs to be increased. This leads to an increase of the energy of the center dot. However,

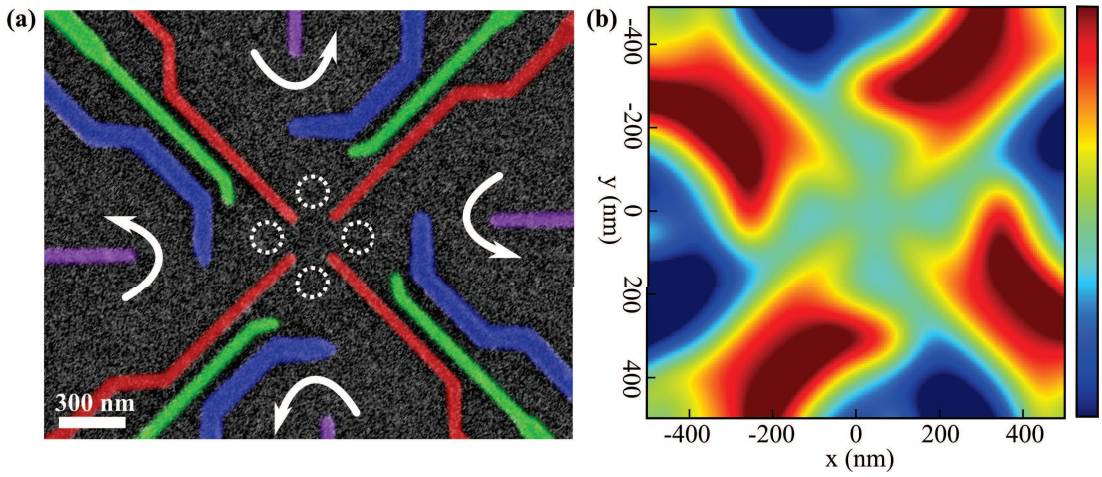


**Figure C.2:** **(a)** False color SEM image of the fabricated sample design. The tunnel gates are colored in red, the barrier defining gates in blue and the added plunger gates are colored in green. The QPCs are defined by the violet gates. **(b)** Electrostatic simulation of the sample in (a). The coloring encodes the potential height as shown on the bar to the right. Red corresponds to high potential while blue corresponds to low potential.

it also resulted in very low coupling between the outer dots as demonstrated in the lower part of Fig. C.3. Here again two adjacent plunger gates (green) are varied at a position close to an inter-dot charge transition. The resulting stability diagram reveals a very narrow inter-dot exchange region that shows a diamond shaped region with sharply varying conductance. In this part of the diagram, the electron occupation jumps abruptly between the two states with a frequency comparable to the measurement frequency (50 Hz). This means that the inter-dot exchange is very slow such that the equilibrium state after an excitation is not reached faster than the measurement time. Similar diagrams have recently been obtained in a double dot with very weak tunnel-coupling by another group and were explained with a model of inter-dot exchange mediated by the occupation of metastable states with different total electron number.[162] The electron transfer is therefore mediated by the coupling to the reservoirs.

This finding leads to a small predicament as there is a compromise between the energy of the center dot and the tunnel-coupling between the four outer dots. These five parameters are controlled by the only four tunnel gates (red in Fig. C.2). Lowering (increasing) the voltage on the tunnel gates reduces (increases) both the potential of the center dot as well as the tunnel-coupling between the outer dots. As our initial situation is also unfavourable for circular coupling, the necessary conditions for high coupling will only be fulfilled locally (only for few dots at a time) in the parameter space. This high coupling is however required

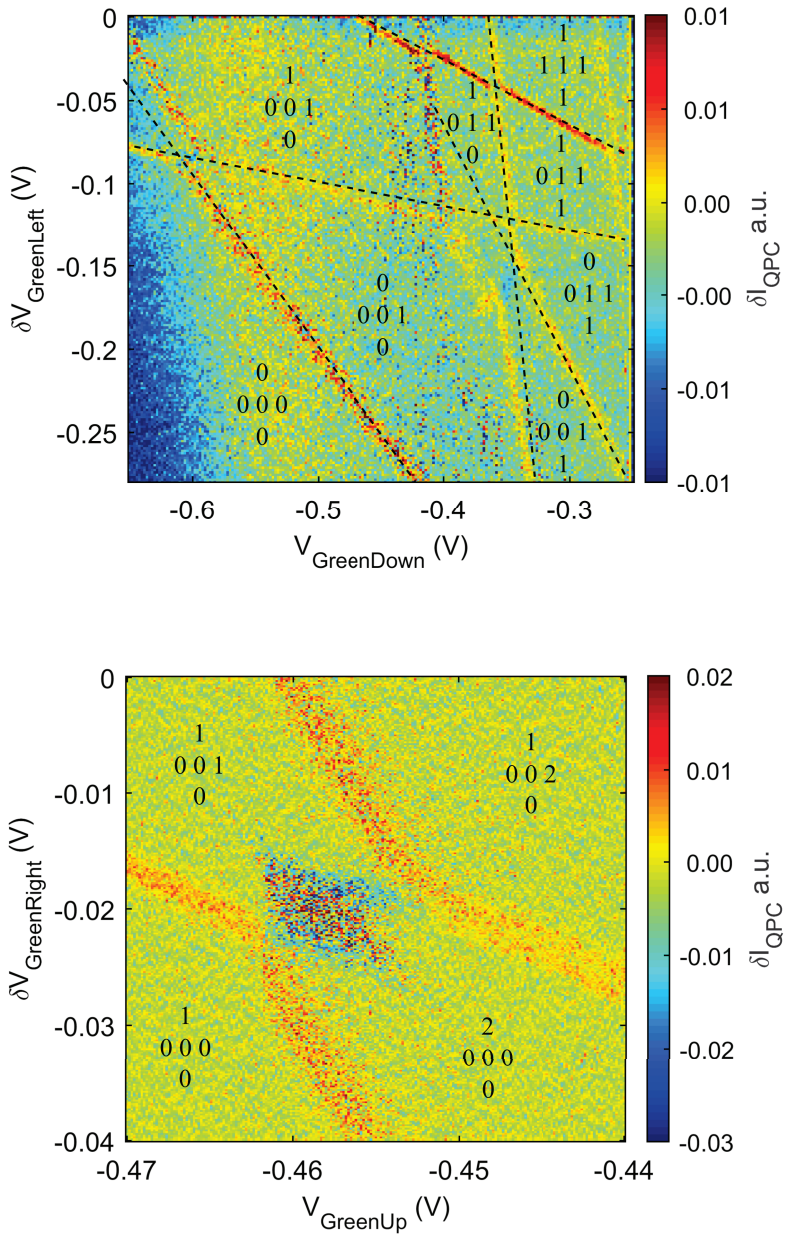


**Figure C.3: (Upper)** Stability diagram of the quadruple dot sample when the 5th dot is not raised in energy. The different slopes corresponding to the charge degeneracy of the five dots are emphasized by black dashed lines. The corresponding electron numbers obtained by varying other gates are added for clarity. **(Lower)** Stability diagram close to the inter-dot exchange region of two outer quantum dots. Electron occupation numbers are added for clarity. The stochastic region at the degeneracy (blue and red dots) correspond to an inter-dot exchange which is slower than the measurement time (20 ms per point).

for coherent transport of electrons. We therefore concluded, that the present sample design was not sufficient to perform coherent transport in a loop of four quantum dots.

## C.3 Discussion of the stochastic tunnelling events observed for mediated electron exchange in the linear chain of quantum dots

In Fig. 3.9(a), the charge state was heavily fluctuating between (100) and (001) close to the corresponding charge transition. We attributed this exchange to a mediated transition via virtual occupation of the center quantum dot. In this appendix, we analyse the stochasticity of the observed charge state and compare it to similar measurements observed in the literature.

The stochastic tunnelling events at $V_{\mathrm{RedBottomRight}} \approx 0.62$ V are found to be similar to the experimental signatures recently observed by Biesinger et al. of a double quantum dot at low tunnel-coupling.[162] In their experiment, they measured a strong fluctuation of the charge occupation close to an inter-dot transition. They explained this observation with a thermally excited occupation of a metastable state with different electron number. This allows a change of dot occupation even in the absence of direct inter-dot exchange. In our experiment, the connections to the reservoirs are cut. Therefore the proposed process of electron exchange with the reservoirs is not possible. The only available state for a similar process in our system is the metastable occupation of the center quantum dot. The observed experimental similarity in the dynamics to the experiment by Biesinger et al. hints at a thermal excitation of an electron to the center quantum dot followed by a tunnelling event to the other quantum dot. The necessary energy for such a process can hereby be provided by the QPC bias window. The observed metastability of the charge state is therefore consistent with our assumption that the exchange between the left dot and the right dot is mediated by the center dot.

## C.4 Photon assisted tunnelling in the isolated configuration

To obtain a direct energy reference of the stability diagram and thereby determine quantitatively correct values for the charging energies and gate capacitances, one can perform photon-assisted-tunnelling (PAT) with a reference frequency.[146] In this measurement, a radio-frequency (RF) signal is applied on one of the gates. This allows the quantum dot to absorb photons from the field and transitions between levels become possible when the level splitting is equal to a multiple of the photon energy. When the excitation is faster than tunnelling processes, this induces a duplication of inter-dot exchange lines, where the splitting can be used as a direct energy reference of $E = hv$. In this appendix we show such a measurement in the isolated configuration.

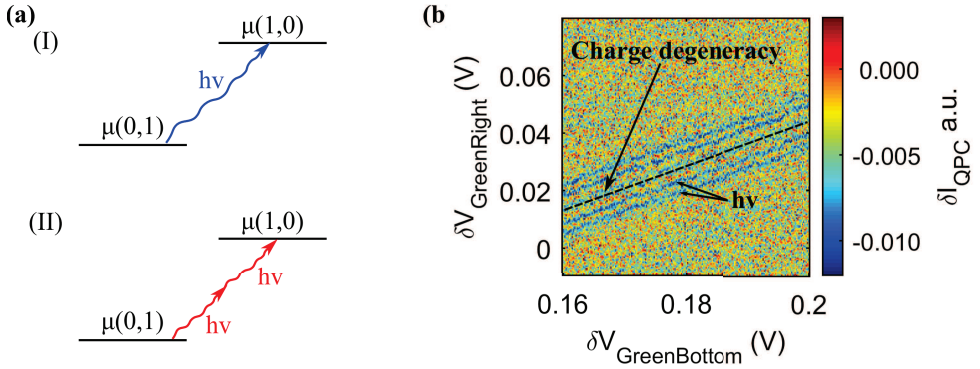


**Figure C.4:** **(a)** Schematic of the photon assisted tunnelling (PAT) process that leads to the emergence of exchange lines detuned from the crossing by multiples of the photon energy for the cases of single- (I) and two-photon (II) absorption. **(b)** Experimental measurement of the PAT induced images of an inter-dot crossing. Derivative of the left QPC current as a function of $V_{\mathrm{GreenBottom}}$ and $V_{\mathrm{GreenRight}}$. The stability diagram was measured in a triple-dot sample with an applied RF signal of 15.9 GHz with a microwave power of -48 dBm (0.9 mV rms signal). The position of the charge degeneracy line is emphasized with a black dashed line.

A schematic of the PAT process is shown in Fig. C.4(a) for single- and two-photon absorption. For this process the photon energy has to be bigger than the tunnel-coupling. Then a transition from one configuration to the other can be made when the energy difference is equal to the photon energy. Such a measurement in the isolated regime is performed in Fig. C.4(a), with a microwave signal at 15.9 GHz applied on one of the gates. In the stability diagram, we can see several parallel lines that are equally spaced around the position of the charge degeneracy (black dashed line). From the splitting $\Delta \approx 3.2$ mV and the photon energy $hv = 65$ μeV we can deduce a gate efficiency of $\alpha \approx 0.02e$ for the plunger gates on the detuning.

# APPENDIX D

## Spin manipulation in multi-dots

### D.1 S-$T_+$ mixing position as a function of magnetic field

In this section of the appendix we give the measurement of the $|S\rangle$-$|T_+\rangle$ mixing position as a function of magnetic field. To perform the measurement, first a singlet state is initialised in the quantum dot and then a 50 ns pulse of varying amplitude is applied close to point B in Fig. 4.5. The triplet probability is again recorded via spin-to-charge conversion and averaged to infer the triplet mixing probability. The measurement of the peak in the triplet probability as a function of magnetic field is given in Fig. D.1. As the magnetic field is

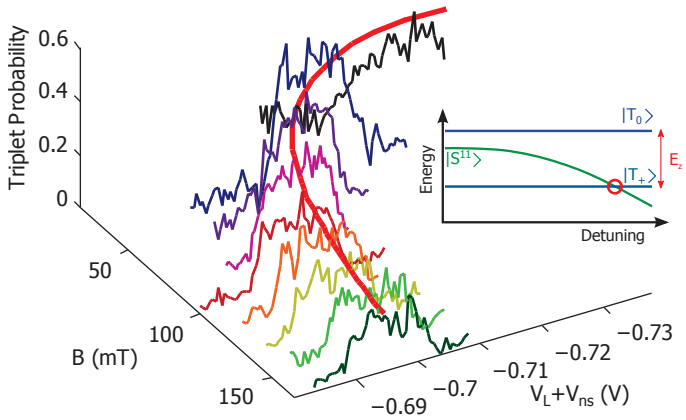


**Figure D.1:** Variation of the $|S\rangle$-$|T_+\rangle$ mixing position with the magnetic field in the isolated double dot experiment. The position of the the peak is traced with an exponential to illustrate the evolution. The inset shows a schematic of the energy dispersion of the $S$, $T_0$ and $T_+$ states as a function of detuning. A red circle indicates the $S$-$T_+$ crossing position. The dispersion of the singlet branch amplifies the small energy shift of the Zeeman energy $E_Z$ in detuning direction and therefore makes the difference in magnetic field measurable. Data taken with permission from the author from [141].

lowered, the observed peak in the triplet probability is shifted to larger detuning values. The center of the peak is traced with a red line to illustrate the evolution. The observed movement is expected for a $|S\rangle$-$|T_+\rangle$ mixing, as the change of the Zeeman energy of the triplet state leads to a different crossing position with respect to detuning as illustrated in the inset of Fig. D.1. The dispersion of the singlet branch hereby leads to an amplification of the change of Zeeman energy (µeV) along the detuning axis (meV) making the effect observable. This measurement allows to identify the observed peak with the $|S\rangle$-$|T_+\rangle$ mixing position. At the mixing position, the exchange coupling is equal to the Zeeman energy $J(\varepsilon) = E_{\mathrm{Zeeman}}(B)$.[31] The red curve in Fig. D.1 can therefore be used to calculate the dependence of the exchange coupling on the detuning.

## D.2 Spin mixing maps for slightly unbalanced inter-dot couplings

In 4.4.3 we have only given spin mixing maps for the case of balanced inter-dot coupling. However, the obtained spin mixing map depends strongly on the exact coupling strengths in between each quantum dot and is strongly altered for unequal coupling as is shown in this appendix. As an example we give a spin mixing map where the inter-dot couplings are only slightly unbalanced. In this position we also performed a complimentary measurement that highlights the origin of some of the features.

The spin mixing map in the case of an initialized two-electron singlet is given in Fig. D.2(a). The singlet is prepared in the bottom dot and then a 50 ns pulse is applied to the gates to probe the mixing probability at a specific point in the diagram. Then the spin state is measured via spin-to charge conversion and averaged 150 times to obtain the triplet probability. For low pulse amplitudes on $V_{\mathrm{Bottom}}$, the system is brought into the charge configuration where one electron is supposed to tunnel to the left quantum dot. For this case, we observe the gradual rise of the triplet probability up to $\approx 0.45$. A similar observation is made for the case of higher pulse amplitudes on $V_{\mathrm{Bottom}}$, where one electron is transferred to the right quantum dot. The exchange coupling in these two configurations is therefore smaller than the nuclear field gradients. The hyperfine interaction with the nuclei then mixes the $|S\rangle$ and $|T0\rangle$ states.

However, for large pulse amplitudes on both gates, no mixing is observed in a large area. This corresponds to the charge configuration where both electrons are separated into the left and right dot. Following our analysis in 4.4.2, this means that the exchange coupling in between the left and the right dot is larger than the nuclear field gradient. As the eigenstate is singlet in this case, no mixing is expected.

Additionally, there is a clear line perpendicular to the detuning direction of the left and and right dot at which the singlet state is mixed. The position of the line can be moved

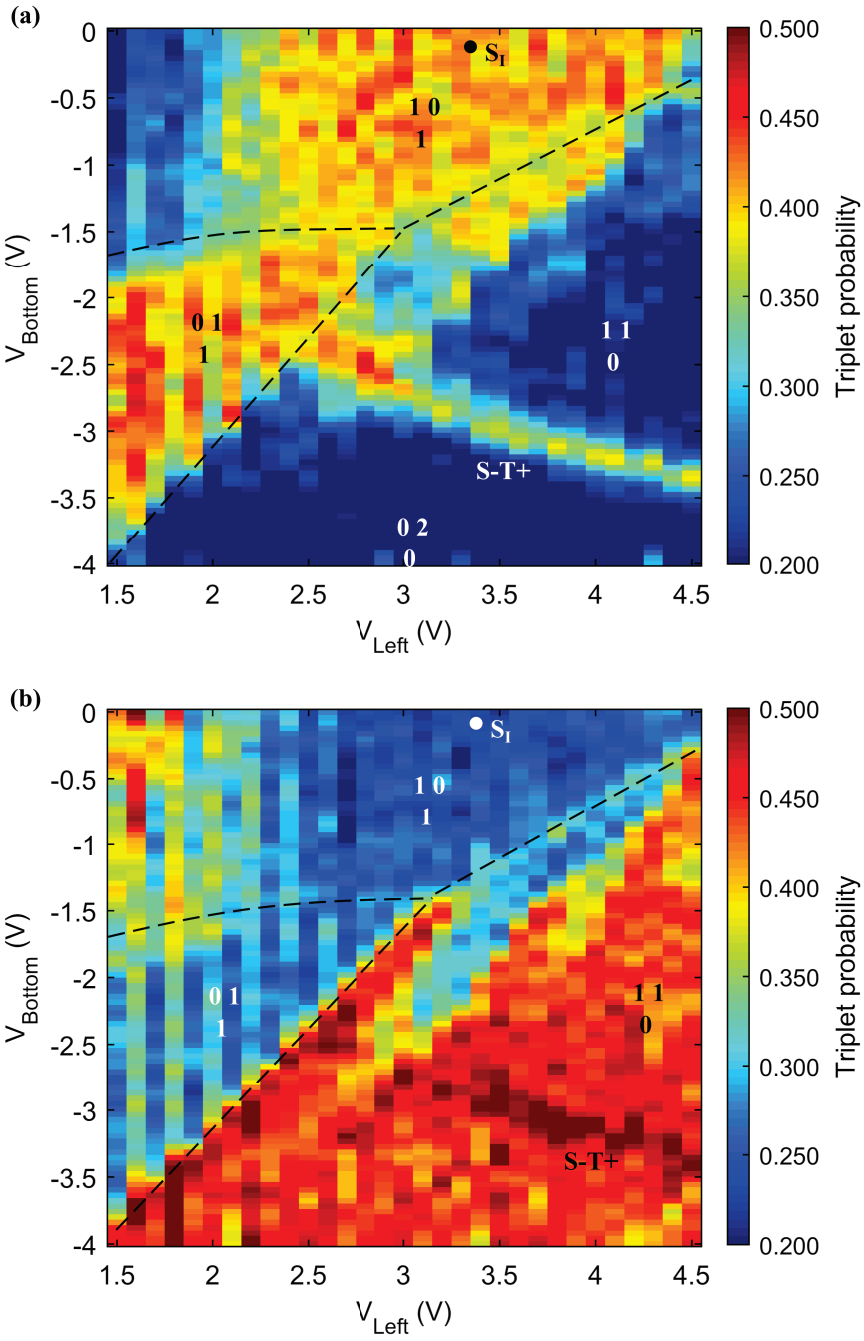


**Figure D.2:** Spin mixing map for different initial states and not perfectly equal inter-dot couplings. Averaged single-shot triplet probability as a function of the amplitudes of simultaneous 50 ns gate pulses on $V_{\mathrm{Left}}$ and $V_{\mathrm{Right}}$. The position of the charge degeneracy lines are indicated by the dashed black lines and the charge configuration was added for clarity. **(a)** A two-electron singlet is initialized in point S in Fig. 4.8 and then two simultaneous 50 ns pulses with varying amplitudes are applied on $V_{\mathrm{Left}}$ and $V_{\mathrm{Bottom}}$ to probe each point of the diagram. **(b)** Instead of starting with singlet as the initial state, we prepare an eigenstate of the nuclear field gradient in point $S_I$ with a 1 µs adiabatic ramp after crossing the $|S\rangle$-$|T+\rangle$ degeneracy. One point of the diagram is then probed for 50 ns and the resulting state measured after an inverse adiabatic ramp.

with magnetic field and when the magnetic field is lowered, a second line appears from the top of the graph (data not shown). We therefore identify it as the $|S\rangle$-$|T+\rangle$ crossing in between the state with two electrons in the right dot and the state with electrons split in between the left and right dots.

The initial state with which the region is probed can also be changed by performing a 1 µs adiabatic ramp to the point $S_I$ before the 50 ns probe pulse. In this way, the system is initialized in an eigenstate of the nuclear field gradient in the $\{|\uparrow\downarrow\rangle, |\downarrow\uparrow\rangle\}$ basis. After the inverse adiabatic ramp, the state is projected back onto the singlet-triplet basis and can be measured. This procedure is similar to the one used for the coherent exchange oscillations. The resulting diagram is shown in Fig. D.2(b) for the same investigated region as in the singlet-probe case.

The diagram shows that the probed region has mostly inverted triplet probability to the previous case, now showing no mixing for the configurations where one electron has been exchanged with the right and left dots, and strong mixing for the case of the electrons split into left and right dot. The $|S\rangle$-$|T+\rangle$ crossing also shows mixing with the probe state, leading to an increased triplet probability when it is probed.

The different mixing behaviour in the three charge configurations allows to infer the relative coupling strengths between the dots following the discussion from 4.4.2. The presence of the $|S\rangle$-$|T+\rangle$ crossings and the missing $|T_0\rangle$-$|S\rangle$ mixing region in between the two lines means, that the tunnel-coupling between the left and right quantum dots is close to, but below $t = 32$ µeV for the left and right dot. The observation of $|T_0\rangle$-$|S\rangle$ mixing in the other two charge configurations signifies that the inter-dot tunnel-coupling is below $t = 7$ µeV between the bottom dot and either of the left or right quantum dots.

For the charge configuration of one electron situated between the left and bottom quantum dot, the $|S\rangle$-$|T+\rangle$ is split off from the $|T_0\rangle$-$|S\rangle$ region. This allowed to initialize the spin state in the $\{|\uparrow\downarrow\rangle, |\downarrow\uparrow\rangle\}$ basis in point $S_I$ to obtain the measurement in Fig. D.2(b). The tunnel-coupling therefore must be larger than the nuclear field gradients $t >> 100$ neV to induce a significantly large splitting of the $|S\rangle$-$|T+\rangle$ crossing

The discrepancy of the charge degeneracy line and the spin mixing region in the top right of the diagram as well as additional measurement close to the (2,0) region indicate, that the coupling in between the bottom and the right dot are slightly too small for fully coherent transport with the sharp rise time of our pulse generator and the coupling is therefore assumed to be slightly smaller than between the bottom and the left dot.

The couplings are therefore almost balanced. An increase of the coupling between the right and bottom quantum dot while at the same time reducing the coupling between the left and right dot is necessary to achieve circular coupling with a high tunnel-rate.

## D.3 Spin mixing map for very low and very high coupling conditions

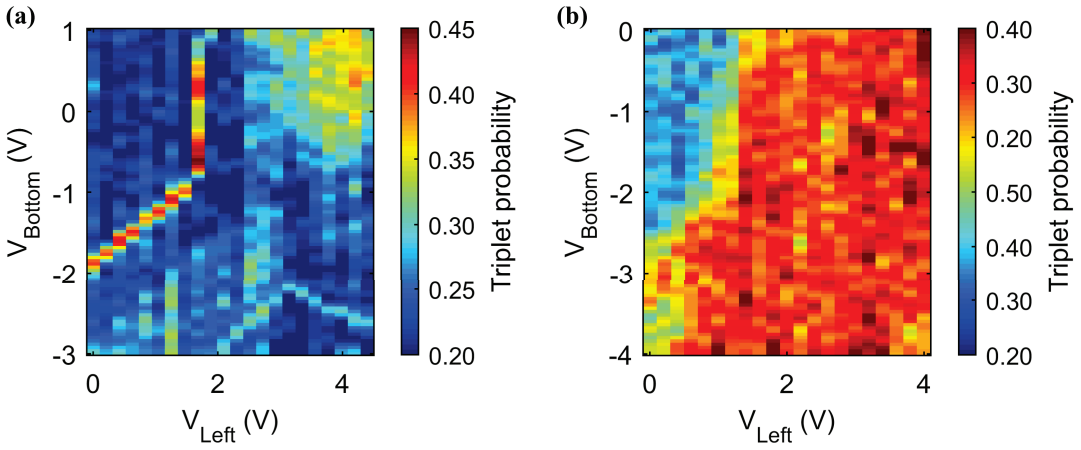


**Figure D.3:** Spin mixing maps for very low and very high inter-dot coupling strengths. The region is probed with a 50 ns pulse and the singlet probability is recorded and averaged to construct the map. **(a)** High coupling condition. The singlet probe almost does not mix any more in the split electron region, but only the $|S\rangle$-$|T_+\rangle$ mixing lines are visible. The mixing region in the top right is associated with not perfectly balanced coupling strength. **(b)** Very low inter dot coupling. The probe pulse is fully mixed once it leaves the region of two electrons in one dot. The absence of further features hints at a non-adiabatic tunnelling process.

In the main text we gave three different spin mixing maps for different inter-dot coupling strengths. In this appendix we also show spin-mixing maps for extremal coupling conditions. In Fig. D.3(a) the case for relatively large inter-dot coupling is presented. In this regime, the exchange energy has become so large, that it suppresses the effect of the nuclear field gradients for almost all detuning configurations. This leads to the observed low probability for $|S\rangle$-$|T_0\rangle$ mixing for electrons split into the right and left dot as well as for the case of electrons split in between the bottom and right dot. The fact that we see a region with a final mixing value of $\approx 0.35$ on the top right of the map shows that the inter-dot couplings are not perfectly balanced and $|S\rangle$-$|T_0\rangle$ mixing is more efficient for electrons split in between the left and bottom dot. However the exchange energy is found to be high for all charge configurations. The observation of the $|S\rangle$-$|T_+\rangle$ mixing lines bounds the coupling strength to be below $t < 32$ µeV by direct comparison with the Zeeman energy following the discussion in 4.4.2.

In Fig. D.3(b), the spin mixing map for very low inter-dot coupling strength is given. In this configuration, the $|S\rangle$-$|T_+\rangle$ mixing lines are no longer observed and the diagram is dominated by a large area of $|S\rangle$-$|T_0\rangle$ mixing. No regions of increased exchange energy in between charge configurations is observed. On the bottom left, we see an increase of the

singlet probability that we attribute to a non-adiabaticity of the probe pulse with respect to the tunnel-coupling. This finding is most likely the reason for the observed difference of the spin evolution during the coherent transfer experiment that was observed in Fig. 4.19 with respect to the configurations with higher tunnel-coupling.

## D.4 Measured output pulse of the function generator for the circular electron motion

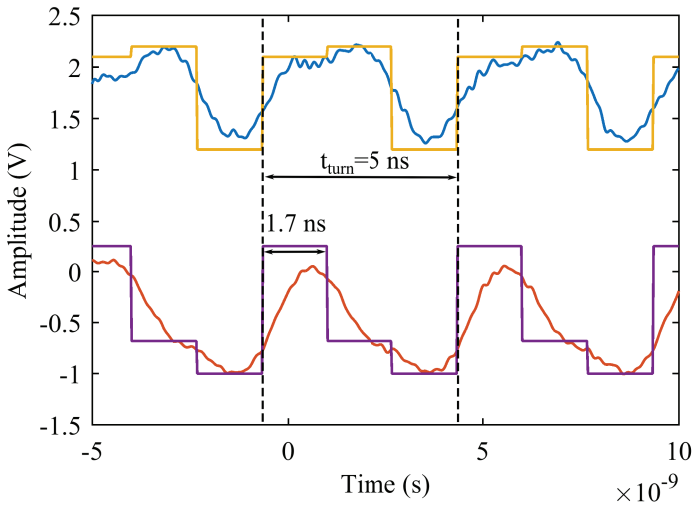


**Figure D.4:** Programmed and resulting waveforms for the transport of two electrons in the circular triple quantum dot. The imposed waveforms are given in yellow and violet for the two involved gates respectively. The output of the arbitrary waveform generator is then sampled with a high bandwidth oscilloscope (16 GHz) to accurately measure the generated waveform. The two waveforms are given in blue and red respectively.

In the measurements of the spin coherence during the turning motion, clear evidence of the limited bandwidth of our function generator was observed. In this appendix we give the directly measured output of the AWG as measured at room temperature with a large-bandwidth sampling oscilloscope. The bandwidth of 16 GHz of the oscilloscope allows to accurately determine the effect of the smaller bandwidth AWG (400 MHz). The measured pulses are given alongside the intended waveform in Fig. D.4 and show that the pulse sequence is strongly warped by the bandwidth of the AWG. The end-positions are only reached for a fraction of the pulse sequence and the evolution is dominated by a constant change of pulse amplitudes. This suggests that at a turning frequency of 5 ns/turn the electrons are constantly moving. This is in accordance with our interpretation of the coherence time in the limit of large turning frequencies.

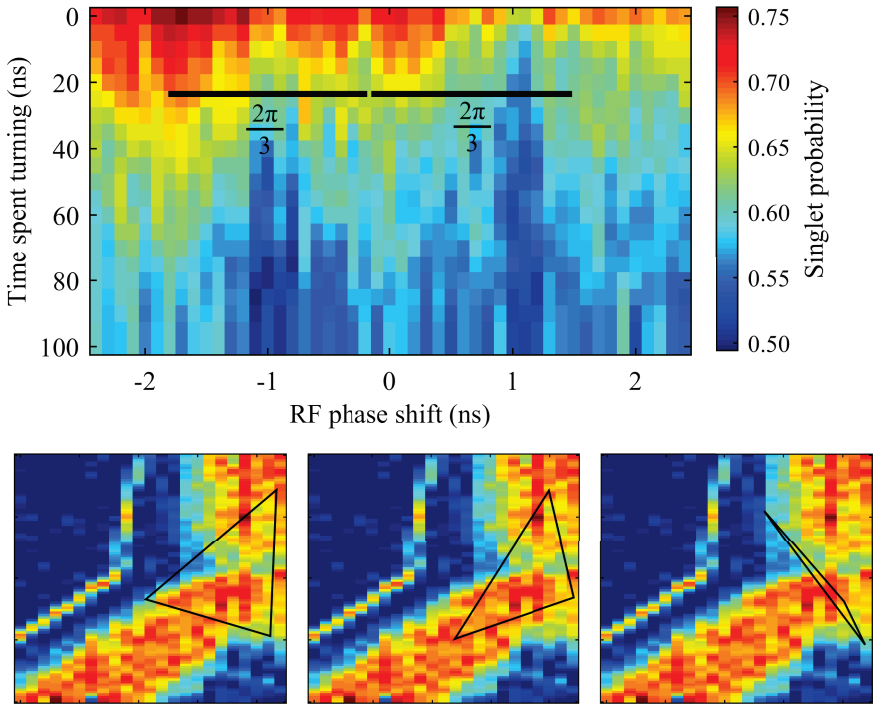


**Figure D.5: (Upper)** Averaged single-shot probability as afunction of $\tau_s$ and a phase delay between the two channels during the turning scheme. The time for one turn is $\tau_{\text{turn}} = 5$ ns. The phase window given on the $x$-axis therefore corresponds to a phase shift of $2\pi$. **(Lower)** Visualization of the warped pulse on the spin mixing map in the three phase positions where the phase shift is $\frac{2\pi}{3}$ and the pulses therefore linearly connect three endpoints. The warped pulses correspond to $-\frac{2\pi}{3}$,0,$+\frac{2\pi}{3}$ going from left to right. The experiment was performed in the medium coupling regime which is exemplified by the corresponding spin mixing map.

## D.5 Pulse synchronization as an error source for the rotational motion

To verify the intended pulse shape and exclude a possible error source, a rotation sequence was performed, where the phase of our two pulse-sequences was intentionally shifted around zero. This leads to a warping of the path in gate space and should therefore affect the decoherence time. The measurement is shown in Fig. D.5. As the time for one turn in this experiment is $\tau_{\text{turn}} = 5$ ns, the phase is shifted by a value of $2\pi$ along the $x$-axis. The dephasing time seems to be maximal for three equally spaced regions with the middle one centered around zero phase shift. In these regions the singlet is conserved longer than between those regions.

We can understand this measurement considering, that for the waveform there will be three possible phase positions where the electrons have fixed endpoints and move only

for a small time between them. The corresponding paths are shown in the lower part of Fig. D.5 on the spin mixing map. For a phase shift of $-\frac{2\pi}{3}$ (left spin mixing map), the electrons also visit all three dots, but at values of high detuning and therefore increased exchange coupling. This is consistent with the first region of slow mixing in the upper part of Fig. D.5 with a phase shift of $\approx -1.7$ ns.

For the case of a phase shift of $\approx +1.7$ ns however, the electrons no longer clearly visit all three configurations but the path is strongly warped as shown on the right spin mixing map. This fact is consistent with the relatively fast decay of the singlet probability in this phase position.

Concluding, this measurement shows good synchronization of the applied pulse sequences. The clear dependence of the coherence time on the phase indicates, that the pulse shape is well reproduced at the sample position. The shape of the performed motion is found to be important for the enhancement of the coherence time. The observed dependence is consistent with the expected motion induced by the different pulse trains. This is an indication for the successful implementation of a rotation sequence at nanosecond timescales.

# Acknowledgments

At the end of the PhD thesis it is also time to thank all the people that have taken part in the experimental work, accompanied me during my life in a foreign country and supported me during the Ups and Downs of this work.

First of all I want to thank my mentors Christopher Bauerle and Tristan Meunier, who have welcomed me in their laboratory and work hard to create an environment where young scientists like me can pursue their ideas free from external constraints. In particular I want to thank my supervisor Tristan who not only guided me throughout these past years, but who often gave me complete freedom over the angle from which I would tackle a problem. At the same time he was always ready to support me when necessary or to discuss the physics of the problem. I think this balance is very critical and allowed me to develop into the person I am now. Most importantly however, he never ceased to encourage me to grow beyond myself and overcome the difficulties during the experiments. I also want to thank Christopher who has introduced me to the intricacies of low temperature physics and his teaching gave me the tools to lay the groundwork for the following experiments. His diligence and structured approach has been integral for the solution of several problems during my work.

While I must thank the whole personnel of the Institut Néel for the warm welcome, I particularly want to thank my colleagues and friends from the "M" building. I can not remember a single time where one of us would not be excited to help another laboratory member. This collegial spirit made our laboratory a special place and allowed for the demanding experiments performed by everyone. I want to thank Tobias and Romain for introducing me to the labwork, from starting a pump to miniature soldering of connectors. I thank Benoit for his readiness to share his insights with me and engage in discussions about isolation and spin measurement. I want to thank Vivien and Gregoire who helped me with nanofabrication in the PTA and the many hours we spent together in the laboratory. I also want to thank Candice, Pierre-André, Shintaro, Marian, Mathias, Matias (the other

one), Guillaume, Olivier, Clement, Baptiste, Hermann Xian and Everton for the time we spent between the cryostats as well as outside the laboratory.

In addition I want to thank the members of the Coherence quantique and Nanospin groups. A special thanks goes to Olivier Buisson and Nicolas Roch who organize our joint group meetings. The informal presentations allowed for everyone to contribute ideas and experience towards the other experiments which lead to fruitful discussions not limited to the weekly format. I also want to thank Wolfgang Wernsdorfer for his advice on cryogenics and presentation quality. The knowledge about low temperature physics he willingly shared with me taught me much about the complexity of dilution cryostat design.

During my work I also interacted with several of the experts in the laboratory and I want to especially thank the members of the *pôle cryogénie* and the *pôle ingénièrie expérimentale* for their support in repairing and maintaining the dilution cryostat I was working with. During my work I could continuously rely on the help of Henry Rodenas whom I want to thank specifically. I am also very grateful for the help of Pierre Perrier, Gilles Pont, Guillaume Donnie Valentin, Julien Jarreau, Eric Eyraud and Laurent Del-Rey who readily provided me with support and advice.

The high quality of our samples would not have been attainable without the diligent work of the members of the *NanoFab* team. I therefore want to thank Thierry Crozes, Thierry Fournier Sebastien Dufresnes, Bruno Fernandez and Gwenaelle Julie for their help and the cheerful atmosphere they were able to create in the clean-room.

The high quality two-dimensional electron gas necessary for this were provided by the group of Andreas Wieck of the University of Bochum and I want to take this opportunity to thank him and and his colleagues for the possibility to work with these extraordinary crystals.

I also thank Sabine Gadal, Florence Pois, Emeline Mendez and Caroline Bartoli for their help in the administrative processes.

I want to particularly thank all the people I met outside the "M"-building, who have shared the past few years in Grenoble with me and who I am happy to call my friends now. I therefore thank Sven Rohr, Anja Backen, John Landers, Dipankar Kalita, Stefan Thiele, Lars Elster, Yani Chen, Cornelia Schwarz, Vitto Han, Katrin Zimmermann, Johanna Seidemann, Joachim Schönle, Iza Petrykiewicz, Kitti Ratter and Sayanti Samada for exciting hikes, cozy cooking evenings and a lot of fun and laughter. Similarly, I want to thank my friends from Germany for their continued support despite the criminally few times I was able to spend time with them during the experimental work for this thesis.

My thanks also go out to my family who not only have supported me during the past years but have also shaped me in the years before. I am very grateful for the bonds we share and your constant encouragement to grow beyond myself.

Finally, I want to thank my wife Farida who had accompanied me to France on her own thesis project and not only supported me, cheered me up and encouraged me during these stressful years for both of us, but who was still ready to marry me at the end of it all. I can call myself extremely lucky to have found you and that you are ready share your life with me. I am excited to see what the future has in store for us!